COMPREHENSIVE CONDITION ASSESSMENT OF ASR AFFECTED PIER CAP AND PIER SHAFT FROM MONTREAL'S CHAMPLAIN BRIDGE

LEAH KRISTUFEK

Thesis submitted to University of Ottawa in partial fulfillment of the requirements for the degree of
DOCTOR OF PHILOSOPHY
In Civil Engineering

Department of Civil Engineering
Faculty of Engineering
University of Ottawa

Abstract

Alkali-Silica Reaction (ASR) is amongst the most harmful damage mechanisms affecting concrete infrastructure in Canada and worldwide. Among ASR affected structures in Canada the Champlain Bridge (CB), a six-lane highway bridge which crossed the St. Lawrence River and St. Lawrence Seaway in the province of Quebec, is a prime example with deterioration leading to closure of the bridge in 2019 after only 57 years in service. During decommissioning of the CB, a number of sections from its structural members (i.e., pier shaft – PS, pier cap – PC) were stored for further coring and analysis. This work presents a comprehensive investigation of an ASR affected PC and PS from the CB including a thorough external appraisal (i.e., comprehensive visual inspection and non-destructive testing) accompanied by laboratory investigation of extracted concrete cores using a multi-level assessment protocol (i.e., microscopic and mechanical test procedures). Microscopic investigations were conducted primarily using the damage rating index and supplemental image analysis while mechanical assessment was conducted through resonant frequency, the stiffness-damage test and compressive testing. This assessment identified ASR as the primary damage mechanism with cores exhibiting high to very high levels of deterioration in both members. Image analysis identified distinct crack orientations in extracted cores corresponding to expected expansion occurring preferentially to the least restrained directions of both the PC and PS members. Finally, a strong correlation between microscopic damage features and mechanical performance of the affected core specimens was observed; induced deterioration was found to be strongly associated to direction, depth and environment of the specimens.

Co-Authorship

All work presented in this thesis was conducted by Leah Kristufek under the supervision of Dr. Sanchez, Dr. Martín-Pérez and Dr. Noël.

Acknowledgements

Thank you to my primary supervisor, Dr. Leandro Sanchez and my co-supervisors, Dr. Beatriz Martín-Pérez and Dr. Martin Noël for their support throughout this thesis project. There were many rounds of both thesis documents and reports, and I appreciate the time taken to provide insightful feedback.

Transitioning to a new university is always a challenge and I very much appreciated the help of Derek, Chloe, Cassandra and Patrick for their kindness helping me get oriented on campus. Specific to the Champlain Bridge project I would like to thank Andisheh for his support during his time as a Postdoc as well as Dana and Issa who made visits to the Montreal storage site possible. Not only did site visits involve drives to Montreal and overnight stays but all three also had to take the multi-day Quebec worksite safety course before site visits were possible. In this project there were also a number of students involved at different stages, including during the original literature review report (Abdulla), during NDT's on the slabs, girders and diaphragms (Nikhil, Haixu and Xiangyu) as well as lab testing more specific to the pier cap and pier shaft (Riley, Rumony and Maria). I would also like to thank the laboratory technical officers, Dr. Elnabelsya and Dr. Majeed, whose support was crucial to completion of this project both through their practical advice and technical support. Similarly, thank you to (newly graduated) Dr. D'Aoust for access to the Environmental lab.

In many ways it took a village to complete this degree. During my time at University of Ottawa I conducted a survey of engineering students' sense of belonging. Thank you to everyone across the engineering faculty who participated in the survey, helped me promote the survey (so many class visits!) and engaged with the results. Hopefully the results posters remain at uOttawa and spark conversations about equity, diversity and inclusion for years to come. Thank you, Dr. Catherine Mavriplis, for the unwavering support of this project even as key deadlines always seemed to happen at the least opportune times. I also very much appreciate how the folks at SEDI have always made me feel welcome.

Last, but certainly not least, I want to thank my Fiancé Donovan and both our families for putting up with me and this graduate degree. I look forward to having more time and energy to spend with everyone.

Table of Contents

List of Figures

List of Tables

List of Abbreviations

Abbreviation	Meaning	Context
Naming		
CB	Champlain bridge	
PC	Pier cap	
PS	Pier shaft	
Damage Mechanisms		
AAR	Alkali-aggregate reaction	
ASR	Alkali-silica reaction	
DEF	Delayed Ettringite formation	
FT	Freeze-thaw	
ISR	Internal swelling reaction	
Tests performed		
DRI	Damage rating index	Microscopic testing
ER	Surface Electrical Resistivity	Non-destructive testing
RBH	Rebound Hammer	Non-destructive testing
RF	Resonant frequency	Mechanical testing (non-destructive)
RE	Residual expansion	Prognostic testing
SDT	Stiffness damage test	Mechanical testing (5 loading cycles)
UPV	Ultrasonic pulse velocity	Non-destructive testing
FIJI ImageJ		Software for image processing
Variables- microscopy		
CAD	Coarse aggregate debondment (aka debon)	
CCA	Closed cracks in coarse aggregate	
CCP	Crack in cement paste	

CCP_RP	Crack in cement paste with reaction product	
DAP	Disaggregated particle	
OCA	Open crack in aggregate	
OCA_RP	Open crack in aggregate with reaction product	

Variables - Mechanical

ME	Static youngs modulus of elasticity	Calculated from SDT in GPa
Dynamic ME	Dynamic young's modulus of elasticity [GPa]	Calculated from the RF test in GPa
f'c	Compressive strength (cylinder)	
NLI	Non-linearity Index	
PDI	Plastic Deformation Index	
SDI	Stiffness Damage Index	

Chapter 1: Introduction

1.1 General

Concrete infrastructure, including reinforced concrete highway bridges and overpasses, are a critical part of Canada's transportation network, facilitating transport of both people and goods. However, concrete infrastructure deteriorates over time with harsh climate conditions often accelerating the degradation process, this highlights the need for timely and effective condition assessments of infrastructure assets. Montreal's Champlain Bridge is an example of a reinforced concrete highway bridge that developed signs of distress over its 57 years in service with increasing severity ultimately leading to premature closure in 2019. Deterioration mechanisms which are most common in Canada include freeze-thaw cycles, reinforcement corrosion due to the use of de-icing salts and alkali-silica reaction (ASR). Among these, ASR, a chemical reaction between unstable mineral phases of aggregates used to make concrete and the alkali hydroxides from the concrete pore solution, presents a significant threat to concrete infrastructure leading to important durability and serviceability issues.

ASR is often called 'concrete cancer' due to the ability of this mechanism to develop throughout affected structures, eventually leading to significant reductions in mechanical properties. The threat of ASR has led to extensive research worldwide to understand the factors involved in the development of this damage mechanism, accompanied by engineering tools to establish the cause and extent of damage. However, data from field structures affected by ASR induced damage continues to be limited, presenting a significant gap in current knowledge. Currently, reinforced concrete bridges constructed between the mid 1950's and early 1980's represent the largest group of bridges with advanced levels of deterioration, due to the age of the structures coupled by rapid innovations in concrete technology during that period. During this period changes such as the use of chemical admixtures (i.e., air entrainment and water reducers), were introduced to address durability issues such as freeze-thaw but inadvertently increased the prevalence of durability issues such as ASR. As these structures approach the end of their service life it becomes increasingly difficult to perform accurate condition assessments due to higher uncertainty in the progression of deterioration coupled with the presence of previous repair works.

Comprehensive assessments of ASR affected field structures are extremely limited in literature. While this is due in part to necessary confidentiality requirements and limitations on accessible areas of in-service structures, it nevertheless reduces the ability of engineers to interpret signs of deterioration in reinforced concrete structures affected by ASR and determine the cause and extent of damage. Conventional condition assessment techniques consist of visual assessments and non-destructive testing followed by the extraction of cores only when high levels of deterioration are indicated biasing assessments to detect mechanisms such as freeze-thaw and corrosion which disproportionately impact the surface. Further, due to stresses present in field structures, ASR may develop in an anisotropic manner impacting interpretation of results.

The demolition of Montreal's Champlain Bridge provided a unique opportunity to perform a comprehensive condition assessment of reinforced concrete structural members. Research specimens were provided to the University of Ottawa by Jacques Cartier and Champlain Bridges Incorporated (JCCBI) following decommissioning of the Bridge due to severe deterioration in reinforced concrete members. The selected pier cap (PC) and pier shaft (PS) segments exhibited different service environments (dry vs. submerged, different loading conditions) and repair histories (the pier cap underwent an encapsulation repair and external post-tensioning). Demolition further permitted extensive coring of the investigated members and visualization of internal reinforcement due to dissection of the members. Comprehensive visual assessment and non-destructive testing were conducted on both the PC and PS members to facilitate linking of external and internal damage. Cores were subsequently extracted and assessed utilizing a multi-level assessment as proposed by Sanchez et al. [1–6] (i.e. microscopic and mechanical). This work provides a valuable contribution to current knowledge about ASR in field structures, facilitating a greater understanding of the development of this mechanism in structural members. The three key stages of this work are presented in Figure 1-1.

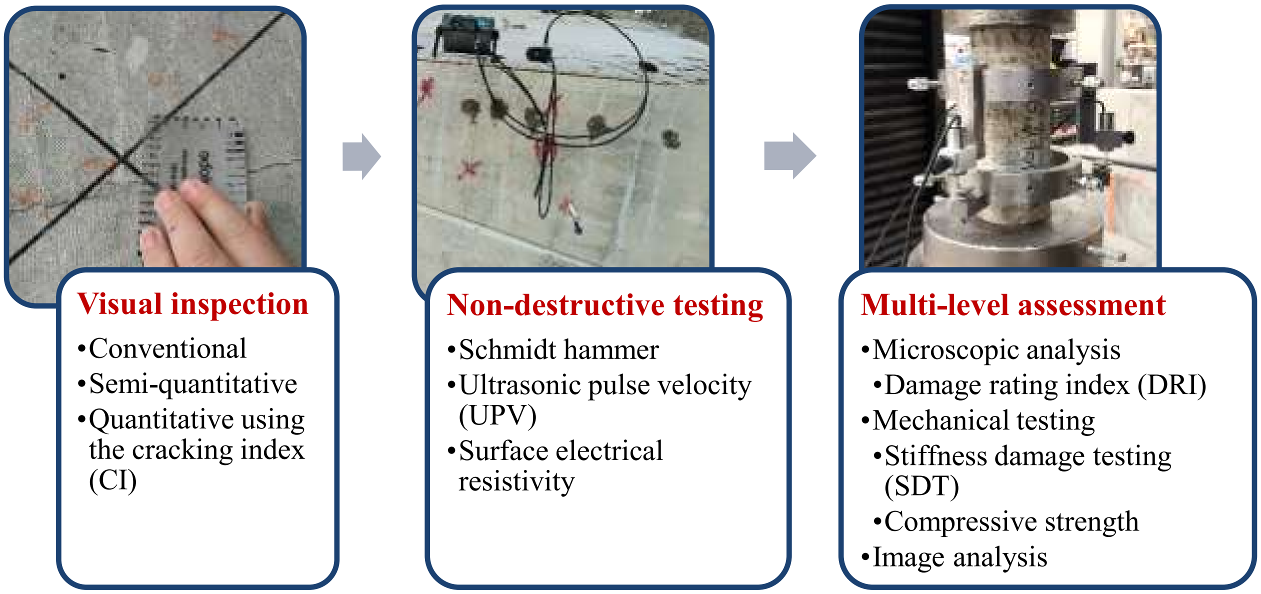

Figure 1-1 Summary of key stages in experimental research program

1.2 Objectives

The main objectives of this project are outlined below:

1. Evaluate the efficiency of conventional visual and non-destructive techniques such as the cracking index, Schmidt hammer, ultrasonic pulse velocity and corrosion measurements to assess the condition of deteriorated segments of a PC and PS extracted from the Champlain Bridge.
2. Use state of the art techniques (i.e. the multi-level assessment protocol which combines microscopic and mechanical testing) on cores extracted from the pier cap and pier shaft to diagnose (i.e., find the cause and extent) of deterioration in these members.
3. Identify impact of restraint and exposure conditions on induced damage in the PC and PS members.
4. To adapt and optimize the use of the multi-level assessment to understand specific parameters related to the overall deterioration of the members such as crack orientation and resultant impact on mechanical properties (i.e. impact of anisotropy).

1.3 Research significance

This work presents a comprehensive condition assessment of the materials level damage in two ASR affected reinforced concrete members, a PC and PS, from a field structure. The condition assessment is considered to be comprehensive because it spans external (i.e. visual and non-destructive testing) and internal (i.e. assessment of concrete cores) assessment using both conventional and state of the art techniques. Furthermore, because the PC and PS members had been removed from the bridge an unusually large number of core specimens were removed allowing a highly in-depth evaluation of the influence of coring direction, proximity to reinforcement (i.e. variations in stress state), impact of repairs and service environments (e.g. semi-submerged and dry regions present in the PS). The in-depth analysis further focuses on the influence of these factors on the development of directional properties within members from ASR reaction products through the proposal of two image analysis procedures, expanding knowledge in an area of ASR development which is currently poorly understood.

In the first portion of the work, qualitative and quantitative visual assessments and non-destructive testing were conducted to evaluate how differences within the members (i.e. orientation of surfaces, wet vs. dry) and between the members (i.e. different geometry, previous repairs) impacted visual and NDT outcomes. The research findings are expected to improve understanding of the relationship between internal concrete damage due to ASR and visual and non-destructive test results for these reinforced concrete members. Extended analysis of qualitative and quantitative visual testing (i.e. observed crack orientations and measured crack widths) will further provide a link to future work evaluating concrete cores.

Concrete cores extracted from the PC and PS were evaluated using a multi-level testing protocol (i.e. microscopic and mechanical assessments). Cores were extracted in three distinct directions (i.e. longitudinally, transversally, and vertically) and distinct service conditions (i.e., tensile vs. compressive regions, dry vs. semi-submerged) from both members. Microscopic testing was conducted using the DRI, conventional and extended versions of the DRI, and supplementary image analysis techniques (i.e. measurement of crack widths and visualization of crack patterns). Mechanical assessment was conducted on cores using non-destructive methods such as resonant frequency (RF) and mechanical procedures including SDT and compressive strength testing. The multi-level assessment protocol was used to combine results of the microscopic and mechanical tests to understand the main cause(s) and extent of deterioration encountered in the members and exhibits the applicability of this protocol for cores from field structures.

Analysis of results focuses on the influence of the orientation of extracted cores (i.e. vertical, transverse, or longitudinal), location of core specimens within the member (i.e. surface vs. interior), impact of geometry (i.e. level of restraint), and service environment (e.g. dry vs. semi-submerged regions) on damage in the specimens. The results are analyzed alongside supplementary image analysis to examine the influence of crack orientation and density on both microscopic damage and mechanical performance. The research outcomes provide valuable insights into the relationship between induced concrete damage and the above-mentioned factors, which are rarely captured in laboratory investigations, and can be used to better understand damage in aging concrete structures.

1.4 Thesis format and organization

This thesis follows a paper-based format including eight chapters, with each containing its own bibliography. The chapters are as follows:

Chapter	Topic
1	Introduction, objectives and scope
2	Literature review
3	Methodology
4	Paper 1: Visual and non-destructive testing performed on the pier shaft and pier cap
5	Paper 2: Microscopic investigation of extracted cores
6	Paper 3: Mechanical investigation of extracted cores
7	Paper 4: Multi-level (i.e., microscopic and mechanical) investigation of longitudinally extracted pier cap cores to investigate anisotropic effects
8	Summary of conclusions and proposed future works

1.5 References

1. Sanchez LFM, Fournier B, Jolin M, Mitchell D, Bastien J (2017) Overall assessment of Alkali-Aggregate Reaction (AAR) in concretes presenting different strengths and incorporating a wide range of reactive aggregate types and natures. Cem Concr Res 93:17–31

2. Sanchez LFM, Fournier B, Jolin M, Bastien J, Mitchell D (2016) Practical use of the Stiffness Damage Test (SDT) for assessing damage in concrete infrastructure affected by alkali-silica reaction. Constr Build Mater 125:1178–1188

3. Sanchez LFM, Drimalas T, Fournier B, Mitchell D, Bastien J (2018) Comprehensive damage assessment in concrete affected by different internal swelling reaction (ISR) mechanisms. Cem Concr Res 107:284–303

5. Sanchez LFM, Fournier B, Bastien J, Mitchell D, Noël M (2016) Overall assessment of an ASR affected overpass “Robert-Bourassa/Charest” after nearly 50 years in service. Conference: 8th International Conference on Bridge Maintenance, Safety and Management

6. Sanchez LFM, Fournier B, Jolin M, Bedoya MAB, Bastien J, Duchesne J (2016) Use of Damage Rating Index to Quantify Alkali-Silica Reaction Damage in Concrete: Fine versus Coarse Aggregate. ACI Mater J 113:395–407

Chapter 2: Literature Review

2.1 Brief history of the Champlain Bridge

The Champlain Bridge (CB) is a 3.4 Km long six lane highway bridge which spanned the St. Lawrence River between Montreal Quebec and Brossard Quebec between June 1962 and July 2019 (Figure 2-1). The location was chosen in 1955 with construction starting in 1957 and continuing until 1964 when the final approaches to the CB were completed. The CB operated as a toll bridge until 1990 and was considered one of the busiest bridges in Canada with approximately 50 million vehicles [1] passing annually. Since 1978 the CB has been maintained by Jacques Cartier and Champlain Bridges Incorporated (JCBBI), a Canadian Crown Corporation responsible for structural health monitoring, maintenance, and management.

Figure 2-1 Annotated image identifying key sections of the Champlain Bridge (reproduced from [2])

The CB design utilized reinforced concrete sections designed by the French company over the St. Lawrence River coupled with a steel truss section to accommodate shipping traffic on the St. Lawrence Seaway. In the reinforced concrete sections, an interconnected pre-stressed girder system was used. The driving surface was constructed such that asphalt was placed directly on girder flanges with transversally post-tensioned infill slabs filling the gaps between girders (Figure 2-2). Each span included seven girders resting on a ‘hammer head’ pier cap and an approximately oval shaped pier shaft and piles.

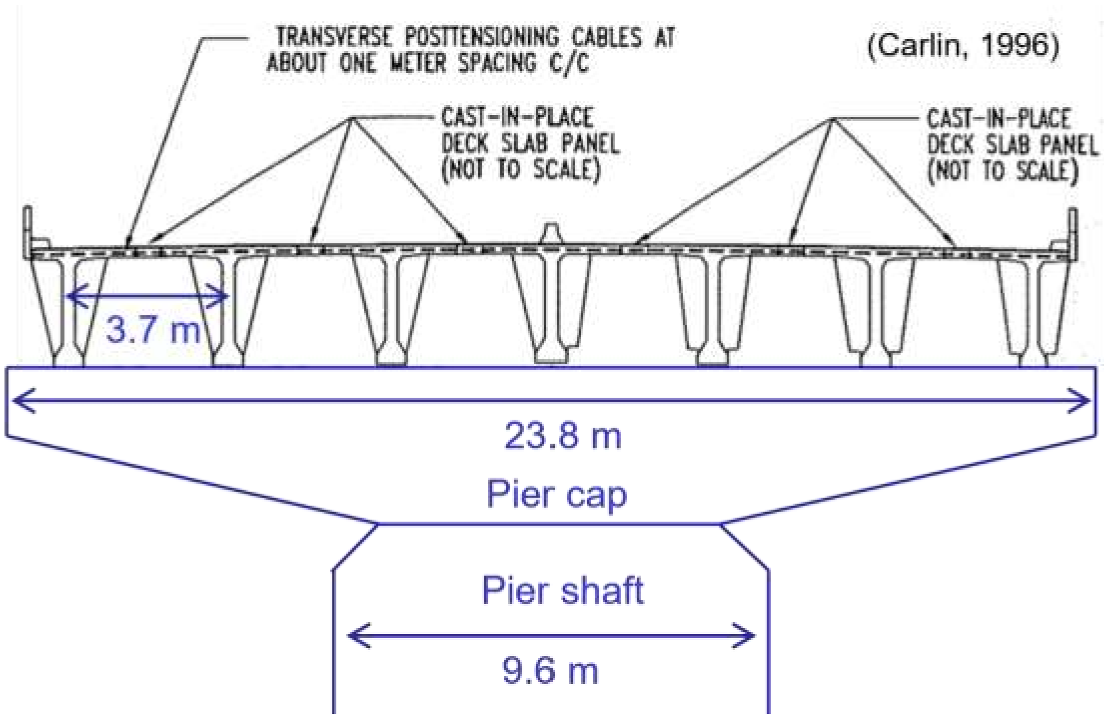

Figure 2-2 Schematic cross-section of the deck and girder sections from Carlin 1996 [3] **modified to identify the location of pier cap and pier shaft members in a typical pier**

The CB has experienced severe deterioration in the concrete sections which has caused significant additional repair costs, especially in the final decade of use. The novel interconnected design limited the initial cost but was problematic for replacing deteriorated members and monitoring of the structural health [4, 5]. Deterioration related to reinforcement corrosion, attributed to the use of road de-icing salt, was the most prominent damage type identified during bridge inspections; however, other deterioration mechanisms expected to be occurring at the materials level include freeze-thaw (FT) damage and internal swelling due to the alkali-aggregate reaction (AAR), which was identified in cores extracted from CB pier shafts [6]. Delayed ettringite formation (DEF) is a possible damage mechanism due to the size of concrete members but has not been identified in the CB.

At the time when the CB was constructed concrete techniques were undergoing significant innovations, such as the inclusion of air to prevent freeze-thaw damage and increased alkalinity in cement due to introduction of technology that allowed more fines to be included during manufacturing. However, high range water reducers (i.e. superplasticizers) which are commonly used in modern concrete were not yet invented [7] resulting in the use of higher water to cement ratios (w/c) and by extension lower concrete durability. Supplementary cementitious materials (SCM's) were not commonly used in Canada when the CB was constructed but were widely available in Europe where the use of pre-stressed concrete originated [8–10]. As a result, the CB has many similarities with structures currently approaching the end of their designed service life which are increasingly exhibiting deterioration which is dissimilar to earlier structures [11]. A thorough investigation of elements from the CB, is important to both understand how deterioration developed leading to the premature closure of the CB as well as facilitating improved evaluations of the damage type and extent (diagnosis) and potential future performance (prognosis) for the management of similar structures.

2.2 Damage mechanisms in concrete

2.2.1 Alkali-aggregate reaction

The Alkali aggregate reaction (AAR) is among the most harmful distress mechanisms affecting the durability and serviceability of concrete infrastructure in Canada and worldwide. AAR occurs when susceptible coarse or fine aggregates containing unstable silica interact with alkali-hydroxides in the cement pore solution producing a secondary reaction product, a silica gel, which uptakes water and generates expansive internal forces within the aggregates and surrounding cement paste. This results in microcracking along with losses in mechanical properties including high reductions in concrete tensile strength and modulus of elasticity even at low induced expansion levels [12]. AAR-affected structures are associated with significant costs due to their decreased service life, as well as the need for frequent inspection, monitoring, and rehabilitation.

The AAR mechanism was first identified in California in 1940 [13] and similar damage in Canada was not formally identified until a decade later [14]. The initial AAR reaction was later called 'alkali-silica reaction' (ASR). The existence of a second cement-aggregate reaction mechanism that differed from ASR was suggested by Swenson in the late 1950's [15, 16] and it was designated as the 'alkali-carbonate reaction' (ACR) in 1964. Aggregates associated with AAR are located in many regions of Canada with both ASR and ACR reactive aggregates found in eastern Canada [14, 17] while only ASR-affected structures have been identified in Quebec [18].

The frequency of AAR occurring in Canadian structures may have been increased by the use of kiln dust in cement, which was introduced in the 1960's [19] because the use of electrostatic precipitators allowed smaller particles to be re-captured during cement production. Alkalinity in cements, measured through the sodium oxide equivalent ($Na_2O_{equiv.}$), have historically been fairly high in Eastern Canada; for example, the Sartigan dam which was built in 1967 contained approximately 1.2% $Na_2O_{equiv.}$ [20] while in the 1960's the Na_2O_{equiv}. of general use cements in Quebec were around 0.90% [14, 17].

Overall, research on AAR has considerably grown in the past decades. Several RILEM State-of-the-Art Reports have been released. These include 'Diagnosis & Prognosis of AAR Affected Structures' released in early 2021 and 'Guide to Diagnosis and Appraisal of AAR Damage to Concrete in Structures' released in 2013. These publications cover the current knowledge for diagnosing the type and extent of damage in structures affected by AAR as well as service life prediction methods. Additionally, there has been significant progress in measures to prevent AAR in modern structures. However, these are outside the scope of this report and will not be discussed in detail. These include testing aggregates prior to use through the concrete prism test (CSA A23.2 -14A) and accelerated mortar bar test (CSA A23.2-25A), then applying those results to alter the mix design to limit the alkalis in concrete depending on expected aggregate reactivity. In existing structures experiencing deterioration due to AAR, mitigation measures can be used. These may include the use of coatings to limit moisture in the concrete, strategic cuts to allow further expansion and strengthening measures for deteriorating concrete members.

2.2.1.1 Factors affecting AAR:

AAR in concrete occurs when three factors are present: reactive aggregates, high moisture and a high alkali content. Variations within a structure (e.g. leaching resulting in a reduction in alkali content at an external surface) can result in variations in the development of AAR within that structure.

ASR reactive aggregates fall under two categories: A) reactions involving poorly crystalline or metastable silica materials or B) reactions involving certain varieties of quartz [18, 21]. The majority of ASR-affected structures in Quebec fall under the second category [18]. ACR is associated with argillaceous dolomitic limestone and has not been associated with deterioration in any Quebec structures [18].

The British Cement Association has found that AAR occurs when the internal moisture exceeds 80-85% [18]. The internal moisture of a massive concrete element, such as the piers in the CB, is typically independent from the climate in which it is placed due to the low surface area to volume ratio. Thin concrete elements, such as girders, experience more moisture exchange with the environment relative to the volume. A study of ASR in five American dams found that the moisture was sufficient to support ASR in all but the outermost several inches of the concrete [22].

The amount of alkalis in the cement is determined by the Na_2O equivalent ($Na_2O_{equiv.}$), where 0.658 is the mass ratio of Na_2O/K_2O as shown in Equation 2-1 The $Na_2O_{equiv.}$ in new structures must not exceed prescribed values specified in Table 5 of CSA A23.2-27A [23] to prevent the development of AAR in new structures where reactive aggregates are used. The $Na_2O_{equiv.}$ is multiplied by the cement content to compute the total alkali content (or alkali loading) of concrete. For example, when mild preventive measures are required, less than 3.0 kg/m^3 $Na_2O_{equiv.}$ should be used while 1.2 kg/m^3 $Na_2O_{equiv.}$ should be used if very strong preventive measures are needed. In Canada, a reinforced concrete that will be exposed to chlorides should be constructed using a minimum of 335 kg of cement per cubic meter to ensure good durability. This corresponds to 0.90% $Na_2O_{equiv.}$ for mild preventive measures (similar to GU cement in Quebec in the 1960's [14, 17]) and only 0.36% $Na_2O_{equiv.}$ if strong measures are required.

$$Na_2O_{equiv}\ (\%) = Na_2O\ (\%) + 0.658\ K_2O\ (\%) \tag{2-1}$$

For practical purposes the Na_2O_{equiv} is presented as a weight percentage of cement, however the overall alkalis content as a function of concrete volume [19] is the key consideration for AAR since most alkalis in hydrated concrete enter the pore solution. Thus, the cement content of concrete per m^3 is highly important. Alternately, alkali content can be inferred from the pH of the concrete. A saturated $Ca(OH)_2$

solution at room temperature displays a pH of approximately 12.6 while the presence of KOH and NaOH further increase the pH. Concrete incorporating a low alkali cement will range from pH 12.7-13.1 while using a high alkali cement results in pH ranging from 13.5-13.9 [24]. The amount of alkalis may be further increased in concrete due to diffusion of de-icing salts (NaCl, $CaCl_2$ and/or $MgCl_2$), seawater, or even by the alkalis released from aggregates [25].

2.2.1.2 Alkali-Silica reaction (ASR) mechanism

Two damage propagation models have been proposed to explain the development of damage due to ASR. These are the gel pocket model (type 'A' cracking, aka 'sharp' [26]) and reaction rim model (type 'B' cracking, aka 'onion skin' [26]) with preferential occurrence of damage depending largely on aggregate characteristics. In the gel pocket model gel is formed at reactive sites inside the aggregate with cracks propagating from the aggregate into the cement paste as the volume of gel products at the initial site increases. In the reaction rim model, cracks are generated along the rim of the aggregate in an 'onion skin' type crack pattern [26]. At higher levels of damage cracks propagate into the cement paste due to increased widths caused by developing gel. The type of aggregates (e.g. chemical composition, ease of pore solution movement into aggregate) as well as the distribution of aggregates (e.g. use of gap grading, dissimilar aggregates used as fine and coarse) [27, 28] are important factors in how damage develops in effected concrete. In both models ASR initiates in the aggregates only propagating to the cement paste as the reaction progresses and thus are indicative of advanced stages of deterioration.

Both gel pocket and reaction rim models were evaluated using computational techniques by Miura et al. [29] with their findings emphasizing the role of aggregate compositions in the type of cracking model. More homogeneous aggregates are more likely to develop damage following the reaction rim model as pore solution interacts with the entire aggregate while in heterogeneous aggregates follow the gel pocket model where pore solution enters the aggregate through an existing crack or vein in the aggregate.

Expansion of concrete due to ASR initially develops slowly while alkali's enter the aggregates and initial reaction products are formed. This is followed by a period of expansion in the concrete material as the ASR gel develops followed by a reduction in the rate of expansion as reactants are used up. The rate of the ASR reaction as well as the maximum amount of extension will depend on a variety of factors including aggregate type as well as availability of alkalis and moisture. During condition assessments of a structure experiencing expansion due to ASR investigators try to establish both the current level of expansion that has occurred as well as estimating future expansion (Figure 2-3).

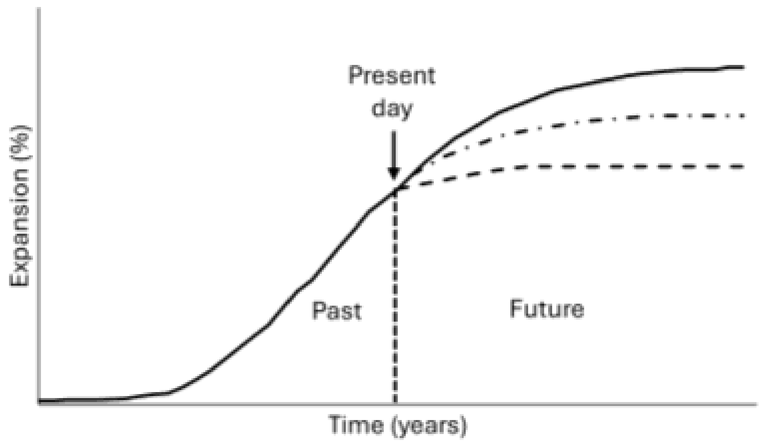

Figure 2-3 Diagram of the potential for expansion over time in ASR affected concrete

2.2.1.3 Variations in ASR gel

Reaction products from ASR can have a variety of appearances and are mainly described as 'amorphous' and 'crystalline'. ASR gel composition is similar to C-S-H and contains Si, Ca^{2+} and may include Al, Na^+, K^+ and OH^-. Calcium is a critical component in the formation of gel without which silica would dissolve into solution until saturation is achieved. The gel produces expansion in concrete when the gel adsorbs water [28].

Significant work has been conducted to understand the composition of gels found in ASR effected concretes. Gels synthesized in laboratory conditions were found to have a variety of appearances and physical properties such as viscosity [30]. Researchers have found that synthesized gels were highly comparable to field samples, with Hou et al. 2005 [31] concluding that ASR gels from the Furnas Dam were highly comparable to low calcium polymerized C-S-H gels. Development of ASR gel is an ongoing process with gel composition and physical properties transitioning over time. Work by Leemann et al. 2020

[32] found amorphous gel to be the first product formed (aka primary product) and linked it to crack initiation with crystalline gel (aka secondary product) formed later within the opened cracks. Previous SEM investigation by Boehm-Courhault and Leeman [33] found that in the primary product there is a higher atomic % of Si and lower atomic % of Ca and (Na + K) while the amount of Si decreased slightly (~72% to ~64.5%) and Ca and (Na + K) increased slightly (~12.5% to ~15.5% and ~15% to ~20% respectively). Since calcium is more accessible in the cement paste secondary product is most often found where gel in aggregates enters the paste. In some aggregates, including siliceous limestones, contact between reactive silica and reactants including calcium and alkalis is delayed since these materials first migrate into the aggregate through pre-existing defects such as microcracks, grain boundaries and veins [28].

Of particular interest to diagnosis of concrete is whether the gel formed in accelerated tests such as the mortar bar test and concrete prism test is comparable to the gel in real structures. Gel viscosity impacts the amount of expansion and thus impacts the damage classification based on microscopic (i.e. DRI) and mechanical properties.

2.2.1.4 Alkali-Carbonate Reaction (ACR) mechanism

The Alkali-carbonate reaction (ACR) is unique to reactive argillaceous dolomitic limestone [18] including Ordovician limestones [14]. ACR involves the reaction of rhombic crystals of dolomite with the alkaline pore solution resulting in a dedolomitization reaction [34]. Concrete might experience both ASR and ACR simultaneously; hence, finding gel deposits does not necessarily eliminate the possibility of ACR development [19]. However, the existence of distinctly separate reaction mechanisms for ACR compared to ASR causing expansive damage has been disputed by some researchers [35–37].

Aggregates which can undergo ACR reactions are prohibited from being used in construction as this damage mechanism cannot be mitigated through the use of low alkali cement and supplementary cementing materials (SCM's) [38]. Cracking damage due to ACR is often seen in structures despite the use of very low alkalis [38] although the de-dolomization reaction associated with ACR is thought to only proceed at pH values greater than 12 [19]. Damage due to ACR appears very quickly, with ACR in sidewalks occurring after only a couple of months [19] and in some larger structures after only a couple of years [18].

The mechanism for induced expansion in ACR was previously thought to be the de-dolomitization reaction [19] as shown in Equation 2-2 where all products from the reaction precipitate from solution.

$$MgCO_3 \cdot CaCO_3 + 2[k,Na]OH \text{ -> } Mg(OH)_2 + CaCO_3 + [k,Na]_2CO_3 \qquad (2\text{-}2)$$

The reaction in Equation 2-2 decreases the pH of the concrete pore solution. This is thought to prompt a subsequent reaction as part of portlandite's role as a buffer since Ca^{2+} solubility increases with decreased pH [39, 40] as shown in Equation 2-3. Experimentally the conversion of dolomite to brucite and carbonate is undisputed; however, the source of expansion is not clear. This is because the molar volume of dolomite is the same as the net molar volume of the products in Equation 2-4.

$$[Na, K]_2CO_3 + Ca(OH)_2 \text{ -> } 2\ [Na, K]OH + CaCO_3 \qquad (2\text{-}3)$$

$$MgCO_3 \cdot CaCO_3 + CaOH_2 \text{ -> } MgOH_2 + 2CaCO_3 \qquad (2\text{-}4)$$

Researchers do not agree on the mechanism of expansion caused by ACR. One theory is that ACR occurs alongside an ASR reaction since some of ACR reactive materials might bear an amount of siliceous mineral phases [19]. Grattan-Bellew et al. investigated two ACR aggregates and an aggregate known to experience ASR (Spratt) and found that the amount of quartz in the HCl insoluble residue from all three aggregates correlated to expansion previously determined using the concrete prism test (CSA A23.2 -14A) [35].

An alternate theory suggests that the migration of moisture and alkalis as part of the de-dolomitization reaction may be responsible for expansion from ACR. This mechanism would occur when moisture and alkalis migrate into the small-grained clay/calcite matrix surrounding the dolomite [18] or penetrate into the dolomite itself [19]. The arrangement of the reaction products, including the intermediary products, around the dolomite crystals may also cause expansion, particularly brucite which is known to be expansive [19]. Crystallization pressure from the formation of brucite and calcite may assist in this movement of pore solution facilitating further reactions [18]. Expansion of clay may occur due to the migration of alkalis and moisture causing expansion in the concrete.

Structures exposed to de-icing salts which contain ACR reactive aggregates but use a low alkali cement can still have damage from this reaction in salt affected regions. The additional Na^{+}, Ca^{2+} and Mg^{2+} can diffuse into the concrete raising the alkali content and facilitate the de-dolomitization reaction (Ozol, 1994).

2.2.2 Freeze-thaw (FT)

Freeze-thaw (FT) cycles occur when water freezes in pores within the cement paste leading to the development of microcracks and deterioration in concrete. In large concrete structures FT damage is expected in exposed regions of structures and does not occur instantly once ambient temperatures drop below zero with many factors, including moisture sources (e.g. fresh vs. salt water) and pore sizes impacting the formation of microcracks. FT damage is more severe at the surface layer due to more frequent temperature variations and exposure to external sources of moisture which facilitate saturation of the material prior to re-freezing. Surface damage may be evident as scaling and flaking. Over time this damage can degrade concrete cover and reduce the distance deleterious ions will need to travel to induce rebar corrosion over time.

Due to its location in Montreal the CB is expected to experience an average of 55 instances per year where the average air temperature drops below 0°C [41]. In Montreal the number of FT cycles per year, defined as ambient temperature dropping below 0°C, increased by ~29% between 1949 and 2015 [42], possibly due to increased night-day FT cycles. However, as local climate continues to change the number of FT cycles may decrease due to a shorter winter period with longer thaw periods [43].

2.2.2.1 FT Mechanism

Microcracking from FT is caused by the 9% increase in volume of freezing water [44] in the capillary pore network which exerts tensile stress on the concrete. Damage to the cement paste is increased over successive FT cycles as liquid diffuses into concrete during warm weather, enters micro-cracks and enlarges them during the next freeze cycle (Figure 2-4). In controlled laboratory testing a sharp increase in water absorption has been observed after 100 and 150 FT cycles indicating that after an initial period of damage the rate of cement paste deterioration will increase [45].

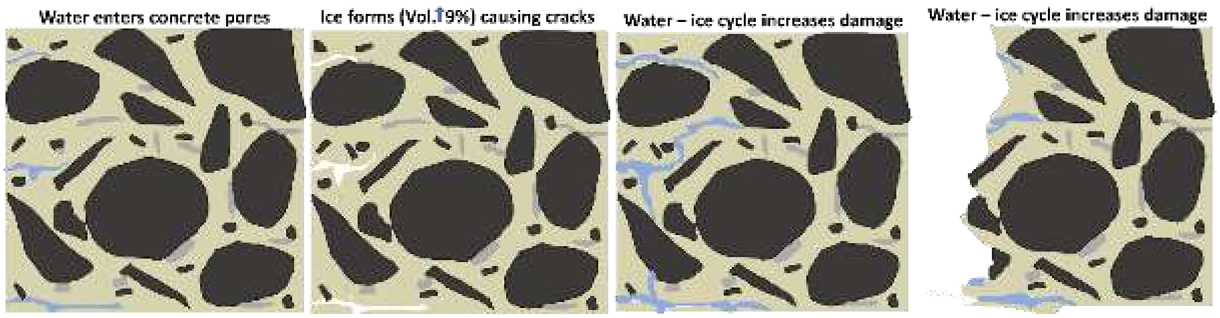

Figure 2-4 Illustration of the development of freeze-thaw damage

Ice formation occurs primarily in the capillary pores since freezing in gel pores does not occur until approximately -78°C [46]. Ice forms first in larger pores with ice formatting occurring in increasingly small pores as the temperature decreases. Damage at temperatures between -10°C and -35°C may be increased due to a combination of thermal contraction of the existing ice and crystallization of water moving back into pores [47]. Where a single damage event would occur for each FT cycle with temperatures higher than -10°C, two or more damage events would occur when temperatures decrease below -10°C, a common event in Montreal's climate where average temperatures are below -10°C two months a year.

The specific mechanisms responsible for FT damage are still disputed. The most commonly accepted mechanisms are 1) hydraulic pressure generated by ice formation [48] and 2) osmotic pressure as a result of the pore solution becoming more concentrated next to locations of ice formation. Less common proposed mechanisms include desorption of water from the CSH phase and ice segregation [49]. Pressure causing microcracking occurs when more than 90% of the pore volume is filled by water prior to freezing [50]. In non-air entrained concrete, FT stresses in the concrete are tensile while in air-entrained concrete stresses become compressive [51].

The extent of FT damage increases in concrete with higher w/c ratios due to higher amounts of capillary water [52]. However, curing conditions [53], air entrainment [54], and the use of SCM's [53, 54] can further improve FT performance [54], even at higher w/c ratios. In Canada w/c ratio should be selected following the exposure class in Table 9-1 of CSA A23.1 [55]. This standard originated in 1977 as CAN3-A23.1-M77 and was not in effect when the CB was constructed.

2.2.2.2 Coarse aggregate susceptibility to FT

Coarse aggregates can have sufficient porosity to be susceptible to FT. The most recognizable symptom of a non-suitable aggregate is the ‘popout’ phenomena. A popout involves the formation of a conical indent when pressure due to expansion of the aggregate relative to the cement causes localized damage. Where popout has occurred, a portion of the aggregate will remain in the concrete at the bottom of the indent [56]. During popout pressure is relieved by cracking which occurs primarily in the mortar surrounding the expanding aggregate resulting in indents in the surface of concrete similar to spalling.

A coarse aggregate with a proven record in the desired service environment is recommended to reduce the possibility of using FT susceptibility. Aggregate soundness is used prior to aggregate selection during the mix design to limit weathering of the final concrete mix. Currently this may be assessed through CSA A23.2 – 9A ‘Soundness of fine and coarse aggregates by use of magnesium sulphate’ or ASTM C88/C88M -18 ‘Standard test method for Soundness of Aggregates by Use of Sodium Sulphate or Magnesium Sulfate’.

2.2.2.3 FT in submerged and partially submerged concrete

During the winter months freshwater bodies, such as the St. Lawrence River, have ice layers at the surface while liquid water persists at a temperature of approximately 4°C. Thus unique FT behaviour is expected in submerged and partially submerged concrete with little FT damage expected in fully submerged regions.

Partially submerged concrete in cold climates are subject to erosion, leaching, and FT deterioration resulting in exposed coarse aggregate at the waterline. A survey of hydraulic structures in Sweden (mostly dams) were found to lose up to 1 mm/year from the surface [57]. Erosion due to the movement of ice on the water surface may facilitate more rapid deterioration in this area while formation of ice adhered to the concrete surface may provide some protection from erosion [58]. Leaching is likely in submerged and partially submerged concrete. In partially submerged regions snow melt, which is typically very ‘soft’, is expected to cause greater dissolution of calcium from the concrete.

The highest deterioration due to FT is expected to occur in partially submerged regions due to high moisture in the pore system and the direct exposure to sub-zero temperatures compared to the fully submerged region. Increased deterioration may also occur on the south facing sides of structures in the southern hemisphere, attributed to increased thermal cycles caused by direct sun exposure [58].

Fully submerged concrete has been found to develop ice layers on the surface which increase in thickness closer to the surface due to concrete being colder than the surrounding water. In dams, a temperature gradient between the exposed surface and the submerged surface on the retaining side is sufficient for significant ice buildup on the submerged surface [57]. In bridge piles, a thermal gradient is expected between the exposed and submerged concrete as well as between the water and concrete. FT damage will be greatest near the surface with reduced damage as the depth increases.

2.2.3 Reinforcement corrosion

Reinforcement corrosion in highway bridges in the United States of America was estimated to cost $13.6 billion annually as of 2013 [59]. In concrete structures, reinforcing bar corrosion is among the most visible deterioration types due to spalling and staining from corroded members. In Canada corrosion is most commonly caused by the ingress of chloride ions (e.g. from de-icing salts used on roadways or salts in marine environments). The presence of harmful ions causes steel de-passivation which can result in localized pitting corrosion. Carbonation of concrete can also lead to depassivation of reinforcing steel however in cold climates carbonation is not the primary mechanism for corrosion, although chloride ingress and carbonation can have a synergizing effect.

Reinforcing corrosion became a prominent issue in North America approximately 20 years after the introduction of road salts for winter road maintenance in the late 1950’s. This led to the implementation of waterproofing measures as well as increases in the required cover depth on highway bridges, from 25 to

40 mm cover in 1965 to 70 mm cover and waterproofing measures required by 1996 in areas exposed to chlorides [60]. Although corrosion due to chlorides has long been an issue in marine environments, the use of chlorides on roadways is more recent. In Quebec this occurred when cheap electricity and self-regulating oil central heating in the 1950's -1960's [61] caused a shift away from coal and wood heating. This limited availability of waste ash for winter road maintenance. By the time the CB opened in 1962, rock salt consisting of NaCl, was being introduced as the primary de-icing material. A decade or more remained before reinforcing corrosion became evident due to the time required for chlorides to diffuse into concrete prior to corrosion initiation. Two types of salt exposure may be expected in field structures the age of the CB: internal chlorides (added during mixing of concrete, e.g. $CaCl_2$) and external chlorides (introduced by activities like spreading de-icing salt). External chlorides are those introduced as anti-icing or de-icing salts and will primarily affect concrete near the driving surface and areas exposed to runoff from that surface.

The use of $CaCl_2$ and $MgCl_2$ salts is now common, either coating traditional rock salt or as part of brine solutions applied to roadways during the winter. $CaCl_2$ and $MgCl_2$ interact more with concrete resulting in accelerated damage to the surface of concrete, potentially reducing the concrete cover in addition to the diffusion of Cl^- ions towards reinforcing bar corrosion.

2.2.3.1 Factors affecting reinforcement corrosion

Steel reinforcing bars are very compatible with concrete. This is because carbon steel forms a protective passive layer in alkaline environments. The level of protection of the passive film decreases as pH decreases, with a stable protective film being formed at pH values as low as 11.5 [62]. Corrosion occurs when the film is de-passivated (e.g. initiation of pitting corrosion by chloride ions) or when the formation of a passive film is inhibited. In existing structures in North America damage due to the ingress of chloride ions is the biggest factor in the development of corrosion in reinforced concrete while carbonation of concrete can also be a significant contributor for reinforcement corrosion in warm climates.

Two types of salt exposure may be expected in field structures the age of the Champlain Bridge: external chlorides (introduced by activities like spreading de-icing salt) and internal chlorides (added during mixing of concrete, e.g. $CaCl_2$). External chlorides are those introduced as anti-icing or de-icing salts and will primarily affect concrete near the driving surface and areas exposed to runoff from that surface. Externally introduced chlorides which have a concentration gradient between the surface and rebar with the chloride concentration at the surface of reinforcing bars being the critical parameter for corrosion initiation. At the time the Champlain Bridge was constructed the use of $CaCl_2$ was encouraged as a set accelerator and was thought to have no impact on reinforcement corrosion [63]. Imperial Chemical Industries (ICI), a British company, proposed that the amounts of $CaCl_2$ used to accelerate the set of concrete should be based on air temperature as shown in Table 2-1. Similar practices are thought to have been used in North America at the time. As such, increased chloride may be present in select concrete lifts depending on the air temperature during construction (e.g. $CaCl_2$ may have been added towards the end of the day if cool temperatures were expected over night).

Table 2-1 Guidelines by Imperial Chemical Industries (1958) for $CaCl_2$ usage to accelerate concrete set time at low temperatures (reproduced from [63]**)**

	% weight by mass of cement			
Air temperature	%$CaCl_2$	%Cl^-	%$CaCl_2$	%Cl^-
	Ordinary Portland cement		*Rapid-hardening Portland Cement*	
<0°C	2.68-3.57	1.71-2.28	1.78-2.68	1.14-1.71
0-4.4°C	2.68	1.71	1.34	0.86
4.4-21.1°C	1.78	1.14	0.89	1.14
>21.1°C	0.89-1.34	0.57-0.86	----	----

For externally introduced chlorides, permeability rather than chloride binding is the main determinant of chloride penetration rate [64]. The permeability of concrete is a function of the combined mechanisms of diffusion and absorption. In a hydrated concrete the stability of existing hydration products containing aluminum and sulphate limit the availability of these elements for further reactions which would bind chloride. The main mechanisms responsible for chloride binding are dissolution of monosulphate and precipitation of Friedel's salt or ion exchange resulting in Kuzel's salt and Friedel's salt depending on the chloride concentration.

Physical salt attack may also occur from external salt exposure due to crystallization in pores caused by evaporation. This damage mechanism is independent of reactions with cement [65] and occurs near the surface where water undergoes wet-dry cycles. Physical salt attack may occur from salts including sodium sulphate (Na_2SO_4), sodium carbonate (Na_2CO_3) and sodium chloride (NaCl) where NaCl is the least aggressive.

The concentration of chloride ions required to break down the passive film of a reinforcing bar depends on many factors including the concrete w/c ratio, presence of other ions such as sulphate [66, 67], and pH. Several ways to quantify the critical amount of chlorides (i.e. a 'chloride threshold' above which active corrosion will occur) have been proposed. However, a universal threshold would need to consider and quantify many factors including pH, types of ions in pore solution, rebar surface treatment and temperature. The use of a Cl^-/OH^- ratio has been proposed as a way to control for different w/c ratios and alkaline contents; however, this approach has not yielded consistent results [68, 69]. One notable issue is accurately quantifying the pH at a given location in a structure because pH decreases rapidly in exposed concrete.

2.2.3.2 Reinforcement corrosion mechanism

Rebar corrosion occurs when there is a flow of electrons through the reinforcement. This causes iron to be oxidized forming rust at the anode (Equation 2-5) while oxygen or hydrogen is reduced at the cathode (Equation 2-6). The anode and cathode can occur in close proximity, for example on a single steel bar (microcell corrosion) or at a distance from each other (macrocell corrosion). The basic reactions occurring in a carbon steel reinforcing bar are shown in Equation 2-5 and Equation 2-6. However, many reactions can occur depending on the pH, oxygen availability and presence of aggressive ions (Cl^-, SO_4^{2-}) [70, 71] resulting in a variety of corrosion products.

$$\text{Anodic reaction of Iron: } \boldsymbol{Fe} \rightarrow \boldsymbol{Fe^{2+}} + 2\boldsymbol{e^{-}} \tag{2-5}$$

$$\text{Cathodic reaction in high pH environment: } \boldsymbol{H_2O} + \frac{1}{2}\boldsymbol{O_2} + \boldsymbol{2e^{-}} \rightarrow \boldsymbol{2OH^{-}} \tag{2-6}$$

Corrosion products form utilizing the Fe^{2+} ion released in Equation 2-5. Many corrosion products are possible resulting in volume increases relative to iron ranging from 1.5x to 6x the volume of iron (Figure 2-5), this results in expansion at the reinforcement which ultimately exerts pressure on the surrounding concrete leading to cracking, spalling and delamination.

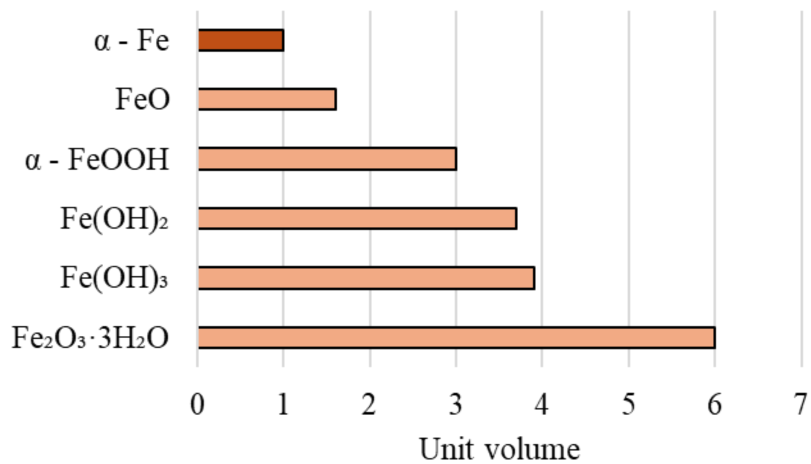

Figure 2-5 Bar graph depicting the volume of different corrosion products relative to iron (adapted from [72]**)**

Pitting corrosion is a localized form of corrosion where a microenvironment is formed in an affected material. Acidification occurs inside the pit which draws in negative chloride ions. The process of acidification reaction due to chloride attack during pitting corrosion [73] is shown by Equation 2-7:

$$\text{Cathodic reaction in high acidic environment: } Fe^{2+} + 2H_2O + 2Cl^{-} \rightarrow Fe(OH)_2 + 2HCl \tag{2-7}$$

Pitting corrosion is a threat to structural integrity due to the localized loss of cross-sectional area and the difficulty of detecting pitting with non-destructive techniques. Steel experiencing pitting corrosion experiences a reduction in tensile strength and will rupture at lower elongation under tension.

2.2.3.3 Factors impacting chloride diffusion rate

The rate of chloride penetration increases with the presence of wet-dry cycles [74] and is impacted by the chloride concentrations at the surface, concrete permeability, RH in the concrete, temperature and the presence of cracking. The dual effect of freeze-thaw and chlorides result in additional deterioration compared to either mechanism in isolation. Chloride ingress occurs through capillary absorption, hydrostatic pressure (permeation), migration or diffusion. Pathways for chloride ingress include the pore system, microcracks and spaces between the paste-aggregate interfaces (ITZ).

Wet dry cycles result in moisture gradients in the concrete. Solution containing chloride is drawn towards lower moisture zones through capillary absorption (i.e. capillary suction) due to surface tension between the liquid and pore walls. Absorption is the main mechanism that occurs in the surface (within the first several mm) but diffusion is the main mechanism that draws chlorides deeper into the concrete because moisture within the bulk of the concrete is relatively consistent. The concentration of chloride at the concrete surface is expected to vary, making determination of the diffusion rate challenging in real structures.

The presence of cracks in concrete may allow chloride solutions to enter the concrete more quickly. Diffusion coefficients based on crack width are commonly used in modeling chloride diffusion in cracked concrete. Experimental testing by [75] indicates that diffusion through the crack is only governed by crack width when cracks are less than 80 μm. However, the size of cracks on the surface are not a clear indicator for the depth since the heterogeneity of concrete means cracks can often change direction and may propagate parallel to the surface. The effect of crack location (parallel or perpendicular to reinforcement), crack width and the number of cracks (a single crack compared to a grouping of cracks) can all impact reactions impacting concrete durability. The characteristics of damaging cracks are a subject of debate among researchers with ACI 222 indicating that cracks less than 0.3 mm are not thought to have an impact on diffusion into concrete. Some researchers suggest that the threshold below which crack widths are equivalent to sound concrete is lower. For example, [76] suggests the width is closer to 0.05mm which is difficult to detect without a magnifying glass. Crack width due to mechanisms such as shrinkage, loading etc. is discussed in detail in ACI 224R.

2.2.3.4 Corrosion in carbonated concrete

Corrosion initiates even when concrete is partially carbonated [77]. In northern climates carbonation is not a significant factor on its own due to the large cover depths used to prevent chloride ingress. In Canada, carbonation still presents an issue as it increases chloride penetration rates [78] and causes the release of sulphate and bound chloride ions due to the carbonation reaction [79].

Rust products may be more soluble in lower pH concrete allowing them to diffuse away from the rebar surface. This may mitigate the more serious cracking and spalling associated with rebar corrosion [78]. However, although cracking is mitigated, a reduction in rebar diameter continues to occur.

Interestingly, carbonation in reinforced concrete may vary from carbonation of plain concrete. In experiments by Revert et al. (2018) it was found that carbonation depths were increased directly above reinforcement which was attributed to microcracks caused by compaction around the reinforcing steel. In field structures it is recommended to test carbonation in closer proximity to the rebar for this reason.

2.2.4 Delayed ettringite formation (DEF)

Delayed Ettringite Formation is a form of internal sulphate attack characterized by the formation of ettringite in the cementitious material once the concrete has hardened. Similar to AAR, DEF results in swelling of concrete with DEF resulting from high internal temperatures in excess of 65-70°C during hydration of concrete in large members causing poorly crystalline monosulphate to form in the solid cement paste matrix [80]. In order for significant DEF to take place, studies have shown that the molar ratio of SO_3/Al_2O_3 present in the cement paste must exceed 0.55 [81]. An increase in temperature and pH levels increases the solubility of ettringite. In addition, sulphate and alumina concentrations in the pore concrete solution both increase under elevated temperatures. After exposure to moisture at ambient temperatures, the C-S-H releases most of the sulphates. This results in the conversion of monosulphate into ettringite, which may occur several months or years after the concrete's exposure to elevated temperatures. DEF leads to the expansion of the cement paste and cracking of concrete due to the growth of ettringite crystals in the small pores. As expansion occurs, gaps slowly form around the aggregate particles and the cement paste begins to crack [80].

Expansion associated with this mechanism may initiate several months after exposure to the required conditions. The degree of damage may increase over time and last several years [82]. This type of distress mechanism frequently takes place coupled with other distress mechanisms, such as freezing and thawing and alkali-silica reactions [83].

2.3 Condition assessment of in-service reinforced concrete structures

Structures that are in service must be regularly evaluated for the development of damage to ensure safety and plan for future works including repairs, rehabilitation work and/or replacement of the structure. Condition assessments can consist of a number of stages, including visual inspections, non-destructive testing in-situ, laboratory testing (e.g. testing on concrete cores) and structural health assessments (e.g. modeling), with results at each stage informing whether additional investigations are required. The source of suspected damage, including whether internal swelling reactions are suspected, will further inform the types of tests undertaken and the frequency of investigations. Damage in the context of a condition assessment can be subdivided into mechanical property losses, stiffness reductions and physical integrity/ durability losses as shown in Figure 2-6.

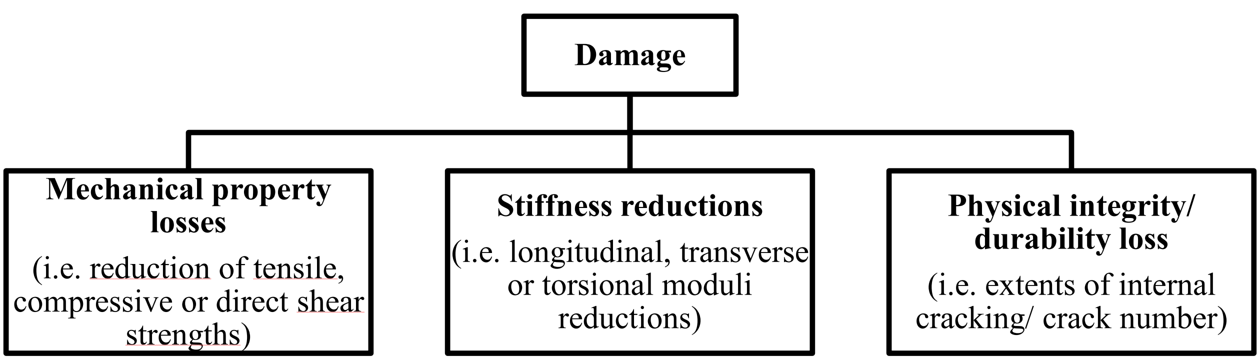

Figure 2-6 Diagram identifying components of damage considered during condition assessments (adapted from Sanchez 2024 [84]**)**

In this section condition assessment techniques are discussed with a focus on recommended procedures for reinforced concrete structures impacted by the alkali-silica reaction [25, 85, 86].

2.3.1 Visual inspections

Visual inspections are recommended to occur every 2 years and involve reviewing previous documentation followed by an on-site inspection. Visual inspections are subjective with high variability between different inspectors presenting a challenge for the consistency of long term monitoring of structures. A 2001 state of the art practiice survey by the United States Department of Transportation [87] highlighted deficiencies in inspector backgrounds (i.e. professional engineers are often not on site for inspections) as a limitation in the reliabillity of inspections on structural members. The 2001 report recommended that research into concrete deck and prestressed concrete superstructures should be a focus of future research.

Inspectors should observe the environment where the structure is located to identify sources of moisture and contaminants (e.g. harmful ions like chlorides or sulphates with areas of interest photographed. A methodical approach should be used to identify the size and location of defects with documentation including photographs and a written record. This step can be completed with high variability between practitioners [87]. Reference objects such as rulers as well as markings on the surface itself are effective. Defects may include discolouration, spalling, cracks, and effluence. Water may also be applied to the surface to identify cracks more easily.

For internal expansion reactions, such as AAR, it is important to identify crack widths and the presence of secondary products (e.g. gels) in cracks. The width of all visible cracks should be measured and all crack widths greater than 0.1 mm should be recorded. Whether cracks are passing through paste or aggregates should also be noted because cracks passing through aggregate may indicate AAR in coarse aggregates. The quantitative ‘cracking index’ technique was developed to compare cracking from internal swelling reactions and will be discussed later in this section. The presence of algae or moss on the concrete or seepage strains and carbonate deposits should be noted because these indicate damp areas which may have a predisposition to AAR [88].

Concrete exposed to salts may experience microcracking due to the interaction of $CaCl_2$ and $MgCl_2$ with cement hydration products or physical salt attack from NaCl [65]. Damage in exposed surfaces can manifest as scaling, surface crumbling or disintegration. Severe cracking and spalling can be observed in structures where rebar corrosion has occurred.

Concrete effected by FT damage may exhibit some or all of the following visible damage [81]:

- Surface pop outs indicating that aggregates in the structure were not sufficiently FT resistant. Part of the aggregate will remain at the bottom of the cone-like indent in the concrete.
- Surface scaling and delamination. Cracks beneath these types of deterioration will be parallel to the surface.
- Cracks around joints, edges, and other discontinuities including 'D-cracks'.

The climate in Quebec means that all outdoor concrete structures will experience FT cycles. Deterioration is increased in structures with high w/c ratios, poor air entrainment (more likely in old structures), and areas with periodic wetting where pores are frequently filled with water.

2.3.1.1 Quantitative visual inspection: Cracking Index (CI)

The 'Cracking Index' is often used to quantify cracking and provide comparison between different areas of a structure. The cracking index involves drawing a square with diagonal lines on a structure, as shown in Figure 2-7, with minimum suggested dimensions are 0.5 m x 0.5 m [89]. The number and width of cracks which pass through these lines are then counted and normalized to 1.0 m as shown in Equation 2-8.

$$CI = \frac{\sum Crack\ openings}{Base\ length} \tag{2-8}$$

Issues within concrete are first indicated when CI in the range 0.4 mm/m to 0.6 mm/m in unrestrained concrete [25] with a criterion of 0.5 mm/m selected by [85] with the further recommendation that cracks in excess of 0.15 mm width trigger additional investigation particularly for pre-stressed concrete [90].

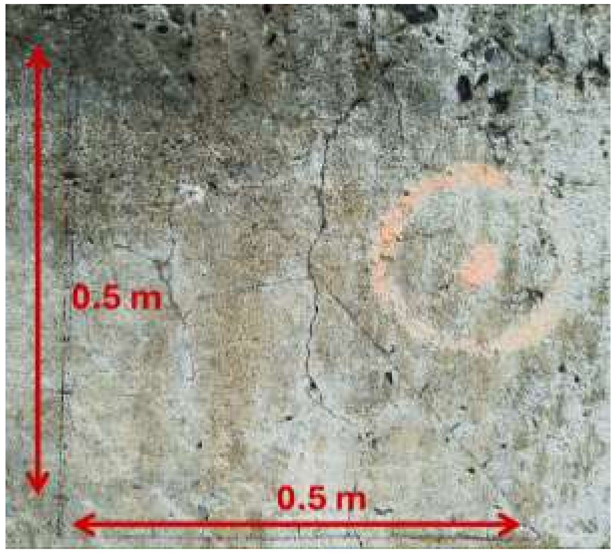

Figure 2-7 Annotated image depicting the cracking index on a deteriorated concrete surface

The cracking index is a good tool for early detection of issues (e.g. when performed in the same location over time) and for comparing the severity of different locations but is susceptible to variability between practitioners as well as changes in crack width due to moisture and temperature conditions. This technique does not differentiate between the source of cracking and gives equal weight to all cracks regardless of direction and appearance.

2.3.1.2 Appearance of cracking in reinforced concrete and prestressed structures

In a real structure concrete elements have different sizes, reinforcement configurations, environmental exposures and loading which cannot be easily reproduced in laboratory experiments resulting in a variety of crack behaviours.

In prestressed and reinforced concretes internal expansion may not exhibit the typical cracking patterns expected in unreinforced concrete (i.e. map cracking). Instead, concrete cracking may develop longitudinally parallel to the direction of dominant restraint rather than transverse due to compression stresses (e.g. due to loading) [25]. The impact of reinforcement on expansion due to ASR in accelerated lab conditions has resulted in distinct anisotropic (i.e. directional) crack patterns with cracking found parallel to the main reinforcement [91–93]. However, cracking parallel to reinforcement is also frequently observed as a result of rebar corrosion. Reddish-brown rust colouring in the crack would suggest that the cause of cracking is corrosion while the presence of a whitish secondary product might indicate AAR.

Figure 2-8 and Figure 2-9 show schematics of cracking in unreinforced and reinforced 0.225 x 0.225 x 0.400 m prisms using a reactive coarse aggregate and accelerated laboratory techniques. The prism depicted on the left is plain concrete while the prism on the right has reinforcement [93]. In reinforced concrete, cracking is found parallel to the main reinforcement [91, 92], as shown in Figure 2-8 and Figure 2-9. Similarly, Prestressed concrete members usually develop cracks parallel to the direction of prestressing [19].

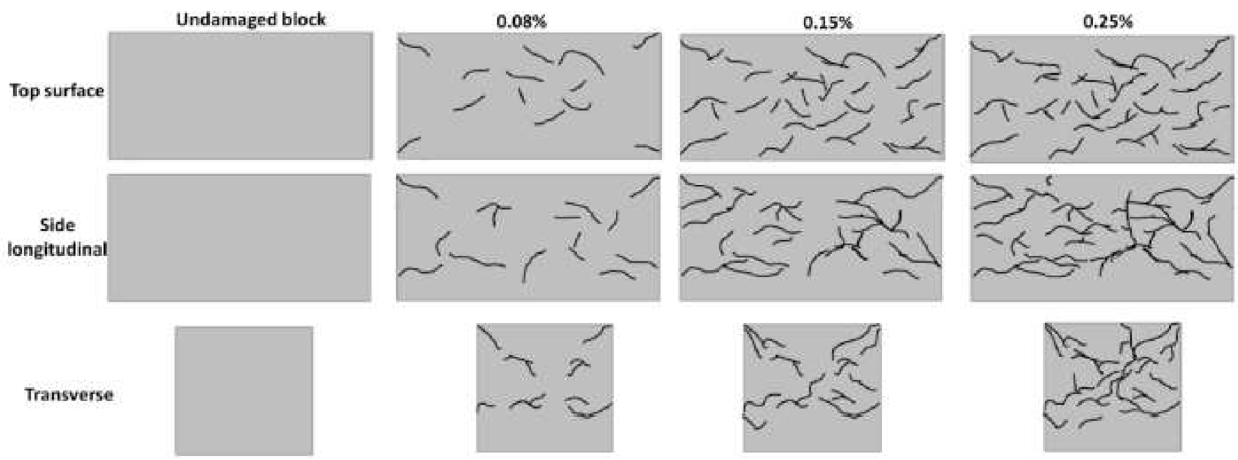

Figure 2-8 Qualitative model by Zahedi et al. 2022 [92] **depicting plain concrete blocks developing internal expansion due to ASR (reproduced from** [92]**)**

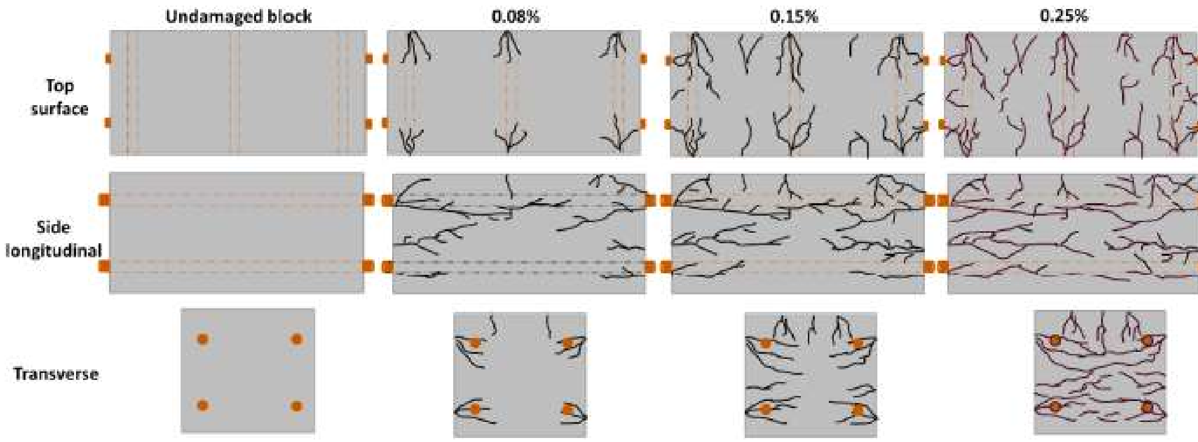

Figure 2-9 Qualitative model by Zahedi et al. 2022 [92] **depicting reinforced concrete blocks developing internal expansion due to ASR (reproduced from** [92]**)**

2.3.2 Non-destructive testing (NDT)

NDT is primarily intended to estimate internal concrete quality and mechanical properties to compare with design specifications and evaluate whether further testing is needed. Non-destructive testing techniques can also be used to evaluate durability with a particular focus on identifying whether chloride ingress and reinforcement corrosion may occur.

2.3.2.1 Surface electrical resistivity

Measurement of electrical conductance through methods like bulk and surface electrical resistivity has been found to correlate to concrete's ability to resist chloride ion penetration [94]. Low electrical resistivity (where ions move easily in the concrete) indicates a higher risk of corrosion [95] although determining a direct relationship is not recommended due to variation in concrete mix designs, cover depths, rebar types, specimen geometry, concrete saturation in the field and the presence of additional deterioration mechanisms and exposure conditions [95–97].

Ion movement in concrete is facilitated by water present in the concrete pore solution, since ER measures ion movement it is very sensitive to moisture in concrete which is why measurements are very influenced by concrete's degree of saturation and temperature [97]. Surface electrical resistivity is considered less reliable than bulk electrical resistivity which can be conducted on cylinders and cores which have been fully saturated. The AASHTO-T-358 standard [98] outlines a procedure to achieve SSD conditions in laboratory cylinders while RILEM TC 154-EMC [95] suggests the use of wetted sponges for measuring surface resistivity in the field emphasizing that a water film on the surface should be avoided. AASHTO T 358-15 and ACI 228-13 [99] indicate that surface resistivity values <12 kΩ·cm would indicate high probability of chloride ion penetration (low durability concrete) while surface resistivity values >254 kΩ·cm indicate low probability of chloride ion penetration (high durability concrete).

2.3.2.2 Rebound hammer

A rebound hammer records the energy absorbed by the concrete on impact [99] and is used to estimate the mechanical properties of the concrete. The value produced in this test represents the elastic properties the concrete and can be correlated to the compressive strength of concrete using equations [100]. This test should be performed on 10 points grouped in a single location following the procedure in ASTM C 805 [101].

2.3.2.3 Ultrasonic pulse velocity

Ultrasonic Pulse Velocity (UPV) uses a transducer and receiver to detect the transmission of sound waves through concrete and is used to assess overall concrete quality as well as defects in concrete such as voids and cracks [102]. This is not an exhaustive method for cataloguing defects but can give a general impression of the material's condition and whether further tests are required [102, 103]. The direct transducer configuration is the most accurate but semi-direct and indirect configurations (Figure 2-10) may be used if geometry is challenging for the direct method or to detect defects, such as cracking, in the concrete surface.

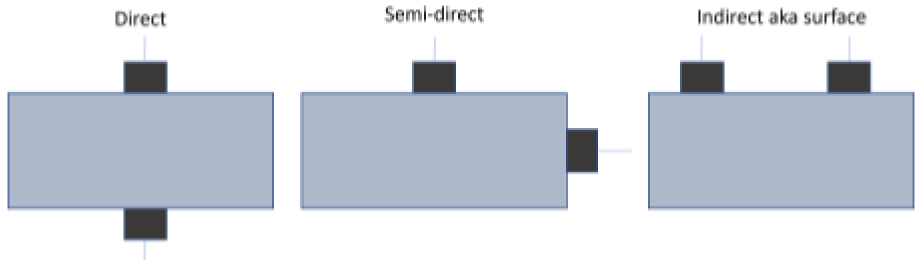

Figure 2-10 Schematic depicting three possible transducer configurations that can be used for ultrasonic pulse velocity measurements

A concrete quality grading system was proposed by the Indian Standards Association for new concrete cylinders [103] in which pulse speeds below 3.0 Km/s were described as indicating 'doubtful' quality requiring further investigation (Table 2-2).

Similar to electrical resistivity, this test method is sensitive to the concrete moisture condition so when used on cylinders or cores in the lab, specimens should be tested in the same moisture condition. The moisture conditions for field samples should be noted (e.g. recent rain etc.).

Table 2-2 Guidelines by the Indian Standards Association (1992) for interpreting UPV results table (adapted from [103]**)**

Pulse velocity by cross probing (i.e. direct UPV) [km/s]	Concrete Quality
> 4.5	Excellent
3.5 to 4.5	Good
3.0 to 3.5	Medium
< 3.0	Doubtful (i.e. poor)

2.3.3 Laboratory evaluation of extracted cores

2.3.3.1 Resonant frequency (mechanical properties)

The resonant frequency technique [104] has been investigated as a method to assess damage in lab and field samples with ASR related damage. Resonant frequency measurements the dynamic modulus of elasticity (dynamic ME) with the transverse mode capturing shear transverse waves (called S-waves), perpendicular to the direction of wave movement while measurements in the longitudinal mode capture compressional longitudinal waves (called P-waves) which are in line with the direction of wave movement. In lab tests RF was found to be able to distinguish between concrete cylinders with and without ASR [105, 106] however Rivard et al. [105] found that resonant frequency results for lab samples did not correlate closely to field samples. Similarly, Olajide et al. [107] found that resonant frequency provided only qualitative assessments of ASR induced damage in laboratory samples, especially when differentiating between low and high damage.

Resonant frequency on cylindrical samples (e.g. cylinders and cores) has gained popularity in the research community due to the non-destructive nature of the test and the relatively low cost. This test can provide an additional method for early assessment of cores, potentially contributing to the triage of samples for different diagnostic tests.

Limitations of this method include reduced reliability when concrete strengths are greater than 30 MPa or samples have a length to diameter ratio less than 2.0 [108].

2.3.3.2 Stiffness damage test – SDT (mechanical properties)

The stiffness damage test (SDT) is a non-destructive cyclic loading procedure to evaluate mechanical losses in concrete core specimens or cylinders. The use of a test using five loading and unloading cycles was first proposed for concrete in 1987 by Crouch [109] and was further evaluated for field structures by Chrisp et al. (1993) [110, 111] as a non-destructive alternative to compressive and tensile tests for the evaluation of the loss of structural strength in concrete with ASR induced deterioration. To ensure the non-destructive nature of the test a slow loading rate (0.5 kN/s and a maximum load of 0 to 15% of the compressive strength) with core specimen subjected to five loading cycles. Stress-strain data was collected with three parameters calculated: the chord loading stiffness – E_C (slope of the loading curve), total energy loss – H (hysteresis area in J/m^3) and the non-linearity index – NLI (half of the slope of the loading curve divided by the chord length). The test was found to be robust and repeatable with the test outputs found to be sensitive to variations in crack patterns within damaged concrete cores (i.e. cracks parallel to loading exhibited higher E_C, low H and NLI <1 while cracks perpendicular to loading exhibited lower E_C, high H and NLI >1) [110].

Work by Smaoui et al. (2004) [112] proposed that a load of 10 MPa be used as it was found to yield more precise results without compromising the non-destructive nature of the test. This was theorized to be because at 10 MPa microcracks caused by ASR closed more completely compared to the lower load of approximately 5.5 MPa used by Chrisp [113]. The hysteresis area of the first curve as well as cumulative plastic deformation over the five loading cycles were found to provide a linear correlation with ASR induced expansion.

High variability was noted in the SDT results, especially the plastic deformation with average coefficients of variation around 20% reported [113, 114] and up to 44% [114]. To address the problem of variability in test results Sanchez et al. (2014, 2015) performed a comprehensive investigation of the test using a variety of concrete strengths (i.e. different mix proportions) and aggregate types [115–117]. Outcomes of this work included: suggesting a maximum load defined as 40% of concrete compressive strength (i.e. 40% of the 28-day strength of companion samples or 40% of a companion core from a less damaged location) and the use of indices for the presentation of SDT results, thus normalizing test outcome to reduce the impact of material specific variability. Measures to reduce specimen related variability, namely a procedure for conditioning samples (storage at room temperature and 100% humidity for 48 hours prior to testing) prior to testing, and the use of samples with a 2:1 length to diameter ratio were also proposed [117].

The SDT, as proposed by Sanchez et al. [115–117], has four outcomes: the stiffness damage index (SDI), representing the ratio of dissipated energy to total energy, the plastic deformation index (PDI), representing plastic deformation relative to total deformation in the sample, the non-linearity index (NLI), representing crack orientation, and the static modulus of elasticity (ME), representing damage extent in the material. The use of indices (i.e. SDI and PDI) allows comparisons between tested specimens which is minimally affected by differences in concrete mix design [83]. In lab specimen in free-expansion conditions cracking in concrete is largely randomly oriented, reducing the applicability of NLI which is related to detection of elasto-plastic deformation in the first loading cycle [116]. Although NLI was found to have some applicability to ASR damage in lab specimen [118] results from testing in this context may not be directly comparable with core specimens from field structures.

SDT has been found to successfully differentiate between different levels of ASR induced damage [116, 117, 119] and between different sources of concrete damage, including internal swelling reactions such as Freeze-thaw (FT) [112, 118] and delayed ettringite formation (DEF) [118, 120, 121] with or without ASR, and damage induced in concrete from other sources [122]. Sanchez et al. [118] undertook a comprehensive assessment of concretes subject to internal swelling reactions, i.e. ASR, FT and DEF, which produced a comprehensive chart. Among these findings, SDI values for concretes with induced damage from ASR and coupled ASR and Freeze-thaw were presented. Concrete with induced damage from coupled ASR and FT was found to present SDI values ranging between 0.27-0.41 and 0.34-0.45 for high and very high expansion compared to only 0.19-0.32 and 0.22-0.36 for concretes affected by only ASR [118].

SDT is considered a minimally destructive mechanical test procedure where samples undergo five loading/unloading cycles performed at 40% of the maximum compressive strength [123] as shown in Figure 2-11.

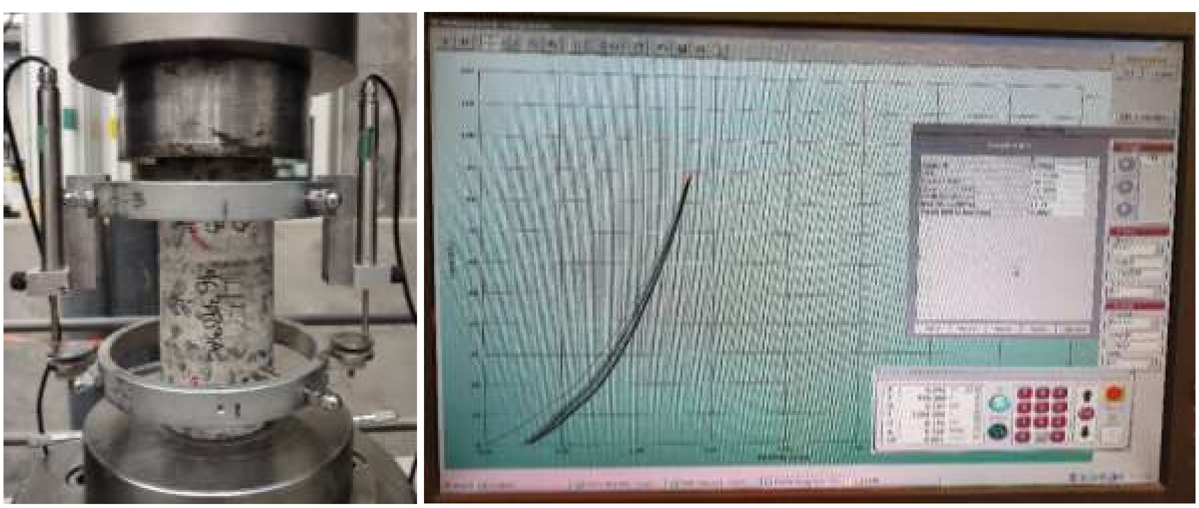

Figure 2-11 Images of the SDT laboratory testing set up (left) and data acquisition screen for a completed test (right) (pictures from uOttawa structures lab)

Calculation of the SDI, PDI, NLI are shown in Figure 2-12 while ME is calculated from the second and third cycles following ASTM C469 [125]. Depending on the damage mechanism and extent of damage, cracks in distressed concrete may occur mainly in the aggregate particles, ITZ or cement paste. As damage develops, cracks enlarge eventually linking to form an interconnected network. This results in non-linear increases in SDI and PDI parameters corresponding to increasing damage. The SDI, PDI and NLI outputs are further described in the following section:

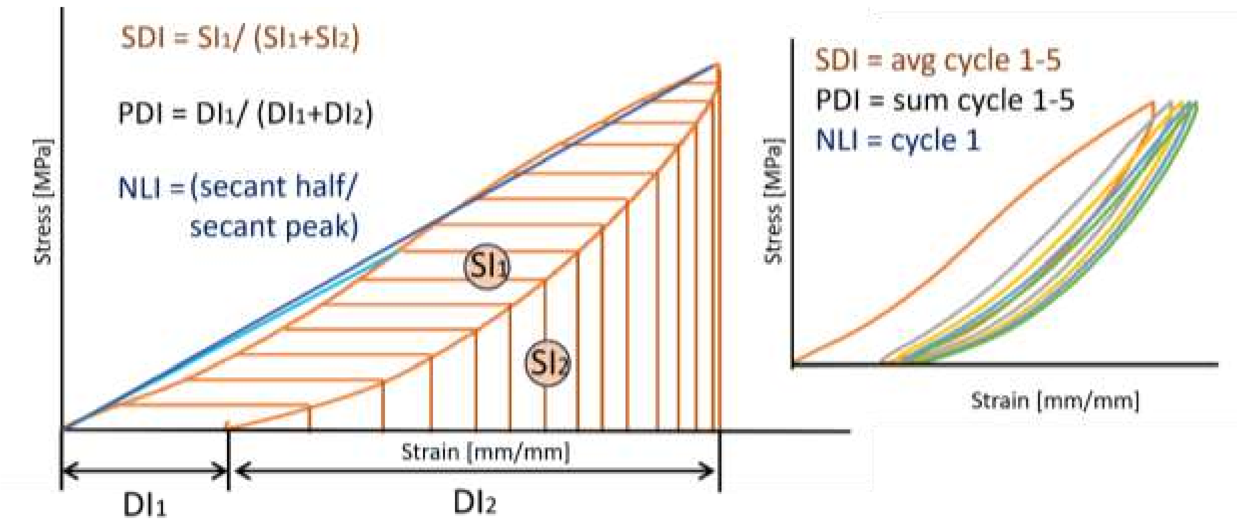

Figure 2-12 Schematic of parameters for the calculation of SDI, PDI and NLI

The **stiffness damage index (SDI)** describes the energy loss (%) in a damaged material due to crack formation during cyclic compressive loading and would approach zero in a sound concrete and increases with increasing damage [123]. It is calculated as the average of 5 cycles where S1 (area between the loading curve and unloading curve) and S2 (area below the unloading curve) are summed for all 5 cycles before calculating the SDI (Figure 2-12).

The **plastic deformation index (PDI)** is calculated from the strain values at the beginning, peak and end of each cycle (Figure 2-12). Similar to SDI, the PDI approaches zero in a sound concrete and increases with increasing damage [123]. D1 is calculated as the initial strain value subtracted from the strain at the end of the cycle. D2 is calculated as the strain value at the end of the cycle subtracted from the strain value at the peak. The final PDI value for the sample is then calculated as the sum of the PDI values found for the 5 individual cycles.

The **non-linearity index (NLI)** value is determined for each curve by dividing the secant of the peak load value by the secant through half the SDT load. In sound concrete the NLI of the first cycle is expected to be approximately 1.05. In concrete effected by ASR this value was found to increase with increasing expansion, for example reaching NLI = 1.30 in a specimen with 0.30% expansion [123]. NLI can be used to investigate whether cracking is occurring perpendicular (NLI >1) or parallel (NLI <1) to the load [110, 111] as shown in Figure 2-13. The direction of cracking can also impact the ME and hysteresis area, for example when cracks are parallel to loading the ME will be high and the hysteresis area will be smaller while the reverse is true for perpendicular cracks [111] this is illustrated in Figure 2-13.

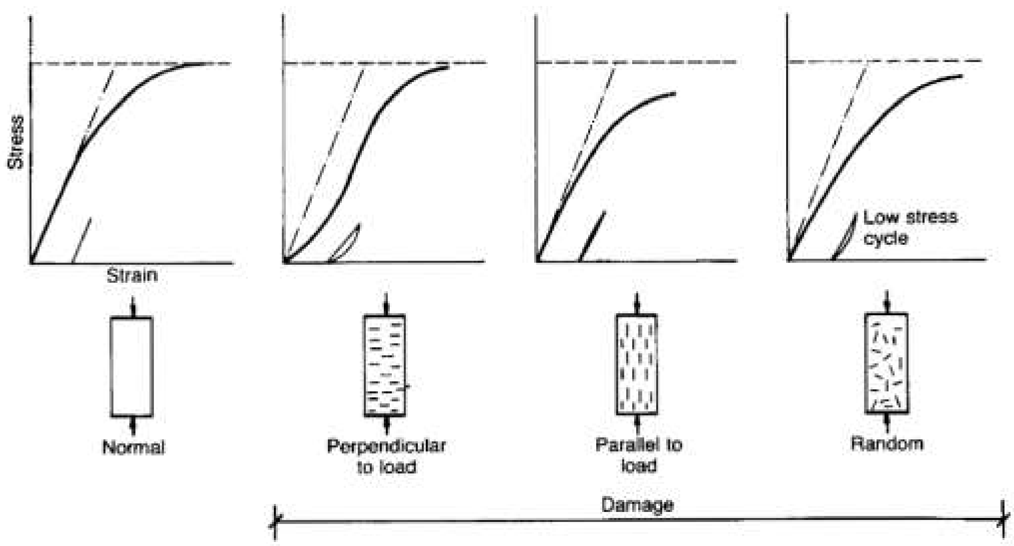

Figure 2-13 Schematic depicting the relationship between stress-strain curve and crack orientation (reproduced from Chrisp et al. 1993 [110]**)**

To limit the variability of this test, cylindrical specimen with a length to diameter ratio of 2.0 should be used [117] while the humidity level of cylinders or extracted cores should be preserved as changes in this variable can alter results [86]. Reconditioning samples by storing at room temperature and 100% humidity for 48 hours prior to testing has been found effective for reducing variability [117]. When assessing damaged structures, the reference strength can be estimated using a core from an undamaged section of the structural element under investigation [111].

2.3.3.3 Damage Rating Index (Microscopic)

The DRI is a semi-quantitative microscopic technique where a stereomicroscope (15-16x magnification) is used to systematically evaluate polished concrete sections using a 1 cm^2 grid system. A numerical value is determined based on counts of various damage features (i.e. cracking in aggregates, cement paste and presence or absence of gel) in each grid square.

The DRI was initially developed as an extended petrographic technique by Grattan-Bellew and coworkers (1992), to quantify ASR-induced development (i.e., chemical reaction development) [132]. This technique aimed to quantify the level of ASR chemical development (i.e., initial stage, moderate, high and very high development) through counting the following petrographic features: gel in voids, reaction rims in aggregates, loose aggregates, cracks in cement paste with or without gel and cracks in aggregates that were closed, open or containing gel. Later, Villeneuve et al. [133] proposed some changes to the method with the aim of achieving a better correlation with ASR-induced expansion while reducing the variability among operators. As part of this work, Villeneuve et al. [133] selected to evaluate only microscopic damage features which impacted damage development associated to ASR (i.e., open cracks in aggregates and cement paste) instead of the petrographic features proposed by Grattan-Bellew and coworkers. Moreover, new weighting factors were proposed for the distinct microscopic damage features as per Table 2-3.

Amongst the weighting factors proposed by Villeneuve et al. [133], the closed cracks in the aggregates (CCA) were selected as microscopic damage features, since they represent weak planes of the aggregates particles prone to break under pressure; however, CCA is not generally associated to ASR-induced damage, being more related to the aggregates' processing and weathering. Therefore, a significantly low weighting factor of 0.25 is attributed to this feature. By contrast, the presence of open cracks in aggregate particles without or with reaction products, OCA and OCA_{RP} respectively, were observed to increase corresponding to induced ASR damage and thus display a high weighting factor of 2.

Similarly, cracks in the cement paste without or with reaction products (CCP and CCP_{RP} respectively) correspond to increasing distress due to ASR, especially when ASR has become more developed. Moreover, through a mechanical point of view, cracks in the cement paste influence more on the mechanical properties of the concrete; therefore, an even higher weighting factor of 3 was selected for this feature.

Sanchez et al. [26, 124] subsequently investigated the use of DRI for assessing ASR-induced expansion and associated damage of concrete mixtures incorporating various reactive aggregate types (i.e., coarse versus fine) and natures (i.e., lithotypes), and mechanical properties (i.e., 25, 35 and 45 MPa). The authors concluded that the weighting factors as per Table 2-3 effectively distinguished numerous levels of ASR-induced damage (i.e., marginal, moderate, high, and very high). Furthermore, the authors also evaluated the use of the DRI employing the proposed weighting factors to appraise other internal swelling reactions, such as freeze-thaw (FT) and delayed ettringite formation (DEF). The findings of these works attested the promising potential of the DRI to appraise internal swelling reactions in general, and a comprehensive table benchmarking the DRI numbers as a function of distinct expansion levels for various deterioration mechanisms (i.e., single or coupled) was proposed [83].

Table 2-3 Weighting factors used for Damage Rating Index (DRI) Microscopic Technique (adapted from Villeneuve et al. [133])

Damage features	Abbrev.	Weight factors
Crack in coarse aggregate	CCA	0.25
Opened crack in aggregate	OCA	2
Crack with reaction product in aggregate	OCA_{RP}	2
Debonded/dislodged aggregate	Debond	3
Crack in cement paste	CCP	3
Crack with reaction product in cement paste	CCP_{RP}	3
Disaggregate/corroded aggregate particle	DAP	2

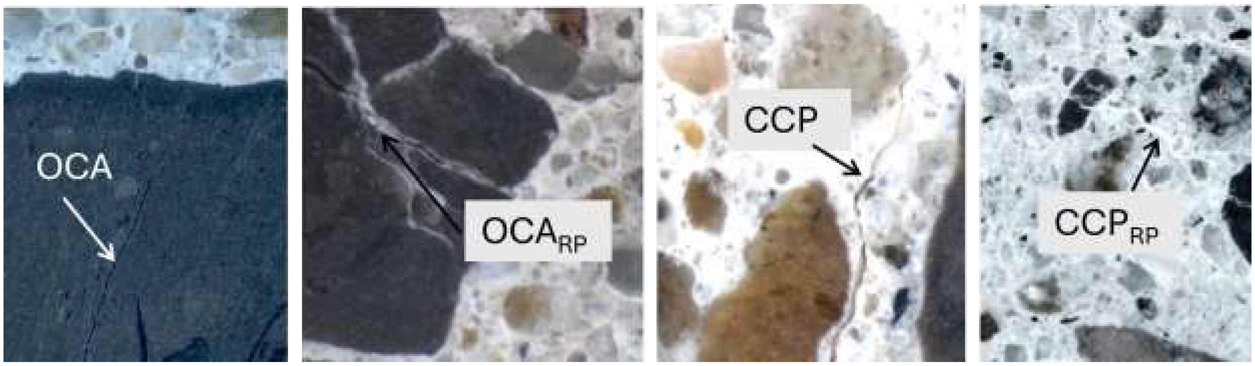

Figure 2-14 Annotated images depicting crack types with and without gel (i.e. reaction product – RP) which may be identified during DRI

Sanchez et al. [26] also proposed a complementary petrographic analysis with the use of the DRI, the so-called 'extended DRI', where the cracks observed in affected concrete are evaluated in absolute (counts) and relative (%) manners. This complementary analysis facilitates a more comprehensive understanding of the damage evolution of distinct deterioration mechanisms in concrete. Furthermore, the extended DRI enables the computation of the crack density (CD), where the number of open cracks in the aggregates and cement paste (with and without gel) present in the affected concrete is normalized to cm^2,

To complete DRI assessments, especially when specimens from field structures are analyzed, supplementary image analysis (i.e. measuring crack widths and lengths, and angles) [126] may further enhance understanding of the impact of various factors (e.g. presence of confinement or restraint, microclimate, etc.), on the overall deterioration of concrete [127, 128].

In recent years, the DRI has also been successfully used to appraise concrete mixtures affected by external mechanisms, such as external sulphate attack [129] and physical salt attack [129]. This ability of the DRI to assess both external and interior deterioration mechanisms (i.e., single or coupled), which commonly occur in the field (particularly in Canada), makes it a versatile and valuable diagnostic tool for evaluating concrete durability under complex exposure conditions.

2.3.3.3.1 Differences in damage patterns caused by different mechanisms

Damage patterns in deteriorated concrete prepared for DRI differ depending on the damage mechanisms present. For ASR affected concretes the pattern of cracking differs depending on whether the reactive aggregate is fine or coarse (Figure 2-15) which also results in different damage feature distributions in DRI. A key difference is that when ASR initiates in reactive fine aggregates cracks propagate through the cement paste without causing cracking in the coarse aggregate.

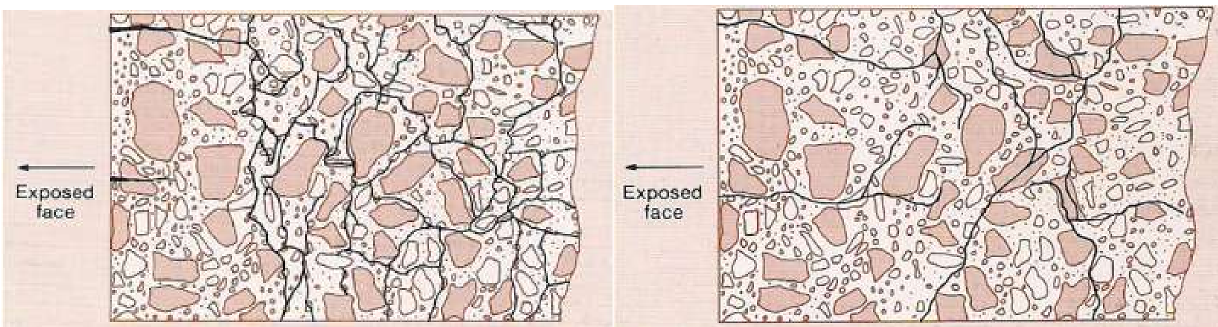

Figure 2-15 Depictions by the British Cement Association (1992) illustrating internal cracking due to ASR caused by reactive sand (left) and reactive coarse aggregate (right) (reproduced from [135]**)**

In structures experiencing FT damage, cracks will be concentrated near the exposed surface of the sample with cracks parallel to the surface as shown in Figure 2-16.

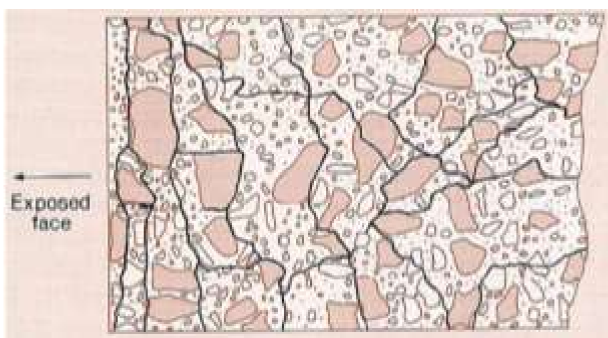

Figure 2-16 Depictions by the British Cement Association (1992) illustrating internal cracking due to FT (reproduced from [135]**)**

DEF causes expansion in the cement paste and may occur in conjunction with AAR. The formation of ettringite in cement paste and damage in the interfacial transition zone (ITZ) at the surfaces of aggregate particles [135] as shown in Figure 2-17. Ettringite around aggregate particles is often used to determine that DEF has occurred but may not be present in all DEF effected concretes. SEM EDX is commonly used to further confirm DEF occurrence [135].

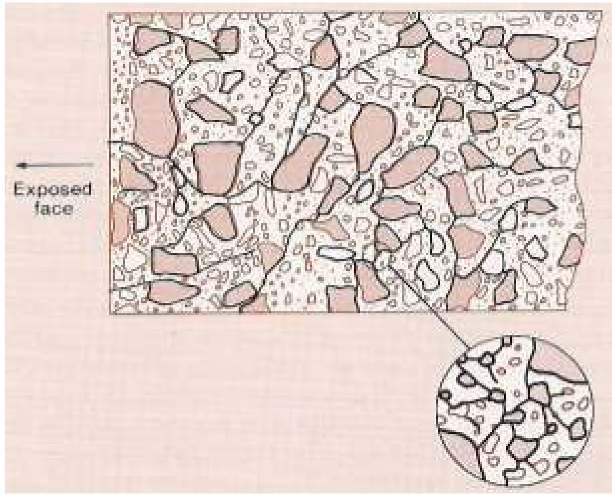

Figure 2-17 Depictions by the British Cement Association (1992) illustrating internal cracking due to DEF (reproduced from [135]**)**

2.4 Limitations of current condition assessment techniques

Condition assessments are intended to identify the extent and cause(s) of damage. In the literature review section common deterioration mechanisms encountered in field structures in Canada were described along with tests performed both externally in-situ (i.e. visual and non-destructive testing) and state of the art testing for cores extracted from field structures (i.e. microscopic and mechanical). This section will briefly discuss inherent limitations of condition assessments for field structures such as the Champlain Bridge, followed by a summary of limitations identified for current and state-of-the-art techniques for assessing reinforced concrete members.

Condition assessments of aged structures, such as the Champlain Bridge, present inherent limitations in terms of availability of records. This may include degradation of physical records (e.g. fading ink, water damage, data corruption and lost documents) which limit knowledge about the original work including aspects such as concrete design compressive strength, material properties (e.g. Na_2O equivalent in cement used, quarry where aggregates were sourced, w/c ratio etc.). It may further be necessary to consult codes from the time of construction to better understand minimum requirements at that time. Limited records related to the service environment (e.g. use of road salts, static and dynamic loading) as well as repairs and modifications to individual members may further introduce uncertainty during condition assessments. Some information, such as de-icing salt use, may have been initially viewed as a low impact change to operation of the structure with the long-term repercussions only realized in subsequent decades.

Visual and non-destructive testing present a number of inherent limitations. In reinforced concrete often superficial damage on the surface of members, such as reinforcement corrosion and freeze-thaw damage, may potentially overshadow internal damage which presents a larger structural concern in field structures. This in part is due to the strong association of the ‘map cracking’ pattern with internal swelling reactions (e.g. ASR, DEF). While this pattern commonly occurs in unreinforced concrete experiencing internal swelling, reinforced concrete has been found to present differently with cracks occurring parallel to reinforcement (discussed in section 2.3.1.2). Non-destructive tests used to estimate concrete damage (i.e. UPV, rebound hammer) are often highly limited by the need to transmit through defects in the concrete cover, reducing the ability of results from these tests to capture internal damage. In severely damaged concrete defects such as delamination and wide cracks may inhibit the use of these tests. The presence of materials such as steel reinforcement may also result in misleading results. This is especially true for UPV where measurements performed parallel to reinforcement may present higher speeds (resulting in less conservative results) due to sound waves being transferred through reinforcement rather than concrete. Ultimately, these limitations mean that where the extent of damage is thought to be high, as defined by tests such as cracking index and UPV exceeding specific thresholds, further investigations should be conducted through extraction of concrete cores.

Analysis of concrete cores is an important step for identifying the cause and extent of internal damage in reinforced concrete members. However, despite large advances increasing the understanding of damage mechanisms, including ASR, primarily through accelerated testing in laboratory settings, gaps persist in evaluation of cores from field structures. Multi-level assessments (i.e. microscopic and mechanical) through the DRI and SDT (sections 2.3.3.2 and 2.3.3.3) have been used to successfully identify a variety of causes (e.g. ASR, FT, DEF) as well as the extent of damage as correlated to expansion in lab specimens. However, despite the adoption of normalized outputs such as the SDI and PDI, the concrete mixture (e.g. aggregate types used, compressive strength) has been found to impact results especially for mechanical testing. Directional cracking, which is common in cores extracted from field structures, is also understood to result in further variability in mechanical results. Although this has been identified in a variety of works [110, 119, 136, 137, 138], anisotropy has been largely addressed through correlation of test results with qualitative observations of cracking on cores. Extracted cores, are also expected to exhibit damage from combined mechanisms. Although combined mechanisms have been investigated in accelerated lab tests literature about the behaviour in field structures remains limited.

2.5 References

1. Carlin GP (2017) The Existing Champlain Bridge - Overview of Issues – The Owner's Perspective. In: 39th IABSE Symposium – Engineering the Future. Vancouver, pp 1505–1512

2. COWI (2017) Champlain bridge: Impacts due to possible delays of new bridge opening. (Report)

3. Carlin GP, Mirza MS, Gaudreault M (1996) Rehabilitation Measures for Champlain Bridge, Montreal, Canada. Canadian Journal of Civil Engineering 23:1326–1340

4. Delcan (2011) The Future of the Champlain Bridge. (Report)

5. Office of the Auditor General of Canada (2018) Report 4—Replacing Montréal's Champlain Bridge—Infrastructure Canada.

6. Bérubé M-A, Frenette J (1995) Évaluation de la Réactivité Alcaline dans le Béton des Piles 12, 18 et 20 W du Pont Champlain. Sainte-Foy, Quebec

7. Zakka ZA, Carrasquillo RL (1989) Effects of High-range water reducers on the properties of fresh and hardened concrete.

8. Passfield RW (2007) Philip Louis Pratley (1884-1958): Bridge design engineer. Canadian Journal of Civil Engineering 34:637–650

9. Bouzoubaâ N, Fournier B (2005) Current situation with the production and use of supplementary cementitious materials (SCM's) in concrete construction in Canada. Canadian Journal of Civil Engineering 32:129–143

10. Cyr M (2024) The Past and the Future of Supplementary Cementing Materials (SCM). In: Ha-Minh C, PCH, VHTH, HDVK (ed) Proceedings of the 7th International Conference on

Geotechnics, Civil Engineering and Structures, CIGOS 2024. Springer, Singapore, Ho Chi Minh City, Vietnam, pp 681–689

11. Van Breugel K (2017) Societal Burden and Engineering Challenges of Ageing Infrastructure. In: Procedia Eng. Elsevier Ltd, pp 53–63

12. Sanchez LFM, Fournier B, Jolin M, Mitchell D, Bastien J (2017) Overall assessment of Alkali-Aggregate Reaction (AAR) in concretes presenting different strengths and incorporating a wide range of reactive aggregate types and natures. Cem Concr Res 93:17–31

13. Stanton TE (1940) Expansion of Concrete Through Reaction Between Cement and Aggregate. Proc ASCE 66:1781–1811

14. Rogers, Grattan-Bellew PE, Hooton RD, Ryell J, Thomas MDA (2000) Alkali-aggregate reactions in Ontario. Canadian Journal of Civil Engineering 27:446–460

15. Swenson EG (1957) A Reactive aggregate undetected by ASTM tests. ASTM Bulletin 226:48–51

16. Swenson EG, Legget RF (1960) Kingston study of cement-aggregate reaction. Canadian Consulting Engineer 2:38–46

17. Rogers C (1993) Alkali-aggregate reactivity in Canada. Cem Concr Compos 15:13–19

18. Bérubé, Snaoui N, Bissonnette B, Fournier B (2005) Outil d'evaluation et de gestion des ouvrages d'art affectes de reactions alcalis-silice (RAS).

19. Ozol MA (1994) Alkali-Carbonate Rock Reaction. In: Concrete and Concrete Making Materials. pp 372–387

20. Bérubé M-A, Fournier B (1987) Le barrage Sartigan dans la Beauce (Quebec), Canada: un cas-type de deterioration du beton par des reactions alcalis-granulats. Canadian Journal of Civil Engineering 14:372–380

21. Thomas MDA, Hooton RD, Rogers CA (1997) Prevention of Damage Due to Alkali-Aggregate Reaction (AAR) in Concrete Construction Canadian Approach. Cement, Concrete, and Aggregates 19:26–30

22. Stark D (1985) Alkali-Silica Reactivity in Five Dams in Southwestern United States.

23. CSA A23.2-27A (2019) Standard practice to identify degree of alkali-reactivity of aggregates and to identify measures to avoid deleterious expansion in concrete.

24. Hobbs DW (1988) Alkali-silica reaction in concrete. ICE

25. RILEM (2013) Guide to Diagnosis and Appraisal of AAR Damage to Concrete in Structures. Springer Netherlands

26. Sanchez LFM, Fournier B, Jolin M, Duchesne J (2015) Reliable quantification of AAR damage through assessment of the Damage Rating Index (DRI). Cem Concr Res 67:74–92

27. Gautam BP, Panesar DK, Sheikh SA, Vecchio FJ (2017) Effect of coarse aggregate grading on the ASR expansion and damage of concrete. Cem Concr Res 95:75–83

28. Rajabipour F, Giannini E, Dunant C, Ideker JH, Thomas MDA (2015) Alkali-silica reaction: Current understanding of the reaction mechanisms and the knowledge gaps. Cem Concr Res 76:130–146

29. Miura T, Multon S, Kawabata Y (2021) Influence of the distribution of expansive sites in aggregates on microscopic damage caused by alkali-silica reaction: Insights into the mechanical origin of expansion. Cem Concr Res. https://doi.org/10.1016/j.cemconres.2021.106355

30. Strack CM, Thornell TL, Jefcoat JA, Borne GJ, Alapati P, Kurtis KE, Moser RD (2023) The viscoelastic behavior of synthetic alkali-silica gels at ambient temperature. Cem Concr Res. https://doi.org/10.1016/j.cemconres.2022.107069

31. Hou X, Kirkpatrick RJ, Struble LJ, Monteiro PJM (2005) Structural investigations of alkali silicate gels. Journal of the American Ceramic Society 88:943–949

32. Leemann A, Shi Z, Lindgård J (2020) Characterization of amorphous and crystalline ASR products formed in concrete aggregates. Cem Concr Res. https://doi.org/10.1016/j.cemconres.2020.106190

33. Boehm-Courjault E, Leemann A (2017) Characterization of ASR products by SEM and TEM. In: 16th Euroseminar on Microscopy Applied to Building Materials EMABM. Les Diablerets, Switzerland, pp 27–30

34. Fournier B, Bérubé M-A (2000) Alkali – aggregate reaction in concrete: a review of basic concepts and engineering implications. Canadian Journal of Civil Engineering 27:167–191

35. Grattan-Bellew PE, Mitchell LD, Margeson J, Min D (2010) Is alkali-carbonate reaction just a variant of alkali-silica reaction ACR = ASR? Cem Concr Res 40:556–562

36. Grattan-bellew PE, Chan G (2013) Comparison of the morphology of alkali-silica gel formed in limestones in concrete affected by the so-called alkali-carbonate reaction (ACR) and alkali-silica reaction (ASR). Cem Concr Res 47:51–54

37. Katayama T (2010) The so-called alkali-carbonate reaction (ACR) — Its mineralogical and geochemical details, with special reference to ASR. Cem Concr Res 40:643–675

38. U.S. Department of Transportation Federal Highway Administration (2013) Alkali-aggregate reactivity (aar) facts book.

39. Gartner EM, Tang FJ, Weiss SJ (1985) Saturation Factors for Calcium Hydroxide and Calcium Sulfates in Fresh Portland Cement Pastes. Journal of American Ceramics Society 68:667–673

40. Lothenbach B (2010) Thermodynamic equilibrium calculations in cementitious systems. Mater Struct 43:1413–1433

41. Environment Canada Canadian Climate Normals 1981-2010 Station Data. https://climate.weather.gc.ca/climate_normals/results_1981_2010_e.html?searchType=stnName&txtStationName=Montreal&searchMethod=contains&txtCentralLatMin=0&txtCentralLatSec=0&txtCentralLongMin=0&txtCentralLongSec=0&stnID=5415&dispBack=0.

42. Lachance R (2020) Climate Change Adaptation Plan for the Agglomeration of Montreal.

43. Prairie Climate Centre Climate Atlas of Canada. https://climateatlas.ca/.

44. Qin X, Meng S, Cao D, Tu Y, Sabourova N, Grip N, Ohlsson U, Blanksvärd T, Sas G, Elfgren L (2016) Evaluation of freeze-thaw damage on concrete material and prestressed concrete specimens. Constr Build Mater 125:892–904

45. Wang Y, Cao Y, Zhang P, Ma Y, Zhao T, Wang H, Zhang Z (2019) Water absorption and chloride diffusivity of concrete under the coupling effect of uniaxial compressive load and freeze-thaw cycles. Constr Build Mater 209:566–576

46. Powers TC, Helmuth RA (1953) Theory of Volume Changes in Hardened Portland Cement Paste During Freezing. In: Proceedings of Highway Research Board 32nd meeting. pp 285–297

47. Li K (2016) Durability Design of Concrete Structures: Phenomena, Modeling, and Practice.

48. Powers TC (1949) The Air Requirement of Frost-Resistant Concrete. Highway Research Board 29:184-202,

49. Mindess S, Young JF, Darwin D (2003) Concrete. Prentice-Hall Inc.

50. Walbert C, Eslami J, Beaucour A, Bourges A, Noumowe A (2015) Evolution of the mechanical behaviour of limestone subjected to freeze – thaw cycles. Environ Earth Sci 74:6339–6351

51. Coussy O, Monteiro PJM (2008) Poroelastic model for concrete exposed to freezing temperatures. Cem Concr Res 38:40–48

52. Chen J, Bharata R, Yin T, Wang Q, Wang H, Zhang T (2017) Assessment of sulfate attack and freeze – thaw cycle damage of cement-based materials by a nonlinear acoustic technique. Mater Struct 50:1–10

53. Afrani I, Rogers C (1994) The Effects of Different Cementing Materials and Curing on Concrete Scaling. Cement, Concrete, and Aggregates 16:132–139

54. Kessler S, Thiel C, Grosse CU, Gehlen C (2017) Effect of freeze – thaw damage on chloride ingress into concrete. Mater Struct 50:1–13

55. CSA A23.1 (2019) Concrete materials and methods of concrete construction/ Test Methods and Standard practices for concrete. 1–876

56. ACI 201.1R (2008) Guide for Conducting a Visual Inspection of Concrete in Service.

57. Rosenqvist M (2016) Frost-induced deterioration of concrete in hydraulic structures Interactions between water absorption, leaching and frost action. Ph.D. Dissertation, Lund University

58. Rosenqvist M, Oxfall M, Fridh K, Hassanzadeh M (2015) A test method to assess the frost resistance of concrete at the waterline of hydraulic structures. Mater Struct 2403–2415

59. NACE Corrosion resources for highways and bridges. https://www.nace.org/resources/industries-nace-serves/highways-bridges.

60. Mermigas K (2018) Evolution of Bridge Practices in Ontario, Canada. In: 2018 Conference of the Transportation Association of Canada. Saskatoon, pp 1–18

61. Sandwell RW (2016) The History of Power, Fuel, and Energy from 1600.

62. Gouda (1970) Corrosion and Corrosion Inhibition of Reinforcing Steel I. Immersed in Alkaline Solutions. British Corrosion Journal 5:198–203

63. Brueckner R, Lambert P (2017) Unexpected effects of historic concrete innovations. International Journal of Heritage Architecture: Studies, Repairs and Maintence 1:549–563

64. Loser R, Lothenbach B, Leemann A, Tuchschmid M (2010) Chloride resistance of concrete and its binding capacity - Comparison between experimental results and thermodynamic modeling. Cem Concr Compos 32:34–42

65. Mehta PK, Monteiro PJ (2006) Concrete, 3rd ed. McGraw-Hill, New York

66. Gouda VK, Azim AAA, Sayed HA El (1974) Some Aspects of Reinforcement Corrosion in Egyptian Structures. British Corrosion Journal 3:185–189

67. Wimpenny D, Slater D (2003) Evidence from the highways agency thaumasite investigation in Gloucestershire to support or contradict postulated mechanisms of thaumasite formation (TF) and thaumasite sulfate attack (TSA). Cem Concr Compos 25:879–888

68. Alonso C, Andrade C, Castellote M, Castro P (2000) Chloride threshold values to depassivate reinforcing bars embedded in a standardized OPC mortar. Cem Concr Res 30:1047–1055

69. Scott A, Alexander MG (2016) Effect of supplementary cementitious materials (binder type) on the pore solution chemistry and the corrosion of steel in alkaline environments. Cem Concr Res 89:45–55

70. Hansson CM (1984) Comments on electrochemical measurements of the rate of corrosion of steel in concrete. Cem Concr Res 14:574–584

71. Ahmed S (2003) Reinforcement corrosion in concrete structure, its monitoring and service life prediction-a review. Cem Concr Res 3:459–471

72. Lide DR (1999) CRC Handbook of Chemistry and Physics. CRC Press, New York, NY

73. Jones DA (1996) Principles and Prevention of Corrosion, 2nd ed. Prentice-Hall Inc., Upper Saddle River

74. Ahlstrom J, Tidblad J, Sederholm B, Wads L (2016) Influence of chloride and moisture content on steel rebar corrosion in concrete. Materials and Corrosion 67:1049–1058

75. Djerbi A, Bonnet S, Khelidj A, et al (2008) Influence of traversing crack on chloride diffusion into concrete. Cem Concr Res 38:877–883

76. Ismail M, Toumi A, Franc R, Gagne R (2004) Effect of crack opening on the local diffusion of chloride in inert materials. Cem Concr Res 34:711–716

77. Revert AB, De Weerdt K, Hornbostel K, Geiker MR (2018) Carbonation-induced corrosion : Investigation of the corrosion onset. Constr Build Mater 162:847–856

78. Poursaee A (2016) Corrosion of steel in concrete structures. In: Corrosion of Steel in Concrete Structures. Elsevier Ltd, pp 19–33

79. De Weerdt K, Plusquellec G, Revert AB, Geiker MR, Lothenbach B (2019) Effect of carbonation on the pore solution of mortar. Cem Concr Res 118:38–56

80. ACI Committee 201 (2016) Guide to Durable Concrete : (ACI 201.2R-16).

81. Poole AB, Sims I (2016) Concrete Petrography: A Handbook of Investigative Techniques, 2nd ed. CRC Press Taylor and Francis group

82. Taylor HFW, Famy C, Scrivener KL (2001) Delayed ettringite formation. Cem Concr Res 31:683–693

83. Sanchez LFM, Drimalas T, Fournier B, Mitchell D, Bastien J (2018) Comprehensive damage assessment in concrete affected by different internal swelling reaction (ISR) mechanisms. Cem Concr Res 107:284–303

84. Sanchez LFM (2024) Internal Swelling Reactions in Concrete. https://doi.org/10.1201/9781003188155

85. Fournier B, Bérubé M-A, Folliard KJ, Thomas M (2010) Report on the Diagnosis, Prognosis, and mitigaton of Alkali-Silica Reaction (ASR) in Transportation Structures.

86. RILEM technical committee 259-ISR (2021) Diagnosis & Prognosis of AAR Affected Structures. Springer Nature Switzerland AG

87. Moore M, Phares BM, Graybeal B, Rolander D, Washer G (2001) Reliability of Visual Inspection for Highway Bridges, Volume I: Final Report (FHWA-RD-01-105).

88. RILEM (2013) Guide to Diagnosis and Appraisal of AAR Damage to Concrete in Structures. Springer Netherlands

89. Godart B, Fasseu P, Michel M (1992) Diagnosis and monitoring of concrete bridges damaged by AAR in Northern France. In: The Ninth International Conference On Alkali-Aggregate Reaction In Concrete. London, UK, pp 368–375

90. Institution of Structural Engineers (ISE) (1992) Structural Effects of Alkali-Silica Reaction – Technical Guidance Appraisal of Existing Structures. Institution of Structural Engineers 45

91. Fan S, Hanson JM (1999) Effect of Alkali Silica Reaction Expansion and Cracking on Structural Behavior of Reinforced Concrete Beams. ACI Mater J 488–495

92. Zahedi A, F M Sanchez L, Noël M (2022) Appraisal of visual inspection techniques to understand and describe ASR-induced development under distinct confinement conditions. Constr Build Mater. https://doi.org/10.1016/j.conbuildmat.2022.126549

93. Fan S, Hanson JM (1999) Length Expansion and Cracking of Plain and Reinforced Concrete Prisms Due to Alkali-Silica Reaction. ACI Mater J 480–485

94. ASTM C1202 (2010) Standard Test Method for Electrical Indication of Concrete's Ability To Resist Chloride Ion Penetration.

95. Polder R, Andrade C, Elsener B, Vennesland O, Gulikers J, Weidert R, Raupach M (2000) RILEM TC 154-EMC: electrochemical techniques for measuring metallic corrosion: Test methods for on site measurement of resistivity of concrete. Materials and structures/ Matériaux et Constructions 33:603–611

96. Layssi H, Ghods P, Alizadeh AR, Salehi M (2015) Electrical Resistivity of Concrete; Concepts, applications, and measurement techniques. Concrete Internationals 41–46

97. Hornbostel K, Larsen CK, Geiker MR (2013) Relationship between concrete resistivity and corrosion rate - A literature review. Cem Concr Compos 39:60–72

98. AASHTO T 358-15 (2015) Standard Method of Test for Surface Resistivity Indication of Concrete's Ability to Resist Chloride Ion Penetration.

99. ACI 228 (2013) Report on Nondestructive Test Methods for Evaluation of Concrete in Structures. American Concrete Institute. https://doi.org/10.14359/51686889

100. Meynink P, Samarin A (1979) Assessment of compressive strength of concrete by cylinders, cores, and non-destructive tests. In: RILEM Symp. Proc. On Quality Control of Concrete Structures. Swedish Concrete Research Institute Stockholm, Sweden, pp 127–134

101. ASTM C 805-02 (2002) Standard Test Method for Rebound Number of Hardened Concrete. United States Am Soc Test Mater

102. ASTM C597 (2016) Standard Test Method for Pulse Velocity Through Concrete. 4–7

103. IS 13311-1 (Part 1) (1992) Method of Non-destructive testing of concrete, Part 1: Ultrasonic pulse velocity [CED 2: Cement and Concrete]. Bureau of Indian Standards 1–7

104. ASTM C215 (2020) Standard Test Method for Fundamental Transverse , Longitudinal , and Torsional Resonant Frequencies of Concrete Specimens. ASTM standard 1–7

105. Rivard P, Saint-Pierre F (2009) Assessing alkali-silica reaction damage to concrete with non-destructive methods: From the lab to the field. Constr Build Mater 23:902–909

106. Sargolzahi M, Kodjo SA, Rivard P, Rhazi J (2010) Effectiveness of nondestructive testing for the evaluation of alkali-silica reaction in concrete. Constr Build Mater 24:1398–1403

107. Olajide OD, Nokken MR, Sanchez LFM (2024) Efficiency of the Dynamic Resonance Frequency in Assessing ASR Induced Damage at Numerous Exposure Conditions. In: RILEM Bookseries. Springer Science and Business Media B.V., pp 28–35

108. Sajid S, Chouinard L, Carino N (2019) Robustness of resonant frequency test for strength estimation of concrete. Adv Civ Eng Mater 8:451–462

109. Crouch RS (1987) Specification for the determination of stiffness damage parameters from the low cyclic uniaxial compression of plain concrete cores. Revision A. Mott Hay & Anderson, Special Services Division, internal technical note

110. Chrisp TM, Waldron P, Wood JGM (1993) Development of a non-destructive test to quantify damage in deteriorated concrete. Magazine of Concrete Research 45:247–256

111. Chrisp TM, Wood JGM, Norris P (1993) Towards Quantification of Microstructural Damage in AAR Deteriorated Concrete. In: International Conference on Recent Developments on the Fracture of Concrete and Rock. pp 419–427

112. Smaoui N, Bérubé MA, Fournier B, Bissonnette B, Durand B (2004) Evaluation of the expansion attained to date by concrete affected by alkali-silica reaction. Part I: Experimental study. Canadian Journal of Civil Engineering 31:826–845

113. Smaoui N, Fournier B, Bérubé MA, Bissonnette B, Durand B (2004) Evaluation of the expansion attained to date by concrete affected by alkali-silica reaction. Part II: Application to nonreinforced concrete specimens exposed outside. Canadian Journal of Civil Engineering 31:997–1011

114. Giannini ER, Folliard KJ (2012) Stiffness Damage and Mechanical Testing of Core Specimens for the Evaluation of Structures Affected by ASR. 14th International Conference on the Alkali-Aggregate Reaction

115. Sanchez LFM (2014) Contribution to the Assessment of Damage in Aging Concrete Infrastructures Affected by Alkali-Aggregate Reaction. PhD, Université Laval

116. Sanchez LFM, Fournier B, Jolin M, Bastien J (2014) Evaluation of the stiffness damage test (SDT) as a tool for assessing damage in concrete due to ASR: Test loading and output

responses for concretes incorporating fine or coarse reactive aggregates. Cem Concr Res 56:213–229

117. Sanchez LFM, Fournier B, Jolin M, Bastien J (2015) Evaluation of the Stiffness Damage Test (SDT) as a tool for assessing damage in concrete due to alkali-silica reaction (ASR): Input parameters and variability of the test responses. Constr Build Mater 77:20–32

118. Sanchez LFM, Drimalas T, Fournier B, Mitchell D, Bastien J (2018) Comprehensive damage assessment in concrete affected by different internal swelling reaction (ISR) mechanisms. Cem Concr Res 107:284–303

119. Zahedi A, Trottier C, Sanchez L, Noël M (2022) Evaluation of the induced mechanical deterioration of alkali-silica reaction affected concrete under distinct confinement conditions through the Stiffness Damage Test. Cem Concr Compos. https://doi.org/10.1016/j.cemconcomp.2021.104343

120. Giannini ER, Sanchez LFM, Tuinukuafe A, Folliard KJ (2018) Characterization of concrete affected by delayed ettringite formation using the stiffness damage test. Constr Build Mater 162:253–264

121. Martin RP, Sanchez L, Fournier B, Toutlemonde F (2017) Evaluation of different techniques for the diagnosis & prognosis of Internal Swelling Reaction (ISR) mechanisms in concrete. Constr Build Mater 156:956–964

122. Nassif AY, Petrou MF (2013) Influence of cold weather during casting and curing on the stiffness and strength of concrete. Constr Build Mater 44:161–167

123. Sanchez LFM, Fournier B, Jolin M, Bastien J, Mitchell D (2016) Practical use of the Stiffness Damage Test (SDT) for assessing damage in concrete infrastructure affected by alkali-silica reaction. Constr Build Mater 125:1178–1188

124. Sanchez LFM, Fournier B, Jolin M, Bedoya MAB, Bastien J, Duchesne J (2016) Use of Damage Rating Index to Quantify Alkali-Silica Reaction Damage in Concrete: Fine versus Coarse Aggregate. ACI Mater J 113:395–407

125. ASTM C469/C469M - 22 (2022) Test Method for Static Modulus of Elasticity and Poissons Ratio of Concrete in Compression. https://doi.org/10.1520/C0469_C0469M-22

126. Zahedi A, Trottier C, Sanchez LFM, Noël M (2021) Microscopic assessment of ASR-affected concrete under confinement conditions. Cem Concr Res. https://doi.org/10.1016/j.cemconres.2021.106456

127. Gautam BP, Panesar DK, Sheikh SA, Vecchio FJ (2017) Effect of multiaxial stresses on alkali-silica reaction damage of concrete. ACI Mater J 114:595–604

128. Zahedi A, De Souza DJ, Zubaida N, Sanchez LFM (2023) Overall assessment of CFRP-wrapped concrete affected by alkali-silica reaction. Cem Concr Res. https://doi.org/10.1016/j.cemconres.2023.107165

129. Zahedi A, Saliba L, Sanchez LFM, Boyd AJ (2023), Reliability of the damage rating index to assess the condition of concrete affected by external sulfate attack. Magazine of Concrete Research, Vol. 75 No. 3 pp. 135–148, doi: https://doi.org/10.1680/jmacr.22.00061

130. Sanchez LFM, Fournier B, Mitchell D, Bastien J (2020) Condition assessment of an ASR-affected overpass after nearly 50 years in service. Constr Build Mater 236:117554

131. Grattan-Bellew PE (1995) Laboratory Evaluation of Alkali-Silica Reaction in Concrete from Saunders Generating Station. Materials Journal 92:126–134

132. Grattan-Bellew PE, Danay A (1992) Comparison of laboratory and field evaluation of AAR in large dams. Proceedings of the International Conference on Concrete AAR in Hydroelectric Plants and Dams

133. Villeneuve V, Fournier B, Duchesne J (2012) Determination of the damage in concrete affected by ASR - the Damage Rating Index (DRI). In: 14th ICAAR International conference on the alkali aggregate reaction. p 033012

134. Sargolzahi M, Kodjo SA, Rivard P, Rhazi J (2010) Effectiveness of nondestructive testing for the evaluation of alkali – silica reaction in concrete. Constr Build Mater 24:1398–1403

135. British Cement Association (1992) the Diagnosis of Alkali Silica Reaction - Report of a working party. 2nd Ed. British Cement Association, Slough.

136. Zahedi A, Trottier C, Sanchez LF, Noël M (2022) Condition assessment of alkali-silica reaction affected concrete under various confinement conditions incorporating fine and coarse reactive aggregates. Cem Concr Res. https://doi.org/10.1016/j.cemconres.2021.106694

137. Barbosa RA, Hansen SG, Hansen KK, Hoang LC, Grelk B (2018) Influence of alkali-silica reaction and crack orientation on the uniaxial compressive strength of concrete cores from slab bridges. Constr Build Mater 176:440–451

138. Bérubé MA, Smaoui N, Fournier B, Bissonnette B, Durand B (2005) Evaluation of the expansion attained to date by concrete affected by alkali-silica reaction. Part III: Application to existing structures. Canadian Journal of Civil Engineering 32:463–479

Chapter 3: Research Methodology

The four main stages of the experimental research program are outlined in Figure 3-1. This research methodology section is intended to provide a comprehensive summary of all tests performed in this work. Theory related to these tests were previously discussed in chapter 2 (section 2.3) while chapters 4 – 7 will re-state the tests used in each paper, including any specific considerations. Prognosis, to determine the remaining capacity for ASR induced damage, is ongoing and results will only be briefly addressed in chapter 8.

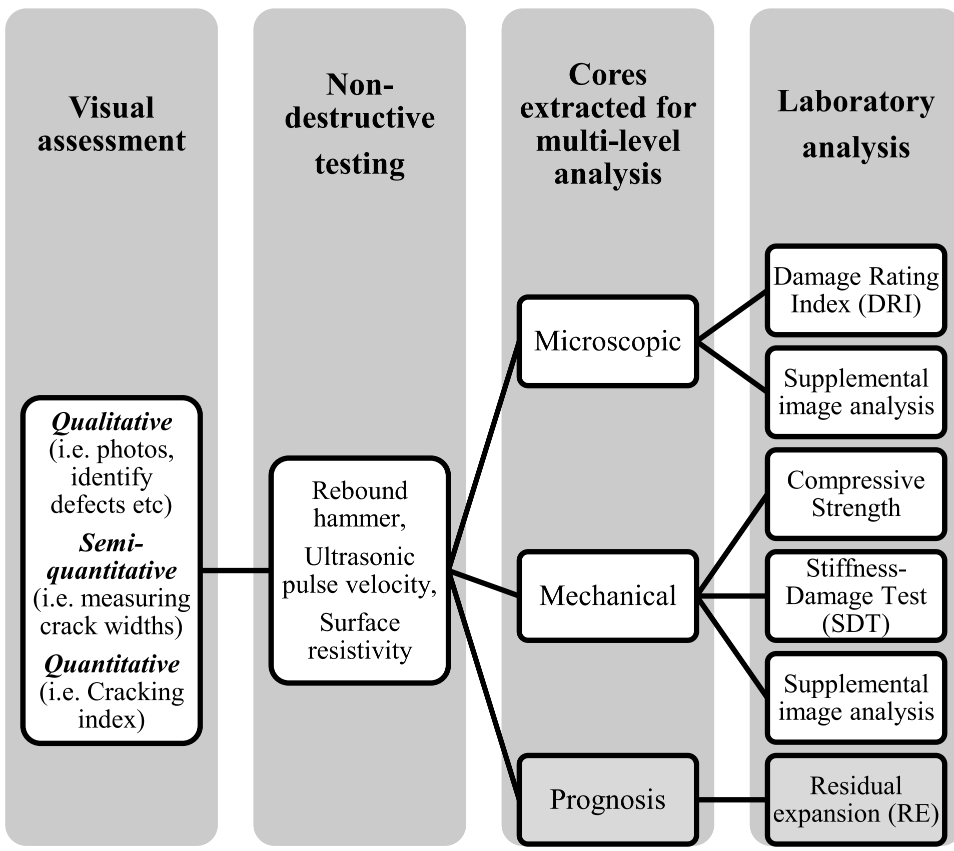

Figure 3-1 Flow chart depicting the steps for the condition assessment of damage in members

3.1 Bridge members under study

The members under investigation include five (5) segments of a pier cap and four (4) sections of a pier shaft (Figure 3-2).

Figure 3-2 Annotated images depicting the concrete members under study and their location in the Champlain Bridge

Member segments were accessed at an outdoor storage site in Montreal (e.g., Figure 3-3) with visual and non-destructive tests performed in this location followed by coring of the segments, with cores subsequently transported to the University of Ottawa laboratory.

Figure 3-3 Image depicting segments of the pier cap (left two segments) and pier shaft (right two segments) at the Montreal storage site

3.2 Visual assessment techniques (diagnosis)

Visual assessment was performed including qualitative, semi-quantitative (using a crack comparator card) and quantitative (cracking index) assessments (Figure 3-4).

Figure 3-4 Images depicting qualitative, semi-quantitative and quantitative visual inspection

Qualitative assessment included photographing concrete segments and identifying points of interest such as discolouration, efflorescence, cracking, rebar corrosion, evidence of previous repairs and objects such as wires and metal plates. Since the concrete members being studied had been cut into segments, it was also possible to identify the locations of reinforcement.

Semi-qualitative assessment was performed using a crack comparator card and magnifying glass to measure cracks at various locations (e.g. starting with the widest cracks). Composite images were subsequently created identifying crack width and locations to visualize the distribution of cracks.

Quantitative assessment was performed using the cracking index (CI). CI was performed at the most cracked location of a given exterior face. Due to limited time at the Montreal storage site, CI was performed on the faces starting with those that appeared the most damaged, and a reduced CI consisting on one line in the horizontal and vertical direction with two diagonal lines was initially performed. A threshold value of 0.5 mm/m for CI, or cracks in excess of 0.15 mm was chosen to indicate the need for further investigation following recommendations by [1, 2]. (Note: since the pier cap and shafts are not prestressed these are considered conservative thresholds for these members).

3.3 Non-destructive testing (NDT)

Non-destructive tests consisting of surface electrical resistivity (ER), rebound hammer (RBH) and ultrasonic pulse velocity (UPV) were conducted on the pier cap and pier shaft segments at the storage site in Montreal (Figure 3-5). These were performed over several visits with results from RBH measurements used in conjunction with CI to identify the least and most damaged segments.

Figure 3-5 Images depicting the rebound hammer (RBH), ultrasonic pulse velocity (UPV) and surface electrical resistivity non-destructive testing techniques

Non-destructive tests can be sensitive to differences in moisture and temperature. The weather and tests performed are summarized in (Table 3-1).

Table 3-1 Summary of environmental conditions [3] **and the corresponding visual and non-destructive tests performed on the PC and PS members**

Date	Weather	Tests performed
Nov. 2-5. 2021	Rain prior to testing period (Oct. 30 and 31st) Temperatures between -5°C and 8°C during testing period.	VI: photos, CW, CI NDT: ER (prelim), RBH
May 5. 2022	Light rain on May 4th, Temperature between 3°C and 17°C.	VI: photos, CI NDT: RBH
May 16-19. 2022	Thunderstorms overnight May 15-16, light rain May 17th and 19th (ER performed May 19th)	VI: Photos, CW

	Temperatures between 6°C and 26°C during testing period.	NDT: ER, RBH, UPV Coring: PS and PC
Oct. 3. 2022 *	No rain in week prior to testing. Temperatures between 6°C and 26°C within 24 hour period.	VI: photos, CI NDT: RBH, UPV
June 27 2023 *	Light to moderate rain on June 26, and June 27th Temperatures between 21°C and 26°C within 24 hour period.	VI: Photos, CW Coring: PS wet region

*Where: VI = visual inspection, CW = crack widths, CI = cracking index, NDT = non-destructive testing, ER = surface electrical resistivity, RBH = rebound hammer, UPV = ultrasonic pulse velocity, PS = pier shaft, PC = PC. * Testing focused on member not included in this thesis.*

Rebound Hammer (RBH) measurements were performed according to ASTM C805 [4] using a Proceq RBH. The 10 Schmidt hammer measurements were performed in groupings of two lines of 5 measurements with points spaced either 30 or 65 mm apart. The rebound hammer was held perpendicular to the concrete surface. All surfaces were smoothed to provide a flat surface for testing. In most cases tests were conducted on dry, bare concrete with a minimum of one set per face on each segment of the member. Corresponding compressive strengths (in MPa) were determined using the calibration curve corresponding to the rebound hammer orientation (i.e. parallel or perpendicular to horizontal) provided with the device.

Ultrasonic Pulse Velocity (UPV) was performed on all members using an Eagle Pundit UPV device following [5, 6]. The indirect method was primarily used due to the size of the members and significant presence of reinforcing bars. Direct UPV measurements were also conducted. Measurements were performed by moving the transmitter at 0.2 m increments from the receiver. The total distance differed depending on the locations being tested. A frequency of 36 kHz was used except where otherwise noted. Several frequencies were used, typically 54 or 24 kHz. The lower frequency was used when there was difficulty getting a UPV reading. The frequency used is noted with the measured values. UPV results less than 3.0 km/s are considered to represent poor concrete quality as per [7].

Surface electrical resistivity (ER) was be performed on all members using a 4-pronged Resipod concrete electrical resistivity device with measurements performed on wet concrete surfaces once a film of water could no longer be observed as per [8]. Measurements were performed at a minimum of 5 locations per exposed face. Following AASHTO-T-358 [9] and ACI 228.2R-13 [10], surface resistivity values <12 kΩ·cm would indicate high probability of chloride ion penetration (low durability concrete), while surface resistivity values >254 kΩ·cm indicate low probability of chloride ion penetration (high durability concrete).

3.4 Core extraction

Cores were extracted from the pier cap and pier shaft segments at the storage site by a coring company using a 100-mm diameter coring bit (Figure 3-6). Cores were labeled once extracted based on an internal numbering system (segment identifier – surface identifier – number of the core extracted from the surface). Cores were then photographed and then wrapped in plastic wrap. Coring of the pier cap and pier shaft segments was performed over a four-day period and cores had a variety of moisture conditions upon wrapping in plastic wrap due to the high variation of weather during this period. Cores were subsequently stored in a temperature-controlled chamber at 12°C, as per Sanchez et al. [11], when not being evaluated.

Figure 3-6 Image depicting core extraction from a pier cap segment at the Montreal storage site

Cores were extracted with a priority on surfaces which would be accessible in situ. Core lengths were varied but it was desired to obtain the equivalent of two 200 mm long samples for the stiffness damage test, two 200 mm long samples for the damage rating index, and two 200 mm long samples for residual expansion. Three extra cores were taken from the segment which was determined to have the least damage as estimated from RBH and CI results at the time of coring. These three cores were intended to test for compressive strength, which is used to estimate the loading that should be used for the stiffness damage test.

Cores were extracted from three distinct orientations from the PC and PS segments representing transverse, longitudinal and vertical orientations in the members with the orientation of cores in the respective members demonstrated in Figure 3-7 and Figure 3-8.

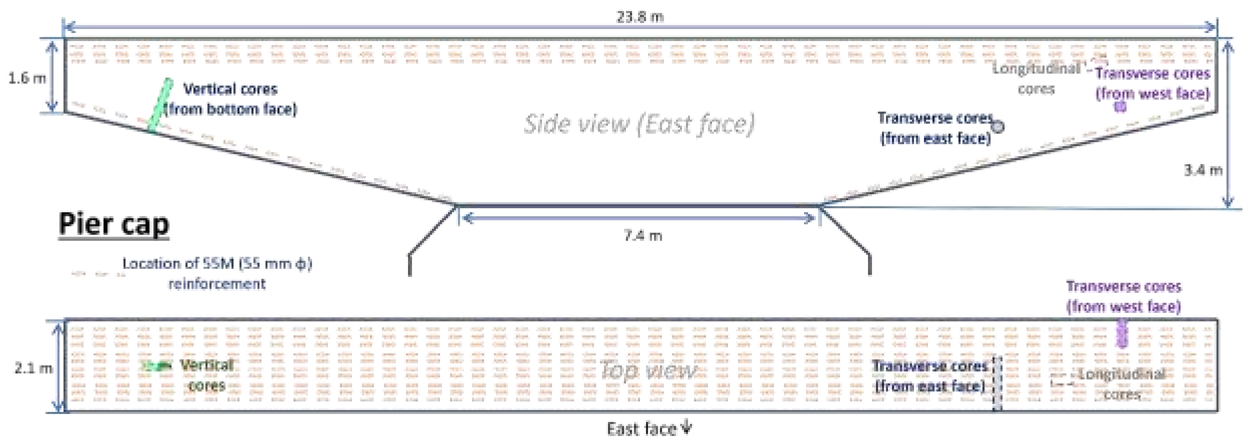

Figure 3-7 Schematic depicting major reinforcement and examples of transverse, longitudinal and vertical core orientations in the PC

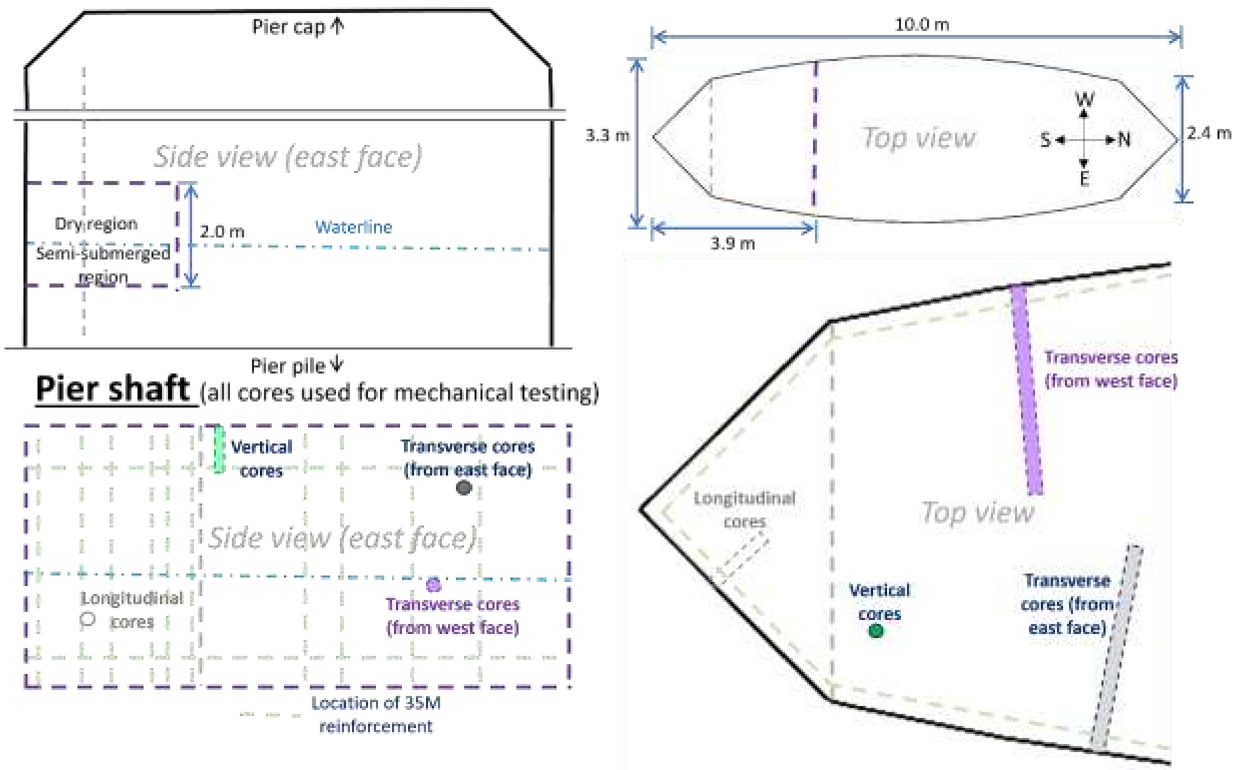

Figure 3-8 Schematic depicting major reinforcement and examples of transverse, longitudinal and vertical core orientations in the PS

Where possible, non-destructive tests such as supplemental image analysis on core exteriors and the resonant frequency test were conducted on cores to obtain additional information to allow further correlation to in-situ testing.

3.5 Analysis of cores

Tests performed on core specimen included resonant frequency (RF), the damage rating index (DRI), the stiffness damage test (SDT) and compressive strength (Figure 3-9). Supplemental image analysis was also conducted for both microscopic and mechanical testing. Cores extracted from the first 200 mm (i.e. from the repair concrete for the pier cap and from the surface for the pier shaft) were designated as ‘surface’ cores.

Figure 3-9 Images depicting the damage rating index (DRI), resonant frequency (RF), stiffness damage test (SDT) and compressive strength tests used in analysis of core specimens

3.5.1 Microscopic analysis – Damage Rating Index (DRI)

Cores for DRI were selected to represent a range of locations of interest (e.g. different core orientations, depths) with specimen lengths varying. Specimens were prepared by cutting longitudinally using a wet saw with one half selected for DRI. To prepare the sample, the cut surface was polished using a 30-grit pad on a table polisher to get a flat surface followed by further polishing using a hand polisher with 50, 100, 200, 400, 800, 1500 and 3000 grit polishing pads. By convention, a minimum surface of 200 cm^2 is recommended [12, 13] to accurately capture the damage in a region of interest for concrete affected by ASR. The area of each sample was recorded to ensure that a sufficient area was evaluated for each area of interest (e.g. different core orientations, specific locations within each member etc).

The DRI was performed using a grid of 1 cm x 1 cm squares as shown in Figure 3-10 with the number of crack types, as defined in Table 2-6 of this document, in a given square recorded in an Excel spreadsheet. The number of each crack type is then counted and multiplied by the appropriate factor as per [14] with the final DRI number normalized to 100 cm^2.

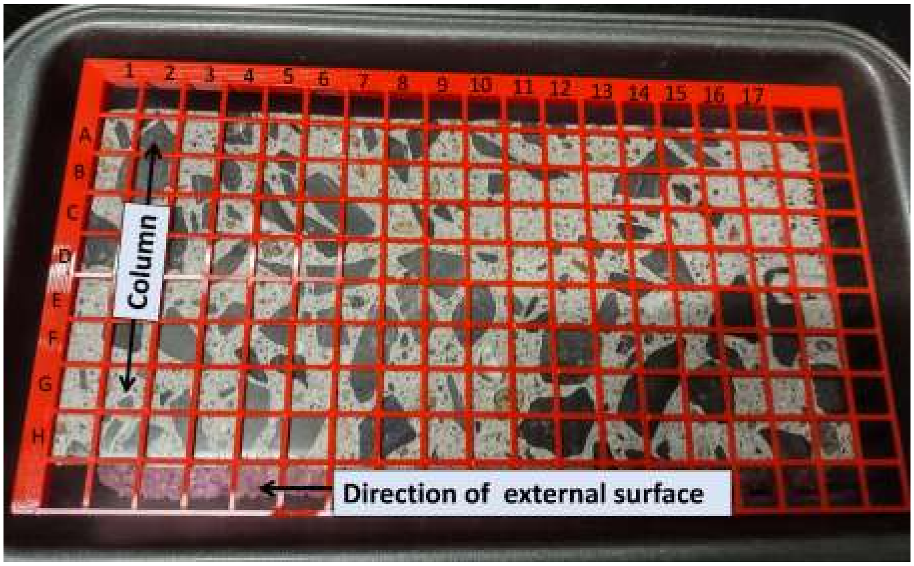

Figure 3-10 Annotated image depicting a grid used for performing the DRI

3.5.1.1 Supplemental Image Analysis of DRI Samples

Crack widths were measured under the stereomicroscope using a cracking index card. The entire surface of a given sample was assessed with locations equal to or greater than 0.10 mm recorded. The locations of cracks greater or equal to 0.10 mm were then traced onto scans of the specimen to identify orientation trends.

3.5.2 Mechanical testing - Resonant Frequency (RF)

Resonant frequency tests were conducted on concrete cores prior to further testing (e.g. compressive testing, the stiffness damage test and residual expansion). Testing was conducted in the transverse and longitudinal directions following ASTM C215-19 to determine the dynamic modulus of elasticity, Dynamic ME.

Eight transverse measurements were conducted in the transverse mode to capture variations in cracking within cores. This was achieved by drawing four equally spaced lines longitudinally on the core, and changing the position of the sensor such that measurements were recorded with the sensor located at either the top or bottom of the specimen as shown in Figure 3-11. Two longitudinal measurements were performed, with the sensor placed at either the top or bottom of the specimen.

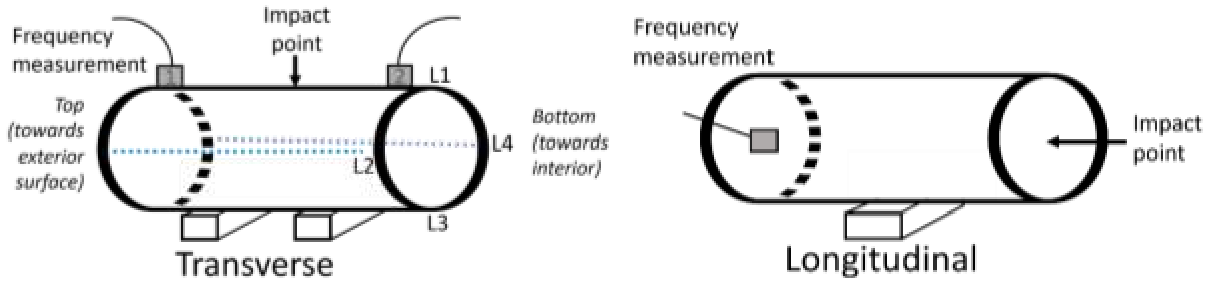

Figure 3-11 Schematic depicting the method for transverse and longitudinal RF measurements

3.5.3 Mechanical testing - Stiffness Damage Test (SDT)

Cores for SDT were selected from locations of interest (e.g. different core orientations, depths) and cut to dimensions of 200 mm ± 30 mm by 94 mm ϕ ± 2 mm. Samples were conditioned for 48 hours in a 100% humidity environment at room temperature prior to testing to reduce variability as per [15].

SDT loads samples to 40% of the compressive strength, with the target 40% load determined from the least damaged area of the member or a comparable member. Results of RF testing indicated a reduced Dynamic ME in pier shaft specimens compared to pier cap, with pier shaft specimens tested at a 40% load of 9.8 MPa while pier cap specimens were tested at a 40% load of 12.8 MPa. Eleven pier cap specimens were chosen for a study comparing the two target loads: cores were tested by performing SDT to the lower target load, allowed to recover for a minimum of 1 week, and the SDT test was repeated using the higher target load. Statistical analysis using a T-test, found no significance between the results at the two loads for SDI, PDI and ME. The NLI value was found to be statistically different; however, this is thought to be due to crack closure during the initial test indicating a high importance of getting NLI from the first SDT performed on the sample.

3.5.3.1 Supplemental Image Analysis of Cores

Analysis of cracking on the surface of the core segments was conducted as shown in Figure 3-12. First, 200 mm long cores were scanned along the longitudinal direction by rolling the core along the surface of the flatbed scanner using a resolution of 11.8 pixels/mm. Cores were scanned twice. Cracks were traced using fine tipped permanent markers prior to the second scan. Using the GIMP software, cracks were outlined such that closed cracks in the aggregates were coloured blue, while open cracks in the aggregates and cement paste were coloured in red and green, respectively.

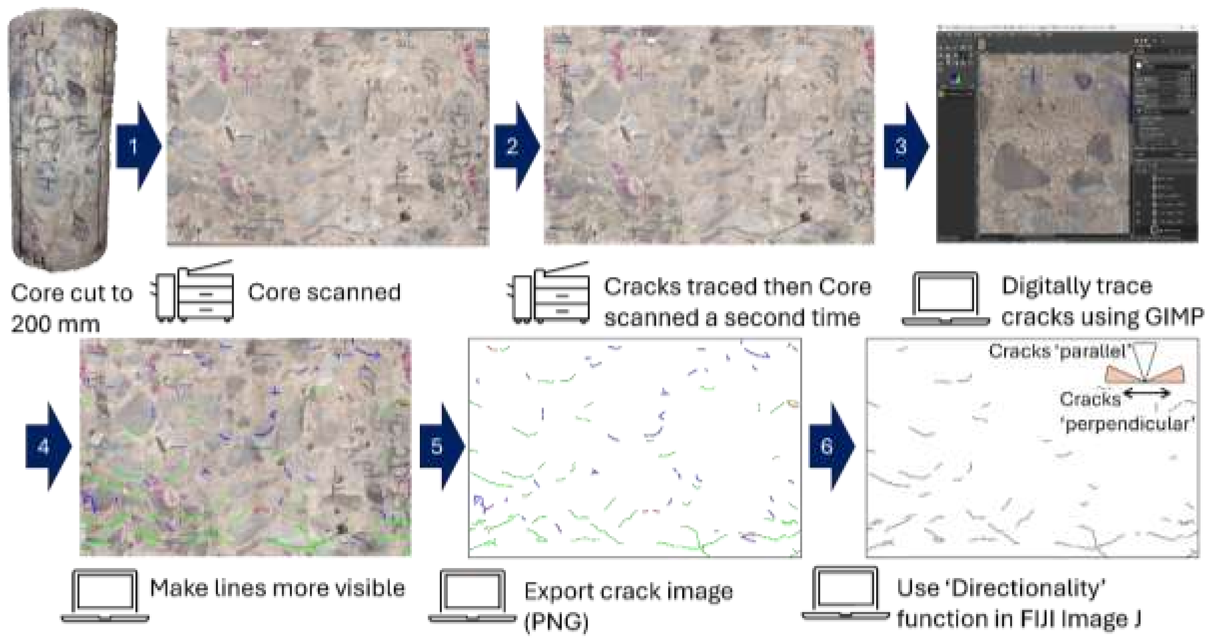

Figure 3-12 Schematic depicting the scanning and analysis process for obtaining crack orientation estimates for core specimens

Traced cracks were subsequently analyzed using the FIJI ImageJ software to evaluate the number of cracks, crack lengths and crack directions for cracks in aggregate particles and cement paste. The number of cracks and crack lengths were obtained using the 'Analyze Particles' function while crack orientation was then determined using the 'Directionality' tool in the FIJI ImageJ software. Directionality identifies the direction of each crack segment and presents the resultant data as the percentage of segments falling into each 2° range out of 180°. This was applied to traced cracks, with cracks in the cement paste and cracks in the aggregate processed separately. The percentage of total cracks oriented in a 38° range (i.e. 18° out of a 90° range) either parallel or perpendicular to the length of the specimen were used to estimate whether cracking was primarily parallel (i.e. lengthwise) or perpendicular (i.e. widthwise) within the cores. The area occupied by traced cracks (i.e. a constant width) was determined using the 'threshold' function which finds the percentage of pixels in an image above or below a specified colour value.

3.5.4 Mechanical testing - compressive

Specimens with dimensions 200 mm x 100 mm ϕ core from the least damaged area of each member were tested in compression as per ASTM C42/C42M-20 [15]. Samples were conditioned in the same manner as for compressive testing as per [16]. For the majority of specimens, compressive tests were performed after completion of SDT.

3.6 Cores – Residual Expansion (RE)

Residual expansion is performed to estimate the potential for future reactivity of concrete cores (i.e. prognosis). Residual expansion at 38°C is ongoing on 16 PC specimens and 12 PS specimens with dimensions 200 mm x 100 mm ϕ. Specimen were split equally between two testing conditions, either submerged in 1 molar NaOH or at 100% relative humidity with specimen further subdivided such that half of the specimen had been tested using the stiffness-damage test. Prior to measurements specimens were removed from the 38 °C chamber and allowing to cool to room temperature for approximately 18 hours. Length measurements were performed using a vertical micrometer device. RE tests on PC specimens were started August 29 2023, while tests on PC specimen were started on Feb 7 2024. Tests of specimens from both members are ongoing.

3.7 References

1. Fournier B, Bérubé M-A, Folliard KJ, Thomas M (2010) Report on the Diagnosis, Prognosis, and mitigaton of Alkali-Silica Reaction (ASR) in Transportation Structures.

2. Institution of Structural Engineers (ISE) (1992) Structural Effects of Alkali-Silica Reaction – Technical Guidance Appraisal of Existing Structures. Institution of Structural Engineers 45

3. WeatherSpark Weather History at Montréal/Saint-Hubert Airport. https://weatherspark.com/h/m/147211/2022/5/Historical-Weather-in-May-2022-at-Montréal-Saint-Hubert-Airport-Canada.

4. ASTM C 805/C805M-20 (2020) Standard Test Method for Rebound Number of Hardened Concrete. 1–4

5. ASTM C597 (2016) Standard Test Method for Pulse Velocity Through Concrete. 4–7

6. Pundit Labs Operating Instructions Pundit.

7. IS 13311-1 (Part 1) (1992) Method of Non-destructive testing of concrete, Part 1: Ultrasonic pulse velocity [CED 2: Cement and Concrete]. Bureau of Indian Standards 1–7

8. Polder R, Andrade C, Elsener B, Vennesland O, Gulikers J, Weidert R, Raupach M (2000) RILEM TC 154-EMC: electrochemical techniques for measuring metallic corrosion: Test methods for on site measurement of resistivity of concrete. Materials and structures/ Matériaux et Constructions 33:603–611

9. AASHTO T 358-15 (2015) Standard Method of Test for Surface Resistivity Indication of Concrete's Ability to Resist Chloride Ion Penetration.

10. ACI 228 (2013) Report on Nondestructive Test Methods for Evaluation of Concrete in Structures. American Concrete Institute. https://doi.org/10.14359/51686889

11. Sanchez LFM, Fournier B, Jolin M, Bastien J (2014) Evaluation of the stiffness damage test (SDT) as a tool for assessing damage in concrete due to ASR: Test loading and output responses for concretes incorporating fine or coarse reactive aggregates. Cem Concr Res 56:213–229

12. RILEM technical committee 259-ISR (2021) Diagnosis & Prognosis of AAR Affected Structures. Springer Nature Switzerland AG

13. Grattan-Bellew PE, Danay A (1992) Comparison of laboratory and field evaluation of AAR in large dams. Proceedings of the International Conference on Concrete AAR in Hydroelectric Plants and Dams

14. Villeneuve V, Fournier B, Duchesne J (2012) Determination of the damage in concrete affected by ASR - the Damage Rating Index (DRI). In: 14th ICAAR International conference on the alkali aggregate reaction. p 033012

15. ASTM C42/C42M-20 Standard Test Method for Obtaining and Testing Drilled Cores and Sawed Beams of Concrete. https://doi.org/10.1520/C0042_C0042M-20

16. Sanchez LFM, Fournier B, Jolin M, Bastien J (2015) Evaluation of the Stiffness Damage Test (SDT) as a tool for assessing damage in concrete due to alkali-silica reaction (ASR): Input parameters and variability of the test responses. Constr Build Mater 77:20–32

Chapter 4: Paper 1

Visual and Non-destructive Testing of ASR Affected Piers from Montreal's Champlain Bridge[1]

Abstract

Montreal's Champlain Bridge was constructed starting in 1957 using an alkali-silica reactive aggregate for some concrete members. The bridge was decommissioned in 2019 due to significant deterioration of concrete members which were requiring costly and consistent rehabilitation measures. Alkali-silica reaction (ASR) is one of several damage mechanisms which commonly affect infrastructure in Canada. Frequent freeze-thaw cycles, and heavy use of de-icing salts in winter as well as high heat and humidity in summer are expected to have intensified ASR induced damage. During the decommissioning process several concrete members were selected for further assessment. Among them are five segments of a pier cap, which had undergone encapsulation repair, and four segments of a pier shaft, which represented both dry and semi-submerged conditions. Preliminary evaluation through visual inspection (conventional, qualitative and quantitative using the cracking index-CI) and non-destructive techniques (Rebound hammer - RBH, ultrasonic pulse velocity - UPV and surface resistivity) was conducted on both internal (i.e. cut during decommissioning) and external (i.e. exposed while in service) surfaces at a storage site. Differences in geometry, exposure conditions and repair history from the two members were found to have limited impact on the results of quantitative tests (i.e. CI, RBH and UPV results) while still exhibiting qualitative differences in visual determination (i.e. crack patterns, surface appearance and crack widths).

---

[1] This chapter has been published in *Buildings* (Kristufek, L., Sanchez, L.F.M., Martín-Pérez, B., and Noël, M.. (2025). "Visual and Non-Destructive Testing of ASR Affected Piers from Montreal's Champlain Bridge." Buildings, 15 (18), 3262. https://doi.org/10.3390/buildings15183262

4.1 Introduction

The Champlain Bridge (CB) was a Canadian highway bridge which experienced significant deterioration in concrete members, ultimately leading to its decommissioning in 2019 after 57 years in service. The bridge, which crossed the St. Lawrence River, experienced a harsh service environment with cold, snowy winters and hot humid summers. Concrete members exhibited signs of deterioration early in the service life with the cause of damage thought to be a combination of damage mechanisms including reinforcement corrosion, freeze-thaw cycles and alkali-silica reaction (ASR), which were identified during inspections as early as the 1980's and 1990's [1]. The presence of ASR in members of the bridge was confirmed through the extraction of cores from several piers during the mid-1990's [2]; however, its long-term impact on concrete performance and potential structural implications were poorly understood. Deterioration of reinforced concrete members necessitated an increasing number of repair and rehabilitation measures both across the whole bridge (e.g. improved drainage system to remove chloride-rich water from the driving surface [1]) and localized to individual deteriorated members (e.g. removal of concrete with high concentrations of chloride from runoff water, implementing external post-tensioning). While repairs undoubtably helped to extend the service life of the structure, repair strategies differed depending on the damage mechanisms present in the members, with ASR often overlooked in condition assessment of in-service structures due to its reduced visibility at the surface of the structure.

Visual and non-destructive testing are the first step in routine inspection for the monitoring of in-service structures. Results from these tests are used to determine if further testing, such as extraction of cores, is needed to determine the cause and extent of damage (i.e. diagnosis), along with the potential for further deterioration (i.e. prognosis); these are critical for the selection of efficient maintenance and repair strategies. However, detection of internal swelling reactions such as ASR presents a significant challenge since cracking in field structures is complex with cracks caused by expansion often be overshadowed by visible damage on the surface, such as discolouration, rust and scaling. Damage caused by freeze-thaw and corrosion can additionally cause surface deterioration resulting in misleading results from non-destructive techniques such as rebound hammers and ultrasonic pulse velocity which rely on transmissions through the damaged layer. Results from investigations of in-service structures are limited in the literature due to confidentiality and safety concerns. Investigation of members from this iconic decommissioned structure provides valuable insights into the presentation of visual and non-destructive damage in reinforced concrete bridges experiencing ASR coupled with other damage mechanisms.

4.2 Background

The Champlain Bridge was constructed using a novel pre-stressed design where the bridge surface consisted of an interconnected system of girders, diaphragms and deck slabs and consisted of six traffic lanes. T-type piers with a 'hammerhead' pier cap design supported seven girders per span with expansion joints positioned directly above the pier cap. Piers in the Champlain Bridge were constructed using local aggregates which have since been found to result in the ASR. Severe damage to reinforced concrete members of the CB led to the decision to decommission the structure at which time a variety of members were set aside for research. Of these, a pier cap, part of pier 42W located in the on-land portion of the Montreal approach, and pier shaft, part of pier 38W located in the river, (Figure 4-1) were of interest due to the high likelihood of ASR [2]. Although ASR has been the subject of considerable research worldwide, there continues to be limited literature available about the long-term impact of this mechanism in reinforced concrete structures [3]. Several factors contribute to this gap in knowledge including confidentiality requirements for many in-service structures as well as the relatively long time span required for ASR to develop in the field in most cases. Moreover, although individual deterioration mechanisms (e.g. reinforcement corrosion, freeze-thaw, ASR) have been researched extensively in isolation they are likely to occur simultaneously in real structures. Multiple mechanisms working together may significantly increase the rate of deterioration compared to a single mechanism [4–7] and their combined effects are important to understand when conducting condition assessments.

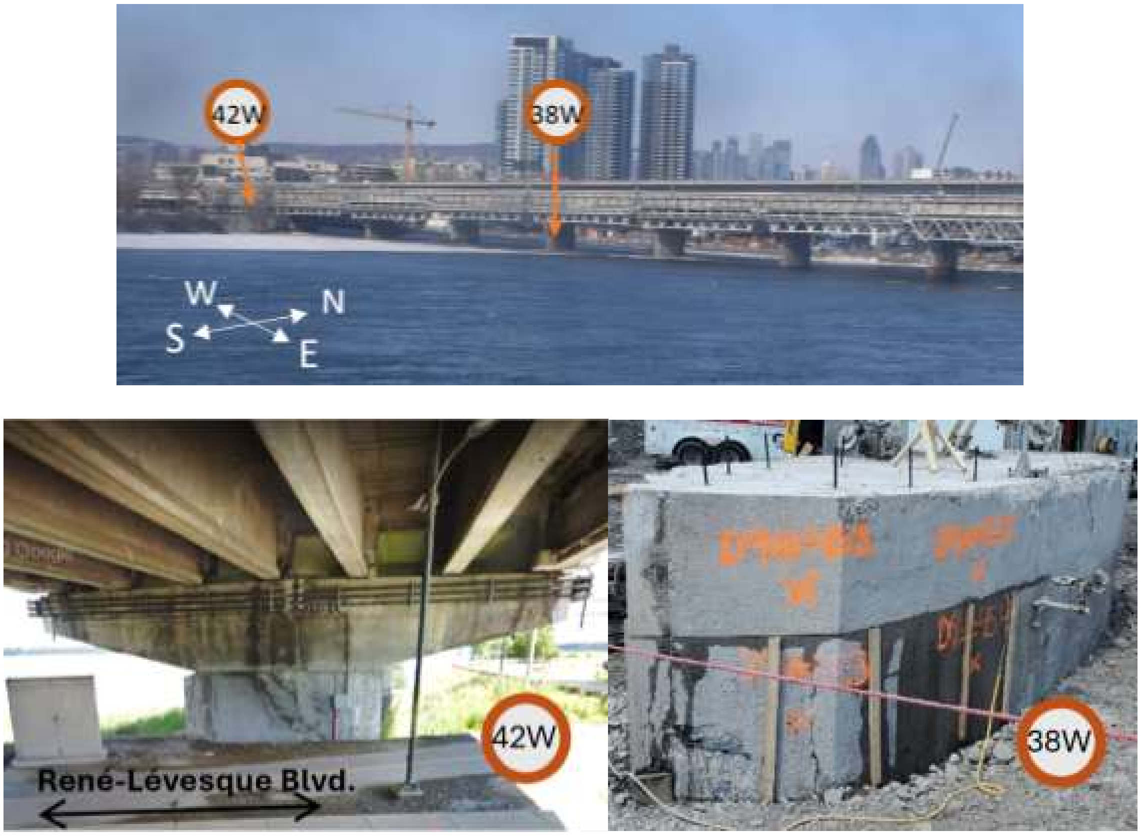

Figure 4-1 Annotated images identifying the location of the pier cap (42W) and pier shaft (38W). (Image sources: top and bottom right images courtesy of JCCBI, bottom left image: Map data ©2022 Google)

Internal swelling reactions, such as ASR, can be challenging to identify in structures. ASR impacts many concrete structures in Canada including numerous structures in Quebec and Ontario [8, 9]. ASR is a chemical reaction between the alkali hydroxides from the concrete pore solution and aggregates containing unstable mineral phases. This reaction produces a secondary product (the so-called ASR gel) which absorbs water resulting in expansion and cracking of the affected concrete [8, 10]. ASR results in significant reductions in mechanical properties, especially the modulus of elasticity [11], and thus is a significant threat to the long-term performance of affected concrete members.

During visual assessments of ASR-affected structures, a characteristic ‘map cracking’ pattern is frequently identified in ‘plain’ (i.e. minimally reinforced) concrete. However, when members are reinforced (e.g. heavily reinforced structural concrete members) crack patterns from ASR often occur parallel to the main reinforcement [12–16] making it difficult to distinguish it from other deterioration mechanisms such as corrosion of steel reinforcement [3]. Reduced alkalinity in surface concrete due to weathering may further reduce the presence of reaction products (e.g. the ASR gel) further complicating detection of ASR during visual inspections.

In older structures, repairs are also common. This is the case for the pier cap investigated in this work which underwent an encapsulation repair in 2004 after 42 years in service. During this repair, concrete was removed up to the outermost layer of reinforcing bars and replaced by a less permeable repair concrete [17, 18] followed by the addition of three Dywidag bars to provide additional longitudinal post-tensioning [19] in 2008 (Figure 4-2).

Figure 4-2 Images depicting the pier cap following removal of the surface concrete in 2004 (left) and in 2018 after addition of external longitudinal reinforcement and the modular truss system in 2018 (right). (reproduced from JCCBI (left), Map data ©2022 Google (right))

Tracking damage development in members of a structure is an important aspect of visual inspections. Qualitative (i.e. identifying crack patterns) and quantitative (i.e. the cracking index [20, 21]) methods are used to enhance visual inspections facilitating comparisons between different members or between the same locations over time. When visual inspections indicate increasing damage in members non-destructive tests (NDT) are often used to determine next steps. Commonly used NDTs include the rebound hammer (to estimate compressive strength), ultrasonic pulse velocity (to estimate interior concrete quality including delamination within concrete), and surface electrical resistivity (to evaluate the likelihood of chloride ingress).

It is widely known that visual and non-destructive tests have important limitations. Temperature and moisture conditions can impact results with similar climatic conditions recommended when the same test is repeated over numerous years [21].Surface resistivity and UPV are especially sensitive to moisture conditions in concrete. NDT are further limited by the condition of the surface concrete since damage such as delamination may block the ability of tests to reach the interior concrete. UPV additionally can underestimate damage when reinforcing bars are parallel to the measurement direction due to faster transmission through steel [22] presenting a challenge for use in highly reinforced concrete members. Otherwise, the non-destructive nature, relatively low costs and ease of use of these methods means that NDTs will continue to be used on in-service structures.

4.3 Scope of Work

This paper presents the results of qualitative and quantitative visual assessments and non-destructive testing performed on ASR-affected members (i.e. pier cap (PC) and pier shaft (PS)) from the Champlain Bridge. Testing was conducted to evaluate how differences within the members (i.e. orientation of surfaces, wet vs. dry) and between the members (i.e. different geometry, previous repairs) impacted visual and NDT outcomes. The research findings are expected to improve understanding of the relationship between concrete damage due to ASR is detected in visual and non-destructive test results for these reinforced concrete members. Extended analysis of qualitative and quantitative visual testing (i.e. observed crack orientations and measured crack widths) with further provide a link to future work evaluating concrete cores from these members using a multi-level testing protocol.

4.4 Materials and Methods

The PC (extracted from pier 42W) and PS (extracted from pier 38W) members were removed from the CB as part of the deconstruction process with sections of the two members accessed in 2021-2023. Visual and non-destructive tests were performed on the primary exposed faces of the PC and PS as well as internal surfaces exposed during deconstruction (Figure 4-3) with the east, west and bottom facing surfaces investigated for all five PC segments (i.e., two from the north end and three from the south end) and all east and west faces investigated from the PS segments (i.e., all from the south end). Visual inspection techniques included conventional, and quantitative (i.e. using the cracking index) methods while non-destructive techniques utilized included Schmidt hammer, ultrasonic pulse velocity and surface resistivity. Preliminary results of investigation of the PC were previously reported in [23] which was presented at the 6th International Conference on Concrete Repair, Rehabilitation and Retrofitting while preliminary results of investigation of the PS were previously reported in [24] which was presented at the Canadian Society of Civil Engineers conference in 2023.

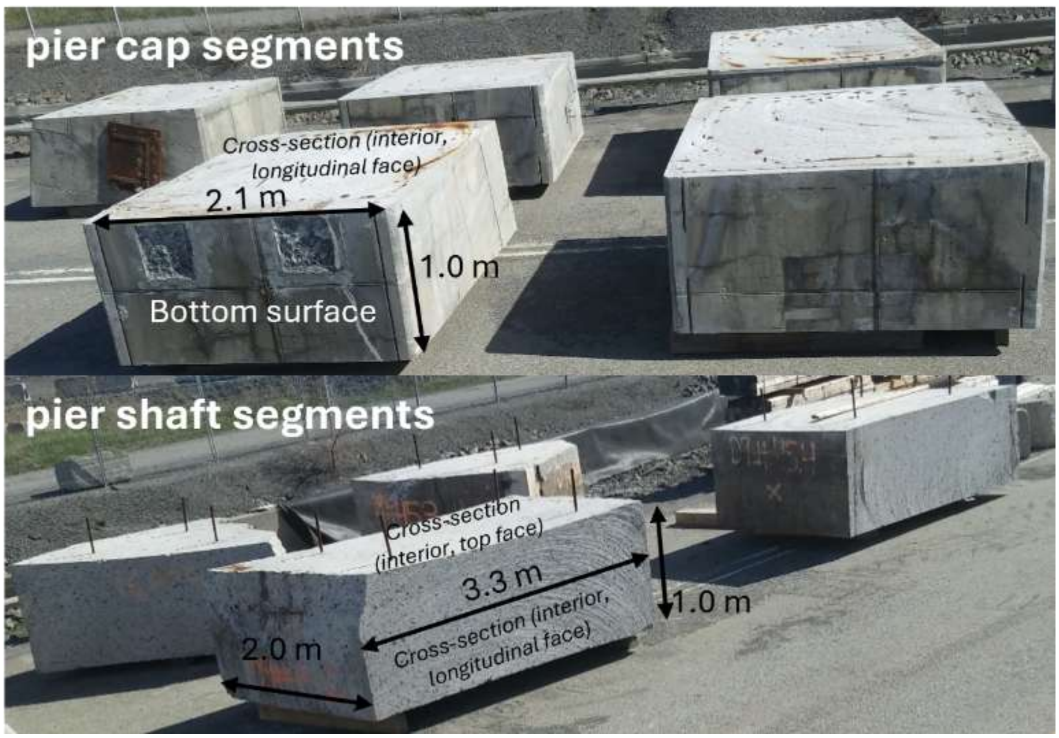

Figure 4-3 Annotated image depicting the pier cap and pier shaft segments investigated

4.4.1 Visual Inspection

Detailed visual inspection was performed on all segments with a focus on surfaces that were exposed to weathering when the members were in service. This included qualitative (e.g. noting discolouration, metal fixtures attached to surfaces etc.), semi-qualitative (i.e., measuring crack widths) and quantitative (i.e., cracking index - CI) assessments of observable damage. Surface crack data collected in situ (i.e. location and width of cracks) were manually traced onto photos using the software GIMP to identify the cracking pattern. The widths of visible cracks were measured, with a priority placed on recording the widest crack widths along with signs of increased moisture which could indicate a predisposition to ASR [21, 25].

The CI, a quantitative visual inspection technique, was performed in the area identified by visual inspection to be the most cracked in each of the west, east and bottom surfaces of each PC segment and the east and west surfaces of each PS segment. A minimum of one vertical and horizontal line with length 0.5 m in an 'L' shape as well as two diagonal lines in the shape of an 'X' were drawn on the surfaces with additional horizontal and vertical lines evaluated in some locations (see Figure 4-3). The width of cracks intersecting the lines were recorded with the CI value in mm/m determined as shown in Equation 4-1. In reinforced concrete a CI value greater than 0.5 mm/m [21] indicates the need for further assessment while crack widths in excess of 0.15 mm also trigger additional investigation particularly for pre-stressed concrete [26]. All cracking indices were performed using a crack comparator card to measure crack widths.

$$CI\ [\frac{mm}{m}] = \frac{\sum Crack\ openings}{Base\ length} \tag{4-1}$$

4.4.2 Non-Destructive Testing

Three non-destructive test techniques were used to investigate concrete quality (i.e. rebound hammer, ultrasonic pulse velocity, and surface electrical resistivity) with measurements performed at several locations on each surface of interest to evaluate variation across different areas of the members. The locations of rebound hammer and ultrasonic pulse velocity measurements shown in Figure 4-4 and Figure 4-5 while surface resistivity was conducted on an average of seven evenly spaced locations per surface and has not been shown in the figure. Surfaces which would have been accessible in situ were prioritized with NDTs also performed on cross-sectional areas exposed when segments were removed from the structure.

Rebound hammer measurements were conducted following the procedure in ASTM C 805 [16]. Tests were performed with the device held perpendicular to the test surface (i.e. device held parallel to the ground). Rebound values were converted to the compressive strength for a standard concrete cylinder using the calibration chart included with the testing device.

Ultrasonic Pulse Velocity (UPV) was conducted as described in ASTM C 597-16 [22]. Tests were performed using 0.2 m spacing increments between the transmitter and receiver; contact to the surface was achieved using petroleum jelly. The indirect method was used due to the large size of the segments and the presence of reinforcing bars which can impact the results. In this work UPV speeds of 3.0 km/s or slower are considered to indicate the need for further investigation following [27] (i.e. need for destructive testing, coring etc.).

Surface resistivity was conducted using a four-pronged concrete electrical resistivity device with surfaces wetted 10-20 minutes before testing to achieve approximate SSD condition at the time of testing and avoid water films on the surface as per [28]. Readings were performed on all members on the same day following a week of periodic rain. Following AASHTO-T-358 [20] and ACI 228.2R-13 [14], surface resistivity values <12 kΩ·cm are taken to indicate high probability of chloride ion penetration (low durability concrete) while surface resistivity values >254 kΩ·cm indicate low probability of chloride ion penetration (high durability concrete).

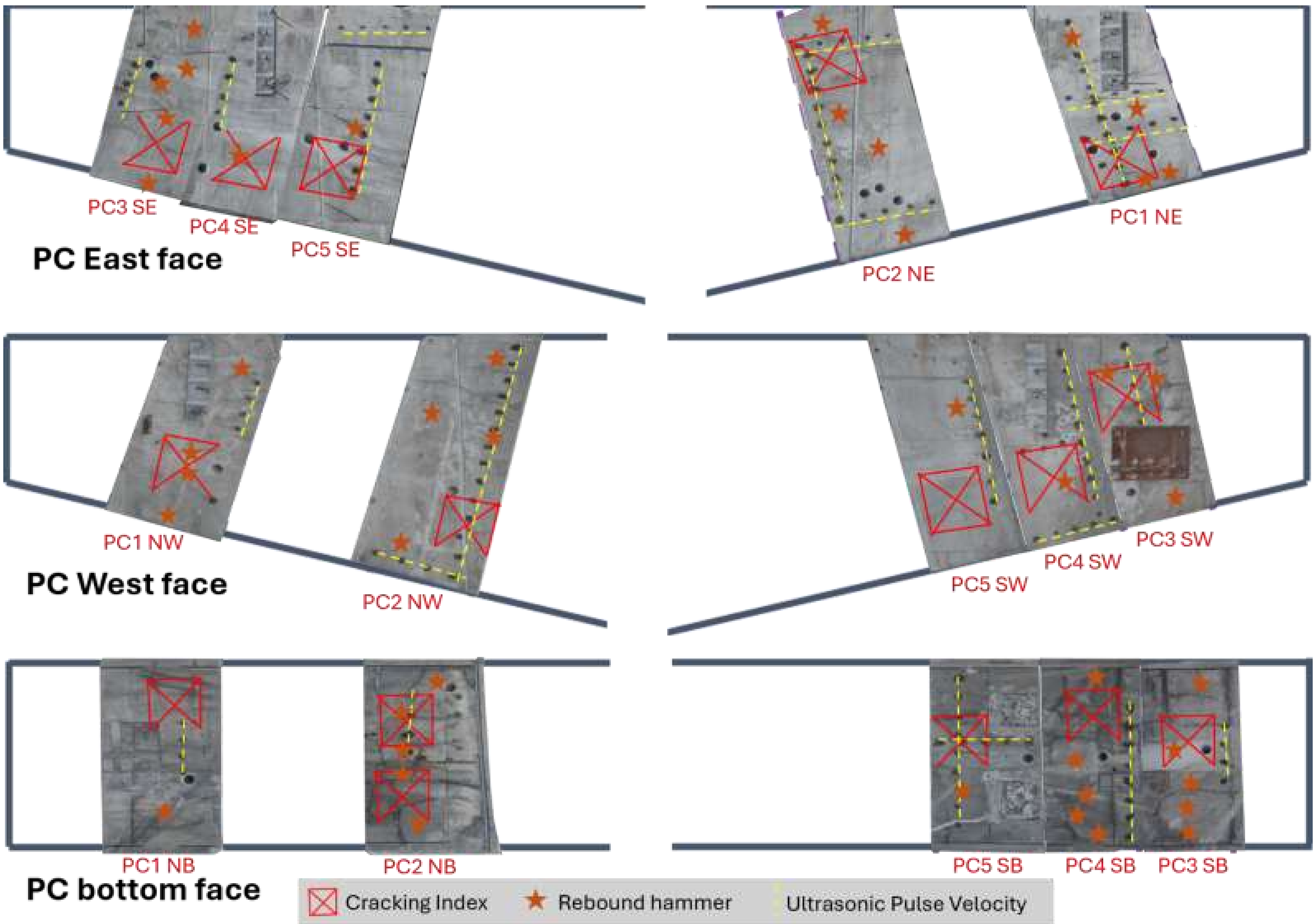

Figure 4-4 Annotated image depicting visual and NDT test locations on the PC

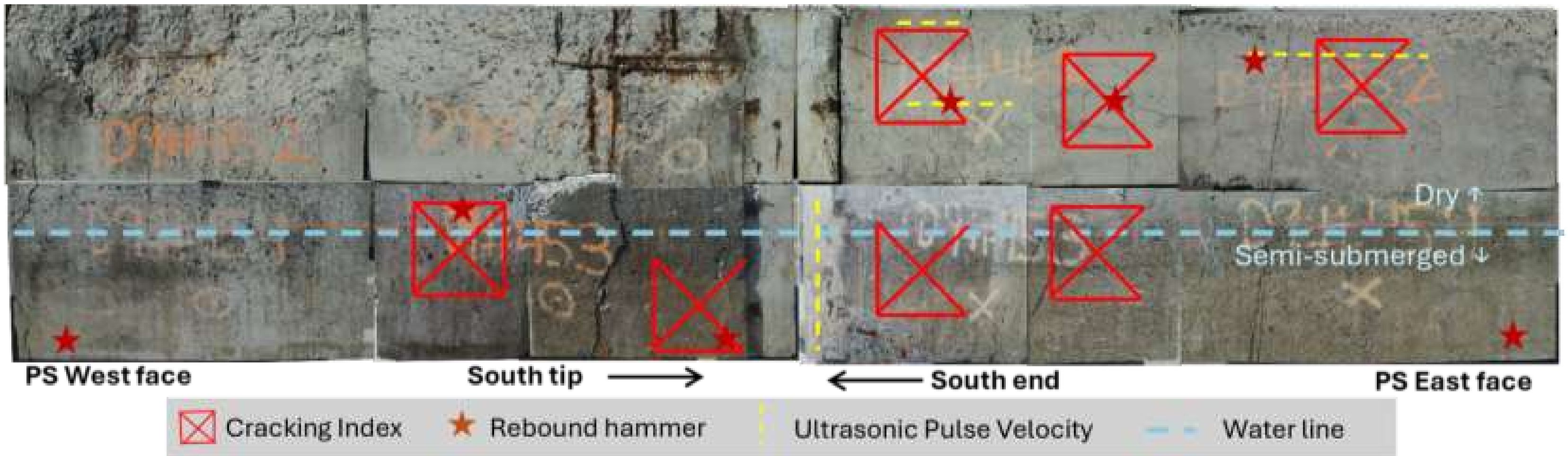

Figure 4-5 Annotated image depicting visual and NDT test locations on the PS

4.5 Results

4.5.1 Visual Inspection (Qualitative)

The initial conventional visual inspection identified clear differences between surface concrete quality in the PC and PS members reflecting the different repair histories (i.e. the 2004 encapsulation repair on the PC) and the localized service environments of the two members (i.e. the submerged and semi-submerged environment of the PS). The bottom surface of the PC member was noted to have a darker appearance compared to east and west surfaces (Figure 4-6). In the PS segment, exposed aggregates were noted to have flaking, or be recessed within the cement paste indicating deterioration of the aggregate in the service environment.

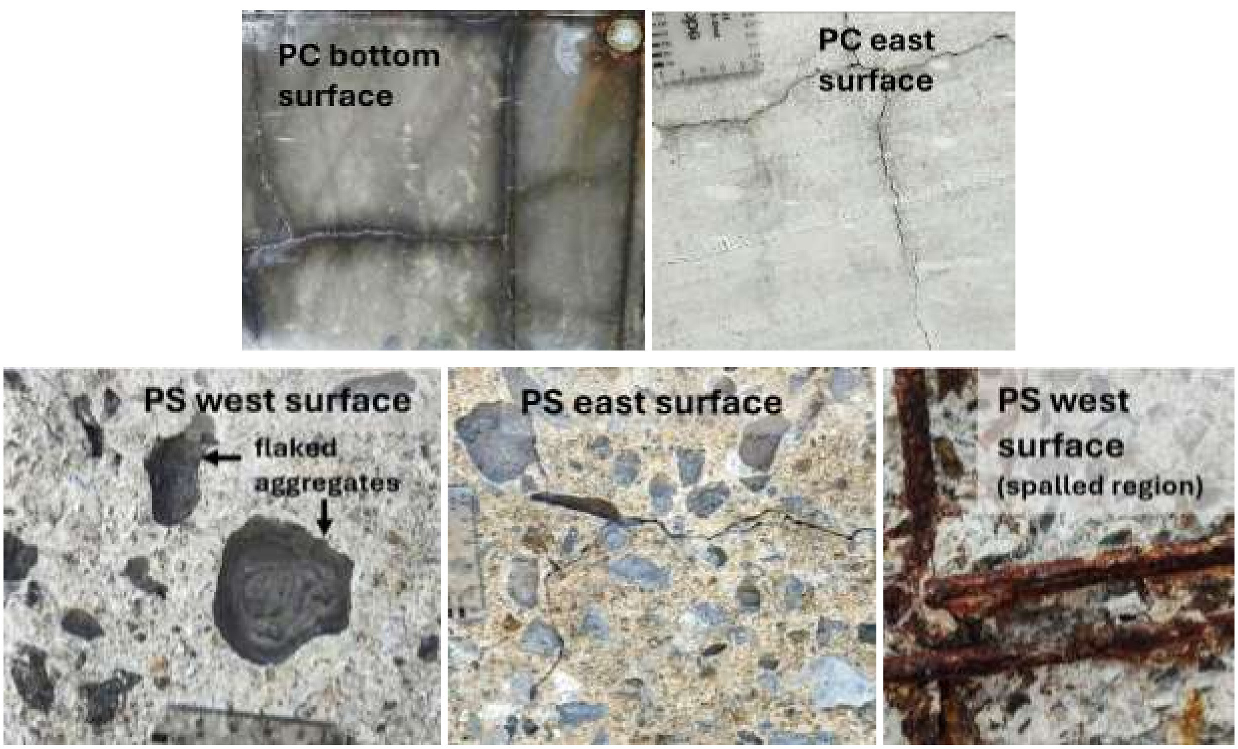

Figure 4-6 Annotated images depicting surface damage on the PC (top row) and PS (bottom row)

Cross-sectional surfaces exposed during decommissioning of the structure allowed observation of internal cracking, repair concrete and rebar spacing which could not be observed while the PC and PS were in service. This revealed that the PC repair concrete displayed cover depths varying between 130 - 230 mm while the PS displayed cover depths of approximately 100 mm. The reinforcement configuration was also visible (Figure 4-7) with the largest diameter rebar (60-mm ϕ) located at the top of the PC members with significantly lower reinforcement density in the middle of the member. In the PS cross-sectional surfaces a lower reinforcement ratio was observed (Figure 4-7). Planes of delamination could additionally be identified parallel to the external surfaces aligned with the locations of reinforcement (Figure 4-8). Cracking and visible reaction products (i.e. white gel) in both the cement paste and aggregates could be observed on cross-sectional surfaces without the aid of magnification while reaction products were not readily visible on external surfaces.

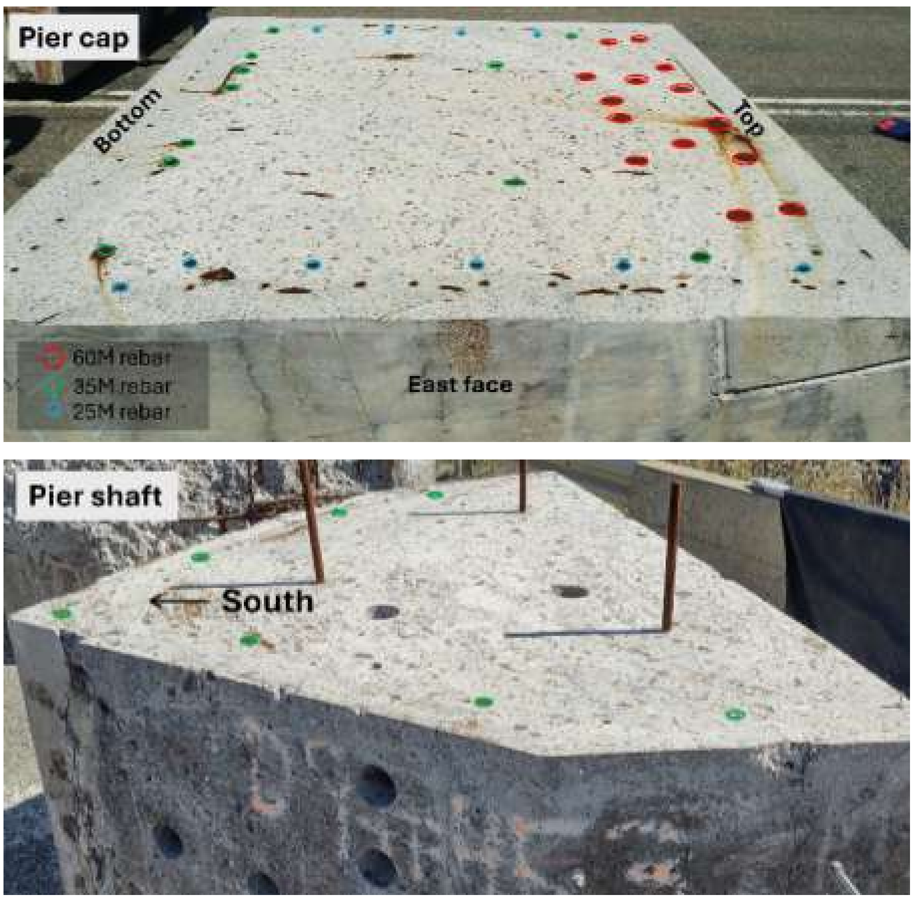

Figure 4-7 Annotated images depicting examples of rebar arrangements inside PC and PS segments

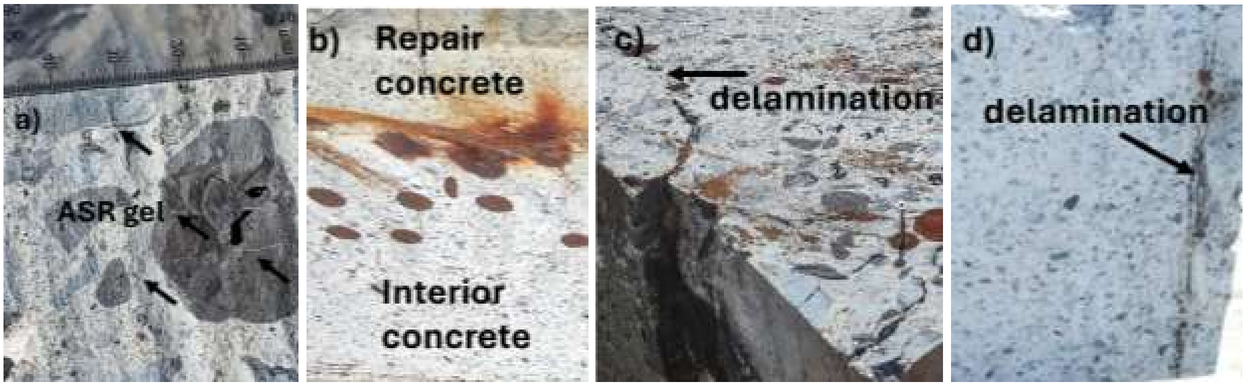

Figure 4-8 Annotated images depicting cross-sectional surfaces of the PC a) cracks suggesting ASR and b) repair and planes of delamination in the PS on c) horizontal surface and d) vertical surfaces

4.5.1.1 Crack Patterns on Members

Crack patterns observed on the PC and PS members are shown in Figure 4-9 and Figure 4-10 respectively. In the PC, cracking was noted to occur parallel to the bottom with a higher crack density in areas of less reinforcement. Longitudinal cracks were also observed to be the longest in all surfaces with transverse cracking extending from the east or west surfaces through the bottom surface. In the PS vertical cracks were seen to be the predominant crack orientation with both cracks occurring horizontally and vertically observed to align with reinforcement. A reduction in cracking was noted in the semi-submerged zone while a long longitudinal crack on the east face was observed to align with reinforcement exposed in the corresponding area on the west face which had experienced spalling. PS cracks oriented vertically within the member were found to be widest with the width frequently exceeding 1 mm (coloured red and orange).

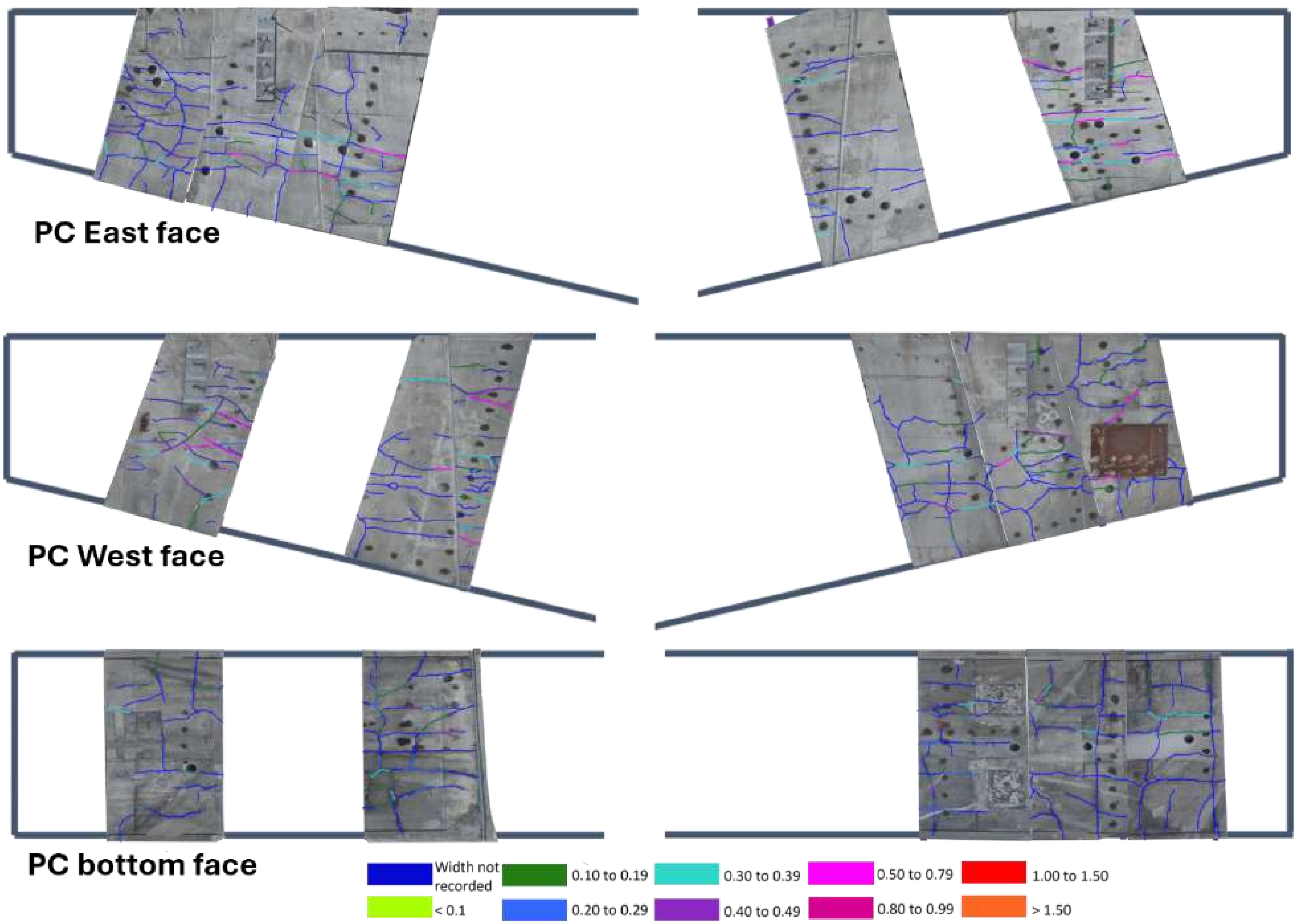

Figure 4-9 Observed cracking overlaid on images of PC member (UPV measurement points and core extraction location visible on samples as dark circles)

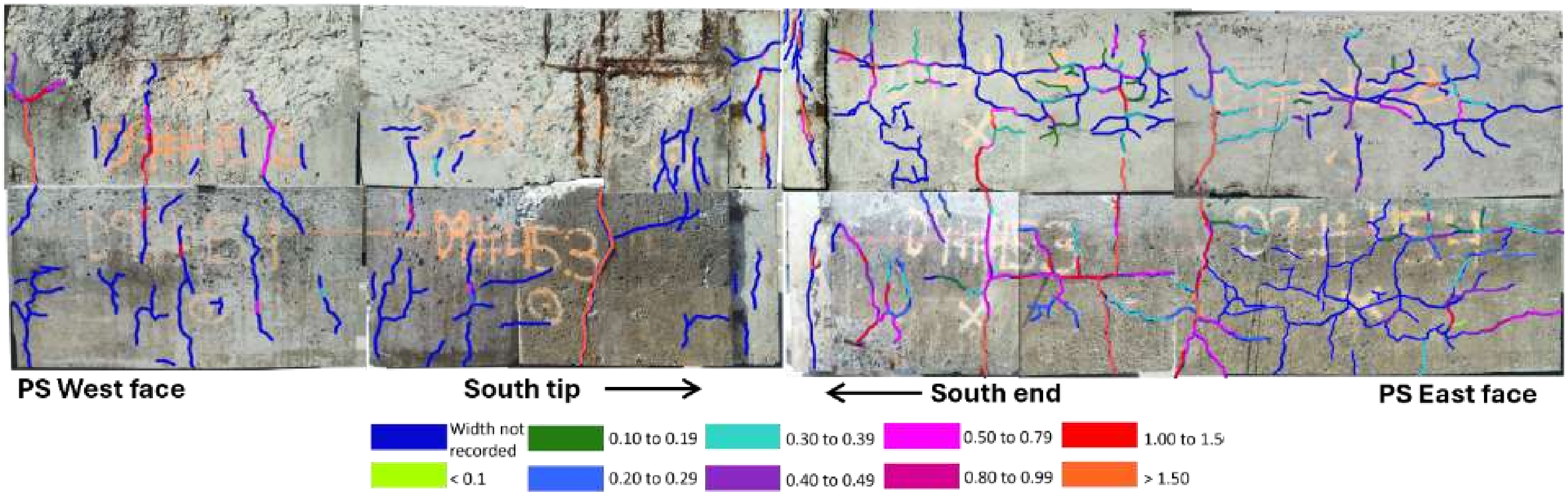

Figure 4-10 Observed cracking overlaid on images of PS Member

4.5.1.2 Cracking Index (CI)

The quantitative visual assessment method, CI, was used to quantify damage on different areas of the members, including different faces (e.g. east vs. west) and compare it between different service environments (e.g. wet vs. dry regions). Due to spalling on the dry portion of the PS west face, CI could not be conducted in this region. Figure 4-11 (A) shows the average CI for all squares on each face (average of 5 CI squares for each PC surface, average of 3 and 4 CI squares for the west and east faces of the PS, respectively). The highest CI values occurred on the east face of the PS, having a value of 2.5 mm/m however, all average CI values were higher than 0.5 mm/m, indicating the need for further investigation of the members [21] (i.e. conducting NDT's and/or extracting cores from the members for further testing). When separated into crack width intersecting lines in distinct directions clear anisotropy was observed for all investigated locations. The highest CI values were obtained along the vertical lines of the CI for all but the PS west face. The opposite was seen for the horizontal CI which were lowest in all but the PS west face with several instances where no cracks intersected horizontal lines of the CI resulting in a value of zero. CI along the diagonal lines of the CI square resulted in an intermediate value between that of the vertical and horizontal CI values.

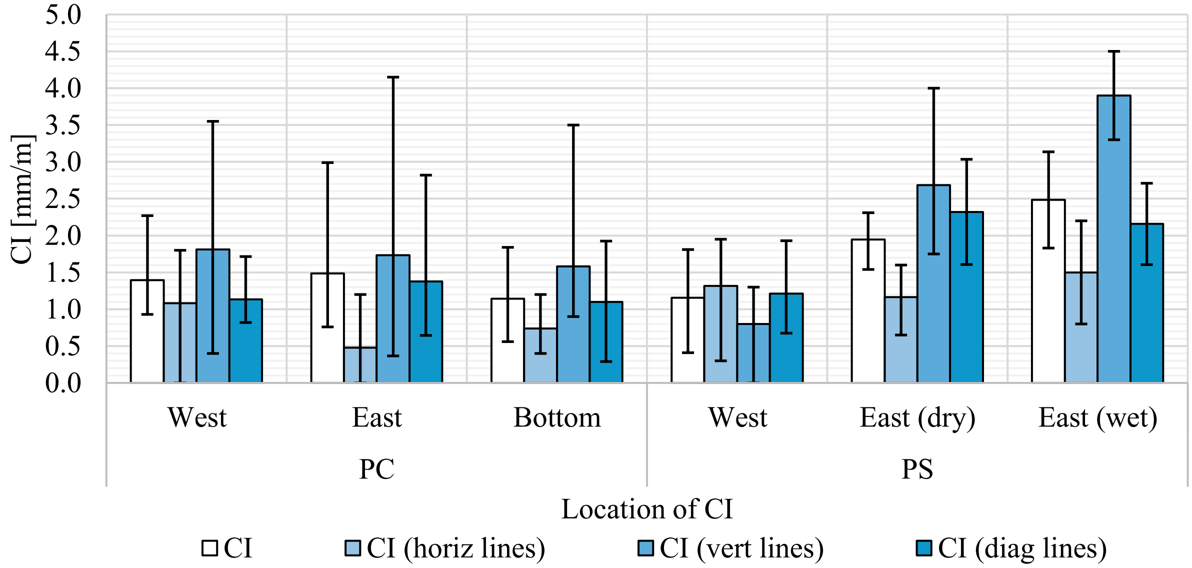

Figure 4-11 Bar graph depicting average, horizontal, vertical and diagonal CI components for different faces of the PC and PS members. Error bars indicate the maximum and minimum recorded values. *Crack outlier with width 12mm omitted

The average crack widths and average number of cracks per meter intersecting the vertical, horizontal and diagonal CI lines are shown in Figure 4-12 and Figure 4-13. Average crack widths for the PC ranged from 0.16 to 0.35 mm while average crack widths for the PS ranged from 0.12 to 0.51 mm. The average number of cracks ranged from 2 to 6 cracks per meter in the PC while the average number of cracks ranged from 4 to 9 cracks per meter in the PS specimen.

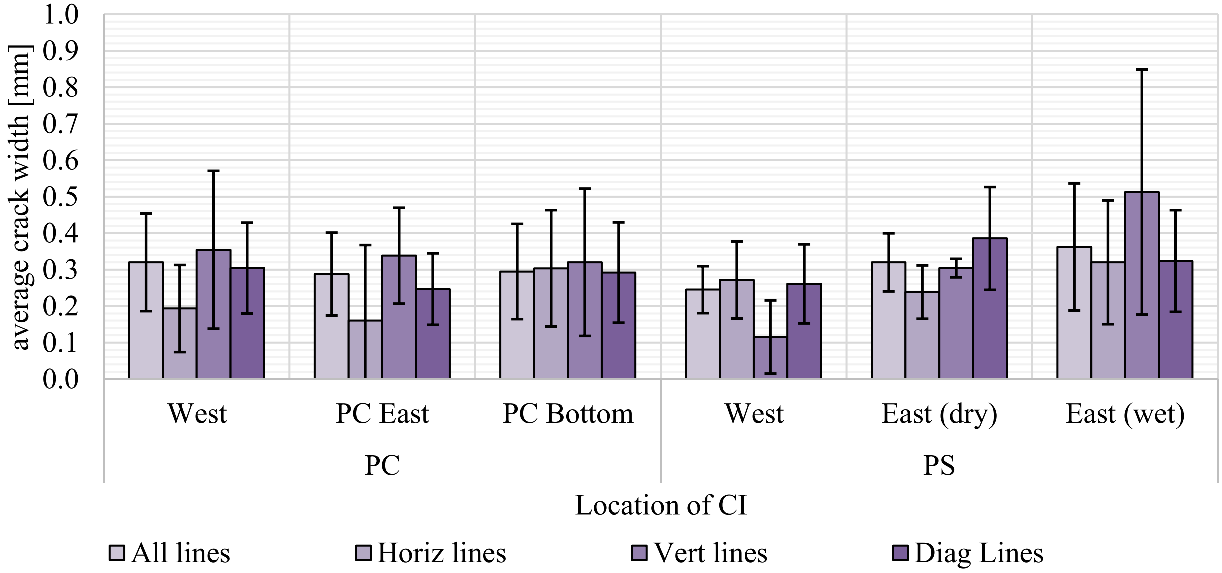

Figure 4-12 Bar graph depicting average crack widths for different faces of the PC and PS members. Error bars indicate one standard deviation.

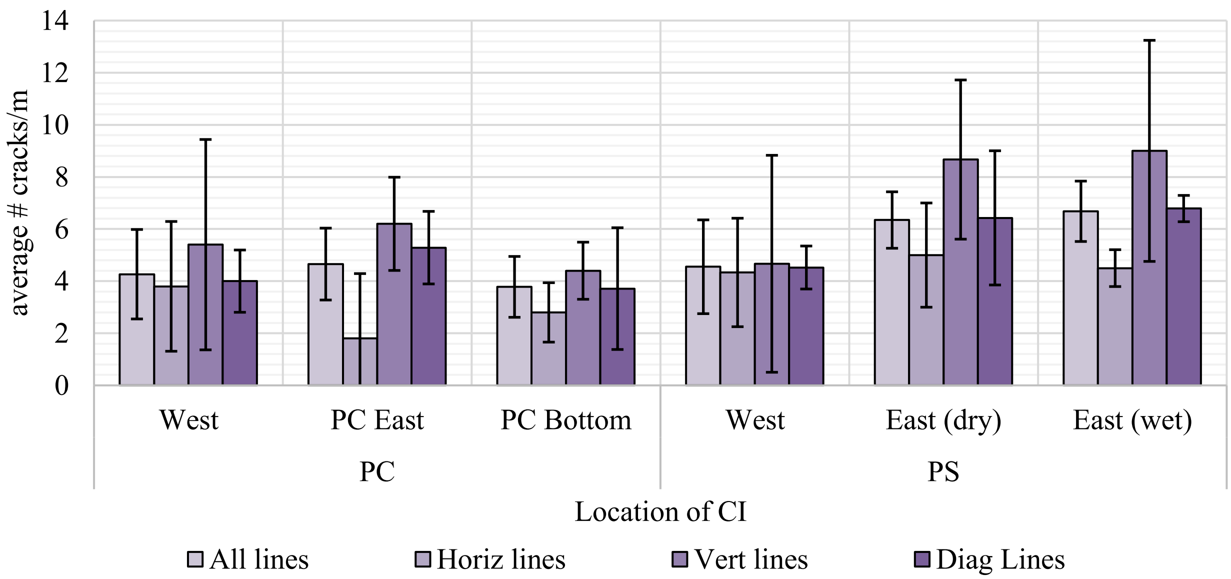

Figure 4-13 Bar graph depicting average number of cracks for different faces of the PC and PS members. Error bars indicate one standard deviation.

4.5.2 Non-Destructive Testing

4.5.2.1 Rebound Hammer

The average compressive strength calculated from the rebound hammer numbers for distinct surfaces of the PC and PS members is shown in Figure 4-14. The external surfaces of the PC (repair concrete) have higher compressive strengths, with the highest average strength of 51 MPa occurring on the bottom surface while average strengths on east and west faces are 38 and 39 MPa respectively. Internal concrete from the cut surfaces of the PC presented a lower concrete strength of 30 MPa. This is more aligned with values in the PS, where average strengths vary from 36 MPa on the east faces to 33MPa in interior locations suggesting similar compressive strengths in the two members.

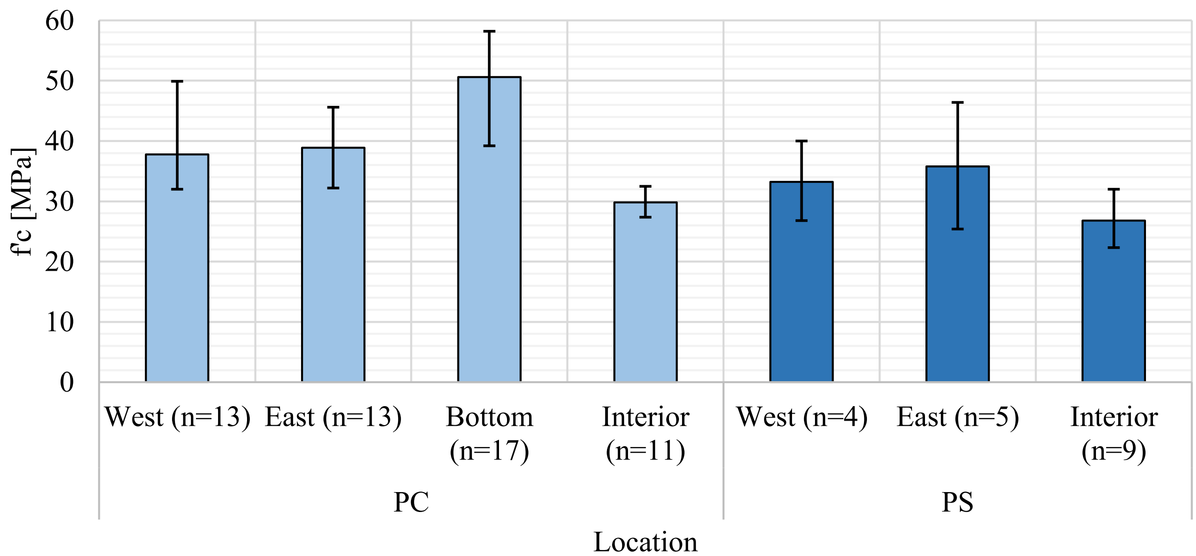

Figure 4-14 Bar graph depicting average compressive strength calculated from rebound hammer numbers for PC and PS members. Error bars indicate maximum and minimum values, and n corresponds to the number of measurements.

4.5.2.2 Ultrasonic Pulse Velocity (UPV)

Individual UPV measurements were performed by taking the average reading over various lengths (up to 1.8 m) and in various locations (e.g. vertical vs. horizontal) as shown in Figure 4-5. UPV values were averaged from various locations on distinct surfaces of the PC and PS and are presented in Figure 4-15.

Average UPV speeds were less than 3.0 km/s for both members indicating the need for further testing [27]. External surfaces in the PC (i.e. repair concrete) had high variability between maximum and minimum measured values. Internal locations in the PC presented a higher average UPV value with the lowest variability, however this value was within the range of UPV found for other PC surfaces.

In the PS, UPV measurements on surface locations were impeded by high surface deterioration coupled with large visible cracks. Measurements in the 'wet' region were unsuccessful due to the frequency of these cracks. Only measurements at on the upper (dry) surface of the PS, which exhibited lower deterioration, and at the southernmost point of the PS, where a metal plate reduced surface deterioration, were conducted successfully on exterior PS surfaces. Both locations resulted in similar UPV speeds around 2.0 km/s.

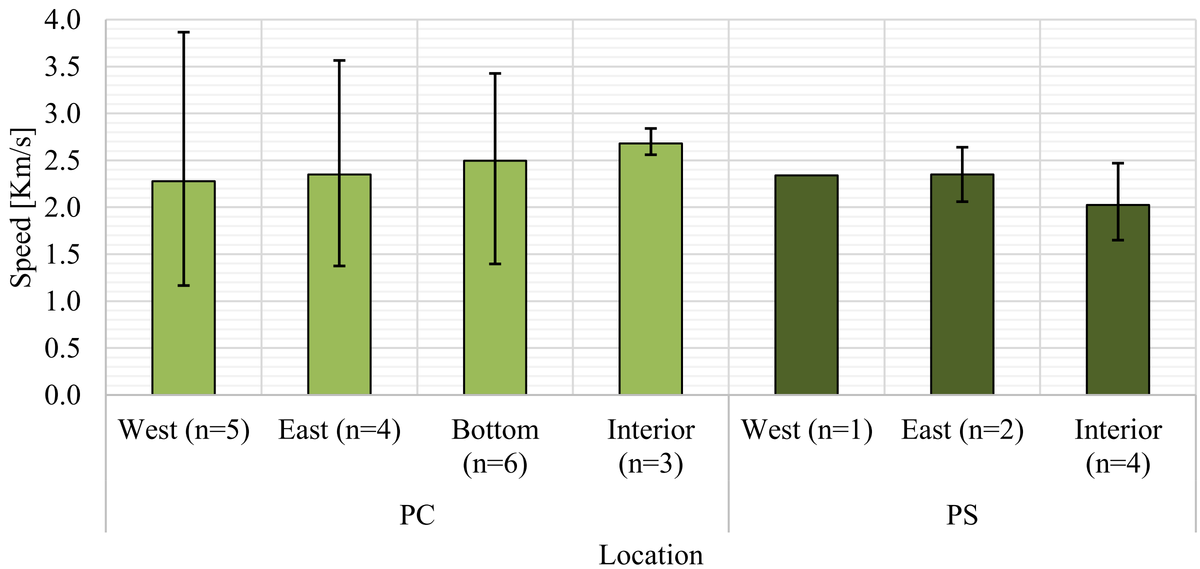

Figure 4-15 Bar graph depicting average UPV speed for PC and PS members. Error bars indicate maximum and minimum values, and n corresponds to the number of measurements.

4.5.2.3 Surface Resistivity

Surface resistivity readings successfully differentiated between the repair concretes on the exterior (average readings of 265 kΩ·cm, with standard deviation of 83.5 kΩ·cm) and the internal concrete (average readings 9 kΩ·cm, with standard deviation of 1.2 kΩ·cm). This indicates that the repair concrete provided a good barrier against the ingress of harmful ions such as chloride while the original concrete would have been vulnerable. Average surface resistivity for segments from the PS was 25 kΩ·cm (with standard deviation of 19.6 kΩ·cm).

4.6 Discussion

The presence of ASR in both members was expected given the previous testing on cores from CB piers [2] and use of the same type of silicious limestone as coarse aggregate. Visual inspection of internal concrete of both members supported the presence of ASR with cracks containing suspected ASR frequently observed. Despite this, differences in geometry (i.e. higher reinforcement in PC) and environment (i.e. submerged, semi submerged and wet regions in PS) resulted in different damage patterns in the two members, namely the greater presence of wide cracks parallel to reinforcement in the PS. However, although damage manifested differently, the quantitative visual assessment techniques (i.e. the CI) and non-destructive testing (i.e. rebound hammer, UPV and surface resistivity) indicated similar results: i.e. high damage requiring further investigation of both members.

4.6.1 Anisotropy Identified in Visual Assessment

4.6.1.1 Observed Cracking

Crack patterns (presented in Figure 4-9 and Figure 4-10) showed areas in both members indicative of 'map cracking'. These areas are located in regions with moderate reinforcement in the PC and PS with PS additionally exhibiting an area of reduced cracking between dry and submerged regions. A higher density of cracking appears in the PC towards the outer ends of the member on the east and west faces while cracking is reduced near the top of the member. There was less cracking in the concrete at the top of the PC where external post-tensioning was used for the final 10 years of service [19]. In the PS, the transition area between wet and dry regions was observed to have less cracking (i.e. less horizontal cracks) while many cracks can be seen to be aligned with the reinforcement, particularly in the spalled region on the west face. The PS exhibited significant scaling and deterioration of exterior aggregates, especially in the wetted region (i.e. submerged or semi-submerged). This agrees with the findings of [29, 30] where the highest damage occurred in the semi-submerged region of hydraulic structures.

4.6.1.2 The CI and Individual Crack Widths

When crack widths and computed CI are considered, anisotropic properties were identified with widths and number of cracks varying depending on direction. The CI is a powerful tool for comparison of damage, especially cracking due to internal swelling reactions, at different locations in a concrete member or between different members in a structure. However, the choice of location for CI which is recommended to be the most damaged portion of the area of interest, can be biased by the presence of large cracks which may indicate types of deterioration other than internal swelling reactions. As such, this may introduce bias when single cracks with large widths are present (e.g. the 1.2 cm crack omitted from Figure 4-11 and Figure 4-13) which could impact CI as a comparative technique. CI results for different line segments (i.e. the vertical and horizontal lines of the CI) as well as average crack widths and number of cracks intersecting these lines are discussed in the following two paragraphs.

In the PC segments, the CI values for vertical lines (i.e. cracks traveling longitudinally) were higher compared to horizontal lines (i.e. cracks travelling vertically); this resulted in an average CI of 1.8 and 1.7 mm/m along vertical lines in the west and east faces, respectively, compared to 1.1 and 0.5 mm/m intersecting horizontal lines. On the east and west surfaces, CI values correspond to both wider and more numerous cracks intersecting the vertical lines of the CI (average widths of 0.35-0.34 mm) compared to smaller width cracks (0.16-0.19 mm) intersecting horizontal lines. Conversely, differences between the CI for horizontal and vertical lines on the bottom surface was caused primarily by different numbers of cracks in the two directions since average crack widths were the same for all CI line orientations (0.30 ±0.02 mm). In the context of the suspected internal swelling reaction (i.e. ASR) the difference in crack widths suggests expansion in the member may have occurred preferentially vertically within the member.

In the PS segments, CI results indicated high variability between surfaces in the member. On the east face the CI presented high readings with a similar trend to the PC where CI for the vertical lines (2.7

and 3.9 mm/m for dry and wet surfaces, respectively) were much larger than the CI for the horizontal lines (1.2 and 1.5 mm/m for dry and wet surfaces, respectively), indicating higher damage occurring longitudinally. CI in these locations resulted from increases in both average crack widths and crack frequency. The widths of cracks intersecting vertical lines were found to be 0.30 mm (dry region) and 0.51 mm (wet region) compared to those of cracks intersecting horizontal lines which were found to be 0.20 mm (dry region) and 0.30 mm (wet region). Conversely, the CI on the west face had the lowest values along the vertical lines, where the average crack width is 0.12 mm compared to 0.27 mm on the horizontal line while a similar number of cracks were identified in all directions.

The magnitude of the CI in both members were greater than 0.50 mm/m, indicating the need for further investigation (i.e. NDT's and/or extraction and testing of cores) [21]. The CI values in the PC segments were found to be lower compared to those in the PS due primarily to a higher number of cracks on the PS east face. The average crack width intersecting vertical lines on the wet portion of the PS east face was notably large (0.51 mm) compared to crack widths in other regions. Furthermore, although locations were chosen to represent areas with the highest damage in each segment, some locations on the PS were not sufficiently flat to use the CI (i.e. the spalled sections on the west face and the large crack near the southern tip of the west face where the surface was displaced outwards).

4.6.2 Assessment of Surface and Internal Damage

Durability issues are evident on external surfaces of both members, including significant cracking, and discoloured regions. In the PS additional signs of damage include spalling along with significant planes of delamination which were visible on cut surfaces. It was expected that the surface of these members would experience higher damage compared to the interior due to the contributions of reinforcement corrosion, freeze-thaw damage and erosion of submerged surfaces with observed damage supporting the presence of these damage mechanisms. Average crack widths identified at the surface of both members were around 0.30 mm, suggesting that in both members the ingress of harmful ions such as chlorides, as well as the ingress of moisture can occur more rapidly through cracks compared to ingress in uncracked concrete [31].

Visual assessments of interior surfaces identified that there was no significant corrosion in interior reinforcing bars (i.e. more than 20 cm from the exterior surface). White products in aggregates, including cracks extending from aggregates containing white material (i.e. the suspected ASR gel), could be observed on internal surfaces without the aid of magnification. However, had internal surfaces not been exposed only the ‘map cracking’ pattern at select locations in each member would have indicated ASR since the secondary product from ASR was not visible from the exterior. This reiterates that the presence of ASR cannot be ruled out prior to extraction of cores.

NDTs conducted on various exterior surfaces (e.g. east vs. west faces) were compared to tests on interior surfaces to evaluate whether these tests represent the interior concrete condition. Rebound hammer readings were found to over-estimate the compressive strength in surface locations. In most cases the rebound hammer and UPV resulted in similar values for both members (33-39 MPa for rebound hammer and 2.0 – 2.7 km/s for UPV), while the surface electrical resistivity indicated clear differences between the original concrete (9 kΩ·cm in the PC and 25 kΩ·cm in the PS indicating high permeability concrete) and repair concrete (265 kΩ·cm indicating low permeability concrete). Rebound hammer results for the bottom surface of the pier cap were found to be high (50 MPa) which may be due to differences in casting of the repair concrete in this location during the encapsulation repair while the highest UPV was found in the PC interior. This suggests that the compressive strength of the repair concrete is comparable to the interior concrete. Surface electrical resistivity successfully differentiated between the repair concrete and internal concrete, indicating that the original concrete was more susceptible to concrete ingress, however it did not have sufficient sensitivity to identify areas of increased concrete damage.

Similar NDT results for the two members are contrary to higher CI values found for the PS east face. This illustrates limitations for both NDTs and the future extraction of cores since wide cracks may prohibit the successful completion of testing (e.g. UPV values cannot be obtained across wide cracks, and there is a difficulty obtaining cores with adequate dimensions for the stiffness damage test - SDT).

4.7 Conclusions

Visual assessments and non-destructive tests conducted on PC and PS segments of the former Champlain Bridge in Montréal consistently indicated high levels of damage. As such, further investigation is needed (i.e. extraction and testing of concrete cores) to assess the cause, likely ASR as per previous assessment of piers in this structure, and the extent of damage in these members. Nevertheless, the main findings obtained in this research were:

Visual assessment:

- 'Map cracking' patterns were noted in areas with moderate reinforcement regions of both members. Reduced cracking was visible in high reinforcement regions of the PC as well as the semi-submerged region of the PS.
- Anisotropy was identified with crack widths varying by direction. In the PC and on the east face of the PS, vertical cracks (i.e., intersecting the horizontal CI lines) were both thinner and less frequent compared to horizontal cracks. In the context of an internal swelling reaction such as ASR these differences in crack widths suggest expansion is occurring preferentially in one direction (i.e. vertically) compared to another.
- The CI indicating the highest damage was obtained on the PS east face. The CI corresponding to this location exhibited wider and more frequent cracks intersecting the CI with cracks primarily oriented horizontally.
- Although the PC was encapsulated in a repair concrete 10 years before decommissioning of the structure, average crack widths were similar to average crack widths recorded on the PS. This suggests that assessment of reinforced concrete members using crack width measurements can provide insight to increasing deterioration within the member.
- The presence of ASR in the members was not clearly indicated by inspection of exterior surfaces, while internal surfaces exposed during decommissioning of the members included clear indicators of ASR gel in aggregates and paste.

Non-destructive testing:

- The rebound hammer estimated an average concrete strength between 33-39 MPa in east, west and interior locations of the PS and PC. The average compressive strength on the PC bottom surfaces was estimated at 50 MPa. In the PC the rebound hammer did not identify significant differences in compressive strength on the exterior (repair concrete) surfaces compared to the interior (original) concrete.
- Ultrasonic pulse velocity results were less than 3.0 km/s indicating the need for further investigation (e.g. extraction of cores for laboratory analysis) which agrees with the extent of cracking observed during the visual inspection.
- Electrical surface resistivity measurements clearly distinguished between the PC repair concrete (low permeability to chloride ingress) and the internal concrete (higher permeability), however there was high variation when used solely on the repair concrete. The electrical surface resistivity was comparable for the PC interior concrete and PS external and internal concrete.
- The application of the investigated non-destructive tests was limited in areas with wide crack widths, such as the east face of the PS.

Visual and non-destructive tests successfully identified the high level of deterioration in both the PC and PS members, however, without access to interior surfaces the cause of the deterioration could not be clearly identified. This suggests that the extraction of concrete cores continues to be necessary to establish the cause and extent of damage in reinforced concrete members even at high levels of deterioration.

4.8 References

1. Carlin GP, Mirza MS, Gaudreault M (1996) Rehabilitation Measures for Champlain Bridge, Montreal, Canada. Canadian Journal of Civil Engineering 23:1326–1340

2. Bérubé M-A, Frenette J (1995) Évaluation de la Réactivité Alcaline dans le Béton des Piles 12, 18 et 20 W du Pont Champlain. Sainte-Foy, Quebec

3. Noël M, Sanchez L, Martin R-P, Fournier B, Bastien J, Mitchell D (2016) Structural Implications of Internal Swelling Reactions in Concrete: A review. In: 15th international conference on alkali aggregate reaction. p 11

4. Diao B, Sun Y, Cheng S, Ye Y (2011) Effects of Mixed Corrosion , Freeze-Thaw Cycles , and Persistent Loads on Behavior of Reinforced Concrete Beams. Journal of Cold Regions Engineering 25:37–52

5. Wang Y, Cao Y, Zhang P, Ma Y, Zhao T, Wang H, Zhang Z (2019) Water absorption and chloride diffusivity of concrete under the coupling effect of uniaxial compressive load and freeze-thaw cycles. Constr Build Mater 209:566–576

6. Panesar DK, Ching G (2018) Implications of coupled degradation mechanisms of cement based materials exposed to cold climates. Int J Mech Sci 144:865–876

7. Sanchez LFM, Drimalas T, Fournier B, Mitchell D, Bastien J (2018) Comprehensive damage assessment in concrete affected by different internal swelling reaction (ISR) mechanisms. Cem Concr Res 107:284–303

8. Bérubé, Snaoui N, Bissonnette B, Fournier B (2005) Outil d'evaluation et de gestion des ouvrages d'art affectes de reactions alcalis-silice (RAS).

9. Rogers C (1993) Alkali-aggregate reactivity in Canada. Cem Concr Compos 15:13–19

10. RILEM technical committee 259-ISR (2021) Diagnosis & Prognosis of AAR Affected Structures. Springer Nature Switzerland AG

11. Sanchez LFM, Fournier B, Jolin M, Mitchell D, Bastien J (2017) Overall assessment of Alkali-Aggregate Reaction (AAR) in concretes presenting different strengths and incorporating a wide range of reactive aggregate types and natures. Cem Concr Res 93:17–31

12. Gautam BP, Panesar DK, Sheikh SA, Vecchio FJ (2017) Effect of multiaxial stresses on alkali-silica reaction damage of concrete. ACI Mater J 114:595–604

13. Fan S, Hanson JM (1999) Length Expansion and Cracking of Plain and Reinforced Concrete Prisms Due to Alkali-Silica Reaction. ACI Mater J 480–485

14. Fan S, Hanson JM (1999) Effect of Alkali Silica Reaction Expansion and Cracking on Structural Behavior of Reinforced Concrete Beams. ACI Mater J 488–495

15. Zahedi A, F M Sanchez L, Noël M (2022) Appraisal of visual inspection techniques to understand and describe ASR-induced development under distinct confinement conditions. Constr Build Mater. https://doi.org/10.1016/j.conbuildmat.2022.126549

16. Zahedi A, Trottier C, Sanchez LF, Noël M (2022) Condition assessment of alkali-silica reaction affected concrete under various confinement conditions incorporating fine and coarse reactive aggregates. Cem Concr Res. https://doi.org/10.1016/j.cemconres.2021.106694

17. Groupe counseil Genivar (2003) Champlain Bridge, Rehabilitation of Piers, Pier Caps, Bearings and Beams (2004) Phases of Demolition.

18. Leroux Beaudoin Hurens & Associes Inc (2005) Pont Champlain, réfection de piles, chevêtres, appuis et poutres (2004) CONTRAT No: 60494.

19. Aecom Tecsult Inc. (2008) Rapport 1879 Pont Champlain, services de consultant, Étude, dessins et devis pour la réfection de piles et de poutres précontraintes (2007-2011).

20. Godart B, Fasseu P, Michel M (1992) Diagnosis and monitoring of concrete bridges damaged by AAR in Northern France. In: The Ninth International Conference On Alkali-Aggregate Reaction In Concrete. London, UK, pp 368–375

21. Fournier B, Bérubé M-A, Folliard KJ, Thomas M (2010) Report on the Diagnosis, Prognosis, and mitigaton of Alkali-Silica Reaction (ASR) in Transportation Structures.

22. ASTM C597 (2016) Standard Test Method for Pulse Velocity Through Concrete. 4–7

23. Kristufek L, Zahedi A, Tawil D, Sanchez L, Martin-Perez B, Noël M (2022) Preliminary evaluation of Pier cap from an ASR affected bridge in Central Canada. MATEC Web of Conferences 364:03005

24. Kristufek L, Sanchez L, Martin-Perez B, Noël M (2023) Condition Assessment of Concrete Pier Shaft Segment from Bridge in Central Canada. CSCE 2023 Conference, Moncton NB, May 24-27 2023

25. RILEM (2013) Guide to Diagnosis and Appraisal of AAR Damage to Concrete in Structures. Springer Netherlands

26. Institution of Structural Engineers (ISE) (1992) Structural Effects of Alkali-Silica Reaction – Technical Guidance Appraisal of Existing Structures. Institution of Structural Engineers 45

27. IS 13311-1 (Part 1) (1992) Method of Non-destructive testing of concrete, Part 1: Ultrasonic pulse velocity [CED 2: Cement and Concrete]. Bureau of Indian Standards 1–7

28. Polder R, Andrade C, Elsener B, Vennesland O, Gulikers J, Weidert R, Raupach M (2000) RILEM TC 154-EMC: electrochemical techniques for measuring metallic corrosion: Test methods for on site measurement of resistivity of concrete. Materials and structures/ Matériaux et Constructions 33:603–611

29. Rosenqvist M (2016) Frost-induced deterioration of concrete in hydraulic structures Interactions between water absorption, leaching and frost action. Ph.D. Dissertation, Lund University

30. Rosenqvist M, Oxfall M, Fridh K, Hassanzadeh M (2015) A test method to assess the frost resistance of concrete at the waterline of hydraulic structures. Mater Struct 2403–2415

31. ACI Committee 222 (2001) Protection of Metals in Concrete Against Corrosion Reported by ACI Committee 222. ACI 1–41

Chapter 5: Paper 2

Microscopic investigation of alkali-silica reaction (ASR)-affected piers of Montreal's Champlain Bridge

Abstract:

Montreal's iconic Champlain Bridge (1962-2019) was constructed using an aggregate susceptible to alkali-silica reaction (ASR). Significant signs of distress in concrete members led to the decommissioning of the bridge, thus enabling a thorough investigation of various components, including pier cap (PC) and pier shaft (PS) sections. Significant damage was identified during visual and non-destructive testing, which was followed by extensive coring of the members as part of a comprehensive multi-level assessment (i.e. microscopic and mechanical tests). Selected cores, extracted from distinct orientations (i.e. vertical, transverse, and longitudinal) and having different service conditions (i.e., varying degrees of internal restraint, external loading, and environmental exposure) from these members were evaluated using the Damage Rating Index (DRI), a semi-quantitative microscopic technique, along with supplementary image analysis. It has been found that both the location of cores (e.g. depth, reinforcement ratio) and service condition influenced the degree of ASR-induced damage. Both the PC and PS were found to exhibit a high level of distress: in the PC, DRI values varied from 760 to 1150 in the moderately reinforced region and from 950 to 1390 in areas with less reinforcement with crack densities of 2.6 to 5.0 cracks per cm^2, whereas cores extracted from the PS had DRI values ranging from 800-1180 in the dry region and 660 to 1000 in the semi-submerged region with cracking densities of 2.1 to 4.0 cracks per cm^2.

5.1 Introduction

Montreal's Champlain Bridge (CB), in service from 1962-2019, was a 3.4 km, six-lane highway bridge that was decommissioned due to significant signs of distress in many of its reinforced concrete members. Deterioration of the structure was largely attributed to reinforcement corrosion due to the use of de-icing salts during winter months [1]; however, alkali-silica reaction (ASR), an internal swelling reaction, was found to be present in cores extracted from CB piers as early as the 1990's [2]. Following decommissioning of the structure, various members were made available for research including the pier cap (PC) and pier shaft (PS) members. Visual and non-destructive assessments of these members identified lightly reinforced areas which exhibited 'map cracking' patterns indicative of internal swelling reactions. However, results from external assessments were limited by the repair history of the two members, with the PC having undergone an encapsulation repair in 2004 [3] as well as external longitudinal reinforcement in 2008 [4]. Despite these different repair histories, results of all visual and non-destructive assessments for both members unanimously indicated high levels of damage requiring further investigation [5]. Cores were subsequently extracted from these members for further laboratory testing to assess their current condition using a multi-level assessment protocol (i.e. microscopic and mechanical testing) [6–8]. This work describes the microscopic evaluations conducted on cores from the PC and PS with the aim of obtaining the main cause(s) and extent of damage present in these members.

5.2 Background

5.2.1 Alkali-Silica Reaction (ASR) and Harsh Climate Associated Damage

ASR is a chemical reaction between unstable mineral phases in the aggregates used to make concrete and the alkali hydroxides from the concrete pore solution; this reaction generates a secondary product [9] that swells upon moisture uptake, leading to expansion and deterioration of the affected material. The development of ASR in field concrete is impacted by the environmental (e.g. moisture conditions, temperature) and the service conditions (e.g. member's geometry, restraint and loading etc.) [10–15]. In restrained conditions, ASR displays anisotropic properties (i.e. material exhibits different properties depending on direction), which in turn complicates determining the overall condition of affected members.

ASR is considered one of the most harmful deterioration mechanisms affecting critical concrete infrastructure in Canada and worldwide. Moreover, due to the harsh climate faced in the country, Canadian infrastructure is prone to develop combined mechanisms, where corrosion of the steel reinforcement and freeze-thaw cycles are the most frequently observed mechanisms alongside ASR. In the CB, a poor drainage system and frequent use of de-icing salts during the winter resulted in heavy moisture and salt exposure of concrete piers leading to visible corrosion [16, 17]. Cracking induced by service loads from the seven girders resting on the PC may have increased ingress of moisture and salt. Conversely, for the bottom portions of the PS, which extend from concrete piles in the St. Lawrence River, moisture rather than salt ingress is the primary concern. While submerged portions of the pier shaft are not expected to experience FT cycles [18, 19], exposure conditions above the water surface would have included increased exposure to precipitation as well as temperature fluctuations due to the direct sunlight [20].

Decommissioning of the CB presented a unique opportunity for the investigation of ASR induced damage in reinforced concrete members in a field structure, with results providing a valuable opportunity to relate ASR induced damage in the field to induced expansion in laboratory environments. The investigated members, a PC from the on-land approach (pier 42W) and a section of a PS from the water level of pier 38W were selected further providing a variety of conditions of interest. The use of an ASR-susceptible siliceous limestone common in reinforced concrete structures in the region, coupled with the variety of factors present in the two members (i.e. service environment, member geometry) represent an important contribution to understanding of ASR-affected field structures in the Canadian context.

5.2.2 Damage Rating Index

Microscopic investigation of structures likely affected by internal swelling reactions such as ASR is important for properly diagnosing the main cause(s) and extent of damage in affected concrete. While techniques such as scanning electron microscopy (SEM) and thin section petrography can provide detailed insights into the main cause(s) associated to the materials deterioration, the extent of damage is difficult to identify from these techniques. In this context, the Damage Rating Index (DRI), a semi-quantitative stereomicroscope technique, can be used to appraise the degree of damage in affected concrete and be further correlated to mechanical testing as part of a multi-level assessment [21, 22].

The DRI is a semi-quantitative microscopic technique where a stereomicroscope (15-16x magnification) is used to systematically evaluate polished concrete sections using a 1 cm^2 grid system. A numerical value is determined based on counts of various damage features (i.e. cracking in aggregates, cement paste and presence or absence of gel) in each grid square. The DRI was initially developed as an extended petrographic technique by Grattan-Bellew and coworkers (1992) to quantify ASR-induced development (i.e., chemical reaction development) [23]. This technique aimed to quantify the level of ASR chemical development (i.e., initial stage, moderate, high and very high development) through counting the following petrographic features: gel in voids, reaction rims in aggregates, loose aggregates, cracks in cement paste with or without gel, and cracks in aggregates that were closed, open or containing gel. Later, Villeneuve et al. [24] proposed some changes to the method with the aim of achieving a better correlation with ASR-induced expansion while reducing the variability among operators. As part of this work, Villeneuve et al. [24] selected to evaluate only microscopic damage features which impacted damage development associated to ASR (i.e., open cracks in aggregates and cement paste) instead of the petrographic features proposed by Grattan-Bellew and coworkers. Moreover, new weighting factors were proposed for the distinct microscopic damage features as per Table 2-3.

Amongst the weighting factors proposed by Villeneuve et al. [24], the closed cracks in the aggregates (CCA) were selected as microscopic damage features, since they represent weak planes of the aggregate particles prone to break under pressure; however, CCA is not generally associated to ASR-induced damage, being more related to the aggregates' processing and weathering. Therefore, a significantly low weighting factor of 0.25 is attributed to this feature. By contrast, the presence of open cracks in aggregate particles without or with reaction products, OCA and OCA_{RP}, respectively, were observed to increase corresponding to induced ASR damage and thus display a high weighting factor of 2. Similarly, cracks in the cement paste without or with reaction products (CCP and CCP_{RP}, respectively) correspond to increasing distress due to ASR, especially when ASR has become more developed. Moreover, through a mechanical point of view, cracks in the cement paste have a greater influence on the mechanical properties of the concrete; therefore, an even higher weighting factor of 3 was selected for this feature.

Sanchez et al. [25, 26] subsequently investigated the use of DRI for assessing ASR-induced expansion and associated damage of concrete mixtures incorporating various reactive aggregate types (i.e., coarse versus fine) and natures (i.e., lithotypes), and mechanical properties (i.e., 25, 35 and 45 MPa). The authors concluded that the weighting factors as per Table 2-3 effectively distinguished numerous levels of ASR-induced damage (i.e., marginal, moderate, high, and very high). Furthermore, the authors also evaluated the use of the DRI employing the proposed weighting factors to appraise other internal swelling reactions, such as freeze-thaw (FT) and delayed ettringite formation (DEF). The findings of these works attested the promising potential of the DRI to appraise internal swelling reactions in general, and a comprehensive table benchmarking the DRI numbers as a function of distinct expansion levels for various deterioration mechanisms (i.e., single or coupled) was proposed and is illustrated in Table 5-1 [7]

Table 2-3 Weighting factors used for Damage Rating Index (DRI) Microscopic Technique [27] (Duplicated for ease of reference)

Damage features	Abbrev.	Weight factors
Crack in coarse aggregate	CCA	0.25
Opened crack in aggregate	OCA	2
Crack with reaction product in aggregate	OCA_{RP}	2
Debonded/dislodged aggregate	Debond	3
Crack in cement paste	CCP	3
Crack with reaction product in cement paste	CCP_{RP}	3
Disaggregate/corroded aggregate particle	DAP	2

Sanchez et al. [25, 26] also proposed a complementary petrographic analysis with the use of the DRI, the so-called 'extended DRI', where the cracks observed in affected concrete are evaluated in absolute (counts) and relative (%) manners. This complementary analysis facilitates a more comprehensive understanding of the damage evolution of distinct deterioration mechanisms in concrete. Furthermore, the extended DRI enables the computation of the crack density (CD), where the number of open cracks in the aggregates and cement paste (with and without gel) present in the affected concrete is normalized to cm^2.

To complete DRI assessments, supplementary image analysis (i.e. measuring crack widths, lengths, and orientation) [12] may further enhance understanding of the impact of various factors (e.g. presence of confinement or restraint, microclimate, etc.), on the overall deterioration of concrete [11, 28].

In recent years, the DRI has also been successfully used to appraise concrete mixtures affected by external mechanisms, such as external sulphate attack [29] and physical salt attack [29]. This ability of the DRI to assess both external and interior deterioration mechanisms (i.e., single or coupled) that commonly occur in the field (particularly in Canada) makes it a versatile and valuable diagnostic tool for evaluating concrete durability under complex exposure conditions.

Table 5-1 Guidelines developed by Sanchez et al. 2018 [7] **outlining expected DRI values corresponding to different distress mechanisms and damage degrees**

Distress Mechanism	*Classification of damage degree (%)*	*Reference expansion level (%)*	*Compressive strength loss (%)*	*DRI*
ASR	Negligible	0.00-0.03	–	100 – 155
	Marginal	0.04 ± 0.01	(-) 10 – 15	210 – 400
	Moderate	0.11 ± 0.01	0 – 20	330 – 500
	High	0.20 ± 0.01	13 – 25	500 – 765
	Very High	0.30 to 0.50 ± 0.01	20 – 35	600 – 925
FT and FT+ASR	Negligible	0.00-0.03	–	147 – 154
	Marginal	0.04 ± 0.01	12 – 32	496 – 684
	Moderate	0.11 ± 0.01	21 – 32	590 – 950
	High	0.20 ± 0.01	22 – 37	677 – 963
	Very High	0.30 to 0.50 ± 0.01	24 – 40	800 – 1300

5.3 Scope of Work

This paper presents the microscopic assessment of cores extracted from sections of the PC and PS members from the CB. Cores were extracted in three distinct directions (i.e. longitudinally, transversally, and vertically) and distinct service conditions (i.e., tensile vs. compressive regions, dry vs. semi-submerged) from both members. The DRI, conventional and extended versions, and supplementary image analysis techniques (i.e. measurement of crack widths and visualization of crack patterns) were performed to understand the main cause(s) and extent of deterioration encountered in the members. Analysis of results will focus on the influence of the orientation of extracted cores (i.e. vertical, transverse, or longitudinal), location of specimen within the member (i.e. surface vs. interior), impact of proximity to reinforcement (i.e. high vs. low reinforcement density), and microenvironment (i.e. dry vs. semi-submerged regions). The research outcomes are expected to provide valuable insights into the relationship between induced damage and the above-mentioned factors which can be used to better understand damage in aging concrete infrastructure.

5.4 Materials and Methods

The microscopic analyses were performed on cores extracted from sections of a PC and PS from Montreal's Champlain Bridge (1962-2019). Details on the concrete mix designs used are unknown, however a 28-day design strength of 24 MPa was specified for piers in the CB [30]. It is unknown if air entrainment was used in the concrete mix design.

The PC was part of pier 42W, located next to the René Lévesque Blvd, which exposed the west face to salt spray from traffic on the roadway. The PC underwent a number of repairs including an encapsulation repair in 2004 [3], where the external concrete was removed and replaced with a repair concrete, and the addition of external transverse reinforcement to strengthen the member in 2008 [4].

The PS was part of pier 38W, with the section investigated comprising dry and semi-submerged regions. This member underwent minimal repairs over its service life with a shotcrete-type layer present on some portions of the dry section.

A comprehensive visual assessment of the PC and PS was previously performed, including a discussion of the reinforcement configuration in both members [5]. In the PC, different stress-states within the member (i.e. differences between regions experiencing tensile and compressive stresses) were anticipated to have impacted damage development, while in the PS, differences between concrete damage in the dry and semi-submerged regions were of interest.

Concrete coring was undertaken as per the locations identified in Figure 5-2 and Figure 5-3. Cores were extracted from three distinct orientations: transversally, longitudinally, and vertically from both members. Core specimens were labeled using the member type (i.e. PC vs. PS), core orientation (i.e. T, L or V), orientation of the surface cores were extracted from (e.g. southeast – SE) and the depth where the core segment began (i.e. surface cores start at depth 0 cm). Due to differences in the geometries of the members, core orientation differs as shown for the PC in Figure 5-2 and for the PS in Figure 5-3 where the 'longitudinal' cores are extracted at an approximately 45° angle relative to the transverse cores. Following extraction, cores were wrapped in plastic wrap and then transported to the University of Ottawa laboratory where they were stored in a temperature-controlled chamber at 12 °C to stop the development of further ASR deterioration if present, as per Sanchez et al. [31]. Cores were classified as 'Surface' (the first 20 cm from the surface in the PS or from the reinforcement cage in the PC) or 'internal' (>20 cm from the surface).

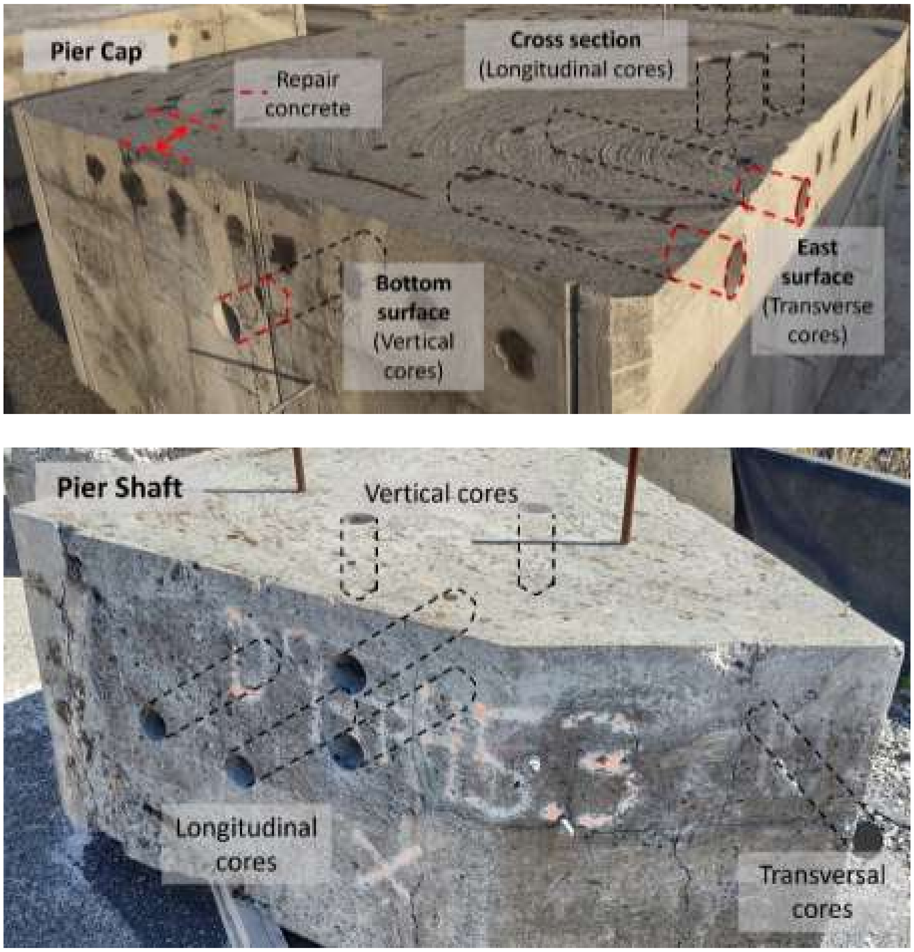

Figure 5-1 Annotated images depicting core orientation in segments from the PC (top) and PS (bottom)

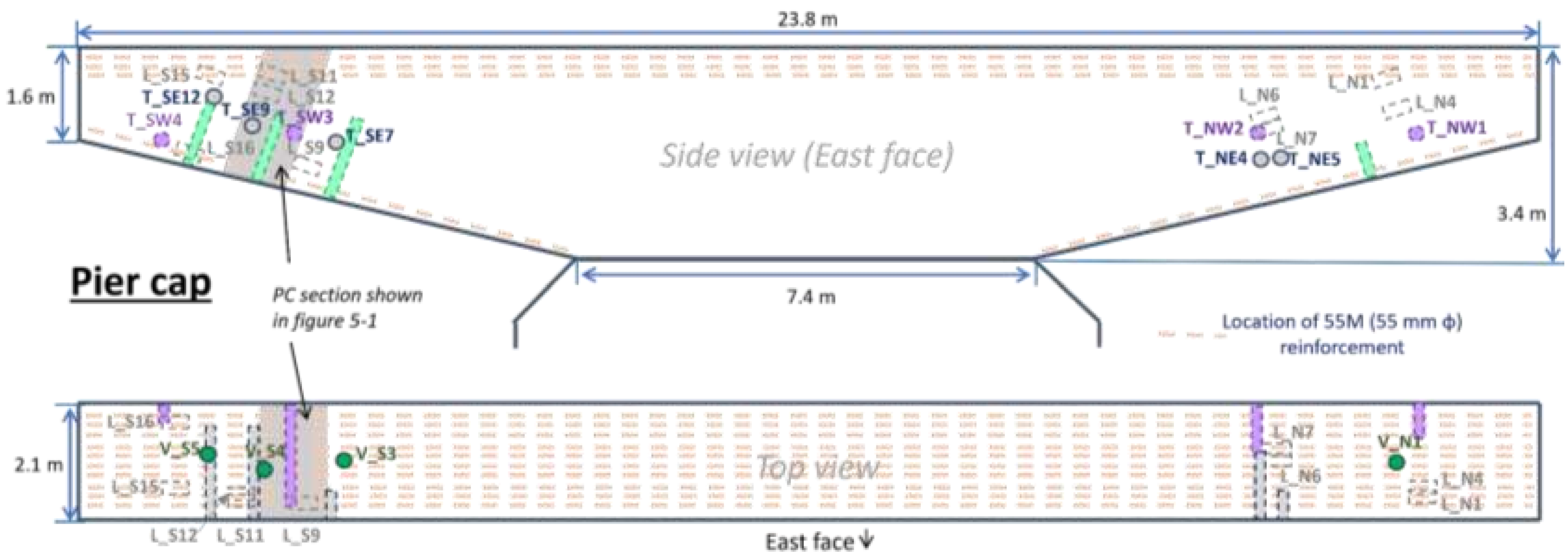

Figure 5-2 Schematic depicting major reinforcement and locations of PC cores used for DRI from transverse (T), longitudinal (L) and vertical (V) orientations. Full cores lengths are shown, not limited to DRI segments

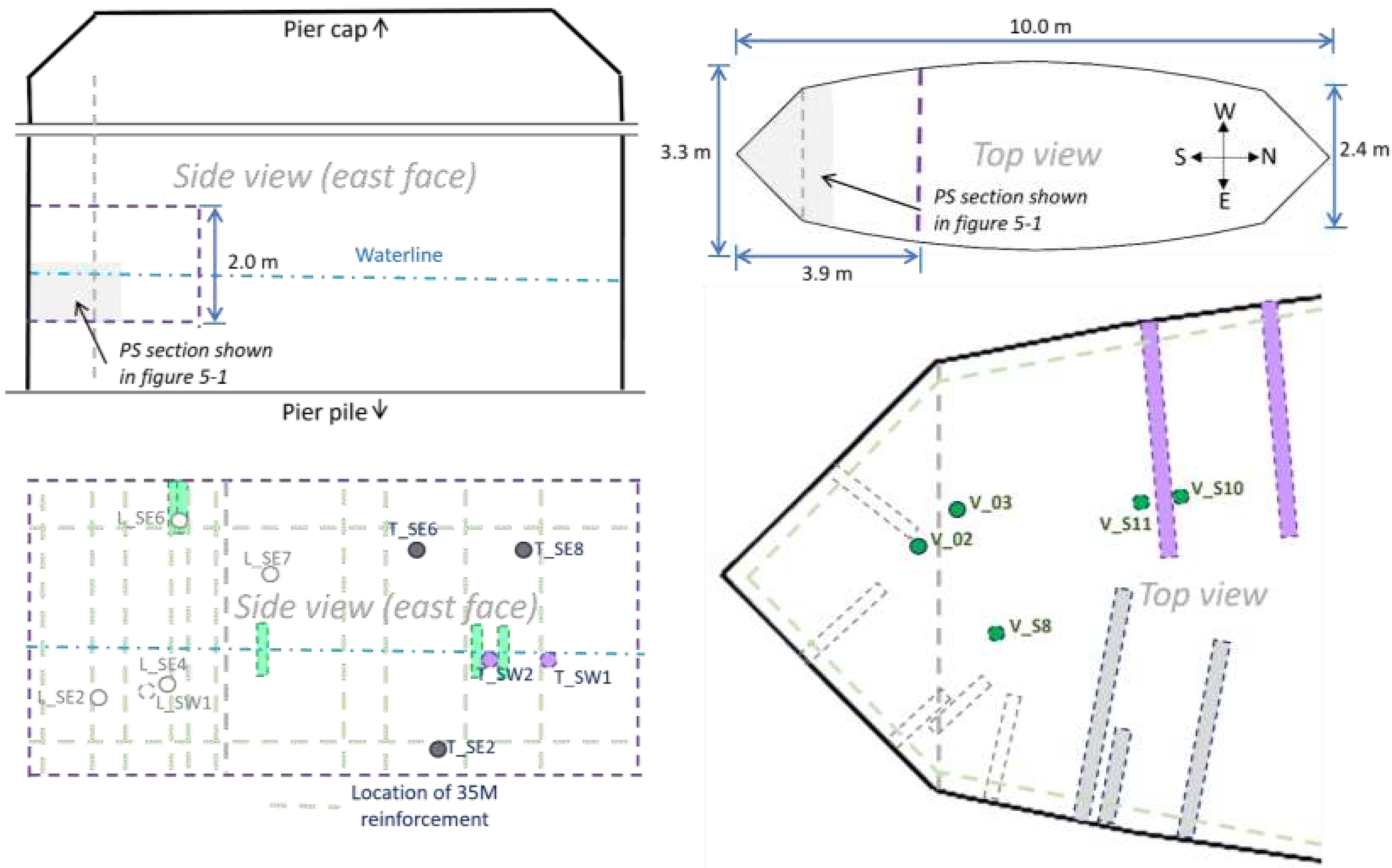

Figure 5-3 Schematic depicting major reinforcement and locations of PS cores used for DRI from transverse (T), longitudinal (L) and vertical (V) orientations. Full cores lengths are shown, not limited to DRI segments.

5.4.1 Methods for Assessment and Analysis

5.4.1.1 Damage Rating Index

The damage rating index (DRI) was performed on cores which were cut along their longitudinal axis. Polishing of the surface was conducted first using a table polisher using a 30-grit pad to flatten the surface and remove cutting defects. Samples were further polished using a hand polishing device with polishing pads of grits 50, 100, 200, 400, 800, 1500 and 3000. Samples were evaluated under a stereomicroscope at 16x magnification. The DRI number was assessed following [25], and DRI values were determined using Equation 5-1, where the area is the number of evaluated grid squares. The final DRI value for each specimen was normalized to an area of 100 cm^2.

$$DRI = \sum\left(\frac{(0.25*CCA+2*(OCA+OCA_{RP}+DAP)\ 3*(\ CCP+CCP_{RP}+Debon)}{area\ [cm^2]}\right)*100\ [cm^2] \tag{5-1}$$

5.4.1.2 Extended DRI

Data was assessed using two extended DRI methods: the percentage of microscopic damage features and the crack density (CD). In both methods, crack counts (i.e. without weighting factors) are evaluated for the entire grid area assessed.

The percentage of microscopic features as per [25] was evaluated as the percentage of closed cracks in aggregate (Equation 5-2), the percentage of open cracks in aggregates without or with reaction products (Equation 5-3), and the percentage of open cracks in cement paste without or with reaction products (Equation 5-4).

$$\%\ microscopic\ damage\ features\ (CCA) = \frac{\sum(CCA)}{\sum(CCA+OCA+OCA_{RP}+CCP+CCP_{RP})} \tag{5-2}$$

$$\%\ microscopic\ damage\ features\ (OCA+OCA_{RP}) = \frac{\sum(OCA+OCA_{RP})}{\sum(CCA+OCA+OCA_{RP}+CCP+CCP_{RP})} \tag{5-3}$$

$$\%\ microscopic\ damage\ features\ (CCP+CCP_{RP}) = \frac{\sum(CCP+CCP_{RP})}{\sum(CCA+OCA+OCA_{RP}+CCP+CCP_{RP})} \tag{5-4}$$

CD is defined as the number of open cracks normalized to 1 cm^2 and was evaluated as per [25], where CCA is omitted as shown in Equation 5-5.

$$CD = \frac{(OCA+\ OCA_{RP}+CCP+\ CCP_{RP})}{area\ [cm^2]} \tag{5-5}$$

5.4.1.3 Supplementary Image Analysis

Crack widths were measured under the stereomicroscope using a cracking index card. The entire surface of a given sample was assessed, with locations where crack widths were equal to or greater than 0.10 mm recorded. The locations of cracks with widths greater than or equal to 0.10 mm were then traced onto scans of the specimen to identify orientation trends.

5.5 Results

5.5.1 Qualitative Microscopic Evaluation

The observations evaluated under the stereomicroscope identified extensive cracking in both aggregates and cement paste (Figure 5-4), which is a sign of a high-level deterioration associated to ASR.

The presence of reaction products was noticeable but variable (Figure 5-5), with the appearance of reaction products showing distinct features, such as different morphologies, colours and textures in specimens from both the PC and PS. Areas of discolouration were observed in the cement paste adjacent to aggregates (e.g. PC T SE11 in Figure 5-5), while cracks containing reaction products were frequently observed passing through multiple aggregate particles.

Corrosion was noted to be common in the PC and PS members during the visual assessment [5]; however, corrosion products (i.e. rust) were mainly observed at the end of core specimens corresponding to planes of delamination observed in the PS. The most prominent examples of observed corrosion products are presented in Figure 5-4 and Figure 5-7.

a)

b)

Figure 5-4 Stereomicroscope images of damage in investigated core specimens showing OCA_{RP} (yellow), CCP_{RP} (green) and rust products (red)

5.5.1.1 Pier Cap

Selected damage features observed in transverse PC specimens are presented in Figure 5-5. Images A and D show open cracks within the aggregates (OCA), some of which are partially or fully filled with reaction products (OCA_{RP}). Images B and E display bright, whitish reaction products, whereas translucent, whitish products are evident in specimens C and F. Images were captured from a variety of transverse PC specimens from surface and interior locations (Figure 5-2 shows the locations of individual cores).

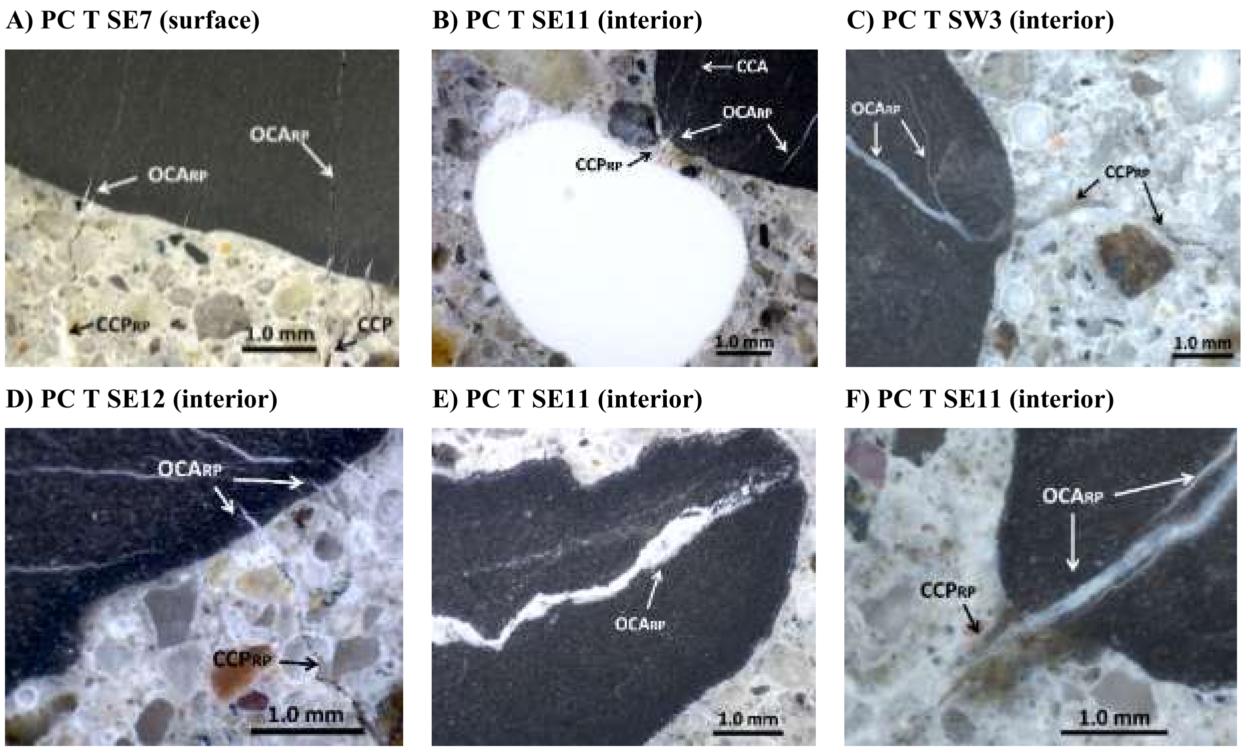

Figure 5-5 Stereoscope images of select damage features observed on PC DRI specimens

5.5.1.2 Pier Shaft

Selected damage features observed in transverse and longitudinal specimens from the PS are presented in Figure 5-6. Although reaction products were identified in specimens from the PS, open cracks in the aggregates (OCA) and cracks in the cement paste (CCP) were more frequently observed compared to those in the PC specimens. Several similarities between the PS and PC specimens can be noted, including the presence of sharp open cracks in aggregates (A) and translucent reaction products within the cement paste (B). However, a greater number of open cracks in the cement paste were observed in the PS specimens (e.g., C, D, and F).

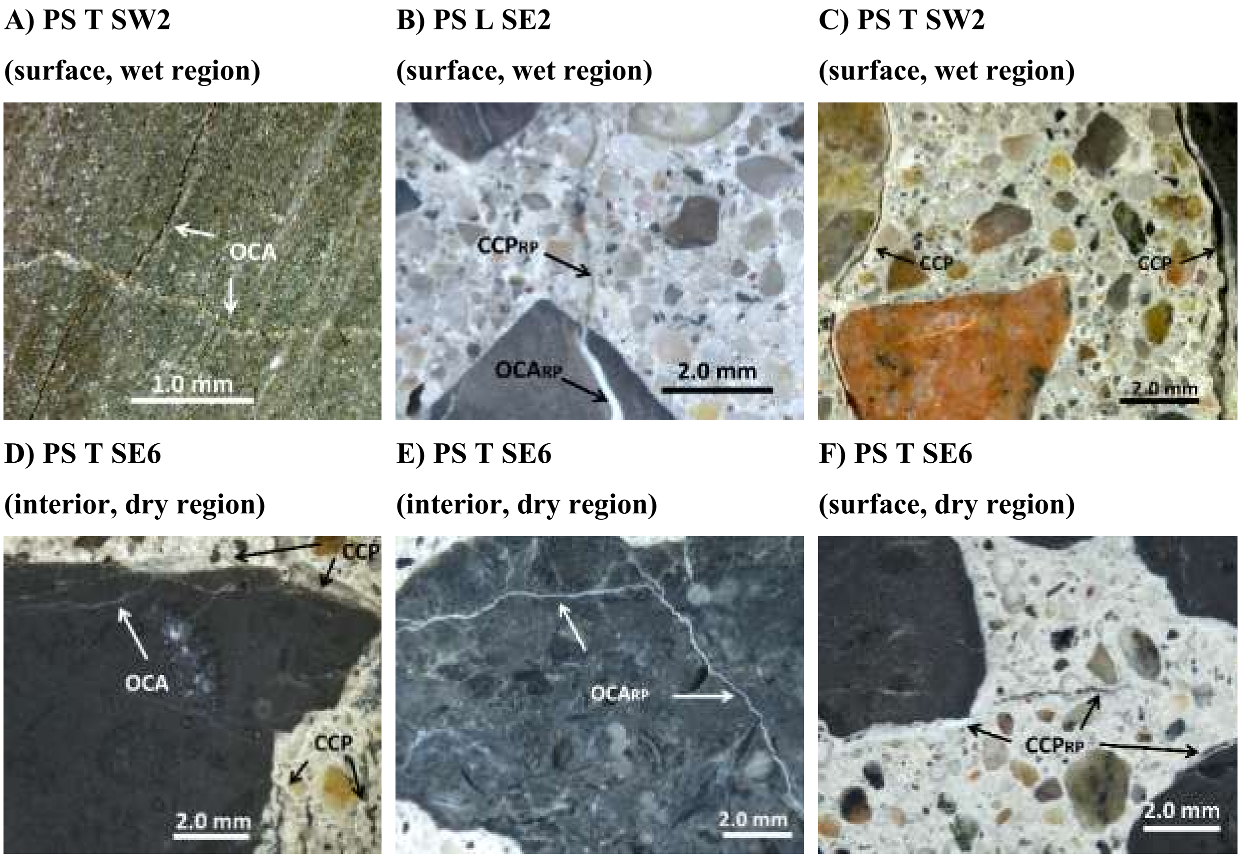

Figure 5-6 Stereoscope images of select damage features observed on PS DRI specimens

Mixed reaction products were observed in PS specimens (e.g., PS_L_SE2), including both whitish ASR and brownish corrosion products distributed throughout the aggregates and cement paste. Square 1 in Figure 5-7 highlights the interaction between these two products. The corrosion products exhibit varied colouration and textures. In Square 2 of Figure 5-7, the corrosion products are observed in the aggregate particles (section 2a) and cement paste (section 2b), mixing with ASR whitish products, which are more prevalent in the specimen.

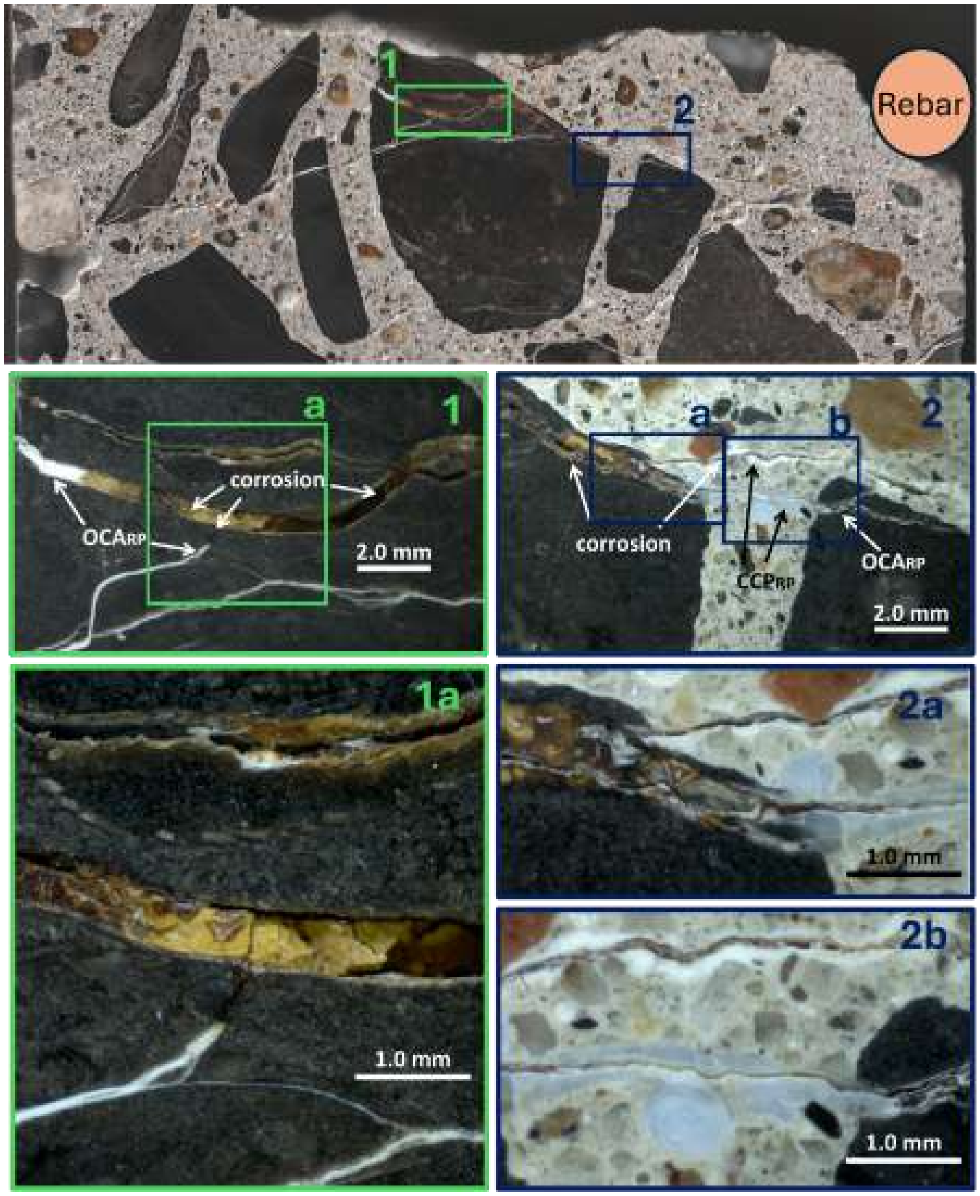

Figure 5-7 Stereomicroscope images of reaction products incorporating white gel and corrosion products (specimen PS_L_SE2)

5.5.2 Semi-Quantitative Microscopic Assessment: DRI

Figure 5-8 presents the microscopic damage features and DRI numbers obtained on cores extracted from surface and interior locations of the PC and PS members from distinct coring locations. Analysing the plots, all specimens presented a roughly similar number of closed cracks within the aggregate particles (CCA) regardless of the condition of the specimen. This is expected since CCA is normally related to the aggregates manufacturing (i.e., crushing, sieving, and cleaning) and weathering and thus not directly associated to ASR-induced development. Otherwise, the number of existing open cracks within the aggregate particles, without and with gel (OCA and OCA_{RP}) indicates the development of ASR-induced deterioration, as do the open cracks in the cement paste without or with secondary products (CCP and CCP_{RP}). The next sections will discuss in detail the results obtained specifically for the PC and PS.

5.5.2.1 Pier Cap (PC)

PC specimens from the surface (i.e., first 20 cm) and internal (i.e., from 20-to-150 cm) sections were evaluated. Analyzing the results, one observes that surface specimens displayed a higher degree of damage than internal samples, with DRI numbers ranging from 1002 to 1133 in the surface and 821 to 1018 internally. Moreover, it is not clear the influence of the direction (i.e., transverse, vertical, and longitudinal) on the induced deterioration, since transverse samples displayed similar damage at both surface and internal locations while vertical specimens exhibited a reduction in damage in internal specimens. Furthermore, the microscopic damage features from the surface and internal sections, and from the three distinct directions evaluated do not seem to significantly change. In all PC specimens, cracks in the aggregate particles and in the cement paste (i.e., with and without secondary products) seem to be the most prominent features, which highlights the presence of ASR at a high-level degree in all specimens as per Sanchez et al [7, 8].

5.5.2.2 Pier Shaft (PS)

PS specimens from both the surface (i.e., the first 20 cm) and internal sections (i.e., from 20 to 290 cm) were evaluated. Analysis of the results indicates that, similar to the PC specimens, surface samples exhibited a higher degree of damage on average compared to internal ones, with DRI values ranging from 773 to 1223 at the surface and 759 to 993 internally. Moreover, surface specimens exposed to dry conditions showed greater deterioration than those from wet environments. The influence of orientation (i.e., transverse, vertical, and longitudinal) on deterioration remains unclear. While internal vertical (V) samples appear to have slightly lower DRI values than those in the other two directions, the differences are minimal, and all orientations reflect a high level of deterioration. Finally, as with the PC specimens, deterioration in the PS samples is primarily characterized by cracking within both the aggregate particles and the cement paste (with and without secondary products), highlighting the presence of ASR, as reported by Sanchez et al. [7, 8].

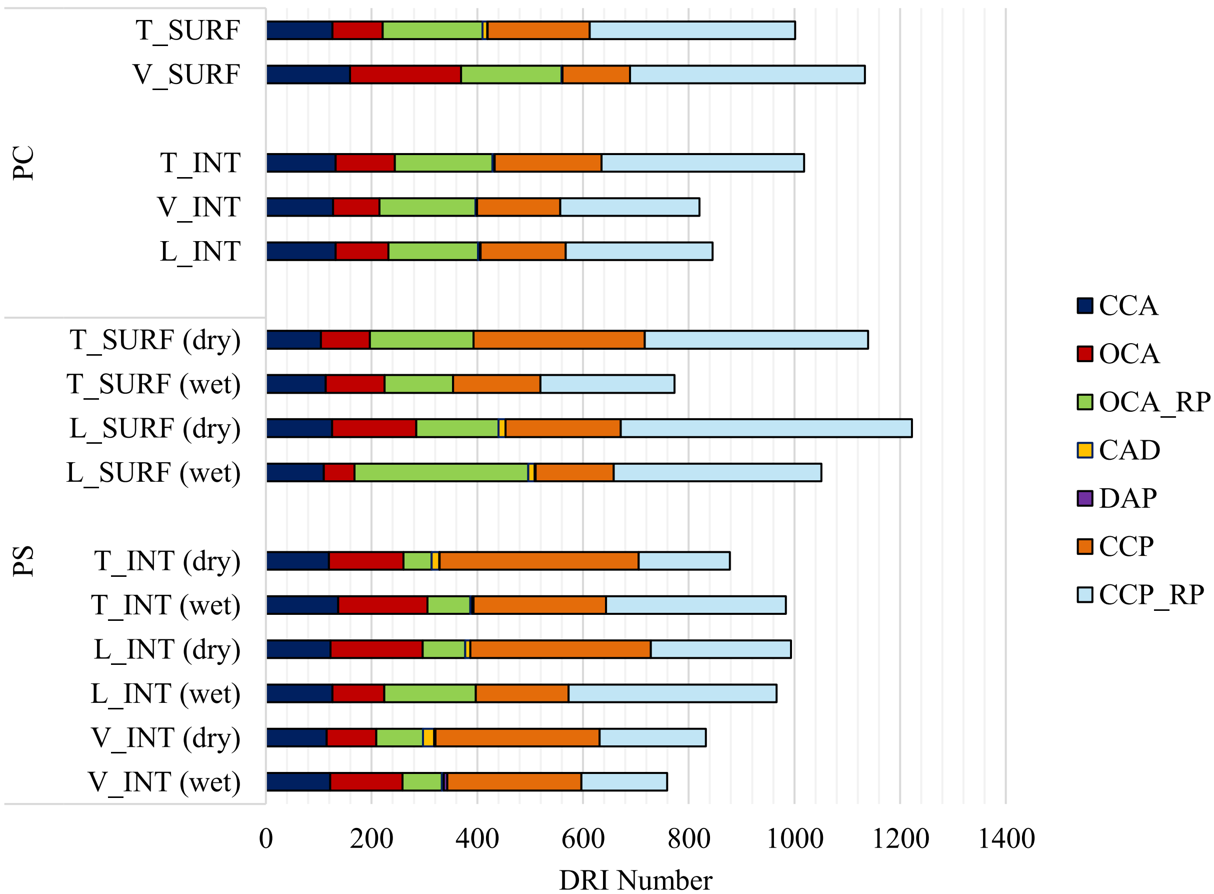

Figure 5-8 Bar graphs depicting DRI results from PC and PS members from distinct core orientations (transverse - T, vertical -V and longitudinal - L) and depths (surface - SURF vs. interior - INT)

5.5.3 Semi-Quantitative Microscopic Assessment: Extended DRI Microscopic Features

Figure 5-9 presents the unweighted percentage distribution of microscopic damage features, categorized as closed cracks in aggregate particles (CCA), open cracks in aggregate particles without and with reaction products (OCA and OCARP), and open cracks in cement paste without and with reaction products (CCP and CCPRP), for both PS and PC specimens. The data show that closed cracks in aggregate particles (CCA) are the most frequently observed damage feature, accounting for approximately 60% of the total. This is followed by open cracks in aggregate particles (OCA and OCARP) and in cement paste

(CCP and CCPRP), representing approximately 18% and 22%, respectively. When compared to the reference database proposed by Sanchez et al. [21], the distribution of microscopic features in both PC and PS specimens is consistent with deterioration patterns typically associated with ASR induced by reactive coarse aggregates. No significant differences were observed between the different members (i.e., PC and PS) or among the various conditions evaluated (i.e., orientation and environmental exposure).

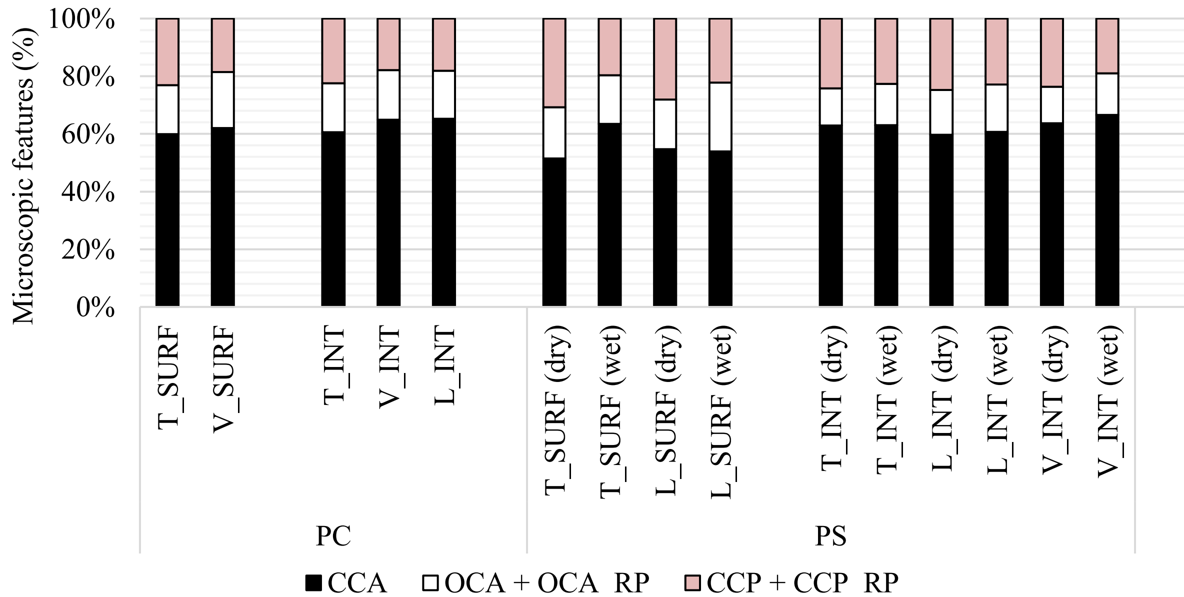

Figure 5-9 Bar graphs depicting microscopic features of deterioration without using the weighting factors normalized to 100 cm^2

5.5.4 Semi-Quantitative Microscopic Assessment: Extended DRI Crack Density

Figure 5-10 presents the unweighted crack densities (CD), expressed as the percentage of open cracks per cm^2, for both PC and PS specimens under the various evaluated conditions.

5.5.4.1 Pier Cap (PC)

CD of PC specimens from both surface and internal sections were evaluated. The results indicate that surface specimens exhibited higher crack densities compared to internal ones (on average), with CD values ranging from 3.4 to 3.9 at the surface and 2.8 to 3.4 internally. Similar to the DRI findings, the influence of orientation (i.e., transverse, vertical, and longitudinal) on CD is not clearly defined. Transverse specimens, for instance, showed lower crack densities at the surface but higher values in internal sections.

Overall, the CD values observed in all PC specimens can be considered high, consistent with the deterioration patterns associated with ASR as reported by Sanchez et al. [25].

5.5.4.2 Pier Shaft (PS)

CD of PS specimens from both the surface and internal sections were appraised. The analysis indicates that, similar to the PC specimens, surface samples exhibited higher crack densities on average compared to internal ones, with CD values ranging from 2.6 to 4.1 at the surface and 2.4 to 3.3 internally. Additionally, surface specimens exposed to dry conditions showed greater crack density than those from wet environments. The influence of orientation (i.e., transverse, vertical, and longitudinal) on CD remains unclear; while internal vertical (V) samples appear to have slightly lower CD values than those in the other two directions, the differences are not significant, and all orientations reflect a high level of cracking as per Sanchez et al [25].

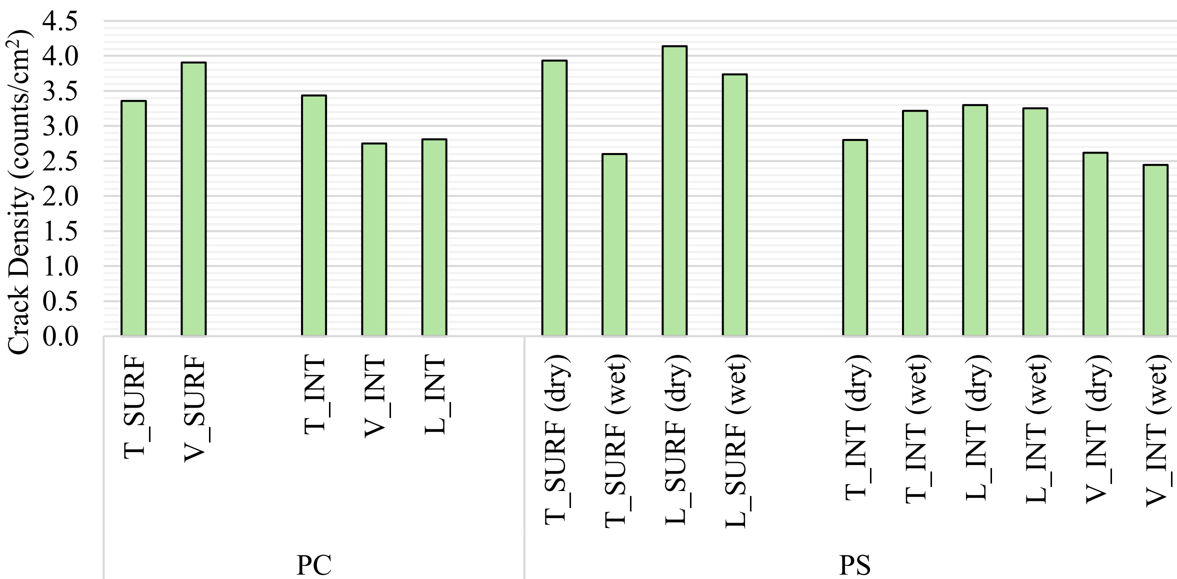

Figure 5-10 Bar graph depicting crack density (sum of opened cracks in the aggregate particles and in the cement paste, with and without reaction products over the surface examined, normalized to counts/cm^2)

5.5.5 Supplementary Qualitative Image Analysis: Crack Widths

Crack widths in the aggregate particles and cement paste were manually measured on selected specimens of the PC and PS. Figure 5-11 and Figure 5-12 illustrate the results obtained.

5.5.5.1 Pier Cap (PC)

No significant differences were observed for crack width measurements between the different conditions evaluated in the PC member. Median crack widths ranged from 0.10 to 0.20 mm in aggregate particles, while consistent median crack widths of 0.10 mm were observed in the cement paste for all PC specimens.

5.5.5.2 Pier Shaft (PS)

Surface specimens in the PS exhibited similar crack widths in aggregate particles but greater crack widths in the cement paste compared to interior specimens. Moreover, greater crack widths in the cement paste were exhibited for specimens from the dry region compared to the wet region for respective core depths. Similar to the PC, median crack widths ranged from 0.10 to 0.20 mm in aggregate particles. In contrast, median crack widths in the cement paste ranged from 0.10 mm to 0.20 mm, exhibiting significantly greater upper quartile values up to 0.80 mm.

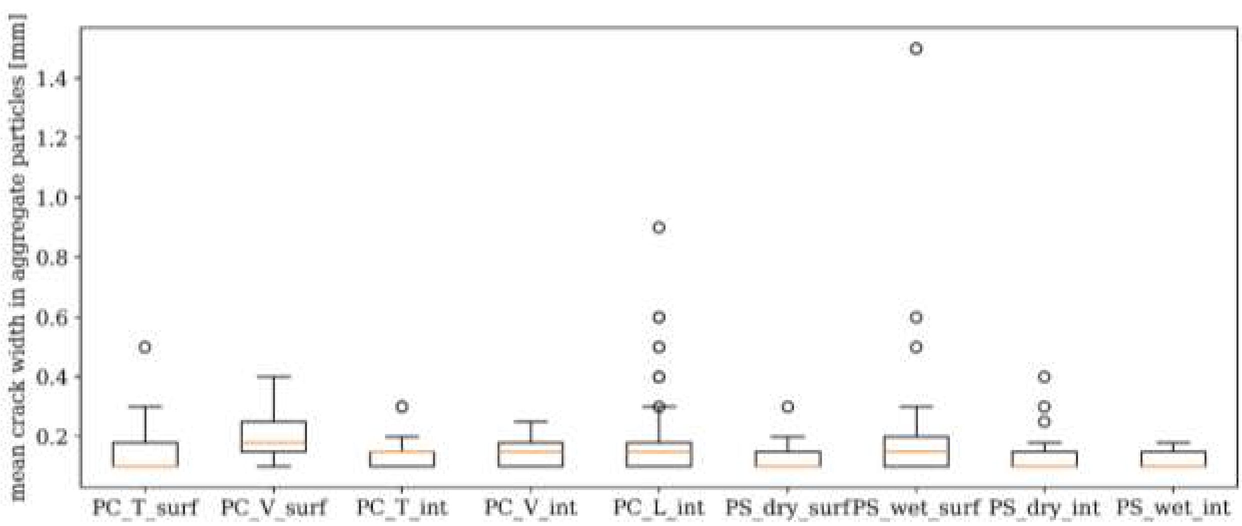

Figure 5-11 Box plots depicting measured crack widths in aggregate for cracks in PC and PS cores from surface and interior locations of cores extracted transversally (T), longitudinally (L) or

vertically (V) with distinction made between dry and wet locations in the PS. Circles indicate outlier values.

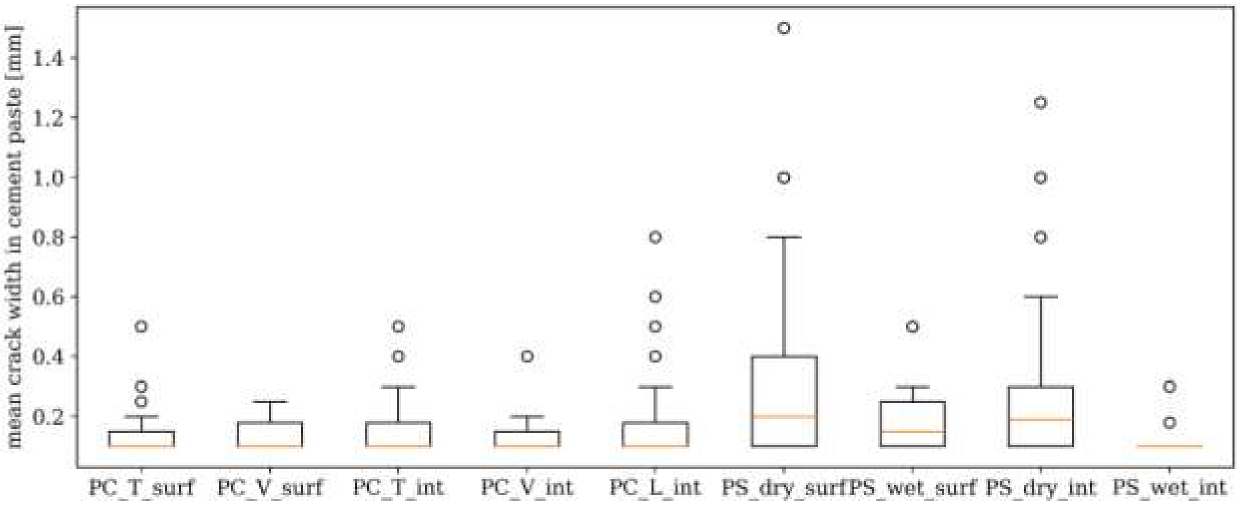

Figure 5-12 Box plots depicting measured crack widths in cement paste for cracks in PC and PS cores from surface and interior locations of cores extracted transversally (T), longitudinally (L) or vertically (V) with distinction made between dry and wet locations in the PS. Circles indicate outlier values.

5.5.6 Supplementary Qualitative Image Analysis: Crack Patterns

Supplementary image analysis was conducted to better understand the crack patterns and potential predominant orientations of cracks observed in the PC and PS members. For this purpose, cracks identified within both the aggregate particles and the cement paste were manually traced, as illustrated in Figure 5-13, for surface core specimens from the PS and PC. In these figures, the left-hand images display all visible cracks, while the right-hand images highlight only those with widths greater or equal to 0.10 mm. Upon examining the images, it becomes evident that the overall crack orientations are predominantly oriented parallel to the surface (i.e. cross-sectionally within the core) in surface specimens—a trend that is even more pronounced when focusing solely on the wider cracks.

5.5.6.1 Pier Cap (PC)

PC specimens present crack widths of 0.10 mm or greater primarily in the aggregate particles. Transverse core specimens exhibit cracks oriented parallel to the surface (i.e. widthwise in the core) while longitudinal and vertical core specimens exhibit cracks oriented lengthwise in the core, as shown in Figure 5-14. Surface vertical and transverse core specimens present the same crack orientation, oriented parallel to the surface. Internal vertical and longitudinal core specimens exhibited cracking oriented predominantly lengthwise in the cores, however, transverse core specimens exhibit cracks oriented vertically cracks (i.e. lengthwise within the cores).

5.5.6.2 Pier Shaft (PS)

In contrast to the PC, PS specimens present cracks with widths of 0.10 mm or greater primarily in the cement paste. Similar to the PC, transverse core specimens exhibit horizontally oriented cracks (i.e. widthwise within the core) while vertical core specimens exhibit vertically (i.e. lengthwise within the core) crack orientations (Figure 5-14). Unlike the PC, longitudinal cores specimens (i.e., extracted at a 45° angle from transverse cores) exhibited approximately horizontal crack patterns. Surface cores presented cracks displayed horizontally for both the longitudinal and transverse specimens.

A) PC vertical specimen (surface) – all traced cracks

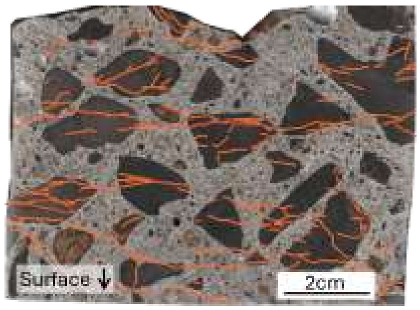

B) PC vertical specimen (surface) – cracks ≥ 0.10mm traced

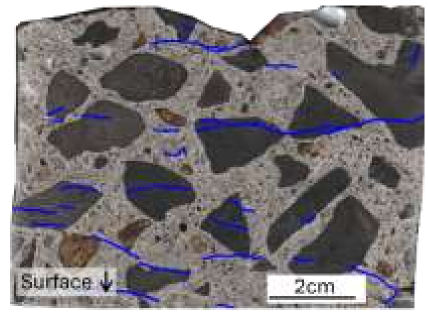

C) PS transverse specimen (surface) – all cracks traced

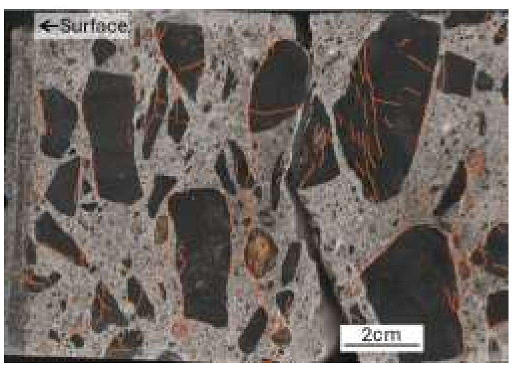

D) PS transverse specimen (surface) – cracks ≥ 0.10mm traced

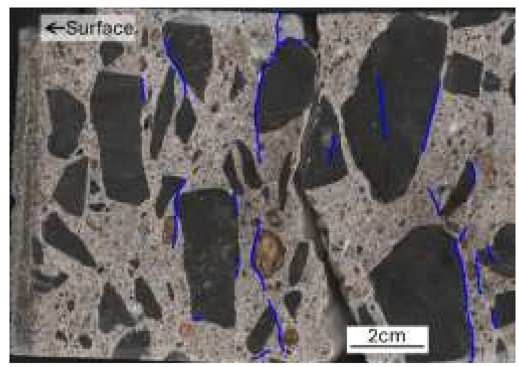

Figure 5-13 Images depicting traced cracks in surface specimens from the PC (A and B), and PS (C and D): all cracks traced (left), and cracks with widths ≥ 0.10 mm (right).

A) PC vertical specimen (internal)

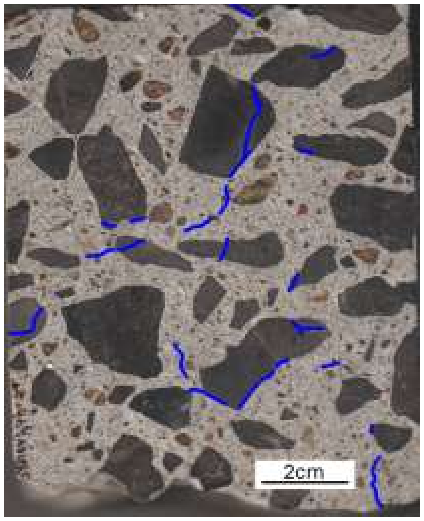

B) PC longitudinal specimen (internal)

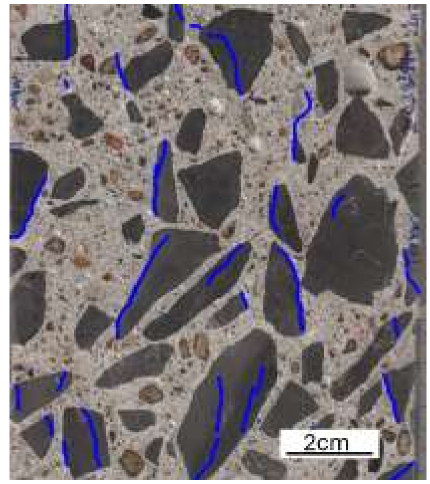

C) PS longitudinal specimen (internal)

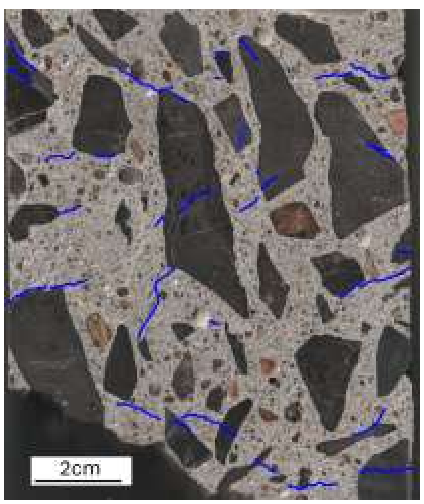

D) PS transverse specimen (internal)

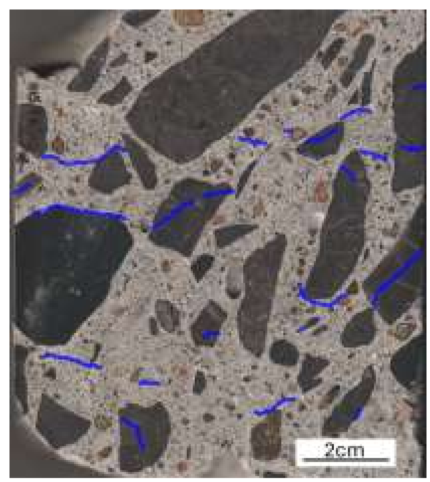

Figure 5-14 Images depicting cracks with widths ≥ 0.10 mm traced in affected internal specimens from the PC (A and B), and PS (C and D).

5.6 Discussion

5.6.1 Estimated Cause and Qualitative Discussion

The microscopic evaluation of induced damage in concrete by Sanchez et al. [7, 8, 21, 25, 26], which investigated a range of concrete strengths (i.e., 25, 35 and 45 MPa), aggregate types (i.e., fine vs. coarse) and natures (i.e., ≠ lithotypes), and deterioration mechanisms (i.e., ASR, FT, DEF), has provided a range of values (e.g. Table 5-1) to support identification of the cause(s) and extent of damage in concrete.

Results of this work, specifically the DRI and extended DRI (i.e., percentage of microscopic features and crack density) obtained from the broad range of core specimens investigated, indicated that ASR-induced damage from the coarse aggregate in the PS and PC members is the primary cause of deterioration. Reaction products observed in aggregates and cement paste cracks were compatible with ASR secondary products features, as previously identified in [25–27]. This conclusion is consistent with the findings from the earlier condition assessment of CB conducted in 1995 [2].

The development of ASR in field structures has been found to differ between members with distinct geometries or within the same member due to micro-environments. Factors such as moisture, temperature and restraint have been found to contribute to the development, or reduced development of ASR [32]. In the PC, core orientations (i.e., transverse, longitudinal, and vertical) and the depth of specimens (i.e., surface vs. interior) additionally represented variable restraint conditions due to the variation between high reinforcement at the top of the member and minimal reinforcement in the middle. Although moisture was a concern for both members, its source differed between the PC and PS. In the PC, inadequate drainage on the CB road surface led to water infiltration through expansion joints [16], which may have contributed to increased damage in the surface specimens.

In the PS, distinct moisture conditions were present, such as dry and semi-submerged regions. The distinction between 'dry' and 'wet' service conditions was defined to reflect discolouration observed on the member [5]. However, despite additional available moisture, polished specimens from the PS presented less reaction products (i.e., ASR gel) and a higher percentage of cracks in the cement paste compared to the PC, especially in interior locations, which could be caused due to leaching experienced in the field. Additionally, ASR reaction products may have been lost during sample preparation, reiterating the value of using the same weighting factors for damage features without and with gel (i.e., OCA and OCA_{RP}; CCP and CCP_{RP})

Secondary damage mechanisms were expected in the CB due to the harsh service environment experienced by both members. Although the PC was exposed to frequent moisture and temperature variations, the encapsulation repair in 2004 where existing concrete cover was entirely removed and replaced, severely limited evidence of secondary damage mechanisms. By contrast, the PS exhibited signs of significant deterioration in surface cores, reflecting findings from visual inspections of the members where a plane of delamination due to reinforcement corrosion was previously identified [5]. Evaluation of DRI damage features further indicated increased proportions of open cracks in the cement paste (i.e. CCP and CCP_{RP}) for both transverse and longitudinal core specimens from the dry surface region. The presence of both the damage features observed and greater DRI numbers compared to specimens in wet regions (i.e. ASR only) suggests a coupled mechanism of ASR & FT as per [21]. This also agrees with the literature for submerged concrete members, where the submerged portion is not (or less) affected by FT damage due to the more stable temperature [18, 20].

Besides ASR and FT damage, some CB members also exhibited signs of reinforcement steel corrosion. Microscopic evaluations conducted in this study revealed interactions between reaction products from these mechanisms (i.e., corrosion and ASR), as shown in Figure 5-7. However, the extent to which this interaction contributes to the overall degree of damage remains unknown.

5.6.2 Estimated ASR-Induced Damage Extent and Associated Expansion

Core specimens from both the PC and PS exhibited high to extremely high levels of damage, as determined through microscopic analysis—specifically based on DRI values and crack density (CD) in accordance with the criteria outlined in [7, 8, 25]. This level of ASR-induced damage indicates significant reductions in mechanical properties of the affected concrete.

According to Sanchez et al [7, 8, 15, 19, 20], the extent of ASR-induced damage is associated with the induced expansion of the affected concrete. The chart proposed by the authors [7, 8, 15, 19, 20] and mentioned in the previous section, can be used to estimate the associated free expansion (i.e., expansion under unrestrained conditions) corresponding to the microscopic damage features observed and quantified through the DRI. Data from the literature presenting DRI results from ASR-affected concrete displaying distinct mechanical properties (i.e., 25 and 35 MPa compressive strength at 28 days), and incorporating a reactive siliceous limestone (i.e., QC + Lav) similar to the aggregate used in the CB are presented in Figure 5-15 as per [8].

The results obtained in this work were extrapolated from the QC + Lav curves in Figure 5-15, so that their associated free expansion could be obtained. Figure 5-15 illustrates the free expansion results obtained for each of the core specimens evaluated.

The results demonstrate that the induced expansion levels of CB members ranged from 0.20% to 0.38%, where the DRI results from surface specimens in both the PC and PS correspond to higher expansion levels (0.21% to 0.38%), while internal specimens correspond to slightly lower expansion levels (0.21% to 0.31%).

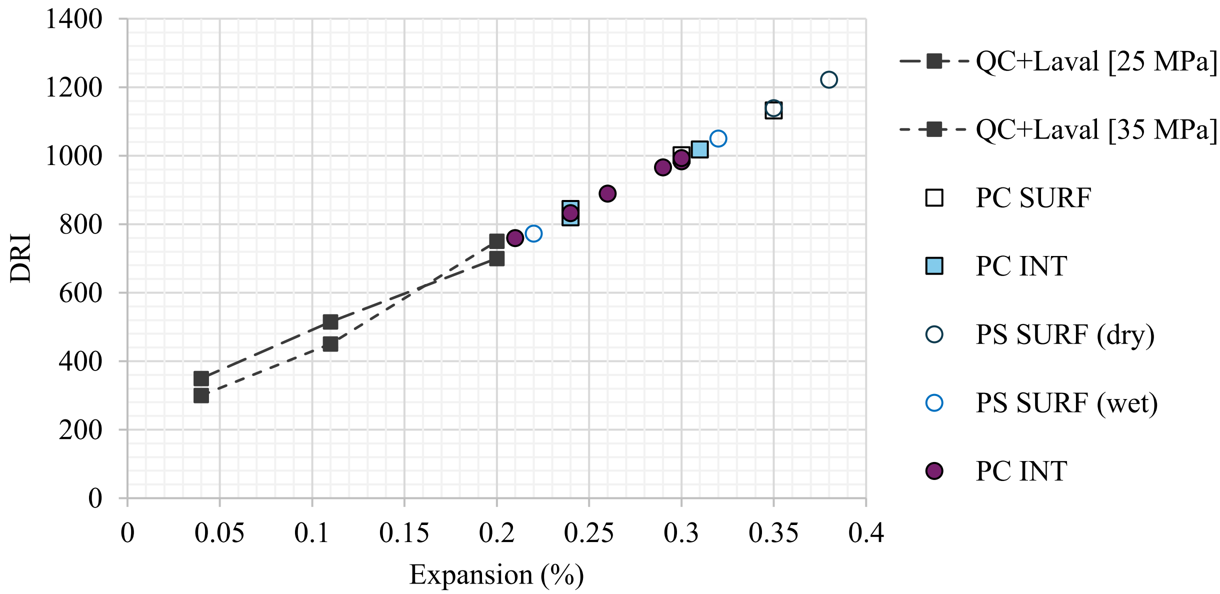

Figure 5-15 Plot depicting the comparison of experimental results to ASR-induced expansion for reactive coarse aggregates from the literature (QC+Laval investigated by Sanchez et al. 2017 [8]**)**

The associated free expansions for different depths were estimated based on DRI results obtained from each of the numerous core samples extracted at various depths and conditions (i.e., vertical versus transverse, dry versus wet) (Figure 5-16). This demonstrates variation in estimated expansion both between surface (i.e. the first 20 cm from the external surface in the PS or the first 20 cm from the repair concrete in the PC) and internal concrete and between internal regions. Notably, in the dry specimens from the PS the estimated expansion decreases from 0.37% to 0.23% between the surface and interior with a subsequent increase in expansion at greater depths (i.e., > 60 cm). In the near surface region (i.e. 20 cm to 60 cm) moisture transport and confinement conditions are expected to differ compared to other regions (i.e. surface and center of the members). In contrast, damage identified in surface specimens is expected to include contributions from damage mechanisms such as reinforcement corrosion and FT as well as cracking caused by the relaxation of tension at the surface of concrete due to lower confinement at the surface of the member [33].

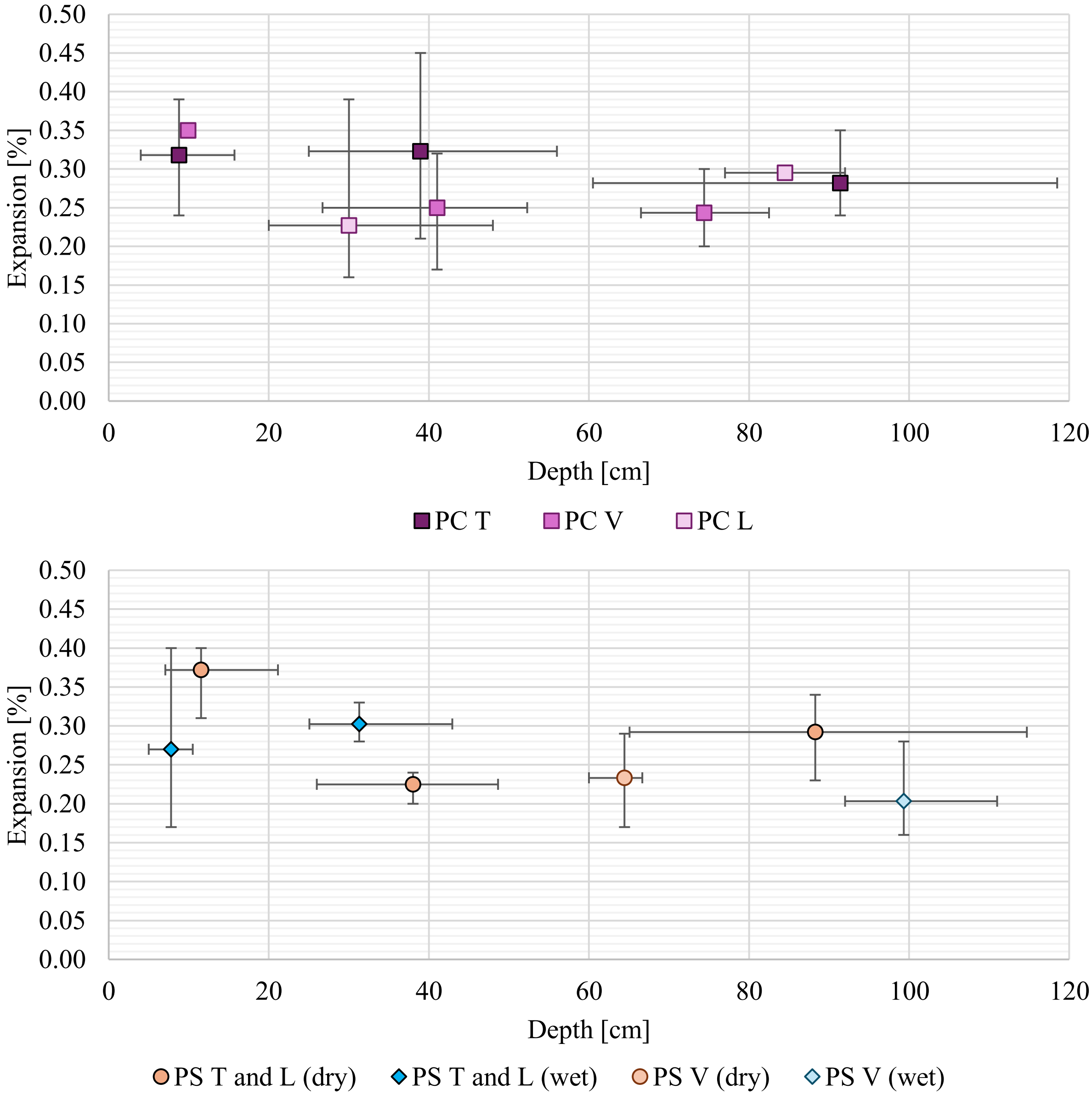

Figure 5-16 Plot depicting free expansion estimated for DRI results for the PC (top) and PS (bottom) using experimental data for mixes incorporating ASR reactive QC limestone from Sanchez et al. 2017 [8]**. Specimen depth is defined as the depth at the center of the specimen. Error bars indicate maximum and minimum values.**

To summarize all the data evaluated in this work (i.e., DRI numbers, main crack orientation, damage level, and estimated induced expansion), Table 5-2 is presented. Estimated crack orientations within cores are further expanded on in Figure 5-17 and Figure 5-18.

Table 5-2 Summary of experimental microscopic test results and corresponding estimated damage level and approximate free-expansion level as per Sanchez et al. 2017

	Depth	Core orientation	DRI	Crack orientation†	Damage level [8]	Approximate expansion [%] [8]
PC	**Surface**	**Transverse**	1002	Horizontal	Very high	0.30
		Vertical	1133	Horizontal	Very high	0.35
	Interior	**Transverse**	1018	Horizontal	Very high	0.31
		Longitudinal	845	Vertical	High	0.24
		Vertical	821	Vertical	High	0.24
PS	**Surface**	**Transverse - dry**	1139	Horizontal	Very High	0.35
		Transverse - wet	773	Horizontal	Very High	0.32
		Longitudinal - dry	1223	Horizontal	Very High	0.38
		Longitudinal - wet	1050	Horizontal	High	0.22
	Interior	**Transverse - dry**	878	Horizontal	High to very high	0.26
		Transverse - wet	984	Horizontal	Very High	0.30
		Longitudinal - dry	993	Horizontal	Very High	0.30
		Longitudinal - wet	966	Vertical	Very High	0.29
		Vertical - dry	833	Vertical	High	0.24
		Vertical - wet	759	Vertical	High	0.21

† Horizontal cracking generally indicates cracking oriented lengthwise in the core while vertical cracking generally indicates cracking oriented widthwise in the cire

5.6.3 Anisotropic Effects

Cracking in reinforced concrete is a complex, three-dimensional phenomenon influenced by numerous factors. In field structures, in-service loading and local restraints—such as confinement and reinforcement—are likely the most critical in determining resulting crack patterns. In concrete affected by internal swelling reactions such as ASR, unrestrained conditions typically result in isotropic, three-dimensional expansion, leading to a random cracking pattern. Conversely, when restraints are present—such as reinforcement or adjacent structural elements—anisotropic behavior often develops. This is characterized by directional expansion and deterioration, typically observed as greater expansion along orientations with lower confinement and cracking patterns aligned parallel to the direction of least restraint [10–15]. The analyses conducted in this study provide clear evidence of anisotropic effects in ASR-induced deterioration observed in the CB members, as detailed below.

5.6.3.1 Pier Cap (PC)

In the PC, cracks in cores from the middle region of the member were observed to be oriented vertically within the member (i.e., yellow cracking pattern highlighted in Figure 5-17). This results in the horizontal (i.e. widthwise) cracks presented in transverse cores and the vertical (i.e. lengthwise) cracks observed in vertical and longitudinal core orientations.

5.6.3.2 Pier Shaft (PS)

In the PS, cracks within the member, are seen to be oriented alongside the members' geometry (i.e., parallel to the member's main sides - yellow cracking pattern highlighted in Figure 5-18). This results in horizontal (i.e. widthwise) cracks in transverse and longitudinal cores, and the vertical (i.e. lengthwise) cracks observed in vertical core specimens.

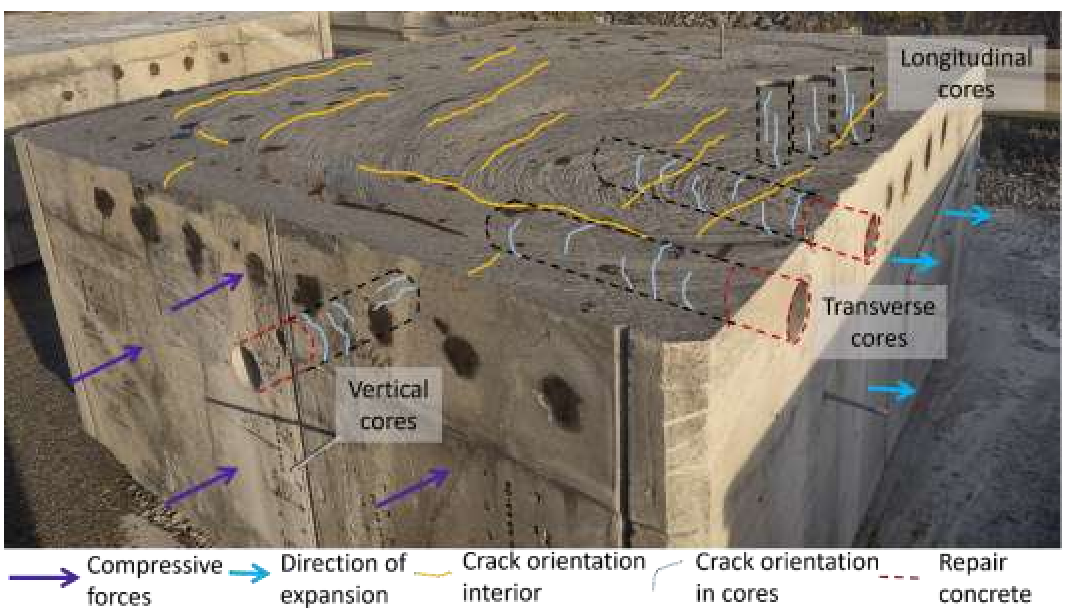

Figure 5-17 Annotated image depicting an example of dominant crack orientations in PC segments

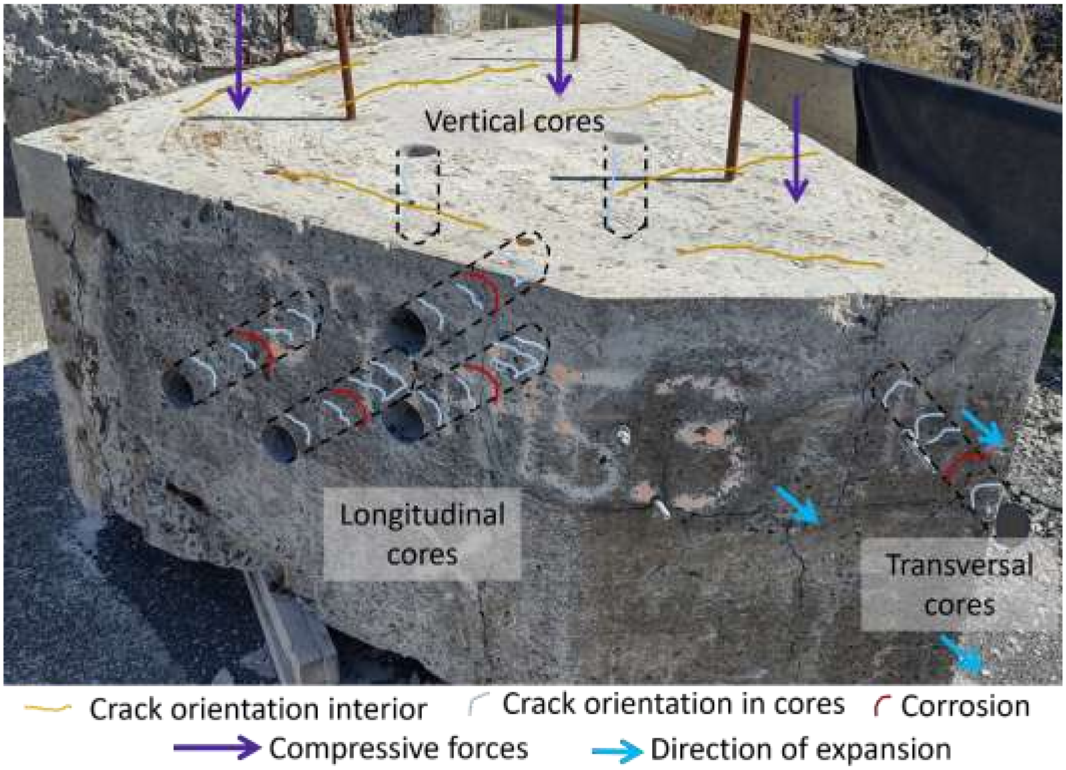

Figure 5-18 Annotated image depicting an example of dominant crack orientations in PS segments

5.6.4 Statistical Analysis

In order to assess the validity and significance of the DRI results obtained in this study, T-test and analyses of variance (ANOVA) were performed, taking into account the different members (i.e., PC vs. PS), depths (i.e., surface vs. internal), core orientations (i.e., transverse, longitudinal and vertical) and environments (i.e., wet vs. dry). All statistical analyses were conducted with a significance level of 5% (i.e., confidence interval of 95%).

First, a T-test was conducted to evaluate differences between DRI results for the PC and PS members, as well as differences between 1) specimens from surface and internal locations in each member, and 2) wet and dry locations in the PS (Table 5-3). The T-test indicated no difference between mean values for specimens from the PC and PS since the 't value' was less than the critical t value (t_{crit}), and the p-value was greater than 0.05. Moreover, the T-test results indicated no difference between surface and internal specimens in the PC and between wet and dry regions of the PS; however, when surface and internal specimens in the PS were compared the differences were found significant, since the ‘t’ value was found to be lower than the t_{crit}, while the p-value was found to be greater than 0.05.

Further statistical assessment was conducted using Levene’s test to determine whether the observed differences in sample variances could be attributed to random sampling from populations with equal variance. The test yielded a p-value below 0.05 for the PS specimens from surface and interior locations, indicating that the variances between these groups were significantly different. To account for this variance inequality, Welch’s t-test was subsequently applied (Table 5-5), as it does not assume equal variances between populations. The results showed no statistically significant difference between the means of the two groups.

Table 5-3 Statistical analysis of DRI results using the T-test for difference in mean values between PC and PS members for α = 0.05

	t	t_{crit}	$t>t_{critic}$	P-value	α	P< α	Levene p-value
PC vs. PS	0.89	1.65	-	0.37	0.05	-	0.739
PC surf vs. int	0.91	1.65	-	0.36	0.05	-	0.813
PS surf vs. int	1.89	1.71	X	0.07	0.05	-	0.047
PS wet vs. dry	0.51	1.71	-	0.62	0.05	-	0.996

One-variable ANOVA was then used to evaluate the significance of the DRI results as a function of different coring orientations (Table 5-4) for internal specimens from the transverse, longitudinal and vertical core orientations. Since longitudinal cores in the PC and vertical cores in the PS do not have specimens from surface locations, only results from internal specimens were considered. Results indicate the differences in core orientation are significant when all internal core specimens are considered since the “F value” is greater than the critical F value “F_{crit}”, and the “p-value” is less than 0.05. Complementary analysis using Welch’s T-test (Table 5-5) identified that such significance comes from the difference between transverse and vertical specimens in the two members. However, when the differences in core orientations are considered only for the PC or PS, the differences between core orientations were not found to be significant, indicating that the means of DRI values for transverse, longitudinal and vertical cores are not significantly different. This agrees with the findings that a similar level of damage was present in both members.

Table 5-4 Statistical Analysis of DRI results using One-way ANOVA for core orientation (i.e. transverse, longitudinal or vertical) in PC and PS members

	F	F_{crit}	$F>F_{critic}$	P-value	α	P< α
PC and PS	**3.54**	**3.18**	**X**	**0.04**	**0.05**	**X**
PC only	2.62	3.32	-	0.09	0.05	-
PS only	2.50	3.50	-	0.11	0.05	-

Due to the findings of Levene's test, which indicated that in some data the samples did not represent populations with the same variance, further assessment of results was conducted using Welch's T-test (Table 5-5) to complement findings from the T-test and ANOVA results. Using this test, transverse and vertical cores were found to have statistically significant differences in the mean values when comparing DRI results for these two orientations for samples from both members.

Table 5-5 Statistical analysis of DRI results using Welch's T-test (two tailed, $\alpha = 0.05$)

	Factor	Var_1/Var_2	t	t_{crit}	$t > t_{critic}$	P-value	$P < \alpha$	df
All data	***Depth (Surf vs. Int)***	1.42	1.59	2.15	-	0.13	-	15
All data	***Member (PC vs. PS)***	1.08	0.90	2.00	-	0.37	-	57
Int	***Orientation (T vs. V)***	**1.35**	**2.76**	**2.06**	**X**	**0.01**	**X**	**25**
Int	***Orientation (L vs. V)***	1.14	1.70	2.06	-	0.10	-	24
Int	***Orientation (T vs. L)***	1.18	0.90	2.05	-	0.38	-	28
Pier cap								
Surf & int	***Surf vs. int***	0.77	0.94	2.02	-	0.39	-	5
Surf & int	***Orientation (T vs. V)***	1.05	1.60	2.20	-	0.14	-	11
Int	***Orientation (L vs. V)***	1.31	0.65	2.18	-	0.53	-	12
Int	***Orientation (T vs. V)***	1.43	2.16	2.23	-	0.06	-	10
Int	***Orientation (T vs. L)***	1.09	1.62	2.09	-	0.12	-	20
Pier shaft								
Surf & int	***Surf vs. int***	2.76	1.45	1.90	-	0.19	-	7
Surf & int	***Orientation (T vs. L)***	1.03	-1.50	2.18	-	0.16	-	12
Int	***Orientation (L vs. V)***	0.45	2.27	2.20	-	0.05	-	8
Int	***Orientation (T vs. V)***	0.80	1.46	2.26	-	0.18	-	9
Int	***Orientation (T vs. L)***	1.77	-1.14	2.37	-	0.29	-	7

5.7 Conclusions

This work investigated microscopic damage in cores extracted from a pier cap (PC) and pier shaft (PS) from the Champlain bridge (1962-2019), a large over-water bridge in Montreal, Quebec. The two members were found to have distinct service conditions and geometries, which impacted damage observed in the concrete cores. The PC had additionally undergone an encapsulation repair.

- Microscopic analyses using the DRI and extended DRI versions (% microscopic features, crack density) identified that the primary deterioration mechanism affecting both the PC and PS members is ASR, corresponding to a high deterioration level of damage (i.e. free expansion of 0.20% or greater).

- Observations of polished specimens from both the PC and PS identified ASR products displaying distinct appearances (i.e., distinct colours and morphologies). Moreover, corrosion products were also observed in the surface specimens from both members. The interaction between ASR and corrosion products is mostly unknown.
- Surface core specimens presented higher DRI numbers (1002 to 1133 for the PC, 773 to 1223 for the PS) compared to internal core specimens (821 to 1018 in the PC, 759 to 993 for the PS), indicating higher levels of deterioration. Differences in observed damage features between surface and interior cores, including a higher contribution of CCP and CCP_RP evident for PS surface cores, suggests damage from mechanisms such as FT and reinforcement corrosion may contribute to the different deterioration levels in surface specimens
- Surface core specimens in the PS exhibited higher DRI values in the dry regions compared to the semi-submerged exposure conditions. The amount of cracks observed in the cement paste and the cracking pattern found in the dry region specimens of PS indicate the presence of ASR coupled with FT. This agrees with expected absence of damage in concrete at or below the waterline since the concrete is fully saturated and the river does not fully freeze in winter months.
- Crack widths ≥ 0.10 mm were measured for select samples from PC and PS members. Evaluation of the location of these cracks within DRI core specimens provided additional insights into the dominant crack orientation (i.e., cracks exhibited a larger width in the direction of lowest restraint) and indicated the presence of anisotropic properties. In contrast, evaluation of all cracks observed at 16x magnification, as used for DRI, exhibited indistinct crack orientations.

5.8 References

1. Carlin GP (2017) The Existing Champlain Bridge - Overview of Issues – The Owner's Perspective. In: 39th IABSE Symposium – Engineering the Future. Vancouver, pp 1505–1512

2. Bérubé M-A, Frenette J (1995) Évaluation de la Réactivité Alcaline dans le Béton des Piles 12, 18 et 20 W du Pont Champlain: Complément au rapport soumis en février 1994. Sainte-Foy, Quebec

3. Groupe counseil Genivar (2003) Champlain Bridge, Rehabilitation of Piers, Pier Caps, Bearings and Beams (2004) Phases of Demolition.

4. Aecom Tecsult Inc. (2008) Rapport 1879 Pont Champlain, services de consultant, Étude, dessins et devis pour la réfection de piles et de poutres précontraintes (2007-2011).

5. Kristufek L, Sanchez LF, Martín-Pérez B, Noël M (2025) Visual and non-destructive testing of pier cap and pier shaft members from the old Champlain Bridge. Buildings 15:3262

6. Bérubé, Smaoui N, Bissonnette B, Fournier B (2005) Outil d'évaluation et de gestion des ouvrages d'art affectés de réactions alcalis-silice (RAS). Québec, Canada

7. Sanchez LFM, Drimalas T, Fournier B, Mitchell D, Bastien J (2018) Comprehensive damage assessment in concrete affected by different internal swelling reaction (ISR) mechanisms. Cem Concr Res 107:284–303

8. Sanchez LFM, Fournier B, Jolin M, Mitchell D, Bastien J (2017) Overall assessment of Alkali-Aggregate Reaction (AAR) in concretes presenting different strengths and incorporating a wide range of reactive aggregate types and natures. Cem Concr Res 93:17–31

9. Leemann A, Shi Z, Lindgård J (2020) Characterization of amorphous and crystalline ASR products formed in concrete aggregates. Cem Concr Res. https://doi.org/10.1016/j.cemconres.2020.106190

10. Berra M, Faggiani G, Mangialardi T, Paolini AE (2010) Influence of stress restraint on the expansive behaviour of concrete affected by alkali-silica reaction. Cem Concr Res 40:1403–1409

11. Gautam BP, Panesar DK, Sheikh SA, Vecchio FJ (2017) Effect of multiaxial stresses on alkali-silica reaction damage of concrete. ACI Mater J 114:595–604

12. Zahedi A, Trottier C, Sanchez LFM, Noël M (2021) Microscopic assessment of ASR-affected concrete under confinement conditions. Cem Concr Res. https://doi.org/10.1016/j.cemconres.2021.106456

13. Multon S, Toutlemonde F (2006) Effect of applied stresses on alkali-silica reaction-induced expansions. Cem Concr Res 36:912–920

14. Fan S, Hanson JM (1999) Effect of Alkali Silica Reaction Expansion and Cracking on Structural Behavior of Reinforced Concrete Beams. ACI Mater J 488–495

15. Kongshaug SS, Oseland O, Kanstad T, Hendriks MAN, Rodum E, Markeset G (2020) Experimental investigation of ASR-affected concrete – The influence of uniaxial loading on the evolution of mechanical properties, expansion and damage indices. Constr Build Mater. https://doi.org/10.1016/j.conbuildmat.2020.118384

16. Carlin GP, Mirza MS, Gaudreault M (1996) Rehabilitation Measures for Champlain Bridge, Montreal, Canada. Canadian Journal of Civil Engineering 23:1326–1340

17. Office of the Auditor General of Canada (2018) Report 4—Replacing Montréal's Champlain Bridge—Infrastructure Canada.

18. Beyene M, Meininger R (2022) A case study of distress mechanism(s) in a concrete structure foundation in the saturated zone and above the saturated zone. J Microsc 286:114–119

19. Rosenqvist M (2016) Frost-induced deterioration of concrete in hydraulic structures Interactions between water absorption, leaching and frost action. Ph.D. Dissertation, Lund University

20. Rosenqvist M, Oxfall M, Fridh K, Hassanzadeh M (2015) A test method to assess the frost resistance of concrete at the waterline of hydraulic structures. Mater Struct 2403–2415

21. Sanchez LFM, Drimalas T, Fournier B (2020) Assessing condition of concrete affected by internal swelling reactions (ISR) through the Damage Rating Index (DRI). Cement 1–2:100001

22. Grattan-Bellew PE, Mitchell LD (2006) Quantitative petrographic analysis of concrete — The Damage Rating Index (DRI)method, a review. In: Marc-André Bérubé Symposium on AAR in Concrete, CANMET/ACI Advances in Concrete Technology Seminar. Montreal, Canada, pp 321–334

23. Grattan-Bellew PE, Danay A (1992) Comparison of laboratory and field evaluation of AAR in large dams. Proceedings of the International Conference on Concrete AAR in Hydroelectric Plants and Dams

24. Villeneuve V, Fournier B, Duchesne J (2012) Determination of the damage in concrete affected by ASR - the Damage Rating Index (DRI). In: 14th ICAAR International conference on the alkali aggregate reaction. p 033012

25. Sanchez LFM, Fournier B, Jolin M, Duchesne J (2015) Reliable quantification of AAR damage through assessment of the Damage Rating Index (DRI). Cem Concr Res 67:74–92

26. Sanchez LFM, Fournier B, Jolin M, Bedoya MAB, Bastien J, Duchesne J (2016) Use of Damage Rating Index to Quantify Alkali-Silica Reaction Damage in Concrete: Fine versus Coarse Aggregate. ACI Mater J 113:395–407

27. Véronique Villeneuve (2011) Détermination de l'endommagement du béton par méthode pétrographique quantitative.

28. Zahedi A, De Souza DJ, Zubaida N, Sanchez LFM (2023) Overall assessment of CFRP-wrapped concrete affected by alkali-silica reaction. Cem Concr Res. https://doi.org/10.1016/j.cemconres.2023.107165

29. Zahedi A, Saliba L, Sanchez LFM, Boyd AJ (2023), Reliability of the damage rating index to assess the condition of concrete affected by external sulfate attack. Magazine of Concrete Research, Vol. 75 No. 3 pp. 135–148, doi: https://doi.org/10.1680/jmacr.22.00061

30. Orcutt C, Cook WD, Mitchell D (2020) Response of Variable-Depth Reinforced Concrete Pier Cap Beams. Journal of Bridge Engineering. https://doi.org/10.1061/(ASCE)BE.1943-5592.0001548

31. Sanchez LFM, Fournier B, Jolin M, Bastien J (2014) Evaluation of the stiffness damage test (SDT) as a tool for assessing damage in concrete due to ASR: Test loading and output responses for concretes incorporating fine or coarse reactive aggregates. Cem Concr Res 56:213–229

32. Barbosa RA, Hansen SG, Hansen KK, Hoang LC, Grelk B, Maag I (2016) Assesment of Severely ASR Damaged Bridges: From Diagnosis to Structural Effects. Proceedings of the 15th international conference on alkali-aggregate reaction in concrete (15th ICAAR)

33. ACI Committee 221 (1998) State-of-the-Art Report on Alkali-Aggregate Reactivity Reported by ACI Committee 221.

Chapter 6: Paper 3

Mechanical investigation of the ASR-affected piers of Montreal's Champlain Bridge

Abstract

Montreal's Champlain Bridge (CB), a critical component of Canadian infrastructure, was decommissioned in 2019 after nearly six decades of service due to significant structural deterioration. The primary causes were alkali-silica reaction (ASR) and reinforcement corrosion, both of which severely compromised the long-term performance and durability of the structure. As part of a condition assessment program, concrete cores were extracted from the pier shafts (PS) and pier caps (PC) of CB under varying conditions, including three orientations (i.e., transverse, longitudinal, vertical), two depths (i.e., surface, interior), and different service environments (i.e., wet and dry in the PS). A multi-level evaluation protocol was implemented, combining non-destructive testing (i.e., resonance frequency), microscopic analysis (i.e., Damage Rating Index), and mechanical testing (i.e., Stiffness Damage Test, and compressive strength) to identify the cause(s) and extent of damage. This paper focuses on the results of the mechanical assessment with results revealing significant differences between the members appraised. PS cores exhibited a lower static modulus of elasticity (ME), averaging 8.5 GPa for internal cores, compared to 15.0 GPa for PC cores, indicating more advanced deterioration. Damage levels ranged from marginal to very high, with Stiffness Damage Index values between 0.16 and 0.40, depending on core location and service conditions. Mechanical performance was influenced by core depth, orientation, and environmental exposure. Finally, a strong correlation was found between crack orientation and mechanical response of affected specimens, suggesting that crack orientation is an important parameter for evaluation of core specimens.

6.1 Introduction

The Champlain Bridge (CB), constructed between 1957 and 1962, was a six-lane highway bridge spanning the St. Lawrence River and St. Lawrence Seaway in Montreal, Canada. By the early 2010s, increasing signs of deterioration across various structural components prompted the construction of a replacement bridge, with the original CB officially decommissioned in July 2019. The deterioration of the concrete was attributed to multiple mechanisms, primarily reinforcement corrosion due to de-icing salt exposure [1, 2], the presence of freeze-thaw cycles (FT) [1], and alkali-silica reaction (ASR) [3], associated to the use of a reactive siliceous limestone coarse aggregate. Following its decommissioning, several structural members of the CB were selected for research to evaluate and confirm the primary causes and extent of the observed damage. Among these, particular attention was given to the pier caps (PC) and pier shafts (PS), which exhibited the most pronounced signs of deterioration [3].

6.2 Background

6.2.1 Alkali-Silica Reaction (ASR) and Reinforced Concrete Field Structures

The CB was a 3.4 km highway bridge that spanned the St. Lawrence River and St. Lawrence Seaway between Montreal and Brossard in the Canadian province of Quebec. This unique bridge consisted of six lanes supported by an interconnected system of girders, infill slabs and diaphragms resting on 52 T-type piers using a 'hammerhead' PC design. Piers in the CB were constructed using a reactive silicious limestone coarse aggregate, which has since been linked to ASR in the province of Quebec [2]. ASR was previously identified in cores extracted from several piers of the CB in the 1990's [3]. The PC evaluated in this work, removed from pier 42W (Figure 6-1), was the final on-land pier in the approach portion of the bridge, with the west face adjacent to René Lévesque Boulevard. The PS section was obtained from pier 38W (Figure 6-1), with the investigated section of the pier removed from the water level such that it presents both dry and semi-submerged regions.

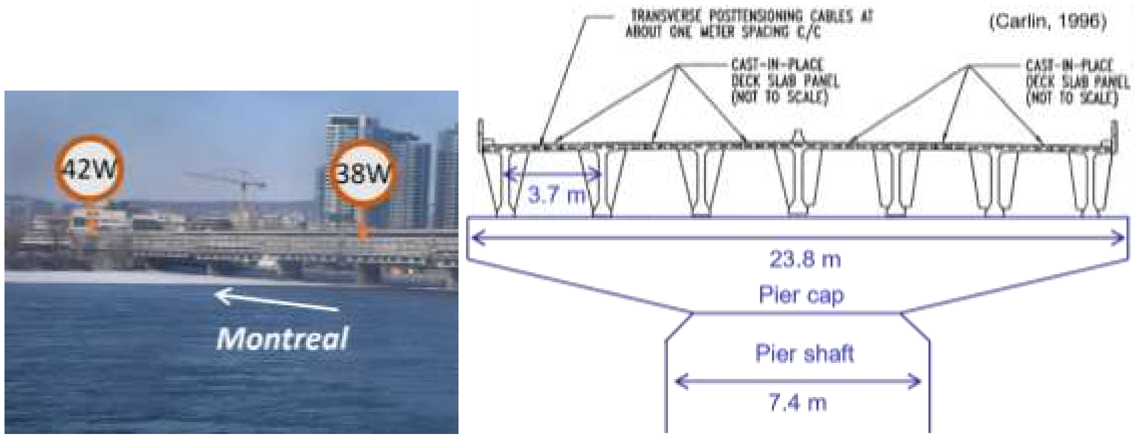

Figure 6-1 Location of investigated PC and PS members (left) and schematic of a bridge pier modified from Carlin 1996 (right)

ASR is a chemical reaction between unstable mineral phases in the aggregates used to make concrete and the alkali-hydroxides from the concrete pore solution. This reaction results in an expansive gel that swells upon moisture uptake, leading to induced expansion and deterioration of the affected material. ASR-induced expansion and damage development may differ due to a variety of factors including concrete mechanical properties [5], aggregate type (i.e., fine versus coarse aggregate) [5–8], aggregate minerology [2, 5–7, 9], alkali loading [10] [11], and aggregate grading [12]. Deterioration of concrete due to ASR results in significant reductions to engineering properties, such as the modulus of elasticity (ME) and tensile strength (TS), even at low levels of expansion, while compressive strength is normally only impacted at moderate to high expansion levels [13–15]. ASR is often observed to manifest in an anisotropic fashion (i.e., different expansion and deterioration levels occur as per distinct directions) due to non-symmetric geometries and restraint conditions experienced by concrete members in the field, where higher expansion is observed to occur in the directions presenting lower reinforcement [16–19], while an important decrease in expansion and deterioration is found in directions displaying higher restraints.

6.2.2 Tools for Evaluating Mechanical Properties of ASR-Affected Concrete

The stiffness damage test (SDT) is a non-destructive mechanical and cyclic loading procedure used to appraise the degree of damage in concrete. This test was initially proposed by Chrisp et al. [20] and Smaoui et al. [7] to evaluate concrete with ASR-induced damage and has since been applied to concrete damaged by numerous deterioration mechanisms (e.g., FT, delayed ettringite formation). In the SDT, concrete cores or cylinders are subjected to five loading/unloading compressive cycles with the maximum load corresponding to 40% of the concrete ultimate capacity (i.e. 40% of the 28-day strength of companion samples or 40% of a companion core from a less damaged location in the structure) [21–23]. Test results are used to compute four parameters to determine the extent of damage in investigated specimens:

- Stiffness Damage Index (SDI): Measures the ratio of dissipated energy due to crack formation (i.e. the hysteresis area) to the total energy implemented in the system (i.e. the area under the loading curves of the stress-strain curve). Higher SDI values indicate the presence of a larger number of cracks (i.e. higher damage) in the evaluated concrete specimen.
- Plastic Deformation Index (PDI): Measures the ratio of plastic deformation (i.e. non-recoverable deformation) to total deformation in the sample. Similar to the SDI, this parameter correlates to the number of cracks within an investigated concrete specimen, with larger values indicating higher damage.
- Non-linearity Index (NLI): Indicates the dominant orientation of cracks within the concrete specimen (e.g., parallel or perpendicular to loading). NLI values are calculated as a ratio between the secant of the stress-strain curve at half the maximum load (i.e, 20% of strength) and the secant of the stress-strain curve at the maximum load (i.e. 40% of strength). NLI values lower than unity indicate cracks that are preferentially oriented parallel to the applied load, while NLI values greater than unity indicate cracks perpendicular to the applied load [20].
- Modulus of Elasticity (ME): Indicates the stiffness of the material and is determined by computing the average slope of the second and third loading/unloading cycles. Lower ME values indicate a loss of stiffness (i.e. higher damage). Further information on the SDT can be found in [22–24].

The SDT has been shown to effectively differentiate between varying degrees of damage caused by a wide range of deterioration mechanisms, including ASR, FT [8, 9], and delayed ettringite formation

(DEF) [8, 29, 30], both independently and in combination with ASR. SDT has also been applied to assess damage in concrete from other sources [31]. Sanchez et al. [8] conducted a comprehensive evaluation of concrete affected by internal swelling reactions, namely ASR, FT, and DEF, resulting in the development of an extensive database. Table 6-1 presents a portion of this database, adapted for use with the SDI, specifically for concrete affected by ASR and the combined effect of ASR and FT cycles [8].

Table 6-1 Guidelines developed by Sanchez et al. 2018 [6] **outlining expected SDI values corresponding to different distress mechanisms and damage degrees**

Distress Mechanism	***Classification of ASR damage degree (%)***	***Reference expansion level (%)***	***Compressive strength loss (%)***	***SDI***
ASR	Negligible	0.00-0.03	–	0.06 – 0.16
	Marginal	0.04 ± 0.01	(-) 10 – 15	0.11– 0.25
	Moderate	0.11 ± 0.01	0 – 20	0.15 – 0.31
	High	0.20 ± 0.01	13 – 25	0.19 – 0.32
	Very High	0.30 to 0.50 ± 0.01	20 – 35	0.22 – 0.36
FT and FT+ASR	Negligible	0.00-0.03	–	0.11
	Marginal	0.04 ± 0.01	12 – 32	0.16 – 0.23
	Moderate	0.11 ± 0.01	21 – 32	0.25 – 0.28
	High	0.20 ± 0.01	22 – 37	0.27 – 0.41
	Very High	0.30 to 0.50 ± 0.01	24 – 40	0.34 – 0.45

While the SDT has demonstrated strong potential for assessing damage in concrete, its application to the evaluation of in-service field structures remains relatively limited [18, 26, 32–34]. Moreover, most existing SDT databases are derived from laboratory conditions, which do not fully replicate the complex and variable environments encountered in the field. In-service structures are exposed to diverse stress states (e.g., compressive versus tensile zones), fluctuating environmental conditions (e.g., seasonal moisture and temperature variations), and varying service environments (e.g., mechanical loading, chemical exposure). These factors introduce significant variability in the deterioration patterns observed in affected structures and members [34]. Additionally, structures impacted by internal swelling reactions such as ASR and FT frequently exhibit anisotropic behavior, leading to “preferred” directions of expansion and damage. This anisotropy alters cracking patterns and influences mechanical responses depending on the direction of loading [23, 25, 34–35]. All the above highlights a critical gap and presents a clear research opportunity for the expanded and systematic use of SDT in the quantitative assessment of field structures exhibiting diverse conditions and anisotropic damage effects caused by internal swelling reactions.

6.3 Scope of Work

This study focuses on the condition assessment of sections of the CB piers, specifically portions of PC and PS, after nearly six decades of service, using non-destructive methods such as RF and mechanical procedures including SDT and compressive strength testing. Cores were extracted from various locations within each member, considering differences in zone, depth, and orientation. The results are analyzed alongside supplementary image analysis to examine the influence of crack orientation and density on mechanical performance.

6.4 Materials and methods

The investigated members were removed from bridge piers 42W and 38W from the Champlain Bridge with the configuration shown in Figure 2-2. The PC belonged to pier 42W, located adjacent to René Lévesque Blvd, where the west face was exposed to salt spray from roadway traffic. This member underwent several repairs over its service life, including encapsulation in 2004 [40, 41]. The PS was part of pier 38W, with the investigated section comprising both dry and semi-submerged regions. This member experienced minimal intervention, with only a shotcrete-type layer observed on portions of the dry section.

A comprehensive visual assessment of both PC and PS members was previously conducted, including documentation of reinforcement configurations in each member [42]. In the PC, varying stress states (i.e., tensile versus compressive regions) were expected to have influenced ASR development. In the PS, differences in concrete damage between the dry and semi-submerged regions were of particular interest.

Figure 6-3 illustrates the coring plan. Cylindrical cores (100 mm diameter by 200 mm length) were extracted in three orientations—transverse, longitudinal, and vertical—from both members. After extraction, cores were wrapped in plastic film and transported to the University of Ottawa laboratory, where they were stored in a temperature-controlled chamber at 12 °C to halt further ASR progression, following the procedure outlined by Sanchez et al. [20]. Cores were categorized as 'surface' (within the first 20 cm from the surface in the PS or outside the reinforcement cage in the PC) or 'internal' (beyond 20 cm from the surface). Individual specimens were labeled using the member type (i.e., PC or PS), the surface orientation (e.g., North West – NW), the orientation of extracted cores within the structure (i.e., transverse -T, vertical -V or longitudinal-L) an identifying number for the core extraction location and the distance from the surface to the core (in cm). The location of extracted cores are shown in Figure 6-2 and Figure 6-3.

6.4.1 Detailed Coring Plan

Core specimens investigated in this work came from locations accessible while the PC and PS members were in service (i.e., vertical and transverse cores in the PC and longitudinal and transverse cores in the PS) as well as locations only accessible due to decommissioning of the structure (i.e., longitudinal cores in the PC and vertical cores in the PS). Longitudinal PC specimens and vertical PS specimens were extracted from cross-sectional surfaces and provided only interior core locations, while other extracted core locations included both surface and interior specimens. Due to the encapsulation repair performed on the PC, the 'surface' specimens are considered to be the first 200 mm of original concrete beyond the external layer of repair concrete. Since the original cover depth on this member prior to the repair is unknown, it is unclear how representative these cores are of external damage during the service life of the member, and thus, they cannot be directly compared to surface PS specimens. It is known that during the repair the concrete cover was removed up to or slightly within the outer cage of reinforcement.

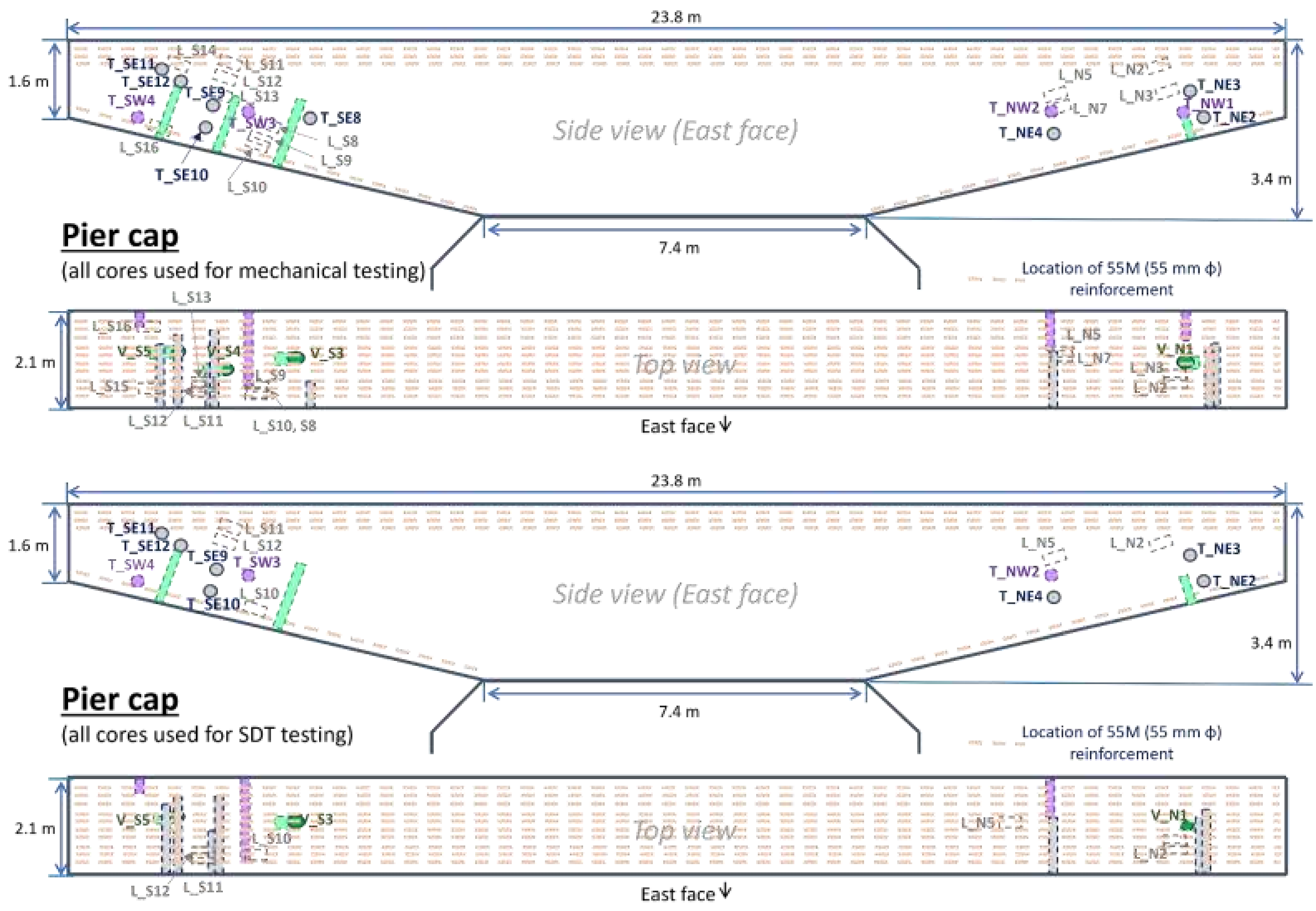

Figure 6-2 Schematic depicting the location of transverse (T), longitudinal (L) and vertical (V) cores extracted from the PC used for RF testing (top) and SDT (bottom)

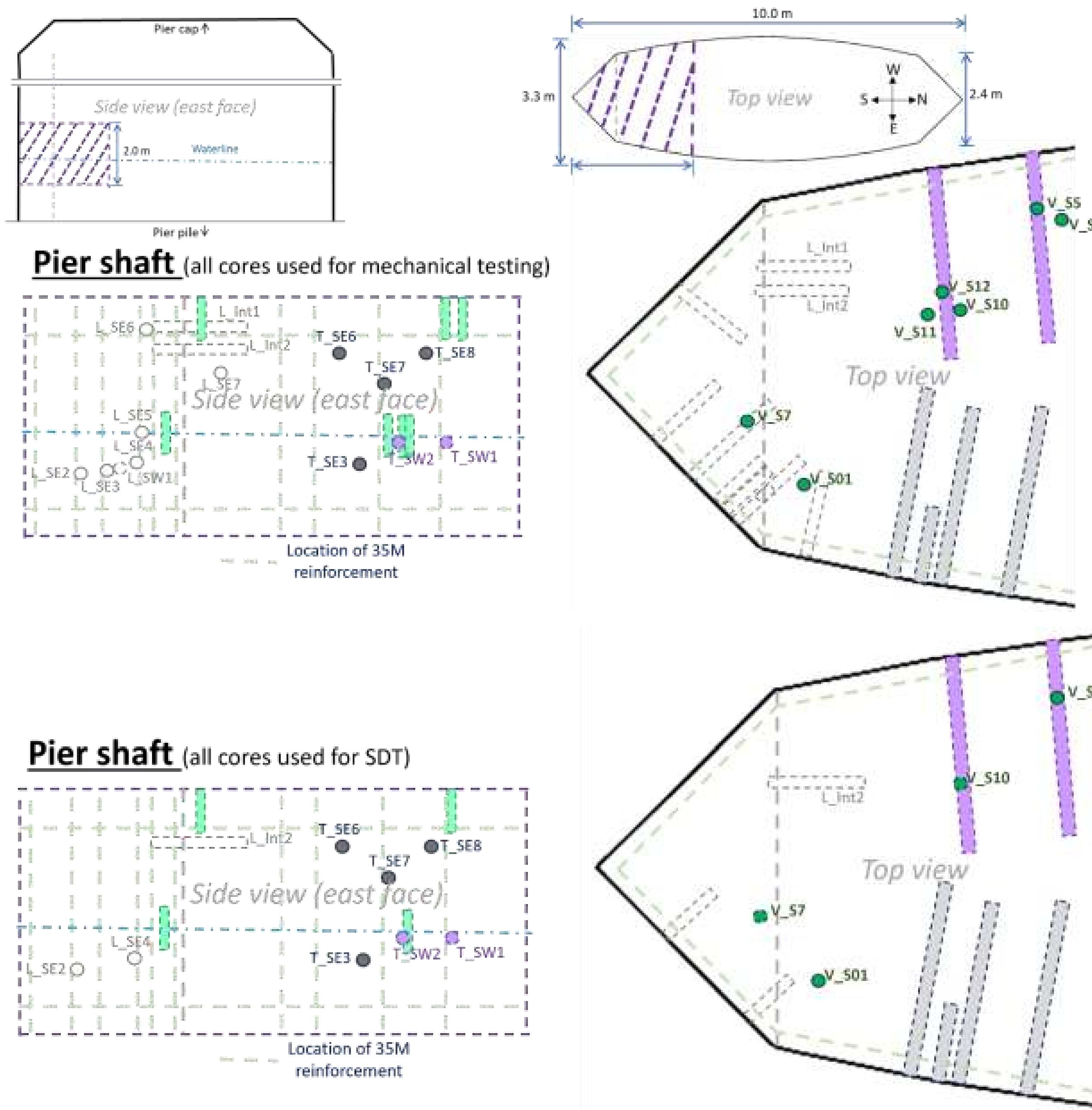

Figure 6-3 Schematic depicting the location of transverse (T), longitudinal (L) and vertical (V) cores extracted from the PC used for RF testing (top) and SDT (bottom)

6.5 Methods for assessment and analysis

6.5.1 Resonant frequency (RF)

Resonant frequency (RF) measurements were performed using transverse (capturing S-waves) and longitudinal (capturing P-waves) modes following the procedure outlined in ASTM C215-19 [25] using a DK-5000 dynamic resonance frequency tester. The dynamic modulus (Dynamic ME) can be calculated from the transverse RF using Equation 6-1 where M is the mass in kg, L is the sample length in m, d is the diameter in m, n is the transverse RF in Hz, and T is a correction factor from ASTM C215-19 which is dimensionless. Dynamic ME can be calculated from the longitudinal RF using Equation 6-2 where n' is the longitudinal RF in Hz.

$$E_{dyn}\ [GPa] = 1.6067({L^3 T}/{d^4}) \cdot M \cdot n^2 \tag{6-1}$$

$$E_{dyn}\ [GPa] = 5.093({L}/{d^2}) \cdot M \cdot (n')^2 \tag{6-2}$$

Eight transverse measurements were performed per core along four equally spaced longitudinal lines, as shown in Figure 3-11 (duplicated below), to capture differences within the core specimen between the top and bottom and to capture how crack orientation might influence RF results along different longitudinal planes. External crack visualization (i.e. cracks traced on outside of core) were used to choose optimal locations to capture the influence of lengthwise cracking (e.g., choosing to align L1 with lengthwise crack). Moreover, two longitudinal measurements were performed per core, with the accelerometer and impact location alternated between the top and bottom ends.

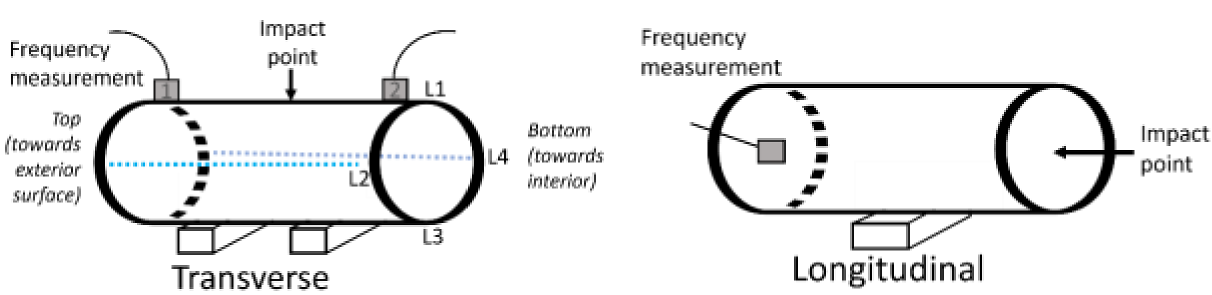

Figure 3-11 Schematic depicting the method for transverse and longitudinal RF measurements (Duplicated for ease of reference)

6.5.2 Stiffness damage test (SDT)

Core specimens were stored at room temperature and 100% RH for a minimum of 48 hours prior to testing to condition the samples and reduce variability of results as per [23]. Five compressive loading cycles were performed using 40% of the compressive strength of a companion sound concrete (i.e. test load of 12.4 MPa for the PC and 9.6 MPa for the PS) at a loading rate of 0.10 MPa/s. The SDT outcomes, SDI, PDI and NLI were calculated as shown in Figure 6-4. The static modulus of elasticity (ME) in GPa was calculated using the average value of the secant of the loading portion of the second and third cycles.

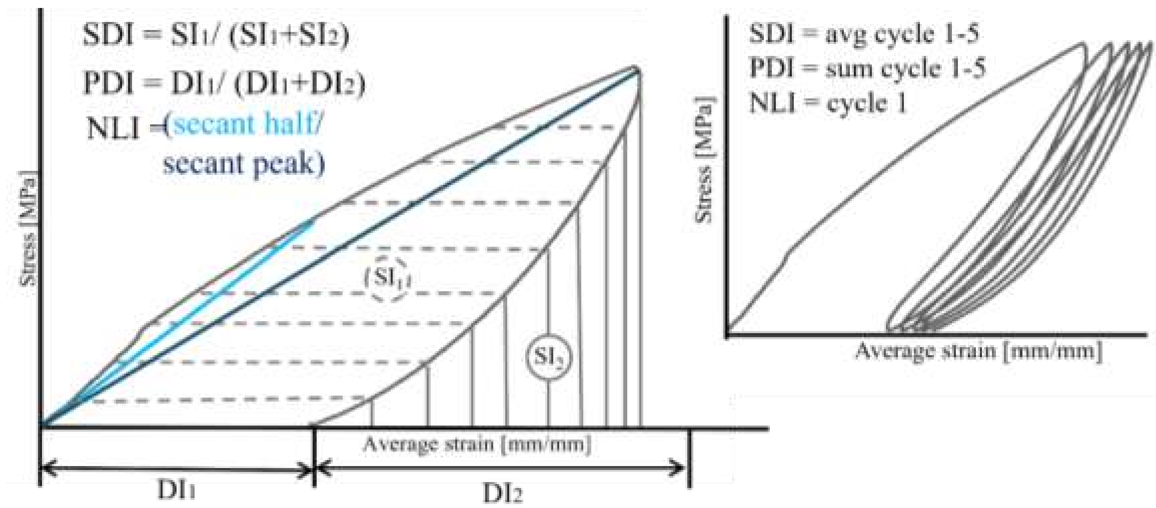

Figure 6-4 Schematic of parameters for the calculation of SDI, PDI and NLI (adapted from Sanchez et al. 2018 [6]**).**

6.5.3 Compressive testing

Compressive testing was conducted as per ASTM C42/C42M-20 [26] after conducting RF and SDT; this procedure was shown to be valid in [22] with specimens conditioned for 48 hours in a 100% humidity environment at room temperature prior to testing. Two specimens, representing the highest dynamic ME from the PC and PS (i.e. least damaged specimens), were tested in compression to estimate the appropriate 40% load for SDT. Seven PC specimens and four PS specimens used for SDT were set aside for prognostic testing (i.e. accelerated testing to evaluate potential for further expansion of concrete cores) and thus were not tested in compression.

6.6 Results

6.6.1 Resonant Frequency (RF) to Determine Dynamic ME

The dynamic modulus of elasticity (dynamic ME) calculated using the transverse and longitudinal RF (S- and P- waves, respectively) is presented in Figure 6-5. Results from the two measurement modes yielded similar average values. Differences between PC (grey) and PS (blue) specimens were observed, with the PC found to exhibit higher dynamic ME compared to specimens from the PS. The following sections will discuss in detail the results obtained specifically for the PC and PS.

6.6.1.1 Pier Cap (PC)

Dynamic ME was evaluated for surface and internal PC specimens from distinct core orientations (transverse, longitudinal and vertical). Transversal surface specimens exhibited lower dynamic ME compared to vertical specimens, with average values of 18 GPa and 24 GPa, respectively. Internal transverse, longitudinal and vertical specimens presented similar dynamic ME ranging from 22 to 26 GPa, with transverse specimens presenting the lowest value. In all cases, both RF measurement modes resulted in equivalent average dynamic ME.

6.6.1.2 Pier Shaft (PS)

Dynamic ME was evaluated for surface and internal PS specimens from distinct core orientations (transverse, longitudinal and vertical) and environments (i.e. dry and wet). Transverse surface cores presented higher dynamic ME compared to longitudinal surface cores, with average values of 19 GPa and 15 GPa, respectively, obtained from the transverse measurement mode. The transverse and longitudinal RF measurement modes resulted in different average dynamic ME for transverse and longitudinal specimens, with transverse core specimens exhibiting an increased average value from the longitudinal measurement mode while longitudinal specimens presented the opposite trend exhibiting a much lower dynamic ME using the longitudinal measurement mode with the most drastic dynamic ME reduction occurring for longitudinal specimens from the dry region. Internal core specimens exhibited dynamic ME values ranging from 7 GPa to 22 GPa. Both RF measurement modes resulted in equivalent average dynamic ME for all internal PS specimens.

While average values from the two RF methods generally show close agreement, results for PS specimens from the dry and wet-dry sections of the PS were found to be lower using the longitudinal method. This may be linked to the strongly perpendicular orientation of cracks in these samples. Previous microscopic evaluation of cores [27] found that crack widths in the cement paste of PS cores from the dry region were notably wider compared to other specimens in both the PC and PS.

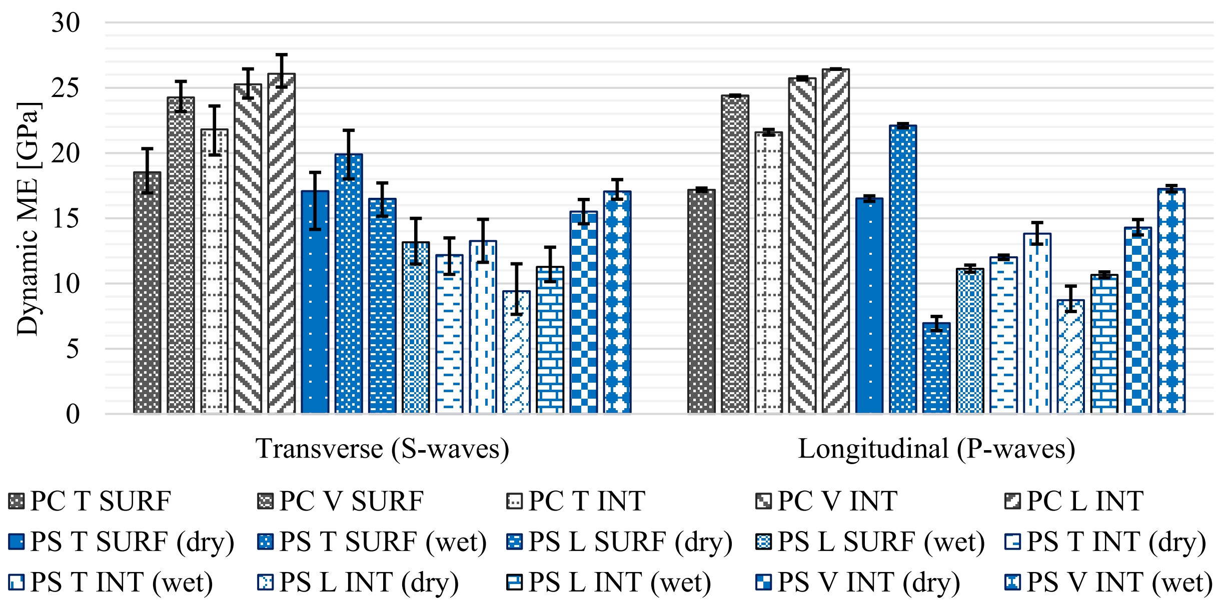

Figure 6-5 Bar graph depicting average dynamic ME determined using the transverse (S-waves) and longitudinal (P-waves) techniques; error bars indicate average maximum and minimum measurements

6.6.2 Stiffness Damage Test (SDT)

Figure 6-6 presents the stress-strain curves obtained from five loading-unloading cycles conducted on SDT specimens, highlighting selected surface samples from both the PC and PS members. The specimens exhibited varying degrees of deterioration. Those with minimal damage showed smaller hysteresis loops and limited plastic deformation (e.g., PC_V_N1_00), indicating lower energy dissipation.

In contrast, specimens with more severe damage demonstrated larger hysteresis areas and greater plastic deformation (e.g., PS_L_SE6_00), reflecting increased material degradation and energy absorption

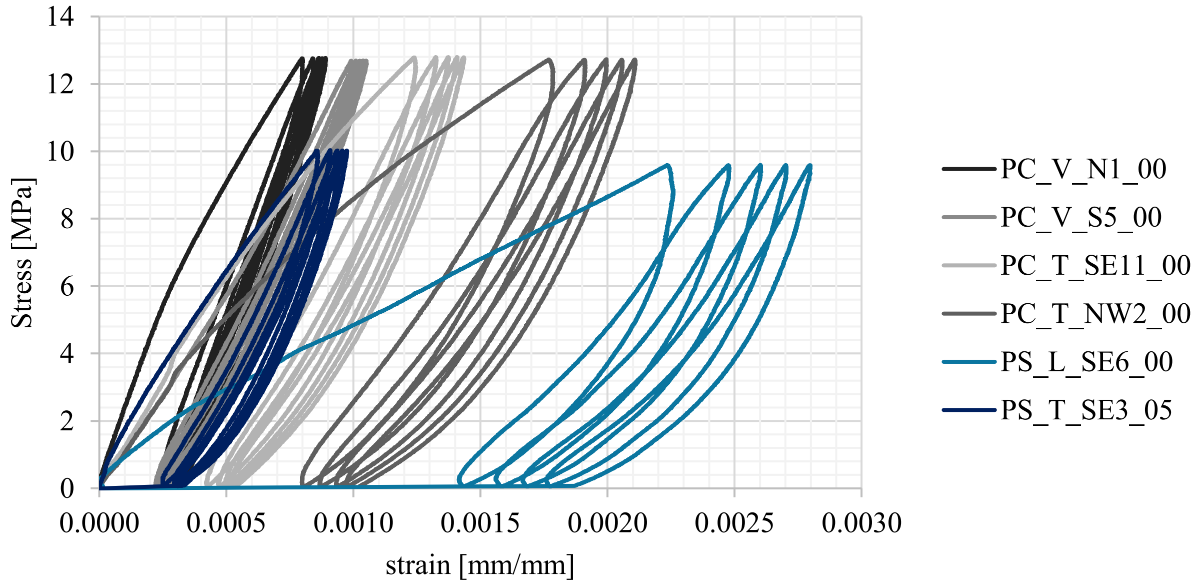

Figure 6-6 Plot of stress-strain curves for selected PC and PS surface cores extracted vertically (V), transversally (T) and longitudinally (L)

SDT results are shown in Figure 6-7, including the SDI, PDI, NLI and ME. Increased damage in concrete is indicated by greater values of SDI and PDI, denoting loss of stiffness and increased plastic deformation, while greater values of ME indicate lower damage in the concrete and are generally accompanied by lower values of SDI and PDI.

6.6.2.1 Pier Cap (PC)

PC surface transverse specimens exhibited higher average SDI and PDI values, along with lower ME, compared to vertical core specimens extracted from surface locations. In contrast, NLI values were similar across both surface orientations. Internal PC specimens showed lower average SDI and PDI, but higher ME values relative to surface specimens. Notably, internal specimens presented a consistent average NLI of approximately 0.90, whereas surface specimens averaged around 1.10. Differences were also observed between core orientations: longitudinal internal specimens displayed the lowest SDI and PDI values and the highest ME, while transverse internal specimens exhibited higher PDI and lower ME, with substantial variability between their maximum and minimum values.

6.6.2.2 Pier Shaft (PS)

PS transverse and longitudinal surface specimens exhibited SDT responses comparable to those of PC surface specimens, characterized by high SDI and PDI values and low ME values. Among them, longitudinal surface specimens showed the most severe deterioration, as indicated by the highest SDI and PDI values and the lowest ME. Unlike the PC specimens, NLI values in the PS specimens varied significantly across locations. Internal PS specimens displayed similar trends to their surface counterparts, with elevated SDI and PDI values and reduced ME. However, vertical interior cores from the wet region showed the least damage, with the lowest SDI and PDI values and the highest average ME. While variations were observed across different specimen locations, including a notably high NLI value for the longitudinal internal specimens in the wet region, ME values remained relatively consistent across all PS specimens, ranging from 7.5 to 10.5 GPa.

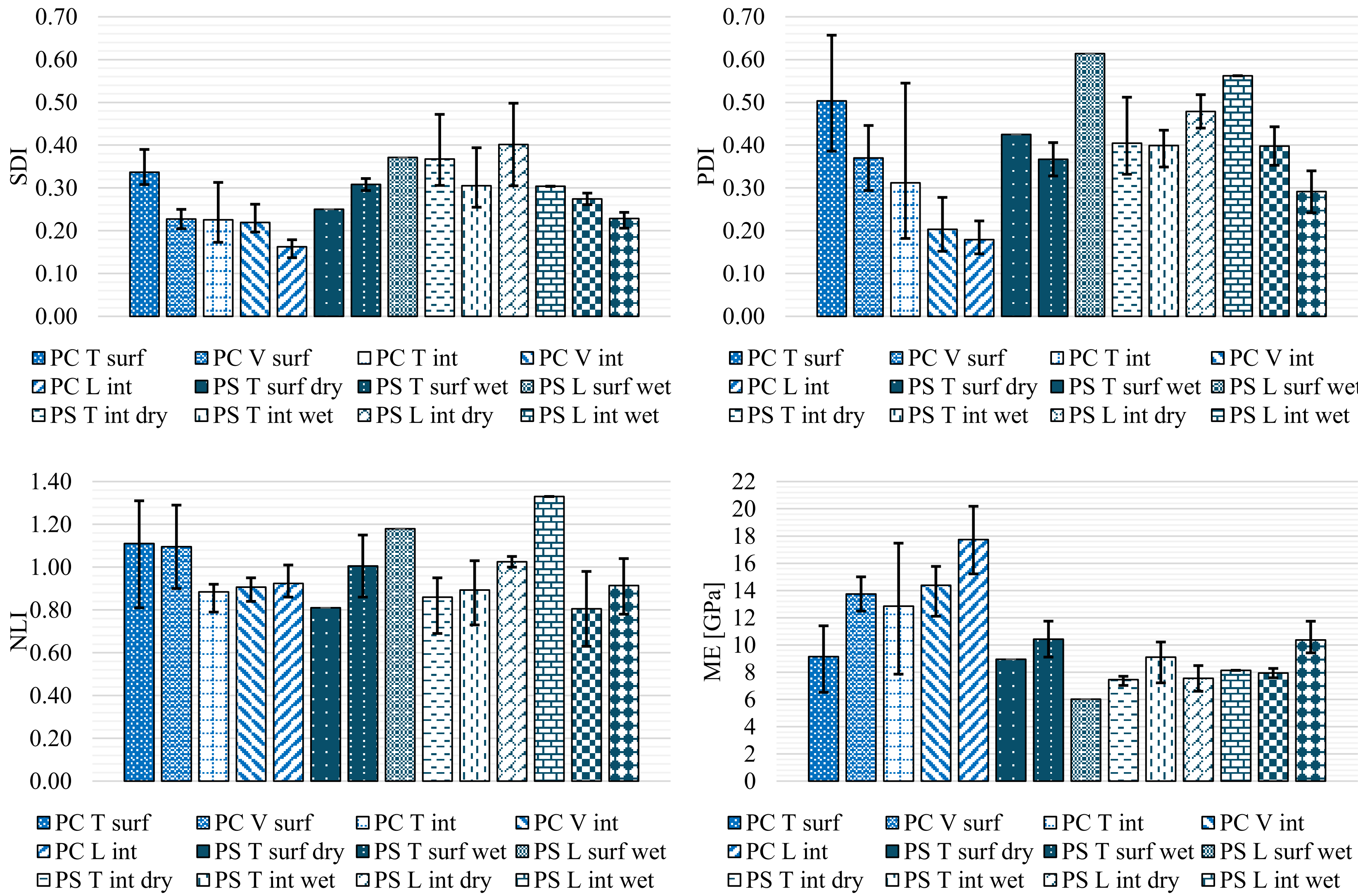

Figure 6-7 Bar graphs depicting average SDI, PDI, NLI and ME for PC (40% load of 12.8 MPa) and PS (40% load of 9.8 MPa). Error bars indicate maximum and minimum values.

6.6.3 Compressive Strength (f'c)

Compressive strength results are presented in Figure 6-8 where specimens were tested using RF and SDT prior to compressive testing as per [22]. The average compressive strength in the PC ranged from 25 MPa to 34 MPa, where internal longitudinal specimens exhibited the greatest average compressive strength, while compressive strengths in the PS ranged from 18 MPa to 28 MPa. Compressive strengths from both members presented similar trends to those observed for ME results. Due to use of some specimens for residual expansion testing, compressive strength data does not represent the full set of specimens used for SDT, due to this approach only one specimen was available for transverse surface cores from the PS. Reference compressive strength specimens used to determine the 40% load are included in Figure 6-8

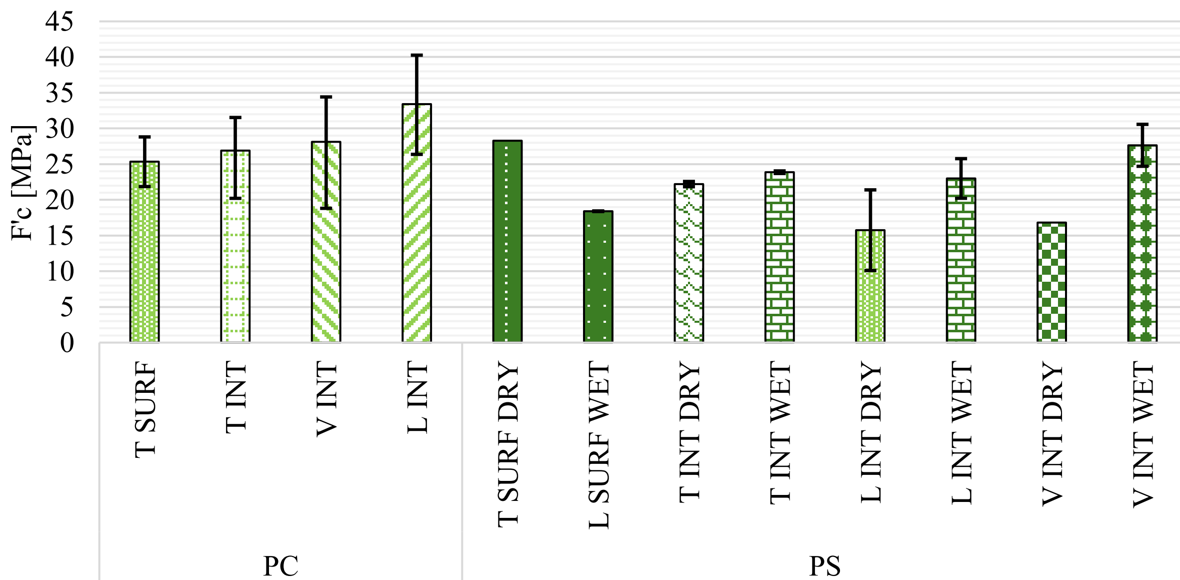

Figure 6-8 Bar graph depicting compressive strength [MPa] of PC and PS cores. Error bars indicate maximum and minimum values.

6.7 Discussion

6.7.1 Effect of Coring Location (Depth and Orientation) on Mechanical Test Results

6.7.1.1 Detailed Coring Plan and Specimens Description

Core specimens investigated in this work were extracted in transverse, longitudinal and vertical orientations from both members. However, due to the different member geometries cores orientated longitudinally and vertically are not directly comparable. Longitudinal PC specimens and vertical PS specimens are extracted from cross-sectional surfaces and thus provide only interior core locations, while other extracted core locations included both surface and interior specimens. Additionally, the meaning of surface core specimens differs in the PC due to an encapsulation surface repair.

Figure 6-9 and Figure 6-10 presents the location of transverse, longitudinal and vertical cores extracted from the PC member. External crack patterns observed during visual inspections (adapted from Kristufek et al. [28]) are presented, as well as internal crack patterns observed via microscopic investigations of cores by the same author [27]. While cracking was observed to be primarily horizontal on the exterior of the member, internal damage observed on extracted cores suggests cracking was oriented vertically within the member.

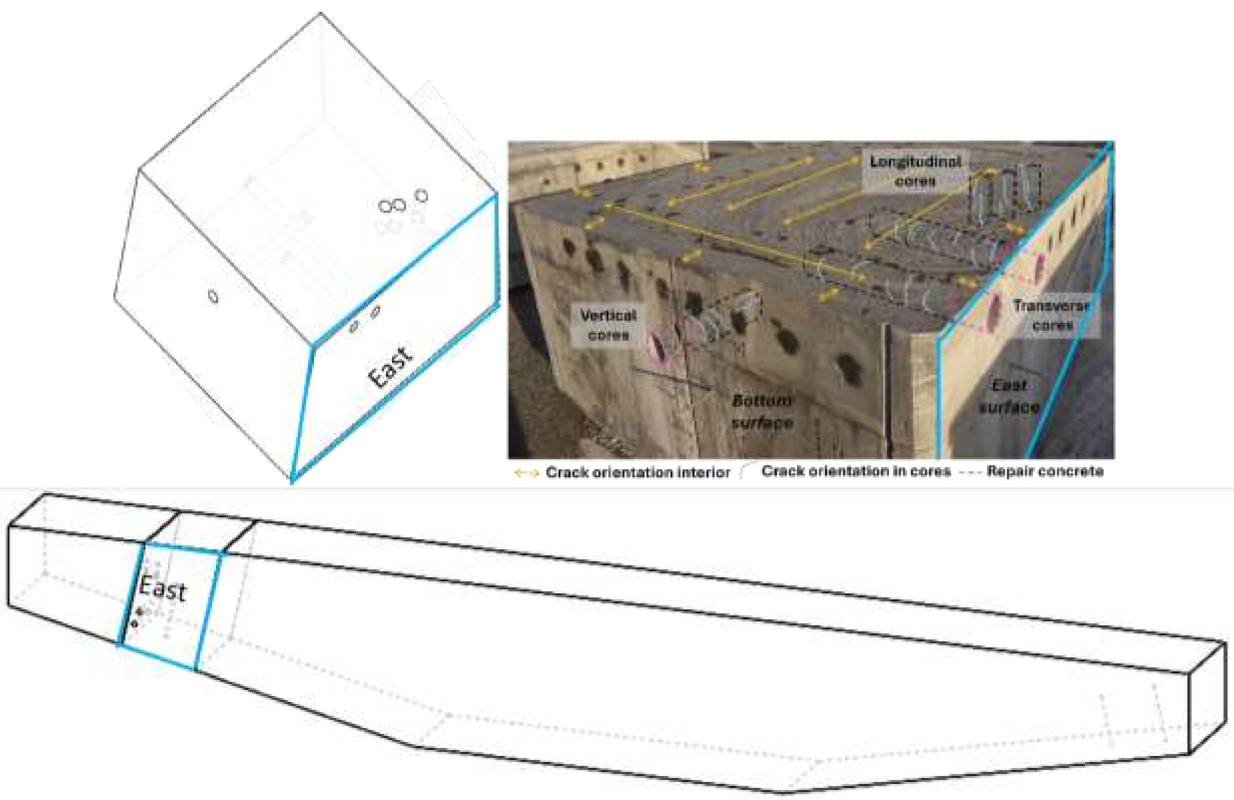

Figure 6-9 Schematic of the locations of transverse, vertical and longitudinal cores in a PC segment with internal crack orientation as per Kristufek et al. [27] and the location of the PC within the member.

Figure 6-10 presents the location of transverse, longitudinal and vertical cores extracted from the PS member. Internal crack patterns determined during previous microscopic evaluations of extracted cores [27] are presented as well as external crack patterns observed during visual inspections (adapted from [28]). Internal cracking was found to be primarily oriented parallel to the length of the member (i.e. north-south) as shown in Figure 6-10. The PS section investigated was located on the southern end of the PS side (i.e. facing upstream) and thus was expected to experience the highest deterioration in the location of the longitudinal cores. Significant cracking was observed parallel to the external surface, including planes of delamination corresponding to corrosion of the reinforcing bars at this depth (i.e., corrosion induced delamination) which is indicated by red lines in Figure 6-10. The presence of the corrosion induced damage limited availability of surface cores with the 200 mm length required for mechanical testing.

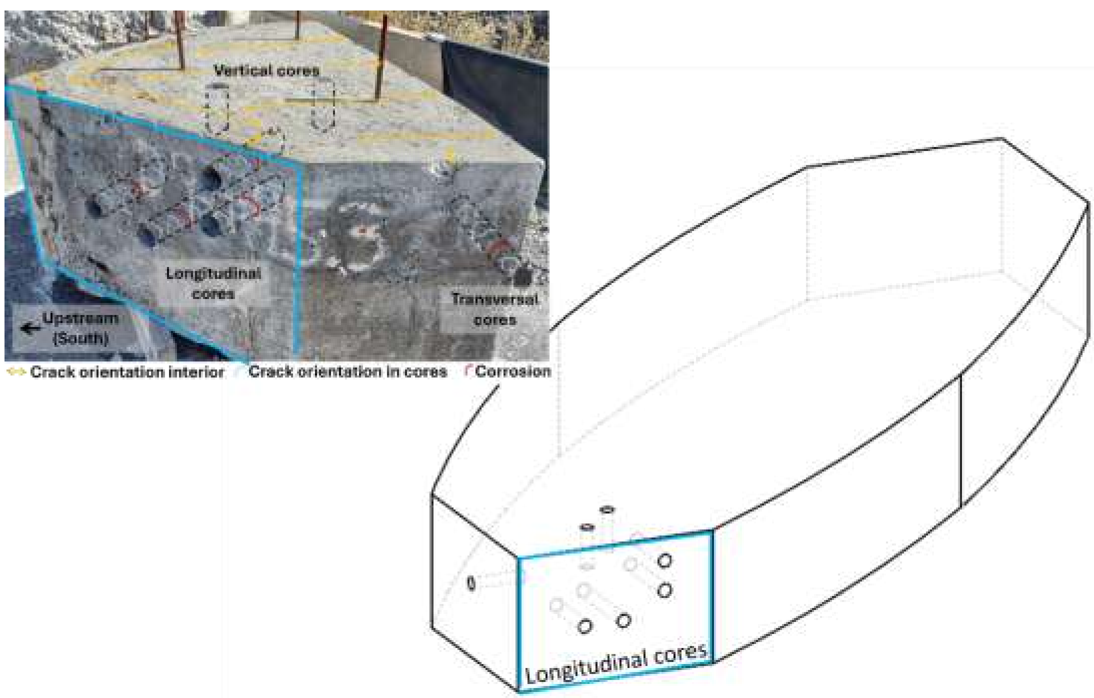

Figure 6-10 Schematic of the locations of transverse, vertical and longitudinal cores in a PS segment with estimated internal crack orientation as per Kristufek et al. [27] **(top left) and the location of the segment displayed within the PS member (bottom right).**

Table 6-2 summarizes all core specimens extracted and evaluated, along with the key findings of this study. The following sections provide a detailed discussion of each result obtained.

Table 6-2 Summary of experimental mechanical test results

	Depth	Core orientation	SDI	PDI	NLI	ME [GPa]	Observed crack orientation
PC	Surf	**Transverse**	0.34	0.50	1.11	9.1	widthwise
		Vertical	0.23	0.37	1.10	13.7	widthwise
	Int	**Transverse**	0.23	0.31	0.88	12.9	widthwise
		Longitudinal	0.16	0.18	0.92	17.7	lengthwise
		Vertical	0.22	0.20	0.91	14.4	indeterminate
PS	Surf	**Transverse - dry**	0.25	0.43	0.81	8.9	widthwise
		Transverse - wet	0.31	0.37	1.01	10.4	widthwise
		Longitudinal - dry	NA	NA	NA	NA	NA
		Longitudinal - wet	0.37	0.61	1.18	6.0	widthwise
	Int	**Transverse - dry**	0.37	0.40	0.86	7.4	indeterminate
		Transverse - wet	0.31	0.40	0.89	9.1	widthwise
		Longitudinal - dry	0.40	0.48	1.03	7.5	indeterminate
		Longitudinal - wet	0.30	0.56	1.33	8.1	widthwise
		Vertical - dry	0.27	0.40	0.81	7.9	lengthwise
		Vertical - wet	0.23	0.29	0.91	10.4	indeterminate

6.7.1.2 Core Depth

Surface specimens are expected to exhibit greater damage than internal specimens, consistent with field exposure conditions and previous observations by Sanchez et al. [29]. Elevated SDI and PDI values, combined with reduced ME, were consistently recorded in surface cores from both the PC and PS members. To extend the analysis, ME and f'c reductions were determined relative to the 24 MPa 28-day compressive strength specified for the CB piers [30], with a reference ME calculated using ACI 318-19 [31]. Due to ongoing hydration after 28-days, it is expected that in the absence of deterioration mechanisms the concrete strength can experience an increase of around 30% [32, 33].

For surface specimens, transverse PC cores exhibited an SDI of 0.34, a PDI of 0.50, and a remaining ME of 9.1 GPa, representing a reduction of 60% (Figure 6-7 and Figure 6-11). However, these specimens presented a compressive strength of 25.0 MPa, corresponding to a strength increase of 6% relative to the design strength of 24 MPa and thus would not exhibit sufficient strength reduction to prompt concern in the absence of further mechanical testing (Figure 6-7 and Figure 6-11). Transverse PS surface specimens exhibited lower SDI and PDI values of 0.25 and 0.43, respectively, with a similar ME of 8.9 GPa (61% reduction) and a higher residual strength of 29 MPa (18% increase). When considering the full surface profile, combining vertical (PC) and longitudinal (PS) orientations, the PC member exhibited an SDI of 0.28, a PDI of 0.44, and a ME of 11.4 GPa (50% reduction), while the PS member presented an SDI of 0.31, a PDI of 0.47, and a ME of 8.5 GPa (63% reduction), with corresponding compressive strengths of 25.0 MPa (6% increase) and 23.0 MPa (3% increase), respectively (Figure 6-7, Figure 6-8 and Figure 6-11).

Interior specimens exhibited more variable results depending on core orientation. In the transverse direction, PC specimens indicated an SDI of 0.23, a PDI of 0.31, and a ME of 12.9 GPa (44% reduction), with a residual strength of 27 MPa (12% increase). In contrast, PS specimens exhibited higher damage, with an SDI of 0.34, a PDI of 0.40, and a ME of 8.3 GPa (64% reduction), and a residual strength of 23 MPa (4% reduction) (Figure 6-7, Figure 6-8 and Figure 6-11). In the vertical direction, PC interior cores showed improved performance, with an SDI of 0.22, a PDI of 0.20, and a ME of 14.4 GPa (38% reduction), along with a strength of 28 MPa (17% increase). PS vertical cores exhibited higher deterioration, with an SDI of 0.25, a PDI of 0.34, and a ME of 9.2 GPa (60% reduction), and a strength of 22 MPa (7% reduction). The most significant contrast occurred in the longitudinal direction: PC cores showed minimal damage (SDI of 0.16, PDI of 0.18, and ME of 17.7 GPa, representing 23% reduction) and the highest compressive strength among all interior samples (33 MPa, 39% increase), whereas PS longitudinal cores exhibited the worst mechanical condition, with an SDI of 0.35, a PDI of 0.52, and a ME of 7.8 GPa (66% reduction), along with the lowest residual strength of 19 MPa (34% reduction) (Figure 6-7, Figure 6-8 and Figure 6-11).

The observed trends are attributed to harsher environmental exposure at the surface, including cyclic wetting and drying, chloride ingress (i.e., de-icing salts), and temperature fluctuations, all of which exacerbate reinforcement corrosion, FT damage, and ASR-induced microcracking. Synergistic effects between different exposure conditions may increase damage as identified by Chen et al. [34], Deschenes et al. [35] and Sanchez et al. [6].

Despite localized repairs performed on the PC member, surface damage remained significant, particularly in the transverse orientation. Vertical surface cores from PC exhibited comparatively lower deterioration, suggesting that repair interventions may have been more effective in zones less directly exposed to external moisture gradients. Conversely, longitudinal surface cores from PS displayed the most severe mechanical degradation, indicating anisotropic damage progression influenced by both geometry (i.e. smaller width and higher reinforcement at the southern tip of the member) and exposure conditions (i.e., wet and dry regions). This directional disparity underscores the importance of considering core orientation when evaluating deterioration severity.

These findings reveal that mechanical deterioration associated with ASR is not only depth-dependent but also orientation-sensitive. The interaction between exposure conditions, reinforcement configuration, and structural geometry must be accounted for when diagnosing current damage levels and forecasting the remaining durability of affected members.

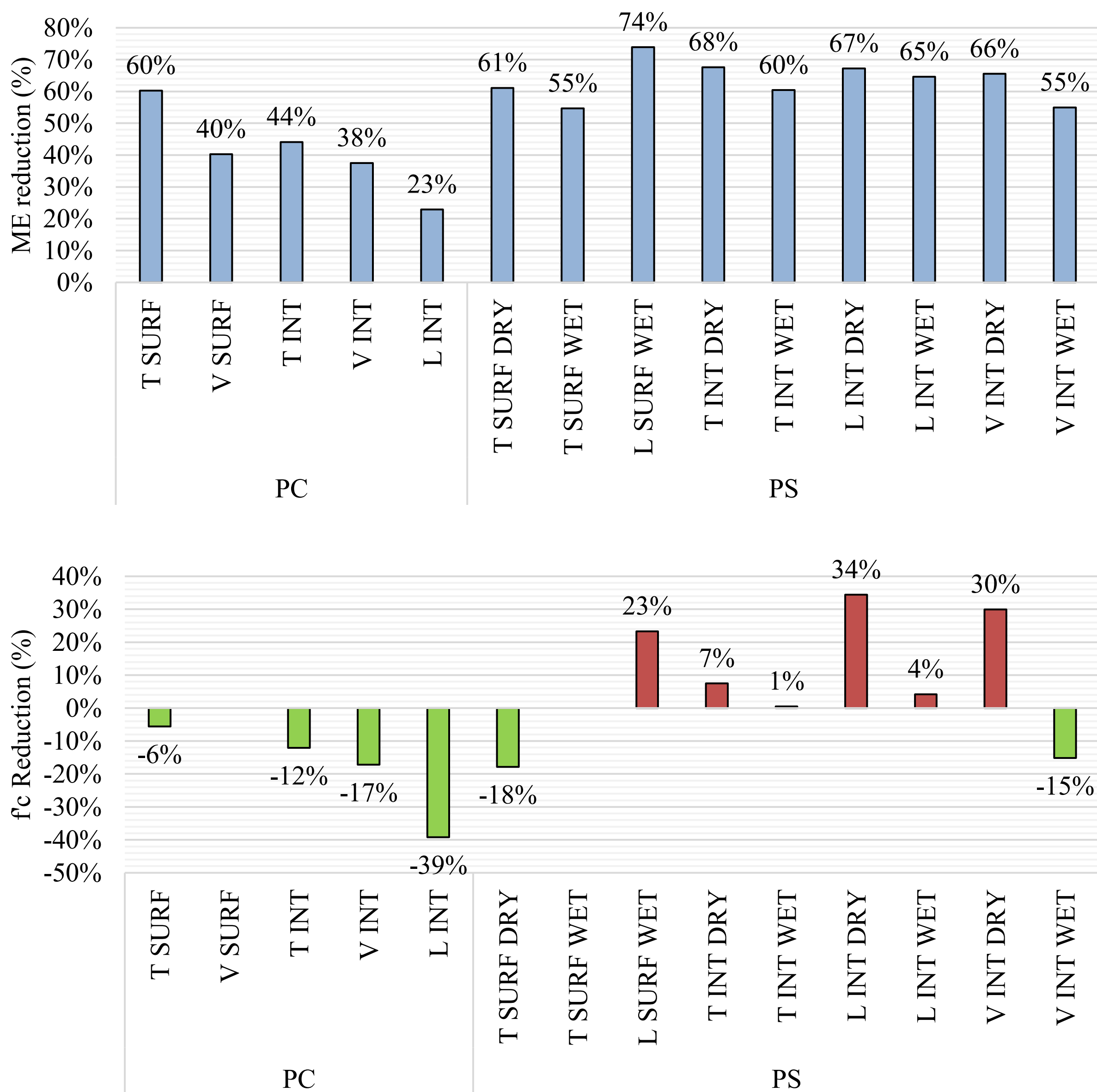

Figure 6-11 Bar graphs depicting reductions in ME relative to ME calculated as per ACI 318-19 [31] **(top) and compressive strength relative to the specified 24 MPa 28-day strength where a negative reduction indicates compressive strengths greater than 24 MPa (bottom).**

6.7.1.3 Core Orientation and Service Conditions

In ASR-affected field structures, non-symmetric geometries and reinforcement result in restraint conditions that have been shown to cause anisotropic expansion and deterioration [31, 32], leading to significant variation in mechanical properties depending on the coring direction [16–19]. "Expansion transfer" effects, wherein reduced expansion and damage are observed in restrained directions, leading to increased expansion and deterioration in less restrained directions, have been reported in the literature [17, 18]; however, the magnitude and underlying mechanisms of this phenomenon remain poorly understood [33]. This section evaluates the interplay between core orientation and environmental service conditions, particularly the differences between wet and dry regions. Emphasis is placed on how these parameters influence SDI and ME, as summarized in Table 1-2.

In the submerged region of the PS member, differences in deterioration across core orientations were relatively moderate. Transverse specimens exhibited the highest SDI among wet-region cores, with a value of 0.31, accompanied by a ME of 10.4 GPa. Vertical cores exhibited an SDI of 0.23 and a similar ME of 10.4 GPa. Internally extracted longitudinal cores in the wet region presented an SDI of 0.30 and a ME of 8.1 GPa. (Figure 6-7). These results suggest that under high moisture availability, the severity of orientation-dependent mechanical degradation is reduced. Saturation reduces internal drying gradients and minimizes the contribution of shrinkage-induced microcracking while providing additional water supply for the swelling mechanism of ASR, thereby homogenizing the damage distribution across orientations. On average, wet-region cores from the PS member presented an SDI of 0.28 and a ME of 9.3 GPa (Figure 6-7), reflecting moderate deterioration levels in this exposure zone.

In contrast, the dry region of the PS member presented more severe and directionally distinct deterioration. Longitudinal cores exhibited the highest SDI (0.40) and the lowest ME (7.5 GPa), corresponding to a modulus reduction of approximately 70%. Transverse cores followed with an SDI of 0.37 and an ME of 7.4 GPa. Vertical cores exhibited comparatively lower damage, with an SDI of 0.27 and an ME of 7.9 GPa (Figure 6-7). This hierarchy of damage, from longitudinal to transverse to vertical, reflects a stronger influence of anisotropic cracking under drying exposure conditions. Orientations perpendicular to the reinforcement direction appeared more susceptible to deterioration, possibly due to preferential crack propagation and reduced restraint. Across all three orientations, the average SDI and ME for internal dry-region PS specimens were 0.35 and 7.6 GPa, respectively. These values indicate that dry exposure significantly amplifies the effects of ASR and coupled mechanisms such as FT.

A comparison of wet and dry regions for each orientation further illustrates the combined effect of environmental conditions and anisotropy. For transverse PS cores, the SDI increased from 0.31 (wet) to 0.37 (dry), and the ME decreased from 9.1 to 7.4 GPa. Longitudinal cores showed a similar trend, with the SDI increasing from 0.30 to 0.40, and the ME decreasing from 8.1 to 7.5 GPa. For vertical cores, the SDI increased from 0.23 to 0.27, and the ME declined from 10.4 to 7.9 GPa (Figure 6-7). These results indicate that, for all orientations, exposure to the dry region resulted in an increased impact on mechanical properties. The typical difference in SDI ranged from 0.04 to 0.10, while ME reductions varied by up to 2.5 GPa. In certain cases, the effect of environmental exposure was more critical than orientation. Work by Rosenqvist et al. [36–38] has also reported increased deterioration in regions subject to partial saturation and FT cycling, particularly near the waterline. The present results align with these findings, as dry-region surface cores consistently exhibited greater damage.

The combined influence of orientation and environmental conditions introduces complexity in interpreting mechanical test data from core specimens. In this study, orientations associated with lower damage, namely, longitudinal cores in the PC member and vertical cores in the PS member, were located in regions that would have been inaccessible during in-service evaluation. In contrast, accessible locations, particularly those from the dry region, exhibited consistently higher SDI values and lower ME values. For instance, PS longitudinal cores extracted from the dry region presented an SDI of 0.40 and an ME of 7.5 GPa, compared to an SDI of 0.30 and an ME of 8.1 GPa (Figure 6-7) for those extracted from the wet region. Zahedi et al. [18] demonstrated that in ASR-affected concrete exhibiting anisotropy, the average of measurements taken along the three principal directions can effectively represent the “overall” extent of ASR-induced deterioration. However, obtaining three distinct core orientations is not feasible in field structures; therefore, the extraction and evaluation of cores from accessible orientations may yield estimates that are either more or less conservative (i.e., indicating higher or lower damage) than the actual overall deterioration of the members. This limitation introduces complexity in interpreting core test results, particularly when anisotropic damage patterns are present. Consequently, engineering judgment must be applied to account for potential sampling bias and to ensure that structural assessments accurately reflect the true condition of the member, especially when decisions regarding rehabilitation or continued service are based on limited core data. In this study, both members exhibited the least damage in core locations that would have been inaccessible while the structures were in service. As a result, the accessible core orientations evaluated would have indicated higher levels of damage than the actual average deterioration of the members, leading to a conservative assessment of their condition.

6.7.2 Impact of Crack Orientation on Mechanical Properties

Cracking patterns in concrete cores significantly influence the mechanical response under loading, particularly when anisotropic damage develops due to internal swelling reactions. Cracks aligned parallel to the loading direction (i.e., lengthwise) tend to preserve stiffness and strength, whereas cracks oriented perpendicularly (i.e., widthwise) are more detrimental to mechanical integrity. This behavior has been documented in both laboratory-produced blocks [18] and field-retrieved cores [39] through the conventional and extended versions of the DRI with additional analysis of cracking orientation. However, the interaction between crack orientation and environmental exposure (e.g., dry versus wet regions) remains insufficiently characterized. In the present study, an additional level of analysis was introduced through digital surface scanning of SDT-tested cores, providing macrocrack orientation and distribution prior to testing. This external visual evidence complements both the microscopic findings (via Damage Rating Index - DRI, see section 1.7.3.1) and the mechanical evaluation (via SDT), potentially enhancing a more comprehensive interpretation of the impact of the damage mechanisms on the mechanical properties.

6.7.2.1 Assessment of Crack Pattern in the Extracted Specimens

To characterize the directionality and extent of macrocracking, all cores tested under the SDT were scanned along their longitudinal axis using a flatbed scanner (11.8 pixels per millimeter). Each specimen was scanned in its original state and again after crack tracing using color-coded markers. Cracks in the cement paste were marked in green, closed cracks in aggregate particles in blue, and open cracks in aggregate particles in red. The digitized images were post-processed using GIMP and then analyzed with FIJI ImageJ to quantify crack orientation, segment density, and surface area. The number of cracks and crack lengths were obtained using the 'Analyze Particles' function, while crack orientation was then determined using the 'Directionality' tool in the FIJI ImageJ software [33]. Directionality identifies the direction of each crack segment and presents the resultant data as the percentage of segments falling into each 2° range, out of a total of 180°. If crack orientation were uniformly distributed (i.e., random), 21% of cracks would fall within each 38° range. The Directionality function was applied to traced cracks, with cracks in the cement paste and cracks in the aggregate processed separately. The percentage of total cracks oriented in a 38° range (i.e., 19° out of a 90° range), either parallel or perpendicular to the length of the specimen, was used to estimate whether cracking was primarily parallel (i.e., lengthwise) or perpendicular (i.e., widthwise) within the cores. Due to unique geometries often used in modern reinforced concrete structures, dominant crack orientations may fall between the ranges for parallel and perpendicular cracking (i.e., cores extracted may not be aligned to principal stresses). The area occupied by traced cracks (i.e., a constant width) was determined using the 'threshold' function, which finds the percentage of pixels in an image above or below a specified color value. Directionality plots were generated for each crack type, and the results were grouped by core orientation and depth. This process is illustrated in Figure 3-12.

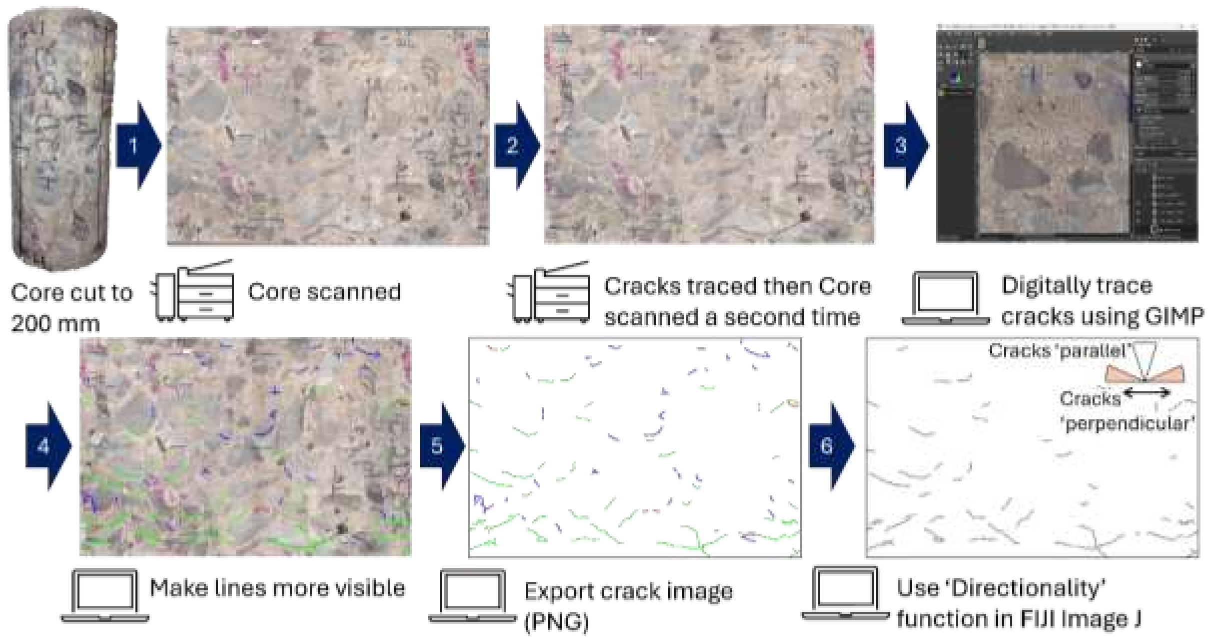

Figure 3-12 Schematic depicting the scanning and analysis process for obtaining crack orientation estimates for core specimens (Duplicated for ease of reference)

Cracking patterns on the surface of core specimens varied considerably (Figure 6-12). Surface cores from the PC and PS members exhibited prominent widthwise cracking within both the paste and aggregate, whereas interior PC longitudinal cores and PS vertical cores revealed fewer cracks, predominantly oriented lengthwise. Cracking in aggregate particles generally occupied a greater percentage of the scanned surface than cracking in the cement paste, though the latter was more closely correlated with mechanical performance.

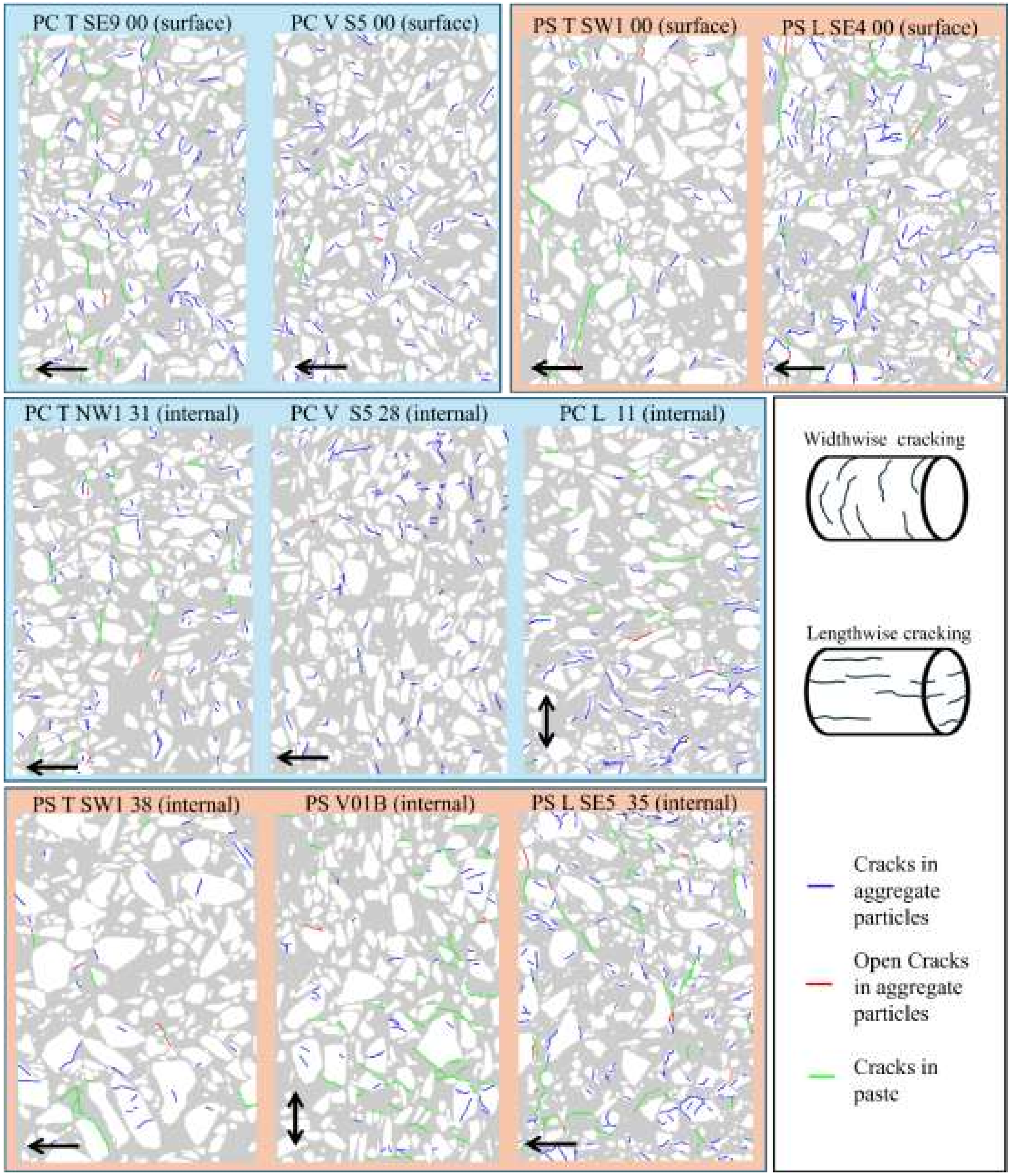

Figure 6-12 Schematics depicting traced cracks on surface and interior core specimen from transverse (T), vertical (V) and longitudinal (L) locations. Cracks are overlaid on the observed aggregate particles (white) and cement paste (grey). Arrows indicate the closest exterior surface.

Crack orientation within the aggregate particles was first analyzed to determine whether preferential paths could be identified in the damaged concrete. Results are presented in Figure 6-13 and organized by member (PC or PS), core orientation (transverse, vertical, or longitudinal), and environmental exposure (dry or wet).

In the PC member, cores exhibited a moderate tendency for widthwise cracking in aggregates, particularly in surface specimens, where over 35% of cracks were found within ±19° of the axis perpendicular to the core length. Transverse and vertical internal cores generally showed a more distributed crack orientation with perpendicular and parallel orientations occurring in roughly equal proportions. In contrast, longitudinal cores displayed a tendency for lengthwise cracking with 40% of cracks occurring within ±19° of the axis parallel to the core length. Crack density, expressed as the area of cracks relative to the scanned surface, averaged 1.5% for most PC specimens; however, a large range of maximum and minimum values indicates that crack density varied between individual specimens, especially for transverse and longitudinal interior specimens.

In contrast, PS cores suggest less variability in aggregate crack orientations. Transverse and longitudinal surface cores exhibited a slight tendency for widthwise cracking, with around 30% of cracks aligned perpendicularly to the coring direction. This effect was less pronounced in interior counterparts, where the distribution of crack directions was more balanced. The highest perpendicular cracking proportions in the PS member were associated with longitudinal interior cores from the wet region, indicating a strong orientation effect related to environmental exposure. Crack density of aggregate particles in PS cores was generally lower than in PC, ranging from 0.6% to 2.0%. Notably, interior vertical specimens exhibited lower crack density, which aligns with their relatively higher modulus of elasticity and lower SDI values. The orientation of the vertical specimens parallel to compressive forces in the PS may have contributed to lower visibility of cracks, and detected deterioration, in these specimens.

These results reflect more severe aggregate damage in PC specimens, with distinct crack orientations identifiable corresponding to core orientation and depth, trends which can be observed for both the PC and PS members.

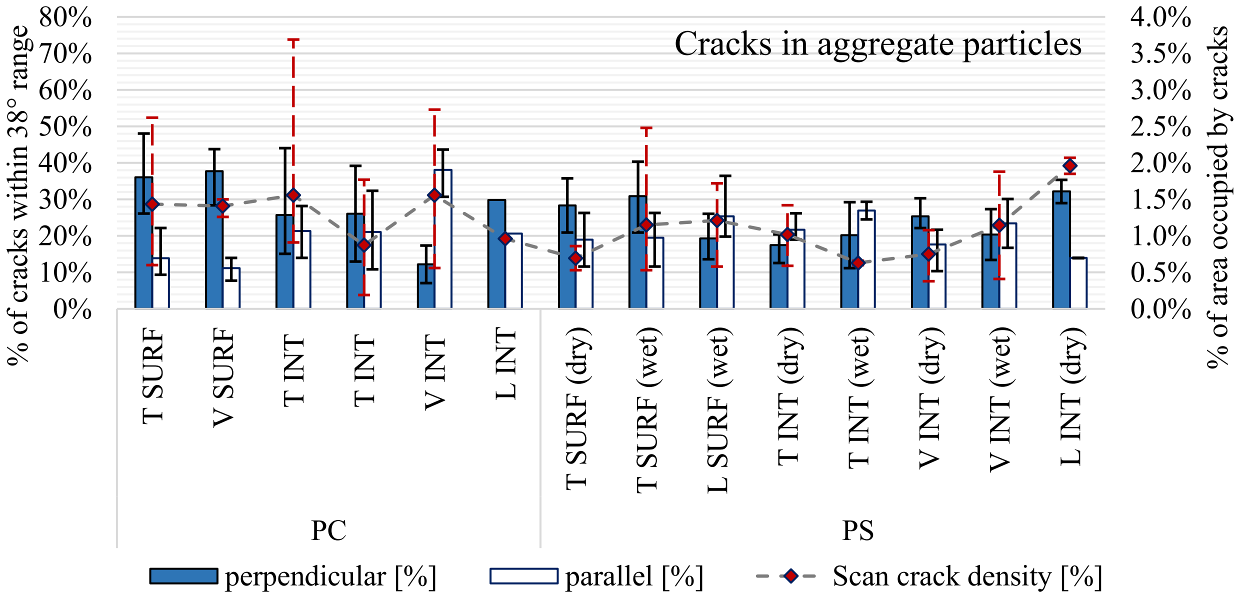

Figure 6-13 Bar graph depicting crack orientation in aggregates relative to the length of core in traced core and the percentage of scanned area occupied by cracks in sample scans from the PC and PS Error bars indicate maximum and minimum values.

Figure 6-14 presents the proportion of cracks oriented parallel and perpendicular to the coring direction in both PC and PS cores, alongside the corresponding scan crack densities within the cement paste.

In the PC member, surface cores extracted in transverse and vertical directions exhibited predominantly widthwise cracking in the cement paste, with perpendicularly oriented cracks exceeding 40% in most specimens. Such configurations are consistent with the exposure of surface regions to environmental gradients, notably drying and rewetting, which has been found to accelerate ASR-induced expansion and cracking in work by Multon et al. [40] and would synergize with surface damage such as FT and reinforcement corrosion. Interior cores extracted transversely and vertically presented more balanced distributions between perpendicular and parallel cracks. Longitudinal interior cores, however, showed a clear dominance of parallel cracking, reinforcing the finding of anisotropic properties linked to core orientation. Overall, low crack densities between 0.2 and 0.7% are consistent with limited damage and relatively high remaining mechanical properties observed in these specimens.

Cracking in the PS member followed a more distinct pattern linked to environmental exposure. Surface transverse cores from the dry region revealed high proportions of widthwise cracks, up to 56% in some cases, along with crack densities around 1.3%. This is indicative of severe deterioration mechanisms, including ASR and potential FT action with damage induced primarily parallel to the surface of the member. In contrast, transverse and longitudinal cores from the wet region exhibited reduced perpendicular cracking and lower crack densities, around 0.6% and 0.8%, respectively, suggesting the protective effect of immersion.

Transverse and longitudinal interior cores from the PS member revealed environmental and orientation-based divergence. Dry-region specimens displayed a balanced mixture of crack directions, whereas wet-region counterparts presented a moderate prevalence of widthwise cracks. Vertical cores followed a similar trend: dry-region specimens exhibited a dominance of parallel cracks (i.e., lengthwise in core), whereas wet-region cores displayed few distinguishable cracks in the cement paste and were excluded from orientation classification due to insufficient data. These findings suggest that there is a heightened sensitivity of cement paste cracking to environmental exposure and core orientation. Widthwise cracks, which are prevalent in dry and surface regions, correspond to zones of elevated mechanical damage and reduced stiffness, as evidenced by lower ME values and higher SDI/PDI indices. In contrast, lengthwise cracking, prevalent in longitudinal PC cores and vertical PS cores from interior regions, is associated with less detrimental mechanical outcomes, highlighting the anisotropic nature of ASR-induced deterioration in reinforced concrete.

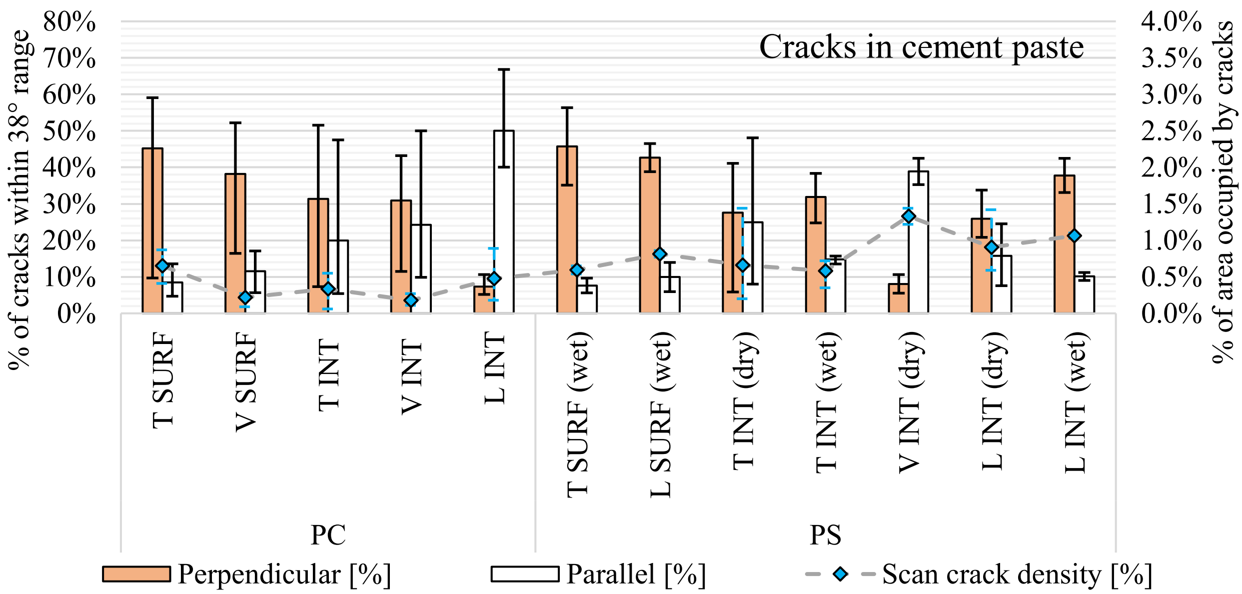

Figure 6-14 Bar graph depicting crack orientation in cement paste relative to the length of core in traced core and the percentage of scanned area occupied by cracks in sample scans from the PC and PS Error bars indicate maximum and minimum values.

6.7.2.2 Mechanical Response as a Function of Crack Patterns

The mechanical implications of crack patterns were examined by correlating surface scan data, previous microscopic results [27], and mechanical outcomes from the SDT and damage indices (SDI and PDI), and the Non-Linearity Index (NLI). The NLI, in particular, provides a directional indicator of internal cracking: values greater than unity denote cracks predominantly perpendicular to the loading direction during SDT (i.e., cracks oriented widthwise), while values below unity suggest parallel cracking.

Specimens exhibiting predominantly widthwise cracks in the cement paste, especially those extracted from surface and dry-region locations, consistently showed greater mechanical deterioration. This was characterized by increased SDI and PDI values, lower ME, and NLI values greater than unity. Otherwise, specimens with mixed or non-directional cracking generally demonstrated intermediate levels of mechanical degradation.

The NLI is linked to crack orientation in concrete, a property of ASR induced damage that is rarely captured in laboratory accelerated testing. Figure 6-15 presents the NLI of individual specimens from both members relative to the corresponding ME. Dominant crack orientations from the supplemental image analysis were multiplied by the density to adjust for damage extent and used to visually sort results to show whether specimens had dominant parallel, perpendicular or indeterminate cracking. Specimens with the indeterminate designation represent higher ME values corresponding to NLI less than unity, while specimens with perpendicular cracking represented the majority of specimens with NLI greater than unity.

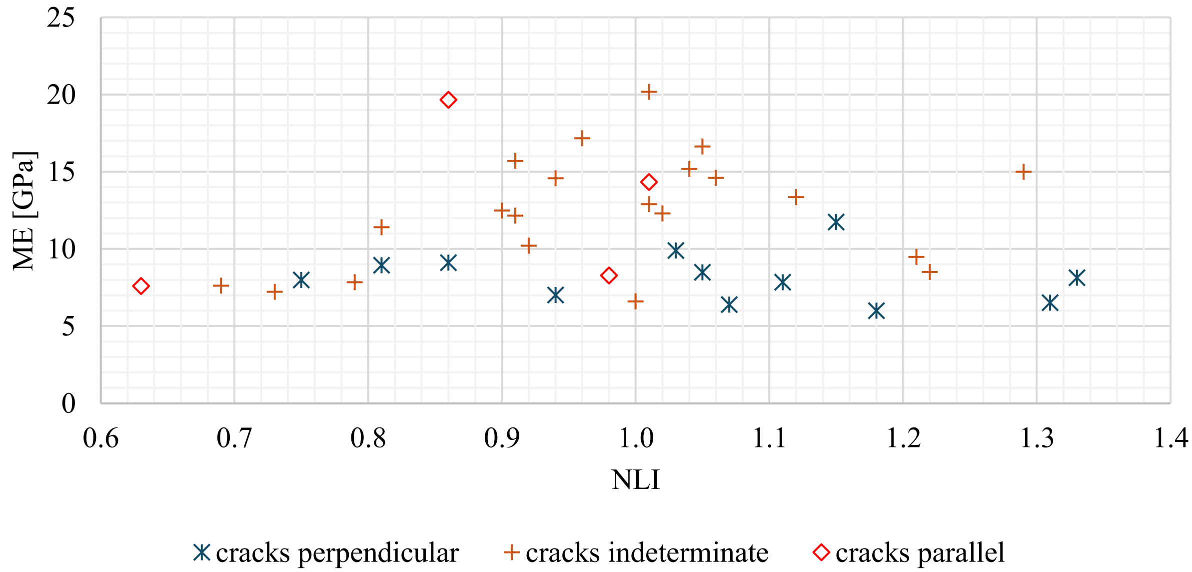

Figure 6-15 Plot depicting ME relative to NLI with dominant crack orientations (determined from the percentage of cracks in the dominant orientation multiplied by the crack density)

6.7.3 Multi-level Assessment

6.7.3.1 Validating SDT for assessing damage in concrete

To validate the mechanical results obtained through the experimental campaign, semi-quantitative microscopic evaluations were performed using the DRI on companion specimens extracted from the member assessed in this study (i.e., PC and PS), with cores drilled in various directions (i.e., vertical, longitudinal, and transverse) resulting in a minimum of 120 cm^2 investigated per condition. Each core was longitudinally cut using a diamond-blade masonry saw, then progressively polished through a sequence of abrasives (grit sizes: 30, 60, 140, 280 [80–100 μm], 600 [20–40 μm], 1200 [10–20 μm], and 3000 [4–8 μm]) to obtain a flat, clean surface suitable for microscopic examination. Following surface preparation, a

1 × 1 cm reference grid was delineated over the polished face of each specimen. The DRI assessment was then conducted using a stereomicroscope at 15–16× magnification. In this protocol, distinct deterioration features, such as open cracks in the cement paste and aggregate particles with and without reaction products, are identified and counted within each 1 cm² square. Each feature is assigned a weighting factor (Table 2-3) that reflects its relative significance in characterizing the distress mechanism under investigation (in this case, the alkali–silica reaction), as proposed by Villeneuve and Fournier [41]. The cumulative weighted score yields the DRI number, where higher scores indicate more severe damage. Although the target evaluation area per specimen for field concrete is 200 cm², the final results are normalized to a 100 cm² reference surface to ensure comparability across specimens.

Table 2-3 Weighting factors used for Damage Rating Index (DRI) Microscopic Technique [42] (Duplicated for ease of reference)

Damage features		Weight factors
Crack in coarse aggregate	CCA	0.25
Opened crack in aggregate	OCA	2
Crack with reaction product in aggregate	OCA_{RP}	2
Debonded/dislodged aggregate	Debond	3
Crack in cement paste	CCP	3
Crack with reaction product in cement paste	CCP_{RP}	3
Disaggregate/corroded aggregate particle	DAP	2

By analyzing SDT and DRI results (Figure 6-7 and Figure 6-16), one notices that in the PC member, which was exposed to drying conditions, the DRI revealed pronounced surface damage. Vertical and transverse surface specimens exhibited DRI numbers of 1120 and 1000, respectively, while the transverse internal zone yielded a value of 1020. By contrast, vertical and longitudinal internal cores showed lower damage, with DRI numbers of 820 and 840, respectively. These trends closely align with the SDT results, where vertical and longitudinal cores exhibited higher modulus values and lower SDI (Table 1-2). The consistency between DRI and mechanical indices supports the assessment interpretation that surface locations depict higher deterioration compared to the internal locations of reinforced concrete members affected by ASR.

The PS member exhibited a more complex deterioration pattern due to the exposure conditions (i.e., dry and wet), Notably, dry-surface longitudinal cores exhibited the highest DRI number (1220), confirming the mechanical observation of greater degradation in this region, which had also registered the lowest modulus of elasticity and highest SDI. Transverse cores from the dry surface also yielded elevated DRI numbers (1120), in contrast to the wet-surface transverse cores, which exhibited a significantly lower number (780). A similar wet-to-dry disparity was observed in the longitudinal direction, with DRI decreasing from 1220 (dry) to 1060 (wet). Vertical internal cores, both in wet and dry conditions, presented the lowest DRI numbers among all PS specimens (840 and 760), consistent with their greater residual mechanical properties.

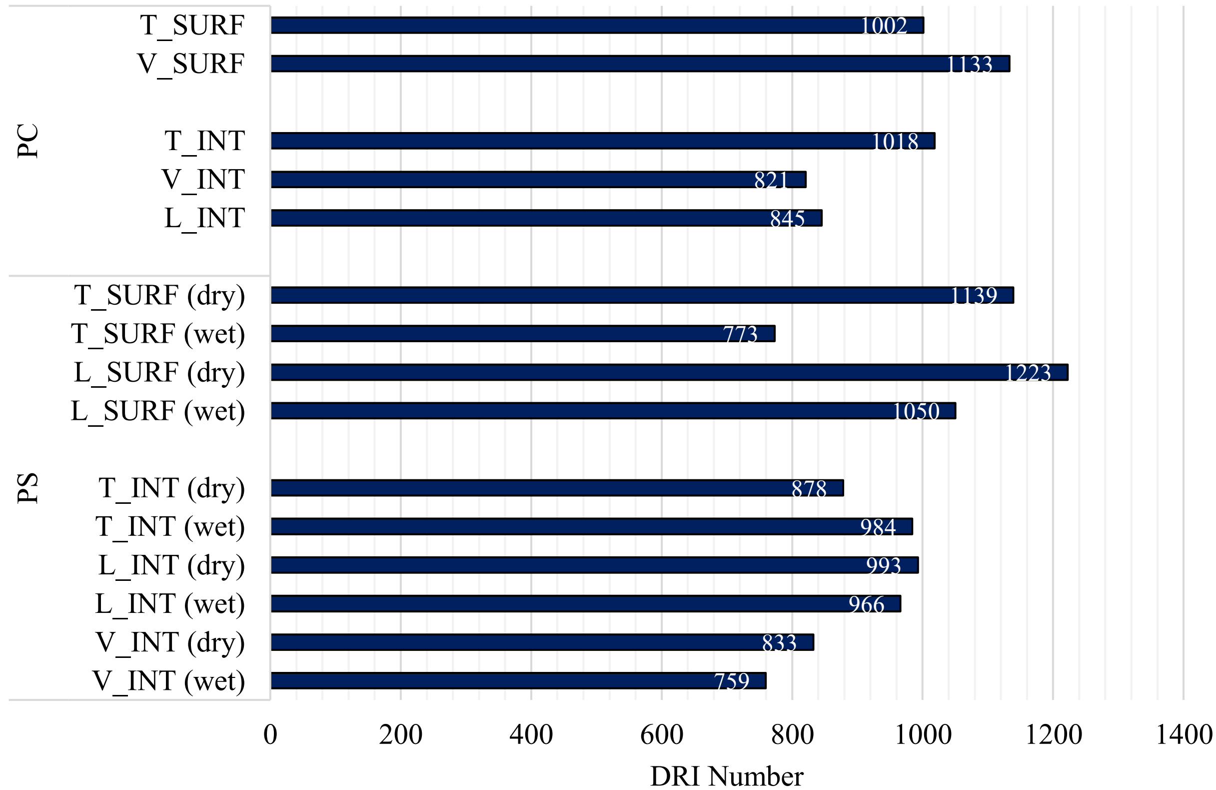

Figure 6-16 Bar graph summarizing DRI results from PC and PS members from distinct core orientations (transverse - T, vertical -V and longitudinal - L) and depths (surface - SURF vs. interior - INT)

The DRI outcomes obtained in this study corroborate the mechanical evaluation results, including both SDT-derived parameters (i.e., SDI, PDI, and ME) and compressive strength. Core specimens with elevated DRI values consistently exhibited higher damage indices (i.e., SDI and PDI) and lower residual mechanical properties (i.e., modulus of elasticity and compressive strength), thereby confirming the diagnostic consistency between microstructural and mechanical deterioration assessments. Furthermore, the directional analysis of PC and PS specimens supports the presence of the "expansion transfer" phenomenon, wherein increased damage is observed along less restrained directions. The results obtained are consistent with those reported by Zahedi et al. [18].

6.7.3.2 Estimated Expansion

Sanchez et al. [6, 21, 43] introduced a multi-level assessment protocol for evaluating concrete experiencing ASR induced expansion and damage. This approach combines results of microscopic (i.e., DRI) and mechanical tests (i.e., SDT, modulus of elasticity, and compressive strength) conducted on cores extracted from the structure under evaluation and compares results to data from accelerated laboratory tests. Sanchez et al. [6, 43] developed a chart of values (Table 6-1) linking internal concrete damage to expansion of concrete laboratory specimens with various natures (i.e. different aggregate types and combinations of fine and coarse) and concrete strengths (i.e. 25, 35 and 45 MPa). As such, this approach seeks to estimate the attained expansion, providing essential insights into the diagnosis, prognosis, and potential structural implications.

The global chart of values proposed by Sanchez et al. [6, 43] provides a comprehensive reference for estimation of expansion due to ASR developed from testing of 12 distinct aggregates. However, the range of DRI or SDT values corresponding to a given expansion level often overlap due to the large selection of concrete mixtures (i.e. intrinsic heterogeneity in concrete) and reactive aggregate types (i.e., distinct types and natures) used in its development. To increase the accuracy of this technique Sanchez et al. proposed that practitioners might use the chart 1) through averaging the envelope values where the specific aggregate was unknown or 2) by selecting data from a specific reference concrete with a similar reactive aggregate to the concrete under analysis. In this work results are compared to reference datasets from free-expansion tests conducted on concrete specimens incorporating a reactive silicious limestone coarse aggregate, (as the ones used in the PS and PC construction), as reported by Sanchez et al. [43]. Reference data sets with 28-day compressive strengths representing compressive strengths of 25MPa and 35 MPa were available. Since the 28-day design strength of the PC and PS was reported to be 24 MPa [30] and ongoing hydration is expected to increase concrete strength by 5 - 30%, an average value of the two reference mixtures was used to estimate expansion.

The results obtained in this study, through mechanical testing and microscopic analysis, were used to estimate the expansion reached by the ASR-affected PC and PS members, as presented in Table 6-3. The associated free expansions for different depths were estimated based on DRI and SDI results representing core samples extracted at various depths (i.e., surface vs. interior) and conditions (i.e., vertical versus transverse, dry versus wet). Comparison of the estimated expansions resulting from the distinct mechanical and microscopic techniques reveal notable discrepancies for PC core specimens while PS core specimens result in similar damage levels regardless of the initial investigative method. These results emphasize the importance of multi-level assessment incorporating both microscopic and mechanical assessments to perform robust assessments, particularly for field structures where the development of ASR induced deterioration is impacted by various stress states within the members of interest. Although the data envelopes proposed by Sanchez et al. [43] has been evaluated for application to reinforced concrete members presenting anisotropic behaviour at the lab scale in the work of Zahedi et al. [19], validation against a wide range of ASR affected structures is still necessary for widespread adoption of this assessment.

Estimated expansion in the PC was found to be notably higher when estimated from DRI values compared to SDI for most core orientations and depths. This indicates that the cracking observed during DRI was more extensive than the corresponding mechanical performance indicated. A cohesive effect of the ASR gel generated in the field structure coupled with anisotropic properties resultant from the stress states within the PC member (i.e. thinner cracks in the direction of high stress) may contribute to the observed mismatch in addition to factors previously discussed for different core orientations (i.e. crack orientations relative to applied load during SDT). A stronger agreement between microscopic and mechanical estimated expansions in PS specimens, which were frequently observed to have fewer locations where secondary products (i.e., ASR gel) were present in cracks. In contrast, higher estimated expansion occurred for PS core specimens from the dry region where wider cracks were observed in cement paste [27] parallel to the surface (i.e. parallel to the direction of loading during SDT) which would be expected to result in a larger height reduction (i.e. larger strain).

Table 6-3 Summary of estimated expansion estimated from experimental DRI and SDT results

	Core orientation	*DRI*	*Damage level (DRI)†*	*Estimated expansion [%] * [43] (DRI)*	SDI	Damage level (SDT)	Estimated expansion [%] * [43] (SDI)
PC Surf	**Transverse**	*1002*	*Very high*	*0.30*	*0.34*	*Very high*	*0.32*
	Vertical	*1133*	*Very high*	*0.35*	*0.23*	*Moderate*	*0.10*
PC Int	**Transverse**	*1018*	*Very high*	*0.31*	*0.23*	*Moderate*	*0.10*
	Longitudinal	*845*	*High*	*0.24*	*0.16*	*Marginal*	*0.05*
	Vertical	*821*	*High*	*0.24*	*0.22*	*Moderate*	*0.10*
PC Int	**Avg. of T, L, V**	**895**	***High***	**0.26**	***0.20***	***Moderate***	***0.08***
PS Surf	**Transverse - dry**	*1139*	*Very High*	*0.35*	*0.25*	*Moderate*	*0.14*
	Transverse - wet	*773*	*High*	*0.22*	*0.31*	*High*	*0.26*
	Longitudinal - dry	*1223*	*Very High*	*0.38*	*0.37*	*Very high*	*0.38*
	Longitudinal - wet	*1050*	*Very High*	*0.32*	*NA*	*NA*	*NA*
PS Int	**Transverse - dry**	*878*	*High*	*0.26*	*0.37*	*Very high*	*0.38*
	Transverse - wet	*984*	*High*	*0.30*	*0.31*	*High*	*0.26*
	Longitudinal - dry	*993*	*High*	*0.30*	*0.40*	*Very high*	*0.44*
	Longitudinal - wet	*966*	*High*	*0.29*	*0.30*	*High*	*0.24*
	Vertical - dry	*833*	*High*	*0.24*	*0.27*	*High*	*0.18*
	Vertical - wet	*759*	*High*	*0.21*	*0.23*	*High*	*0.23*
PS Int	**Avg. T, L, V**	**902**	***High***	**0.27**	***0.31***	***High***	***0.26***
	Avg. T, L, V - dry	**901**	***High***	**0.27**	***0.35***	***Very high***	***0.34***
	Avg. T, L, V - wet	**903**	***High***	**0.27**	***0.28***	***High***	***0.20***

** relative to mixture incorporating a similar aggregate (i.e., lithotype and reactivity level*

† reference expansion ranges were used as follows: Negligible (0.000-0.030), Marginal (0.031-0.070), Moderate (0.071-0.150), High (0.151-0.300), Very high (0.301-0.500) and Ultra-High (0.501-1.000)

The outcomes of this overall condition assessment approach are presented in Figure 6-17, depicting that estimated expansion levels varied across the members, reflecting the combined influence of restraint and environmental exposure conditions.

In the PC member, higher estimated expansions were found in the transverse and vertical surface and internal cores (ranging from 0.17% to 0.31%). In contrast, longitudinal cores presented the lowest expansion estimate (0.15%). These results confirm that expansion was more pronounced in directions associated with reduced restraint, supporting the hypothesis of the expansion transfer phenomenon [17, 18].

In the PS member, the estimated expansions exhibited the largest variation due to moisture exposure. Longitudinal and transverse cores from the dry surface reached estimated expansions of up to 0.38%. In contrast, cores from wet-surface regions exhibited substantially lower expansion values (e.g., 0.24% in PS T surf wet). This disparity is further observed in vertical internal cores, which displayed the lowest expansion values in both dry (0.21%) and wet (0.22%) regions, in alignment with their limited deterioration.

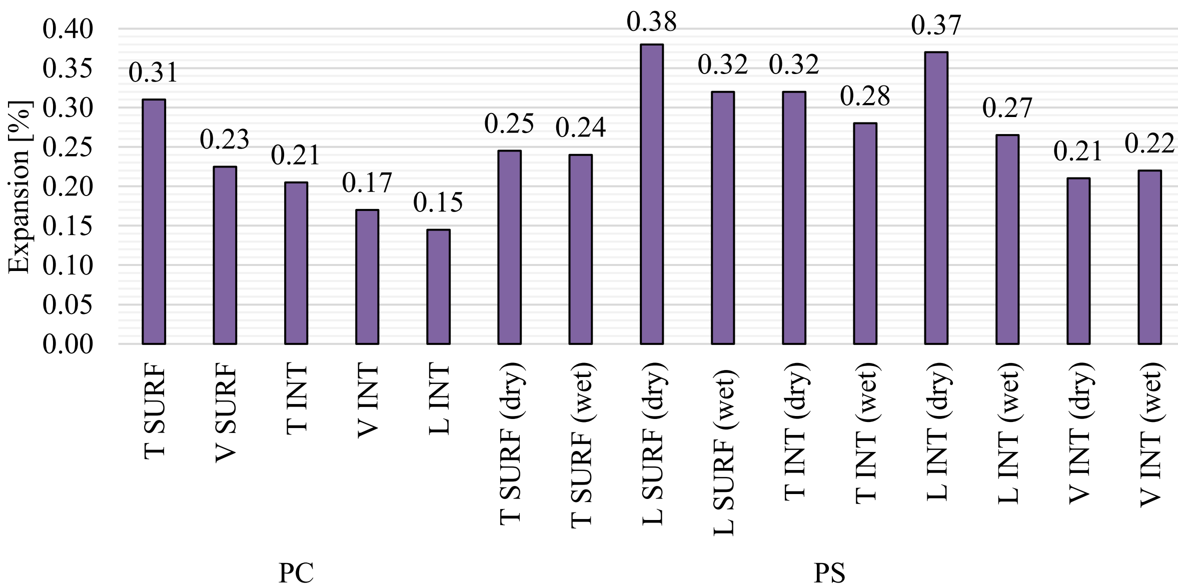

Figure 6-17 Bar graph depicting estimated expansion associated with PC and PS core specimens at distinct conditions (estimated expansion represents the average of expansion estimated from DRI and SDI tests).

6.7.4 Statistical Analysis

In order to assess the validity and significance of the DRI results obtained in this study, multivariable analysis of variance (MANOVA) was performed, taking into account the different members (i.e., PC vs. PS), depths (i.e., surf vs. internal), core orientations (i.e., transverse, longitudinal and vertical), environments (i.e., wet vs. dry), and crack orientation within cores. All statistical analyses were conducted with a significance level of 5% (i.e., confidence interval of 95%).

The statistical analysis identified statistically significant differences (i.e., an 'F' value greater than the critical F value and p value less than 0.05) in the ME between the PC and PS, agreeing with observed trends wherein the static and dynamic modulus of PS specimens were observed to be lower than PC specimens. Differences in SDI value for cores exhibiting distinct crack orientations as per section 6.7.2 were also found to be statistically different, agreeing with observed trends wherein cracking oriented parallel to loading or determined to exhibit lower ('mixed) damage presented lower SDI values.

Table 6-4 Statistical analysis of experimental SDI and ME results using MANOVA to compare the impact of member type (i.e., PC vs. PS) and depth (i.e., surface vs. internal)

	SDI						ME					
	F	**F_{critic}**	**$F>F_{crit}$**	**p**	**α**	**p< α**	**F**	**F_{critic}**	**$F>F_{crit}$**	**P**	**α**	**p< α**
PC vs. PS	0.85	3.32	-	0.167	0.05	-	***5.05***	***3.32***	***X***	***0.012***	***0.05***	***X***
surf vs. int	0.39	3.32	-	0.681	0.05	-	0.01	3.32	-	0.990	0.05	-
PC: T vs. V	0.02	3.98	-	0.976	0.05	-	0.21	3.98	-	0.816	0.05	-
PS: T vs. L	0.34	4.26	-	0.721	0.05	-	1.05	4.26	-	0.390	0.05	-
PC: surf vs int	2.69	3.63	-	0.099	0.05	-	0.11	3.63	-	0.901	0.05	-
PS: surf vs. int	0.01	3.74	-	0.996	0.05	-	0.08	3.74	-	0.925	0.05	-
PS: wet vs. dry	0.24	3.74	-	0.790	0.05	-	1.58	3.74	-	0.242	0.05	-
Crack orient.	***6.68***	***2.92***	***X***	***0.001***	***0.05***	***X***	0.71	2.92	-	0.553	0.05	-

6.8 Conclusions

This study presented a mechanical assessment of the PC and PS members from Montreal's Champlain Bridge (CB), decommissioned in 2019 after nearly 60 years of service. The structure experienced significant deterioration primarily due to ASR, FT, and reinforcement corrosion. A multi-level evaluation protocol was applied, integrating primarily mechanical testing (i.e., SDT, compressive strength), non-destructive testing (i.e., RF), and microscopic analysis (i.e., DRI), to characterize the cause(s) but especially the extent of damage. The key findings include:

- Mechanical testing:
    - Damage severity varied by member, depth, and orientation. The PS, exposed to dry and semi-submerged conditions, exhibited more advanced deterioration than the PC, with ME reductions exceeding 50% and compressive strengths ranging from 16 to 28 MPa.
    - Core orientation and depth significantly influenced mechanical performance. Cores extracted in three distinct orientations (transverse, longitudinal and vertical) exhibited distinct trends. Additionally, in some core orientations specimens displayed different trends in surface and interior locations. The lowest damage was observed in internal longitudinal PC cores and vertical PS cores from the wet region. In contrast the highest damage was found in surface transverse PC cores and longitudinal PS cores from the dry region.
    - Environmental exposure conditions impacted mechanical performance. This was most evident for specimens from surface locations which exhibited higher damage and are expected to have been more affected due to cyclic moisture and FT. In the PS, dry regions exhibited higher damage compared to specimens from the wet region for both surface and internal concrete.
    - Anisotropic damage patterns were evident, with crack orientation (i.e. lengthwise or widthwise in the core) influencing mechanical response. Anisotropy observed in core specimens was strongly linked to core orientation.
    - Crack orientation was a key indicator of mechanical degradation. Specimens with predominantly widthwise cracks (perpendicular to loading) exhibited higher SDI and lower

ME, while those with lengthwise cracks (parallel to loading) showed better mechanical performance.

- Multi-level assessment:
    - RF testing was validated. Dynamic ME trends obtained from RF measurements closely matched static ME results. RF represents a useful tool for evaluating core specimens.
    - The multi-level approach proved effective. SDT and DRI resulted in consistent trends, and estimated overall expansion levels aligned with observed damage trends. Estimated expansion for the PC ranged from 0.23% to 0.31% and 0.15% to 0.21% for surface and internal core specimens respectively while in the PS expansion ranged from 0.24% to 0.38% and 0.21% to 0.37%. Estimated expansion for the dry region in the PS was found to be notably higher than the wet region.
    - Supplemental image analysis enhanced interpretation. Crack density and orientation data obtained via digital scanning and ImageJ analysis provided valuable insights into damage anisotropy and its mechanical implications.

6.9 References

1. WeatherSpark Weather History at Montréal/Saint-Hubert Airport. https://weatherspark.com/h/m/147211/2022/5/Historical-Weather-in-May-2022-at-Montréal-Saint-Hubert-Airport-Canada.

2. Bérubé M-A, Durand B, Vézina D, Fournier B (2000) Alkali-aggregate reactivity in Québec (Canada). Canadian Journal of Civil Engineering 27:226–245

3. Bérubé M-A, Frenette J (1995) Évaluation de la Réactivité Alcaline dans le Béton des Piles 12, 18 et 20 W du Pont Champlain: Complément au rapport soumis en février 1994. Sainte-Foy, Quebec

4. Carlin GP, Mirza MS, Gaudreault M (1996) Rehabilitation Measures for Champlain Bridge, Montreal, Canada. Canadian Journal of Civil Engineering 23:1326–1340

5. Sanchez LFM, Fournier B, Jolin M, Duchesne J (2015) Reliable quantification of AAR damage through assessment of the Damage Rating Index (DRI). Cem Concr Res 67:74–92

6. Sanchez LFM, Drimalas T, Fournier B, Mitchell D, Bastien J (2018) Comprehensive damage assessment in concrete affected by different internal swelling reaction (ISR) mechanisms. Cem Concr Res 107:284–303

7. Smaoui N, Bérubé MA, Fournier B, Bissonnette B, Durand B (2004) Evaluation of the expansion attained to date by concrete affected by alkali-silica reaction. Part I: Experimental study. Canadian Journal of Civil Engineering 31:826–845

8. Multon S, Cyr M, Sellier A, Leklou N, Petit L (2008) Coupled effects of aggregate size and alkali content on ASR expansion. Cem Concr Res 38:350–359

9. Smaoui N, Fournier B, Bérubé MA, Bissonnette B, Durand B (2004) Evaluation of the expansion attained to date by concrete affected by alkali-silica reaction. Part II: Application to nonreinforced concrete specimens exposed outside. Canadian Journal of Civil Engineering 31:997–1011

10. Berra M, Faggiani G, Mangialardi T, Paolini AE (2010) Influence of stress restraint on the expansive behaviour of concrete affected by alkali-silica reaction. Cem Concr Res 40:1403–1409

11. Bérubé M-A, Fournier B, Côté T (2012) Using the Damage Rating Index for Assessing the Expansion of Concrete Affected by Freeze-thaw, Sulphate attack, or ASR. 14th International Conference on Alkali-Aggregate Reaction

12. Gautam BP, Panesar DK, Sheikh SA, Vecchio FJ (2017) Effect of coarse aggregate grading on the ASR expansion and damage of concrete. Cem Concr Res 95:75–83

13. Rivard P, Saint-Pierre F (2009) Assessing alkali-silica reaction damage to concrete with non-destructive methods: From the lab to the field. Constr Build Mater 23:902–909

14. Sargolzahi M, Kodjo SA, Rivard P, Rhazi J (2010) Effectiveness of nondestructive testing for the evaluation of alkali-silica reaction in concrete. Constr Build Mater 24:1398–1403

15. Kongshaug SS, Oseland O, Kanstad T, Hendriks MAN, Rodum E, Markeset G (2020) Experimental investigation of ASR-affected concrete – The influence of uniaxial loading on the evolution of mechanical properties, expansion and damage indices. Constr Build Mater. https://doi.org/10.1016/j.conbuildmat.2020.118384

16. Multon S, Toutlemonde F (2006) Effect of applied stresses on alkali-silica reaction-induced expansions. Cem Concr Res 36:912–920

17. Gautam BP, Panesar DK, Sheikh SA, Vecchio FJ (2017) Effect of multiaxial stresses on alkali-silica reaction damage of concrete. ACI Mater J 114:595–604

18. Zahedi A, Trottier C, Sanchez L, Noël M (2022) Evaluation of the induced mechanical deterioration of alkali-silica reaction affected concrete under distinct confinement conditions through the Stiffness Damage Test. Cem Concr Compos. https://doi.org/10.1016/j.cemconcomp.2021.104343

19. Zahedi A, Trottier C, Sanchez LF, Noël M (2022) Condition assessment of alkali-silica reaction affected concrete under various confinement conditions incorporating fine and coarse reactive aggregates. Cem Concr Res. https://doi.org/10.1016/j.cemconres.2021.106694

20. Chrisp TM, Waldron P, Wood JGM (1993) Development of a non-destructive test to quantify damage in deteriorated concrete. Magazine of Concrete Research 45:247–256

21. Sanchez LFM (2014) Contribution to the Assessment of Damage in Aging Concrete Infrastructures Affected by Alkali-Aggregate Reaction. PhD, Université Laval

22. Sanchez LFM, Fournier B, Jolin M, Bastien J (2014) Evaluation of the stiffness damage test (SDT) as a tool for assessing damage in concrete due to ASR: Test loading and output responses for concretes incorporating fine or coarse reactive aggregates. Cem Concr Res 56:213–229

23. Sanchez LFM, Fournier B, Jolin M, Bastien J (2015) Evaluation of the Stiffness Damage Test (SDT) as a tool for assessing damage in concrete due to alkali-silica reaction (ASR): Input parameters and variability of the test responses. Constr Build Mater 77:20–32

24. Sanchez LFM, Fournier B, Jolin M, Bastien J, Mitchell D (2016) Practical use of the Stiffness Damage Test (SDT) for assessing damage in concrete infrastructure affected by alkali-silica reaction. Constr Build Mater 125:1178–1188

25. ASTM Standard C215 (2020) Standard Test Method for Fundamental Transverse , Longitudinal , and Torsional Resonant Frequencies of Concrete Specimens. ASTM standard 1–7

26. ASTM C42/C42M-20 Standard Test Method for Obtaining and Testing Drilled Cores and Sawed Beams of Concrete. https://doi.org/10.1520/C0042_C0042M-20

27. Kristufek L, Sanchez L, Martín-Pérez B, Noël M PAPER 2: Microscopic investigation of surface and interior cores from members of Montreal's Old Champlain Bridge.

28. Kristufek L, Sanchez LF, Martín-Pérez B, Noël M (2025) Visual and non-destructive testing of pier cap and pier shaft members from the old Champlain Bridge. Buildings 15:3262

29. Sanchez LFM, Fournier B, Mitchell D, Bastien J (2020) Condition assessment of an ASR-affected overpass after nearly 50 years in service. Constr Build Mater 236:117554

30. Orcutt C, Cook WD, Mitchell D (2020) Response of Variable-Depth Reinforced Concrete Pier Cap Beams. Journal of Bridge Engineering. https://doi.org/10.1061/(ASCE)BE.1943-5592.0001548

31. ACI Committee 318 (2019) Building code requirements for structural concrete (ACI 318-19) : an ACI standard. Farmington Hills, MI

32. Kosmatka SH, Wilson ML (2011) Design and Control of Concrete Mixtures, 15th ed. Portland Cement Association, Skokie, Illinois, USA

33. Lange DA (1994) Long-Term Strength Development of Concrete.

34. Chen C, Wang L, Liu R, Zhu P, Liu H, Wang X, Yu J, Chen Y (2023) Chloride penetration of concrete exposed to dry-wet cycle with various dry-wet ratios and temperature. Constr Build Mater. https://doi.org/10.1016/j.conbuildmat.2023.132883

35. Deschenes RA, Giannini ER, Drimalas T, Fournier B, Hale WM (2018) Effects of moisture, temperature, and freezing and thawing on Alkali-Silica reaction. ACI Mater J 115:575–584

36. Rosenqvist M, Bertron A, Fridh K, Hassanzadeh M (2017) Concrete alteration due to 55 years of exposure to river water: Chemical and mineralogical characterisation. Cem Concr Res 92:110–120

37. Rosenqvist M (2016) Frost-induced deterioration of concrete in hydraulic structures Interactions between water absorption, leaching and frost action. Ph.D. Dissertation, Lund University

38. Rosenqvist M, Pham LW, Terzic A, Fridh K, Hassanzadeh M (2017) Effects of interactions between leaching, frost action and abrasion on the surface deterioration of concrete. Constr Build Mater 149:849–860

39. Medeiros R, Bergmann A, Olajide O, Trottier C, Sanchez L, Fournier B (2025) Impacts of anisotropy and exposure conditions on ASR-induced deterioration in columns from the Robert-Bourassa/Charest overpass after nearly 50 years of service. Magazine of Concrete Research. https://doi.org/10.1680/jmacr.25.00077

40. Multon S, Toutlemonde F (2010) Effect of moisture conditions and transfers on alkali silica reaction damaged structures. Cem Concr Res 40:924–934

41. Villeneuve V, Fournier B, Duchesne J (2012) Determination of the damage in concrete affected by ASR - the Damage Rating Index (DRI). In: 14th ICAAR International conference on the alkali aggregate reaction. p 033012

42. Véronique Villeneuve (2011) Détermination de l’endommagement du béton par méthode pétrographique quantitative.

43. Sanchez LFM, Fournier B, Jolin M, Mitchell D, Bastien J (2017) Overall assessment of Alkali-Aggregate Reaction (AAR) in concretes presenting different strengths and incorporating a wide range of reactive aggregate types and natures. Cem Concr Res 93:17–31

Chapter 7: Paper 4

Condition assessment of pier cap affected by alkali silica reaction (ASR) after 57 years of service[2]

Abstract

The Champlain Bridge, which stood from 1962 to 2019, was a significant highway structure spanning the St. Lawrence River and St. Lawrence Seaway. It was constructed using concrete incorporating an alkali-silica reactive aggregate. Decommissioning of the structure presented a unique research opportunity to investigate how ASR-induced damage developed in a concrete member with various levels of restraint. Following decommissioning of the pier cap, cores were extracted longitudinally from a number of restraint locations within the member (i.e., top, middle, and bottom regions) and investigated using a multi-level assessment protocol through microscopic (i.e., damage rating index - DRI) and mechanical (i.e., stiffness-damage test - SDT) test procedures. Cracking traveling parallel to the coring direction in extracted cores (i.e., parallel to main reinforcement) was observed in all regions, indicating an influence of restraint conditions on ASR-induced development. Moreover, increased expansion due to ASR, similar to reference cores extracted transversally, was identified in cores extracted from the highest reinforcement region while cores from the middle and bottom regions displayed a reduced deterioration.

7.1 Introduction

The iconic Champlain Bridge in Montreal, Canada, was a 3.4 km highway bridge passing over the St. Lawrence River and St. Lawrence seaway which was in service between 1962 and 2019. The reinforced concrete structure utilized a T-shaped pier cap – pier shaft support system to support 6 lanes of traffic including significant truck traffic as part of a critical shipping route between Canada and the USA. The pier caps from the Champlain Bridge were noted to be demonstrating signs of internal swelling reactions (ISR)

---

[2] This chapter has been published in *Magazine of Concrete Research* (Kristufek, L., Sanchez, L.F.M., Martín-Pérez, B., and Noël, M.. (2025). "Condition assessment of a decommissioned pier cap affected by alkali-silica reaction after 57 years of service." Magazine of Concrete Research, 1-14. https://doi.org/10.1680/jmacr.25.00078

after 20 years of service. A condition assessment was then conducted, and alkali-silica reaction (ASR) was confirmed to be affecting the pier shafts in the mid 1990's [1] with ASR in pier caps confirmed more recently [2]. ASR is a chemical reaction between unstable mineral phases from aggregates and the alkali-hydroxides from the concrete pore solution (i.e. Na+, K+, OH-). ASR generates a secondary product that swells upon moisture uptake, resulting in concrete cracking. Such cracking results in reductions in stiffness, tensile strength and eventually compressive strength [3].

The extraction of cores is frequently used to assess concrete structures experiencing signs of ISR induced deterioration (i.e. following visual inspection and non-destructive tests). Upon extraction, laboratory test procedures are conducted to identify the major cause(s) leading to deterioration along with the extent of current and potential for further deterioration. This can be used for long-term planning of repairs and/or replacement of structures. However, it is known that ASR-induced deterioration varies in reinforced concrete due to the location (e.g. exposed vs. non-exposed), direction (i.e., vertical vs. transverse vs. longitudinal) and restraint conditions [4, 5]; therefore, appraising and quantifying ASR induced damage is quite challenging [6] and a comprehensive approach is often required.

Comprehensive assessments after core extraction are generally composed of non-destructive techniques (NDT's) such as resonant frequency, modulus of elasticity (i.e., static), and the stiffness-damage test (SDT) along with destructive testing such as compressive strength. Moreover, microscopic evaluation may include the damage-rating index (DRI), scanning electron microscopy (SEM with or without EDS/EDX) and petrography. Sanchez et al. [3] proposed using a multi-level protocol comprising microscopic and mechanical techniques (e.g. SDT and DRI) to assess the current condition of ISR affected concrete. This protocol has been successfully used to identify both the cause and extent of ISR-induced deterioration [4, 7, 8]. However, given the geometry and reinforcement ratios within reinforced concrete members, ASR-induced deterioration may present anisotropic behaviours, which leads to unique patterns of induced damage as a function of distinct directions [5, 9–13]. In this work, cores were extracted from different locations (i.e., varying distances from the reinforcement) and directions (i.e., perpendicular and parallel to the main reinforcement bars) from an ASR- affected pier cap. Using the multi-level assessment and other imaging techniques, the anisotropic behaviour within the pier cap member is investigated. Discussions then focus on the impact of anisotropy—defined as the directional dependency of properties—on the outcomes of microscopic and mechanical tests.

7.2 Background

In Canada, ASR-induced deterioration is a common concern for concrete infrastructure including bridges and dams [4, 14–17]. The development of ASR depends on a number of factors such as the concrete mixture (e.g. amount of alkali-hydroxides in concrete and reactivity of aggregates used), exposure conditions (e.g. moisture conditions, average temperatures) and restraint conditions (e.g. high vs. low reinforcement ratios). Due to the variability of these factors, exacerbated by the harsh climate faced by infrastructure in Canada signs of deterioration often vary, making it challenging to visually assess the current level of deterioration. In Montreal temperatures range from average minimum temperatures in January of -13.5 °C to average maximum temperatures in July of 26.7 °C [18] with the environment around the Champlain Bridge experiencing high humidity due to the St. Lawrence River. The restraint conditions in reinforced concrete members further introduce a variety of stress states that impact ASR development with increased expansion occurring in areas with less restraint while reduced expansion due to ASR occurring in highest restraint regions. Therefore, a deeper understanding of the behavior of ASR in reinforced concrete under various stress states is essential to better identify its impact on induced damage, such as stiffness, mechanical properties, and physical integrity losses of affected members.

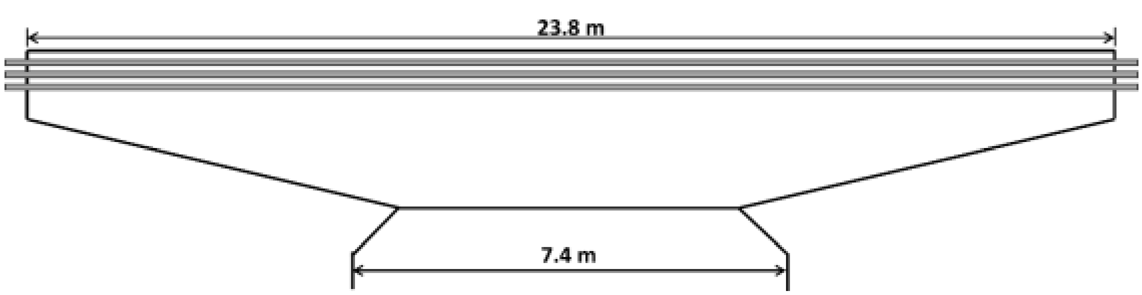

Figure 7-1 Schematic of the hammer head pier cap with location of external post-tensioning at top of member (grey)

The ‘hammer head’ pier cap discussed in this work (Figure 7-1) is one of 48 similar pier caps in the Champlain bridge and is a commonly used design in T-type concrete highway structures. Trends identified in this member are expected to be relevant to many structures constructed between the early 1960’s and 1980’s in this region due to the similar geometry and concrete practices. The pier cap investigated is highly reinforced; deterioration including discoloration from de-icing salt exposure and cracking were noted during condition assessments of the member. Ultimately, rehabilitation procedures were undertaken, including an encapsulation repair (replacing surface concrete of the entire member) to increase durability after 42 years in service [19, 20] and three Dywidag bars were added to provide additional longitudinal post tensioning after 46 years in service [21].

7.2.1 Deterioration of reinforced concrete members experiencing various stress states

Cracking due to ASR in reinforced concrete has been found to be mainly developed parallel to the main reinforcement bars [5] with ASR damage in a given direction being inversely proportional to the level of restraint [10, 13, 22]. It has been previously found that ASR expansion is anisotropic and stress-state dependent [13] with anisotropy becoming more pronounced with increasing expansion [23]. This presents a challenge for the evaluation of more complex reinforced concrete members, such as pier caps, which often have non-uniform reinforcement configurations resulting in variable stress-states within the member which in turn leads to variable levels of ASR-induced deterioration. Confidentiality issues for in-service structures as well as the potential for added complexity of deterioration mechanisms such as corrosion [24] has resulted in limited literature on real-world performance of ASR affected structures.

Concrete with a high degree of anisotropy results in distinct SDT outcomes per core orientation [11]. Although averaging results from three distinct directions have been found to give representative estimates of ASR damage [11] this may not be representative for all reinforced concrete members and stress-states.

In ASR-affected concrete, the modulus of elasticity is most affected by ASR due to cracking of the aggregate as opposed to reductions in compressive strength which are only significant at high levels of deterioration when cracks propagate into the cement paste [3]. It has been found that the direction of cracking within a concrete specimen influences the concrete's modulus of elasticity [11] due to the 'crack closure effect' under test loading. Consequently, the ability to close cracks parallel to the test load direction results in higher modulus of elasticity when compared to cracks perpendicular to the test load direction (i.e., lower modulus of elasticity) [5, 13]. Gautam et al. (2017) found an elastic modulus reduction of up to 26% for samples oriented parallel to primary restraint compared to samples oriented perpendicular to primary restraint (i.e. cracks oriented cross-sectionally rather than lengthwise in a test specimen) in biaxially restrained samples [13] while Zahedi et al. (2022) found a modulus reduction of 59% at only 0.15% expansion in 2D restrained blocks [5]. In cores extracted from slab bridges experiencing ASR in fine aggregates, Barbosa et al. 2018 [12] noted a high reduction in modulus of elasticity for cores with cracking perpendicular to the test loading. It was further observed that when severe lengthwise cracking was present, cores behaved as a collection of 'slender columns' making the distribution of the crack planes in the core significant. Low uniformity in crack distribution could result in eccentric behaviour and potentially reduce the modulus of elasticity.

The SDT can be used to further evaluate damage in ASR-affected concrete using three indices: the stiffness damage index (SDI), plastic deformation index (PDI) and non-linearity index (NLI) [8, 11]. Anisotropy in concrete was found to impact these parameters with lengthwise cracking resulting in lower SDI and PDI compared to cross-sectional cracking [11]. The third parameter, NLI can be used to determine preferential cracking orientations in concrete [11, 25]. Cracking perpendicular to the test load direction results in an NLI above unity, while NLI <1 indicates cracking parallel to the direction of test loading [25].

7.2.2 Microscopic features of concrete experiencing various stress states

The use of DRI for investigating concrete experiencing various stress states in different reinforcement configurations continues to be an active research area [5, 10, 13]. In addition to the magnitude of the DRI number, investigating the types of microscopic distress features occurring are crucial to better understand the induced damage development (e.g. cracking in aggregates vs. cement paste and presence of reaction products). At more advanced stages of ASR, increased anisotropy is thought to be due to the preferential growth of cracks in one direction (i.e., increased crack length and width) [12]. Research in laboratory settings on small to medium size samples (i.e., cylinders and cores from blocks and beams) have investigated anisotropic effects [10, 11, 13, 23]. These works have identified differences in how ASR develops in aggregates and cement paste (e.g. crack widths and lengths at different locations, presence of secondary ASR products) due to different stress-states in the concrete (different reinforcement configurations and restraint) [10]. The type of restraint has further been found to change the extent of anisotropy, i.e., the percentage of directional vs. random cracks [10, 13].

The presence of secondary ASR products (i.e. the expansive gel) has been found to be affected by different confinement conditions. In a study of cores extracted from reinforced concrete blocks, Zahedi et al. (2021) [10] noted a change in distress features with cores extracted from highly restrained blocks which had reached 0.15% expansion, with increased reaction product in aggregates (i.e. OCA_{RP}) along with more open cracks in non-reactive aggregates (not observed in unrestrained companion cores). Distinct crack features (i.e., sharp and onion skin cracks) were found to be in the direction of the restraint [9, 10]. Cracking parallel to the primary reinforcement was found to be longer and wider compared to unrestrained specimens [10]. Similarly, Gautam et al. (2017) found that crack widths increased in the low restraint direction and crack opening was prevented in the restraint direction [13] which likely contributes to preferential damage development.

Ultimately, the development of cracks due to ASR is a complex phenomenon related to a number of factors. Although many aspects of damage development can be captured in the laboratory, evaluation of specimens from real structures continues to be necessary to fully understand the development of this damage mechanism in more realistic field scenarios.

7.3 Scope of Work

This paper presents a condition assessment of a Champlain Bridge pier cap affected by ASR after 57 years of service. In 2022 cores were extracted longitudinally (parallel to main reinforcement) and transversally from regions with various ratios of restraint (i.e., reinforcement). The multi-level assessment proposed by [3, 8, 26–28] was then performed and comparisons between the test outcomes and cracking patterns were made for locations of the member bearing distinct stress states. Particular attention was given to cores extracted longitudinally from regions closer or farther from the main rebars (i.e., within the concrete cover) to better understand the effect of restraint and anisotropy on the extent of ASR damage in these regions. The research outcomes are expected to provide valuable insights into the relationship between ASR induced damage as a function of the core extraction direction and location.

7.4 Materials and Methods

7.4.1 Concrete Mix Design

The specific mix design is not known for the pier cap. A silicious limestone was used for the coarse aggregate. Due to the age of the structure it is uncertain whether air entrainment or low-range water reducers were used while high range water reducers would not have been available.

7.4.2 Coring

Sixteen cores with diameter of 94 mm were extracted parallel to the main reinforcement from the Champlain Bridge's reinforced concrete pier cap (length of 23.8 m and width of 1.9 m). Three regions were investigated, the top (T), middle (M) and bottom (B) representing different restraint conditions in the member with reinforcement ratios of approximately 7.1%, 0.6% and 1.5%, respectively. Three transversally extracted cores have been included as a control (TR) representing cores from the direction that would be normally cored and evaluated when the member was in service. TR cores were extracted from low to medium reinforcement areas and are oriented perpendicular to the main reinforcement.

Reinforcement on this pier cap included 60M tensile reinforcement (red circles in Figure 7-2) with smaller reinforcing bars used in other areas including 35 M rebars (yellow) and 25 M rebars (white). 15M rebars were used during an encapsulation repair in the early 2000's (along the outer edges of the cross-sections). Ten cores were tested using resonant frequency (RF) with six of those evaluated using SDT to appraise mechanical properties while, six cores were cut and polished for evaluation under a stereomicroscope using the DRI. Core locations are illustrated in Figure 7-2). Uses for specific cores are shown in Table 7-1

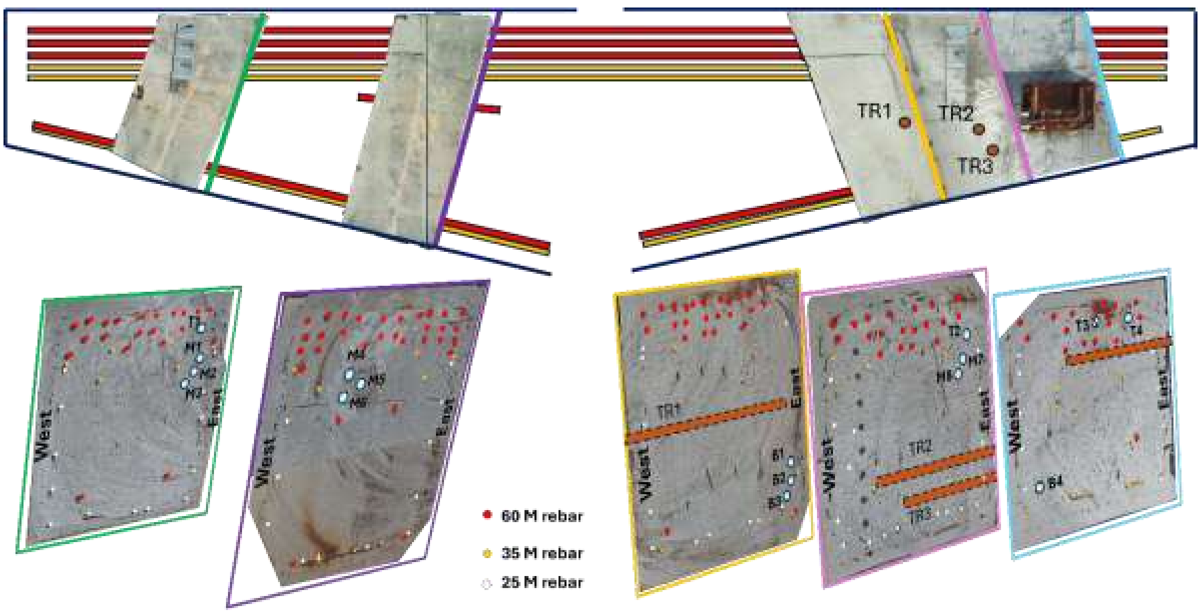

Figure 7-2 Schematic identifying locations of the 16 cores extracted longitudinally from pier cap segments. Reinforcing bars of size 60M (red), 35M (yellow) and 25M (white) are identified on the cross-sectional surfaces.

Table 7-1 Summary of experimental testing performed on longitudinally extracted cores and transversally extracted reference cores

Name	*Length [cm]*	*RF*	*Image analysis – cracks in agg*	*Image analysis – cracks in paste*	*DRI*	*Crack width*	*SDT*	*Comp. strength*
T1	13				X	X		
T2A	21	X	X	X			X	X
T2B	14				X	X		
T3	19				X	X		
T4	21	X	X				X	X
M1	21	X	X	X				X
M2	21	X	X	X				
M3								
M4	21	X					X	X
M5	16				X	X		
M6	21	X	X	X	X	X		
M7A			X	X			X	X
M7B	8				X	X		
M8	21	X	X	X				
B1	21	X	X				X	
B2	21			X	X	X		
B3	21	X	X				X	X
B4A	21	X	X					
B4B	6				X			
TR1	80				X	X	X	
TR1	21	X	X					
TR2	20		X				X	X
TR2	21				X			
TR3	21		X					
TR3	21	X	X	X	X		X	
TR3	10				X			

7.4.3 Digital Assessment of Cracking of Cores

Analysis of cracking on the surface of the core specimens was conducted as shown in Figure 3-12. First, 200mm long cores were scanned along the longitudinal direction by rolling the core along the surface of a flatbed scanner. All the images obtained present a resolution of 11.8 pixels/mm. Cracks were traced based on visual assessment, where cracks were outlined using fine tipped permanent markers prior to a second scan. Closed cracks in the aggregates were coloured in blue, while open cracks in the aggregates and cement paste were coloured in red and green, respectively.

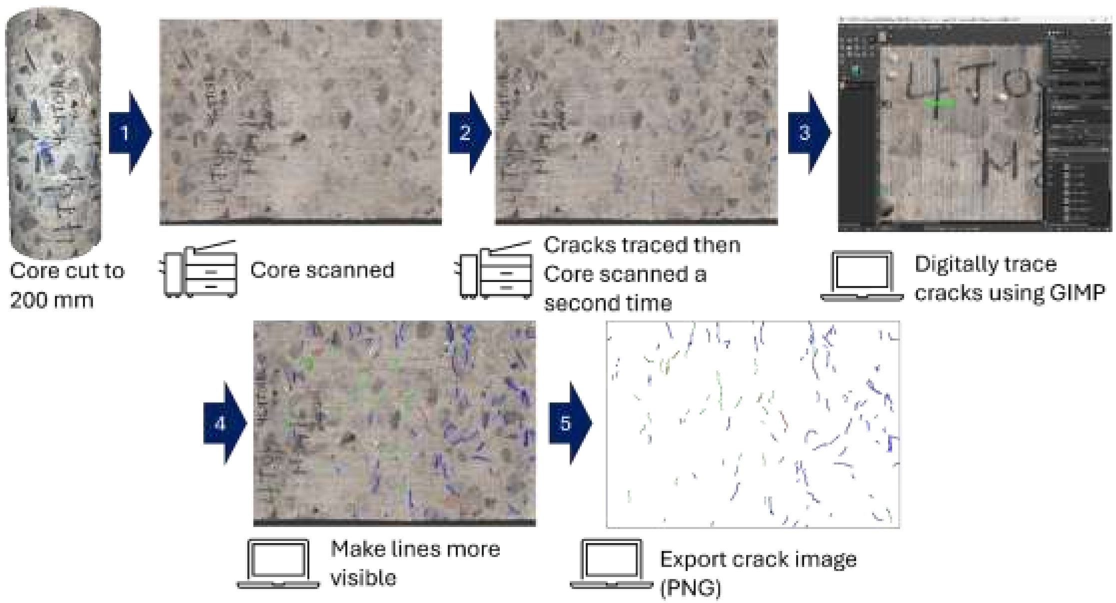

Figure 7-3 Schematic depicting the scanning and analysis process for obtaining crack orientation estimates for core specimens

Crack orientation was then determined using the 'Directionality' tool in the FIJI ImageJ software [29] which identifies the orientation of particles, in this case traced cracks, in an image and computes the percentage of particles oriented in a given direction within a 180 ° range. This was applied to traced cracks, with cracks in the cement paste and cracks in the aggregate processed separately. The percentage of total cracks oriented in a 36° range (i.e. 18° out of a 90° range) either parallel or perpendicular were used to estimate whether cracking was primarily lengthwise or cross-sectional within the cores. The area occupied by traced cracks (i.e. a constant width) was determined using the 'threshold' function which finds the percentage of pixels in an image above or below a specified colour value.

7.4.4 Resonant frequency (RF)

Resonant frequency (RF) was performed on 200 mm long cores. Measurements were performed using transverse (capturing S-waves) and longitudinal (capturing P-waves) modes following the procedure outlined in ASTM C215-19 using a DK-5000 dynamic resonance frequency tester. The dynamic modulus (dynamic ME) can be calculated from the transverse RF using Equation 7-1 where M is the mass in kg, L is the sample length, d is the diameter, n is the transverse RF and T is a correction factor from ASTM C215-19. Dynamic ME can be calculated from the longitudinal RF using Equation 7-2 where n' is the longitudinal RF.

$$E_{dyn}\ [GPa] = 1.6067({L^3T}/{d^4}) \cdot M \cdot n^2 \tag{7-1}$$

$$E_{dyn}\ [GPa] = 5.093({L}/{d^2}) \cdot M \cdot (n')^2 \tag{7-2}$$

Eight transverse measurements were performed per core along four equally spaced longitudinal lines to capture differences in the core between the top and bottom and to capture how crack orientation might influence resonant frequency results along different longitudinal planes. External crack visualization (i.e. cracks traced on outside of core) were used to choose optimal locations to capture the influence of lengthwise cracking. Moreover, two longitudinal measurements were performed per core, with the accelerometer and impact location alternated between the top and bottom ends.

7.4.5 Damage Rating Index (DRI)

Concrete samples were prepared for DRI by polishing their surface using a hand polishing device using polishing pads with grits 30, 50, 100, 200, 400, 800, 1500 and 3000. Samples were evaluated under a stereomicroscope at 16x magnification, using a 3D printed grid to divide the surface into 1 cm by 1 cm. The DRI number, which is always normalized to 100 cm², was determined by counting the distress features and applying weighting factors as outlined in Table 2-3 [30]. Weighting factors were first proposed in the early 1990s [31, 32]. However, revised weighting factors were introduced in 2012 [30] to reduce variability among operators and better describe the deterioration encountered in the samples [30–32].

Table 2-3 Weighting factors used for Damage Rating Index (DRI) Microscopic technique [30] (Duplicated for ease of reference)

Distress features	Abbrev.	Weight factors
Closed crack in aggregate	CCA	0.25
Opened crack in aggregate	OCA	2
Crack with reaction product in aggregate	OCA_{RP}	2
Debonded/dislodged aggregate	Debon	3
Crack in cement paste	CCP	3
Crack with reaction product in cement paste	CCP_{RP}	3
Disaggregate/corroded aggregate particle	DAP	2

7.4.6 Compressive strength

Compressive strength was conducted on select core samples as per ASTM C39/39M-23 [33]. Due to the limited number of available cores, samples were tested for compressive strength after conducting RF and SDT.

7.4.7 Stiffness Damage Test (SDT)

To perform the SDT, 200 mm – long cores were first stored at room temperature and 100% RH for a minimum of 48 hours prior to testing to condition the samples [34]. Five compressive loading cycles were performed using 40% of the compressive strength of a companion sound concrete (i.e. test load of 9.6 MPa) at a loading rate of 0.10 MPa/s. The SDT outcomes were calculated as shown in Figure 7-4.

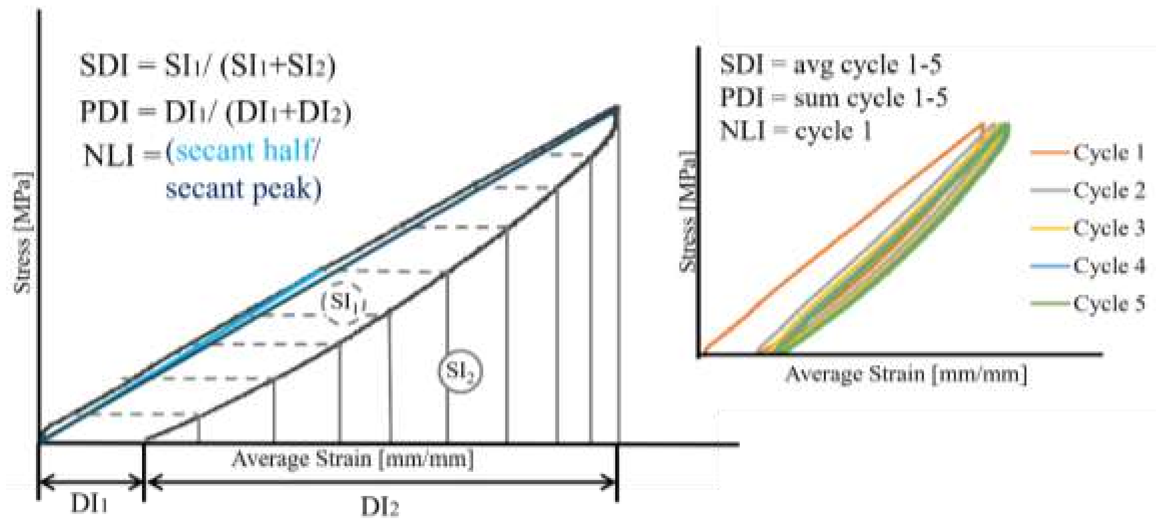

Figure 7-4 Schematic depicting calculation of SDI, PDI and NLI

7.5 Results

An overview of the cross-sections along with the DRI and SDT results (i.e. DRI number and SDI, respectively) are illustrated in Figure 7-5 for reference. Lines have been added to indicate the plane along which DRI samples were cut for investigation. Core sample T3 was cut on a diagonal relative to the ground to avoid cutting through a segment of rebar in the core sample. Cores from the top region (T1-T4) are located in a high reinforcement region, which is expected to experience primarily tensile stresses under regular service loads, cores in the middle (M1-M8) are located in a medium reinforcement region below the main reinforcing bars. Cores in the bottom region are located in a medium to low reinforcement region and are expected to experience mainly compressive stresses. All longitudinal cores are 'interior' cores since they are located 20 cm or more from the exterior surface.

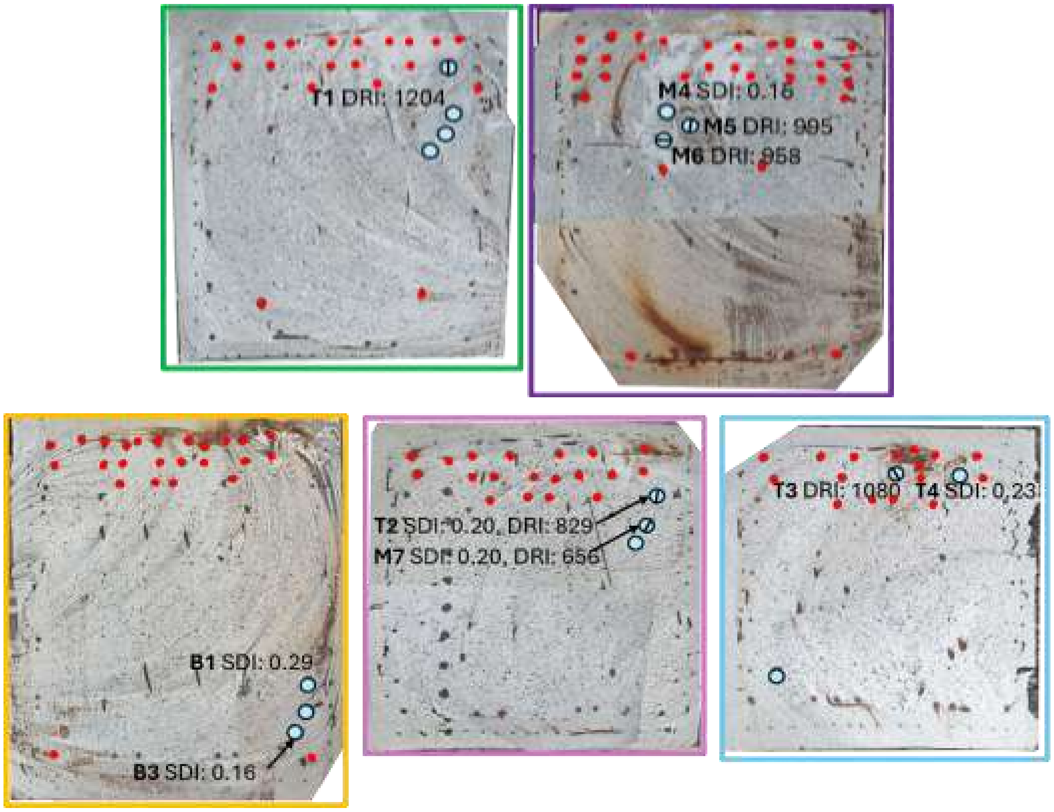

Figure 7-5 Schematic identifying DRI and SDT results from tested cores extracted longitudinally from top (T) and middle (M) regions along with DRI and SDT results from transversally extracted cores TR1-TR3. Black lines on DRI cores indicate how the core was cut for the investigated surface. Rectangular blue cores indicate the transversally extracted reference cores while orange indicates unused areas.

7.5.1 Dynamic modulus of elasticity: Resonant frequency (RF)

The dynamic modulus of elasticity measured using the transverse and longitudinal (S- and P-waves, respectively) methods is presented in Figure 7-6. Specimens in the top region, which are closest to the reinforcement, were found to have a lower dynamic modulus of elasticity with an average value of 25 GPa compared to specimens from the middle region which presented an average value of 28 GPa. Specimens from the transverse region presented an average value of 28 GPa. The dynamic modulus of elasticity obtained from specimens in the top zone presented 23 and 27 GPa, while values from the middle zone ranged between 23 GPa and 30 GPa and values in the bottom region ranged between 19 and 30 GPa. Finally, cores extracted transversally (i.e., avg TR) presented values of 24 to 31 GPa.

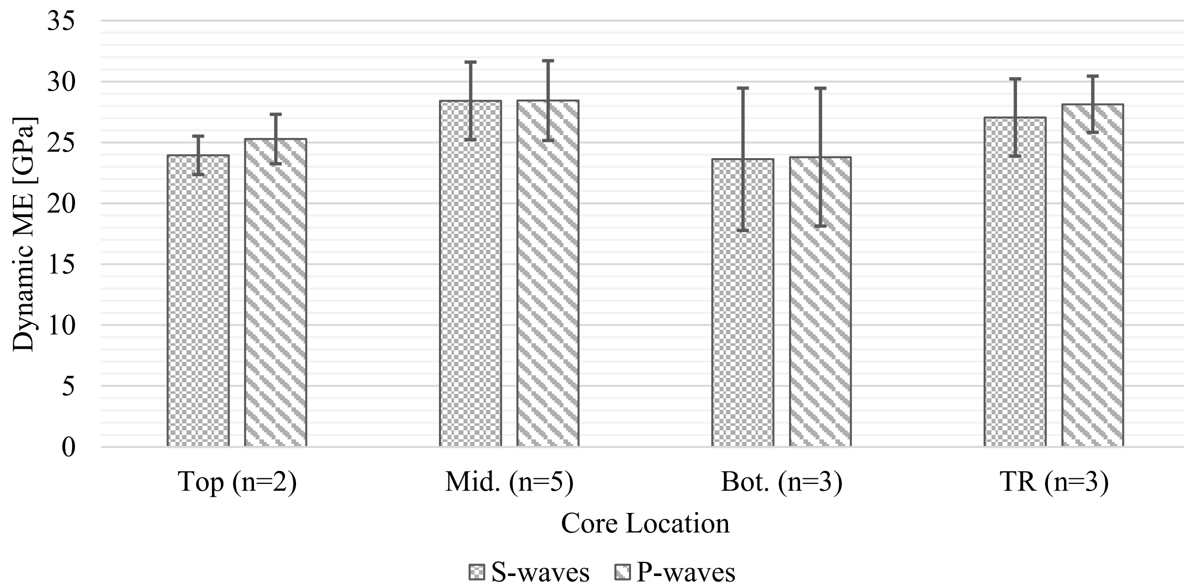

Figure 7-6 Bar graphs depicting dynamic ME (calculated from S and P waves using RF)

7.5.2 Qualitative image analysis to distinguish crack orientation

Cracking observed on the surface of scanned cores are shown in Figure 7-7. Cracking was expected to be oriented parallel to primary reinforcement [5] which for cores extracted in this orientation would be lengthwise cracking as shown in the diagram. Although this method is a low-resolution procedure, a preferential lengthwise orientation of cracks in aggregates and cement paste is evident. Specimens T2 and B1 were noted to have a higher amount of lengthwise cracking in the cement paste compared to other samples, while sample M2 exhibits cracking in the cement paste indicative of cracking which has propagated through the specimen (Figure 7-7). Otherwise, transverse cores exhibit largely random cracking.

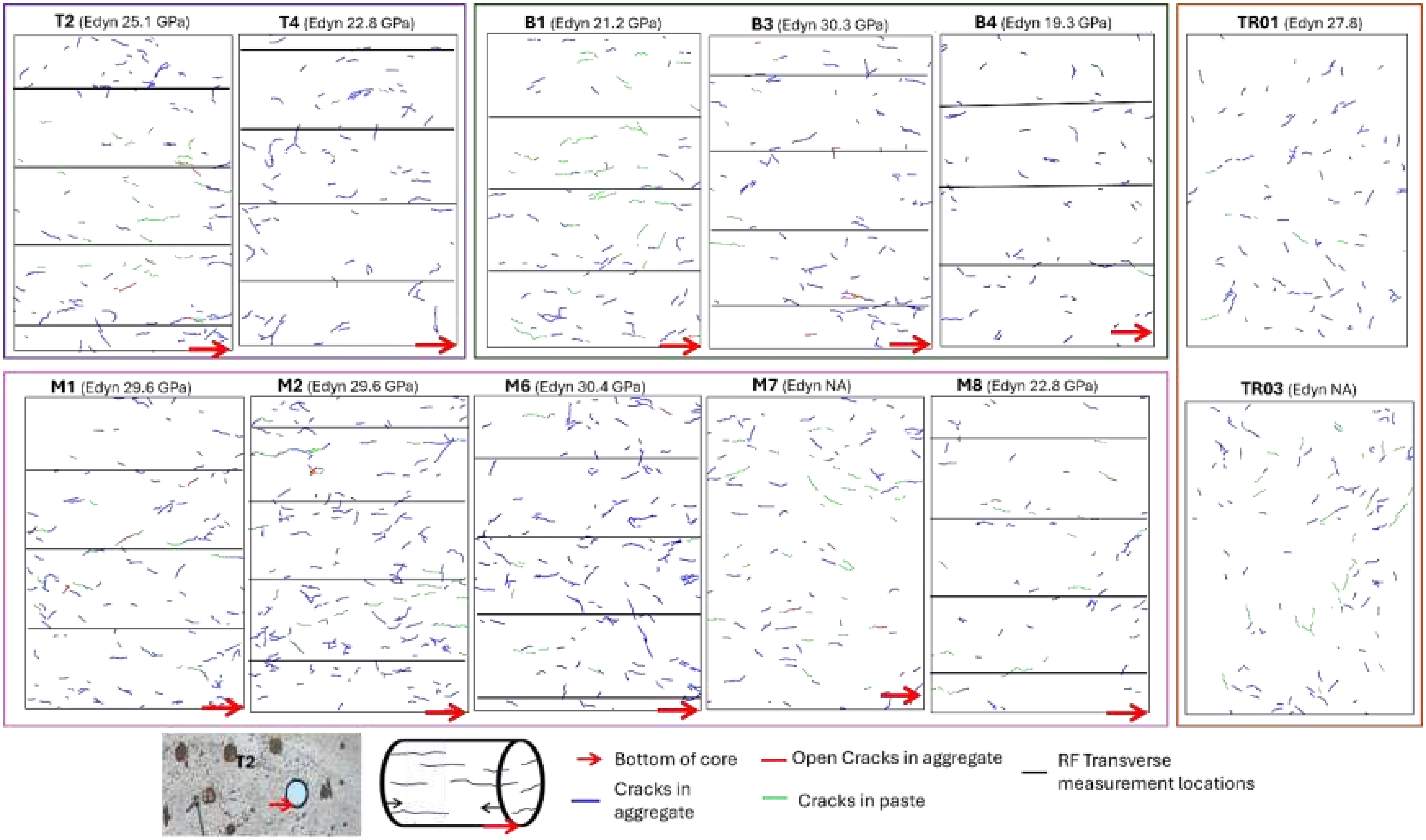

Figure 7-7 Schematics depicting traced cracks for the scanned exterior of longitudinal and transverse core specimen. Arrows indicate the closest exterior surface while black lines indicate the locations of transverse RF measurements (i.e. S-waves).

7.5.2.1 Crack orientation

Cracking was found to occur preferentially parallel to main reinforcement (i.e. oriented longitudinally in the core specimen) in both the aggregates and cement paste in the investigated longitudinal cores (Figure 7-8). The percentage of area occupied by cracks indicates a higher frequency of cracking in the aggregates compared to the cement paste over the surface area investigated. Samples T4, B3, B4, TR1 and TR2 were omitted from analysis of the cracks in the cement paste due to the limited number of cracks, as can be seen from the green lines in Figure 7-7.

Longitudinal core specimens exhibit similar crack orientations in both the aggregates and cement paste. However, distinct crack orientations can be seen for the transversal cores (TR) which exhibit non-directional cracking in the aggregate and preferentially perpendicular cracking in the cement paste.

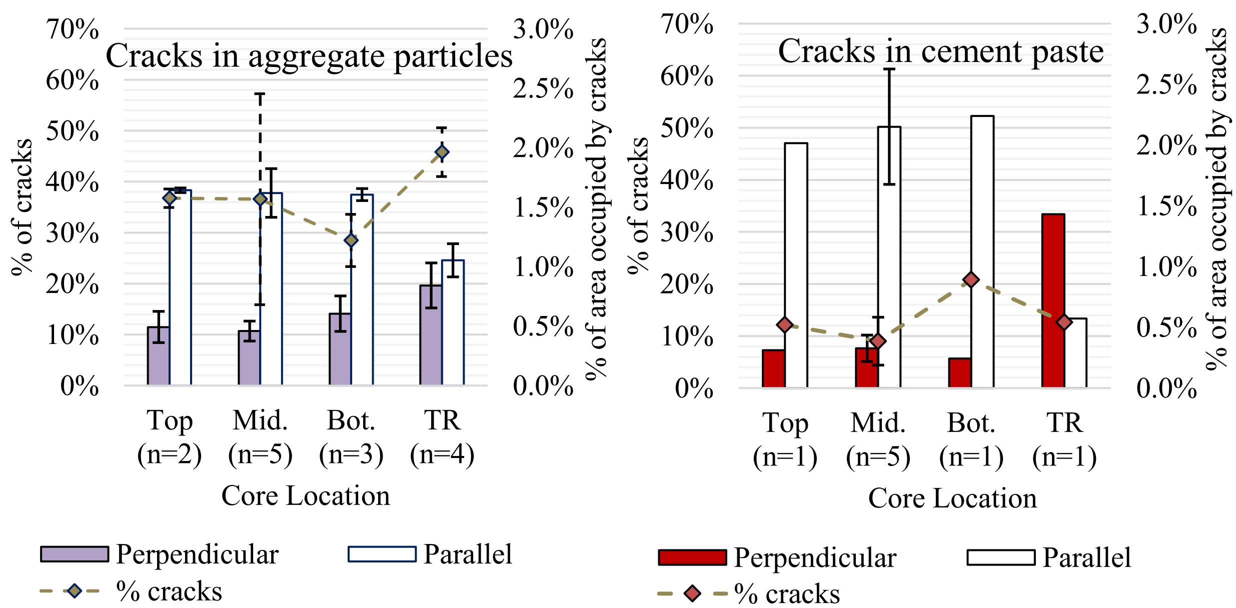

Figure 7-8 Bar graphs depicting the percentage of cracks in perpendicular (cross-sectional in core) and parallel (lengthwise in core) and the percentage of the total area occupied by cracks in aggregates (left) and cement paste (right). Error bars indicate one standard deviation

7.5.3 Quantitative microscopic analysis: The damage rating index (DRI)

Specimens investigated using the DRI were observed to have secondary products in both the aggregates and cement paste. Figure 7-9 illustrates micrographs of reaction products within the aggregate particles (i.e., opaque) and propagating into the cement paste (i.e., translucid). Cracks generated in the aggregates and propagating to the cement paste, partially or fully filled with reaction products, are indicative of the advanced stages of ASR [35].

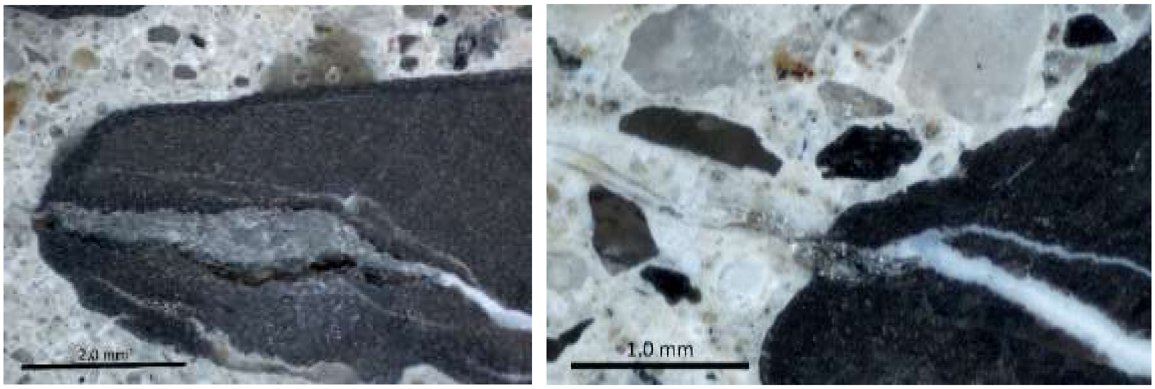

Figure 7-9 Stereomicroscope images of OCA_{RP} extending into the cement paste.

The DRI results are presented in Figure 7-10 with specimens in the top region presenting a high DRI value of 1038 while specimens in the middle and bottom regions showing lower DRI values of 870 and 845, respectively. Transverse specimens displayed a similar DRI value to the top specimens with an average value of 992.

Damage features in the top region indicate higher damage in the aggregate (i.e. OCA, OCA_{RP}) compared to the middle region. Damage features in the transversally extracted cores exhibit high amounts of reaction products in the cement paste (i.e. CCP_{RP}) but otherwise have similar proportions of damage features seen in the middle and bottom regions.

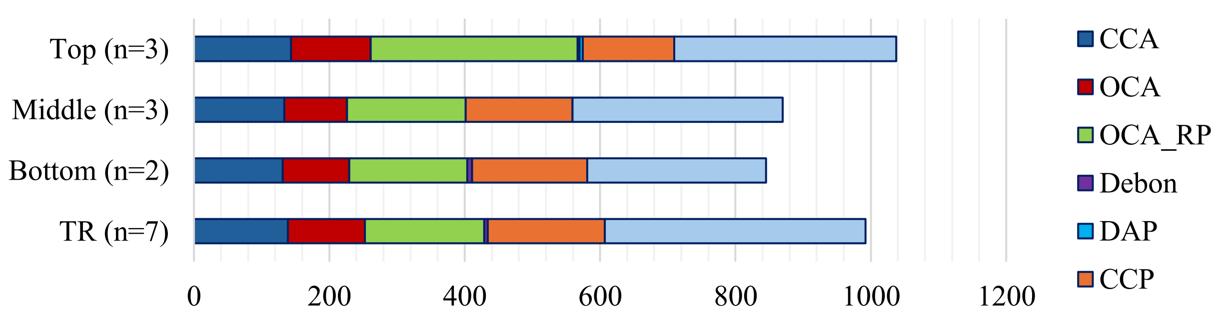

Figure 7-10 Bar graph depicting DRI results from longitudinal cores from the top, middle and bottom regions in comparison to the transversally extracted cores.

The results of crack measurements conducted on DRI samples are presented in Figure 7-11. Average crack widths in investigated samples were between 0.12 and 0.18 mm while the number of cracks with widths 0.10 mm or greater varied from 40 to 15 cracks per 100 cm^2. Specimens from the top region, exhibit higher average crack widths in the aggregates with an average value of 0.16 mm, while crack widths in the cement paste are lower with an average value of 0.12 mm. This is not seen in the specimen from the middle region where average crack widths in the aggregate and paste are similar with average values of 0.15 mm in the aggregates and 0.14 mm in the cement paste. In the transverse specimen, average crack widths in the aggregates and cement paste were found to be the same at 0.15 mm.

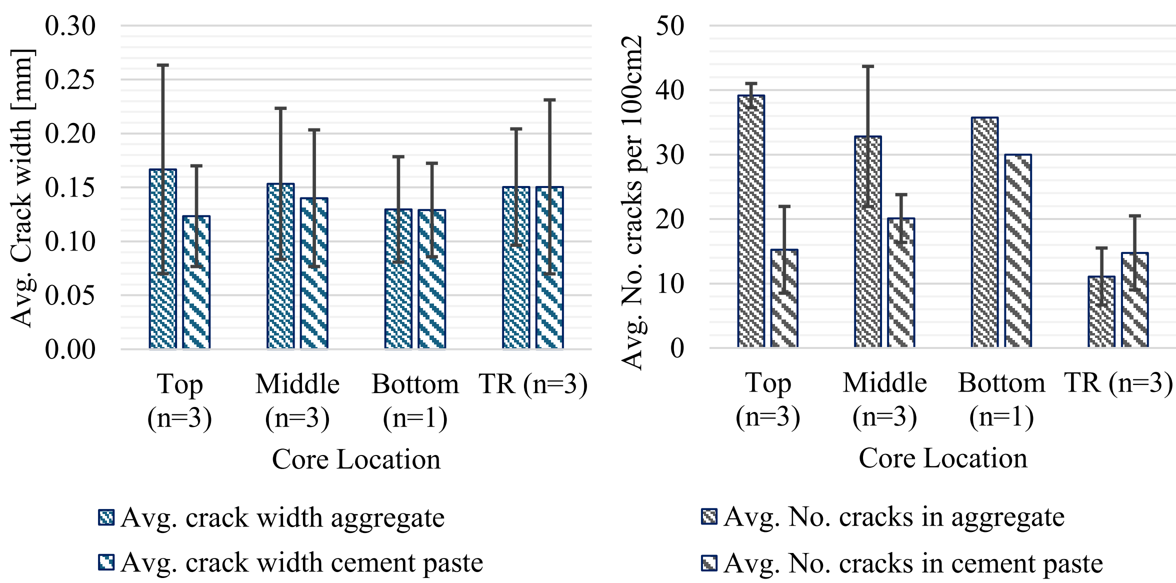

Figure 7-11 Bar graphs depicting average crack widths (left) and number of cracks (right) measured in DRI samples. Error bars indicate 1 standard deviation.

7.5.4 Extent of deterioration through mechanical testing

7.5.4.1 Stiffness damage test (SDT)

SDT results are shown in Figure 7-12, including the SDI, PDI, ME, and the NLI (i.e., indicator of preferential crack orientation). Specimens from the top region present higher SDI, PDI and NLI values compared to specimens from both the middle and bottom regions, except for the SDI value of the bottom whose scattered results increased the average value. These differences, although less pronounced for ME, displayed the same trend: specimens from the top region presented a lower modulus compared to specimens from other investigated regions (i.e., middle and bottom). Transverse cores presented SDI, PDI and ME in between the values from the top and middle regions.

SDI values range from 0.33 to 0.15, PDI values range from 0.34 to 0.17 and NLI values range from 0.94 to 1.05. The ME ranges from 13 to 19 GPa.

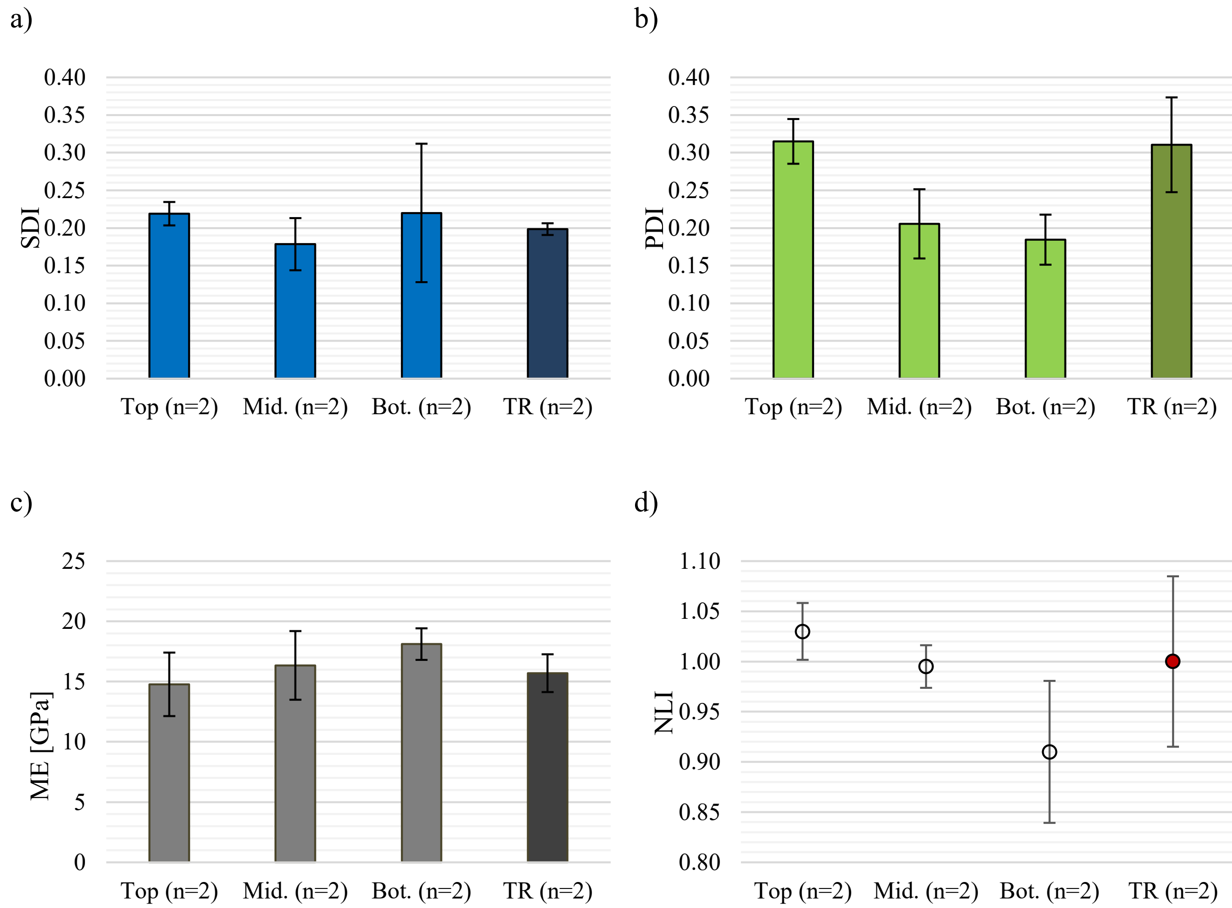

Figure 7-12 Bar graphs depicting SDT outputs as a) SDI, b) PDI, c) ME and d) NLI. Error bars indicate 1 standard deviation.

7.5.4.2 Compressive strength

Compressive strength results are presented in Figure 7-13 with the average compressive strength in the longitudinally extracted specimen from the top, middle and bottom regions showing average values of 34, 35 and 27 MPa, respectively. In comparison, the compressive strength of the specimen transversally extracted reference core was 31 MPa.

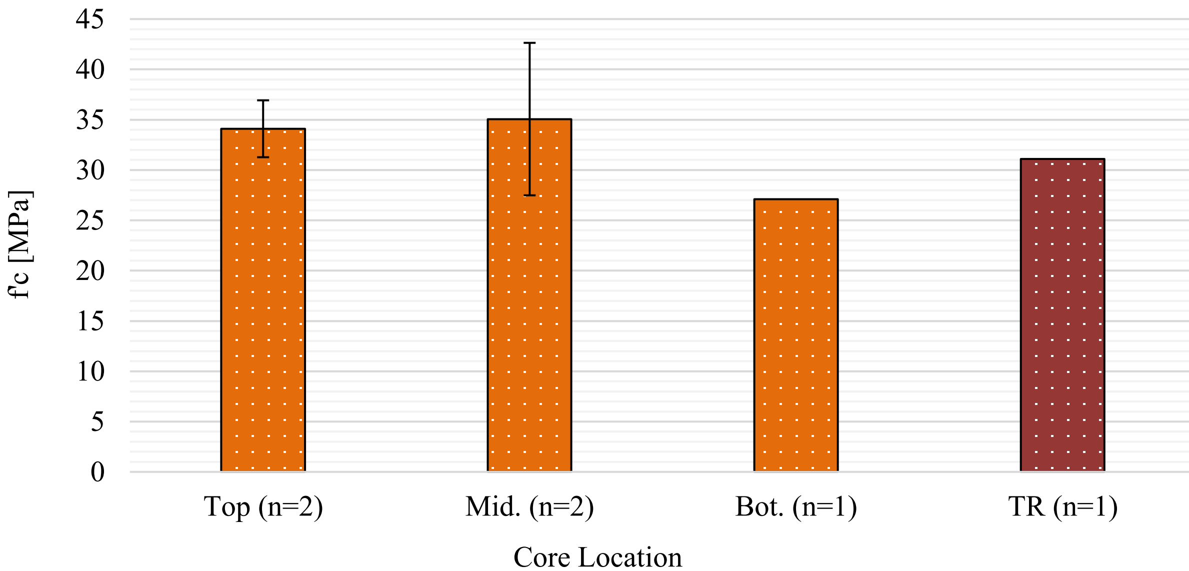

Figure 7-13 Bar graph depicting compressive test results for cores from the top middle and bottom regions compared to a transversally extracted core. Error bars indicate 1 standard deviation.

7.6 Discussion

7.6.1 Understanding the effect of coring location and direction on extent of deterioration

The pier cap investigated presents a complex geometry, various stress-states regions (i.e. tensile – top, and compressive – bottom), and a service environment which constantly changes over time (i.e. seasonal changes in moisture and temperature). The investigation conducted in this work, longitudinally along the main reinforcement, on concrete specimens retrieved from the top, bottom, and middle regions of the pier cap, was only made possible by the decommissioning of the Champlain Bridge. Given that the pier cap was part of an in-service structure for nearly 60 years, ASR is unlikely to be the sole damage mechanism. The surface rebars in the member are known to have experienced significant reinforcement corrosion, potentially exacerbated by water pooling on the top surface. However, since the investigated core specimens were extracted from interior locations of the member, corrosion-induced damage within the member is expected to have a negligible impact on extracted cores. Additionally, the stress states in the pier cap may have been further influenced by the addition of external longitudinal post-tensioning during the final 10 years of service.

The investigated cores were extracted parallel to the reinforcement from three regions of the pier cap presenting distinct restraint conditions (i.e. top region with a reinforcement ratio of approximately 7.1%, middle region with a reinforcement ratio of approximately 0.6% and bottom region with a reinforcement ratio of approximately 1.5%). Results from the multi-level assessment (i.e. RF, SDT and DRI) indicate clear differences in the level of deterioration at these different regions with the lowest damage occurring in the middle region (low reinforcement). This was indicated by lower SDI and DRI numbers, along with high modulus of elasticity (dynamic ME from resonant frequency and ME from SDT).

This finding emphasizes the importance of considering stress states within a member since a lower reinforcement region might be initially expected to have increased ASR damage [5]. However, when supplementary induced stresses within the pier cap are considered due to service loading from the seven girders that rest on the pier cap, similarities can be identified between high confinement regions in Zahedi et al.'s work and middle and bottom regions in this work. Specimens from the middle region were found to have a reduced number of cracks in aggregates (i.e. OCA and OCA_{RP}) compared to the top region and reference transverse cores, similar to the findings of [10]. Lower damage was also identified in the middle and bottom specimens through the SDT with specimens at the top region and transverse reference cores exhibiting higher damage, the same trend identified for high and low confinement regions in [11].

Anisotropy, the presence of directional properties in a material, was identified in both cores extracted longitudinally (parallel to main reinforcement) and transversally (perpendicular to main reinforcement). Directional cracking was present in DRI samples with lengthwise cracking in both the aggregates and cement pastes corresponding to the main reinforcement direction for longitudinal cores while transversally extracted cores were found to have cross-sectional cracking. This pattern was also captured in cracks traced from scanned cores with the percentage of cracks in the aggregates oriented parallel to reinforcement found to be 2-6x more frequent than cracks oriented perpendicular for longitudinal cores. Conversely, transverse cores were found to have approximately random cracking in aggregates, while cracking in cement paste displayed a higher percentage of transversally oriented cracks.

7.6.2 Crack patterns and microscopic distress features in different regions of pier cap

All locations in the investigated pier cap exhibited signs of advanced ASR with evidence of secondary products in both the aggregates and cement paste identified in all DRI. Following crack width measurements, locations of cracks with width 0.10 mm or greater (i.e. larger cracks) were traced on DRI specimen (Figure 7-14) allowing crack patterns to be visualized. The DRI results were then plotted using a 'heat map' to further visualize areas of high and low damage following [36].

In unrestrained concrete, ASR-induced cracking typically exhibits a random orientation. Therefore, it is significant that the cracks observed in the longitudinally extracted cores from the pier cap were predominantly oriented lengthwise (i.e., parallel to the main reinforcement). Interestingly, these cracks were observed to present similar spacing between cracks at the top and middle regions, with cracks spaced around 2.5 cm apart (Figure 7-14). These results agree with findings in the literature [9, 10, 13]. Moreover, the cracks generation and propagation appear to be different depending on the region within the pier cap, where cracking at the top region remains largely within the aggregate particles, with limited propagation to the cement paste. This is likely caused by rebar configuration, with [13] having previously found that tri-axial restraint could decrease ASR-induced cracking in the cement paste. It is unclear though at this point how the addition of external longitudinal reinforcement for the final 10 years of service impacted on existing ASR deterioration. Further research and modeling could help understanding such an impact.

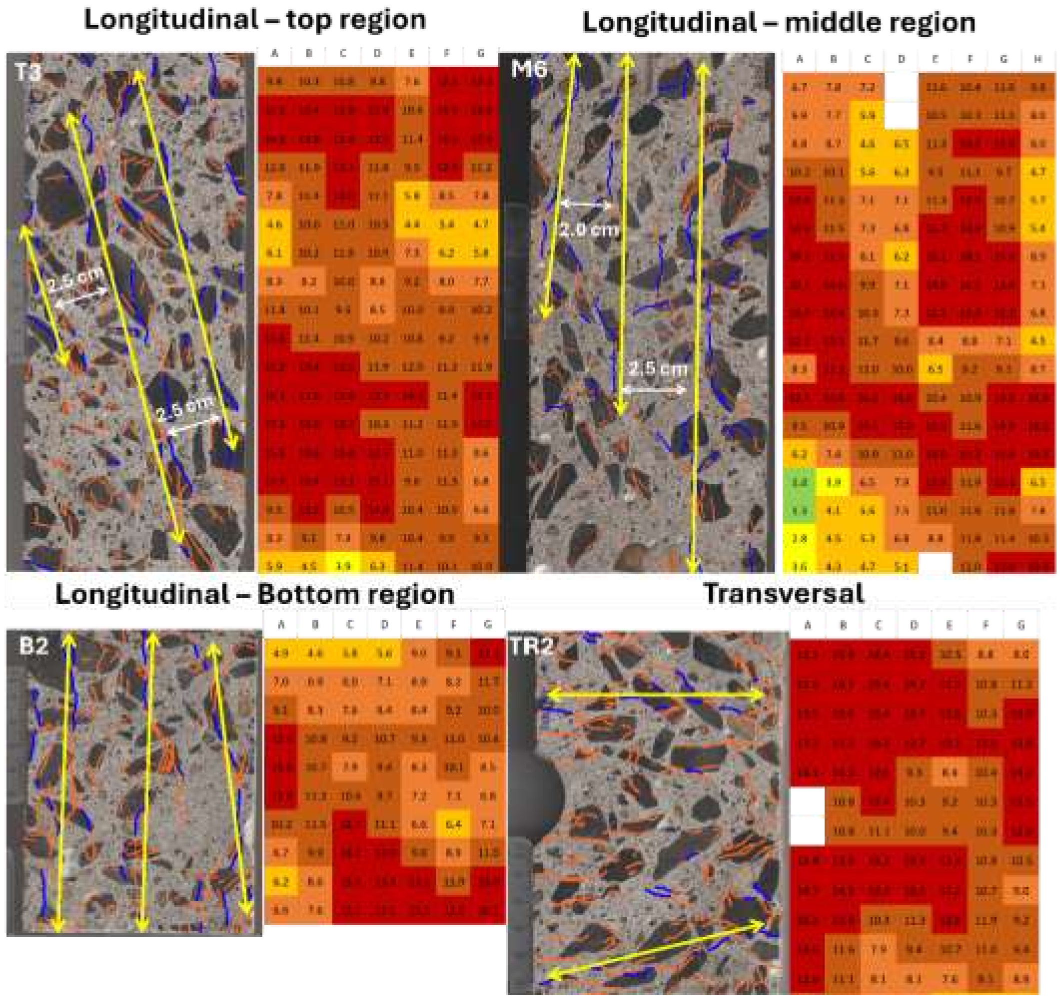

Figure 7-14 Image analysis of DRI samples where blue lines indicate locations of cracks 0.10 mm and greater, orange lines indicate cracks less than 0.10 mm and heat maps show distribution of damage captured through the DRI.

7.7 Conclusions

This work reports the results of a condition assessment performed though a multi-level assessment protocol (i.e., mechanical and microscopic testing) of cores extracted longitudinally from a pier cap from a decommissioned highway bridge. The main findings of this investigation can be summarized as follows:

- All core specimens investigated indicated high levels of ASR damage (i.e. high SDI, PDI and DRI numbers and reductions in modulus of elasticity).

- Cores extracted from the high reinforcement top region presented higher damage when compared to cores from the middle and bottom regions. This indicates that the stress state of the concrete member caused by service loading and reinforcement influenced the overall deterioration over time.
- Specimens at the top region exhibited higher microscopic damage features with increased amounts of reaction products in cracks within the aggregate particles (i.e. increased OCA_{RP}) along with notable differences in average crack widths in aggregates (larger width cracks) compared to the cement paste (smaller width cracks). Specimens in the middle and bottom regions exhibited reduced damage features within the aggregate particles and similar average crack widths in the aggregates and cement paste.
- Observed crack patterns on DRI surfaces and scans of the cores used for SDT indicated primarily lengthwise cracking in both aggregates and cement paste of the longitudinal core specimens investigated. This parallel cracking to the main reinforcement agrees with past research and was captured through the various multi-level tools implemented in this research.
- Results indicate the need for research efforts to be undertaken into the effects of stress state (e.g. concrete in tension versus compression) on ASR-induced development (i.e., expansion and cracking) to better identify the impact of this damage mechanism on reinforced concrete structures with a variety of geometries, reinforcement configurations, and stress states.

7.8 References

1. Bérubé MA, Frenette J (1994) Évaluation de la Réactivité Alcaline dans le Béton des Piles 12, 18 et 20 W du Pont Champlain.

2. Khaleghi-Esfahani M, Fournier B, Bissonnette B, Fecteau P-L, Conciatori D, Khani S (2024) Diagnostic and Prognostic Assessments on a 50-Year-Old Bridge Subjected to Severe Environmental and In-Service Conditions. In: Proceedings of the 17th International Conference on Alkali-Aggregate Reaction in Concrete. pp 597–605

3. Sanchez LFM, Fournier B, Jolin M, Mitchell D, Bastien J (2017) Overall assessment of Alkali-Aggregate Reaction (AAR) in concretes presenting different strengths and

incorporating a wide range of reactive aggregate types and natures. Cem Concr Res 93:17–31

4. Sanchez LFM, Fournier B, Mitchell D, Bastien J (2020) Condition assessment of an ASR-affected overpass after nearly 50 years in service. Constr Build Mater 236:117554

5. Zahedi A, Trottier C, Sanchez LF, Noël M (2022) Condition assessment of alkali-silica reaction affected concrete under various confinement conditions incorporating fine and coarse reactive aggregates. Cem Concr Res. https://doi.org/10.1016/j.cemconres.2021.106694

6. RILEM (2013) Guide to Diagnosis and Appraisal of AAR Damage to Concrete in Structures. Springer Netherlands

7. Martin RP, Sanchez L, Fournier B, Toutlemonde F (2017) Evaluation of different techniques for the diagnosis & prognosis of Internal Swelling Reaction (ISR) mechanisms in concrete. Constr Build Mater 156:956–964

8. Sanchez LFM, Drimalas T, Fournier B, Mitchell D, Bastien J (2018) Comprehensive damage assessment in concrete affected by different internal swelling reaction (ISR) mechanisms. Cem Concr Res 107:284–303

9. Zahedi A, De Souza DJ, Zubaida N, Sanchez LFM (2023) Overall assessment of CFRP-wrapped concrete affected by alkali-silica reaction. Cem Concr Res. https://doi.org/10.1016/j.cemconres.2023.107165

10. Zahedi A, Trottier C, Sanchez LFM, Noël M (2021) Microscopic assessment of ASR-affected concrete under confinement conditions. Cem Concr Res. https://doi.org/10.1016/j.cemconres.2021.106456

11. Zahedi A, Trottier C, Sanchez L, Noël M (2022) Evaluation of the induced mechanical deterioration of alkali-silica reaction affected concrete under distinct confinement conditions through the Stiffness Damage Test. Cem Concr Compos. https://doi.org/10.1016/j.cemconcomp.2021.104343

12. Barbosa RA, Hansen SG, Hansen KK, Hoang LC, Grelk B (2018) Influence of alkali-silica reaction and crack orientation on the uniaxial compressive strength of concrete cores from slab bridges. Constr Build Mater 176:440–451

13. Gautam BP, Panesar DK, Sheikh SA, Vecchio FJ (2017) Effect of multiaxial stresses on alkali-silica reaction damage of concrete. ACI Mater J 114:595–604

14. Rogers C (1993) Alkali-aggregate reactivity in Canada. Cem Concr Compos 15:13–19

15. Rogers, Grattan-Bellew PE, Hooton RD, Ryell J, Thomas MDA (2000) Alkali-aggregate reactions in Ontario. Canadian Journal of Civil Engineering 27:446–460

16. Bérubé M-A, Fournier B (1987) Le barrage Sartigan dans la Beauce (Quebec), Canada: un cas-type de deterioration du beton par des reactions alcalis-granulats. Canadian Journal of Civil Engineering 14:372–380

17. Bérubé MA, Smaoui N, Fournier B, Bissonnette B, Durand B (2005) Evaluation of the expansion attained to date by concrete affected by alkali-silica reaction. Part III: Application to existing structures. Canadian Journal of Civil Engineering 32:463–479

18. Environment Canada Canadian Climate Normals 1981-2010 Station Data. https://climate.weather.gc.ca/climate_normals/results_1981_2010_e.html?searchType=stnName&txtStationName=Montreal&searchMethod=contains&txtCentralLatMin=0&txtCentralLatSec=0&txtCentralLongMin=0&txtCentralLongSec=0&stnID=5415&dispBack=0.

19. Leroux Beaudoin Hurens & Associes Inc (2005) Pont Champlain, réfection de piles, chevêtres, appuis et poutres (2004) CONTRAT No: 60494.

20. Groupe counseil Genivar (2003) Champlain Bridge, Rehabilitation of Piers, Pier Caps, Bearings and Beams (2004) Phases of Demolition.

21. Aecom Tecsult Inc. (2008) Rapport 1879 Pont Champlain, services de consultant, Étude, dessins et devis pour la réfection de piles et de poutres précontraintes (2007-2011).

22. Fan S, Hanson JM (1999) Length Expansion and Cracking of Plain and Reinforced Concrete Prisms Due to Alkali-Silica Reaction. ACI Mater J 480–485

23. Allard A, Bilodeau S, Pissot F, Fournier B, Bastien J, Bissonnette B (2018) Expansive behavior of thick concrete slabs affected by alkali-silica reaction (ASR). Constr Build Mater 171:421–436

24. Chen S, Duffield C, Miramini S, Nasim Khan Raja B, Zhang L (2021) Life-cycle modelling of concrete cracking and reinforcement corrosion in concrete bridges: A case study. Eng Struct. https://doi.org/10.1016/j.engstruct.2021.112143

25. Chrisp TM, Waldron P, Wood JGM (1993) Development of a non-destructive test to quantify damage in deteriorated concrete. Magazine of Concrete Research 45:247–256

26. Sanchez LFM, Fournier B, Jolin M, Bastien J, Mitchell D (2016) Practical use of the Stiffness Damage Test (SDT) for assessing damage in concrete infrastructure affected by alkali-silica reaction. Constr Build Mater 125:1178–1188

27. Sanchez LFM, Fournier B, Bastien J, Mitchell D, Noel M (2016) Overall assessment of an ASR affected overpass "Robert-Bourassa/Charest" after nearly 50 years in service. Conference: 8th International Conference on Bridge Maintenance, Safety and Managemen

28. Sanchez LFM, Fournier B, Jolin M, Bedoya MAB, Bastien J, Duchesne J (2016) Use of Damage Rating Index to Quantify Alkali-Silica Reaction Damage in Concrete: Fine versus Coarse Aggregate. ACI Mater J 113:395–407

29. Liu (1991) Scale space approach to directional analysis of images. Appl Opt 30:1369–1373

30. Villeneuve V, Fournier B, Duchesne J (2012) Determination of the damage in concrete affected by ASR - the Damage Rating Index (DRI). In: 14th ICAAR International conference on the alkali aggregate reaction. p 033012

31. Grattan-Bellew PE (1995) Laboratory Evaluation of Alkali-Silica Reaction in Concrete from Saunders Generating Station. Materials Journal 92:126–134

32. Grattan-Bellew PE, Danay A (1992) Comparison of laboratory and field evaluation of AAR in large dams. Proceedings of the International Conference on Concrete AAR in Hydroelectric Plants and Dams

33. ASTM Int'l (2023) ASTM C39/C39M-23 Standard Test Method for Compressive Strength of Cylindrical Concrete Specimens. https://doi.org/10.1520/C0039_C0039M-23

34. Sanchez LFM, Fournier B, Jolin M, Bastien J (2015) Evaluation of the Stiffness Damage Test (SDT) as a tool for assessing damage in concrete due to alkali-silica reaction (ASR): Input parameters and variability of the test responses. Constr Build Mater 77:20–32

35. Sanchez LFM, Fournier B, Jolin M, Duchesne J (2015) Reliable quantification of AAR damage through assessment of the Damage Rating Index (DRI). Cem Concr Res 67:74–92

36. Champagne MM (2020) Applying the Damage Rating Index for the spatial damage assessment in concrete specimens affected by alkali-silica reaction (ASR).

Chapter 8: Concluding Remarks

8.1 Introduction

The present work detailed the results of a comprehensive, state-of-the-art condition assessment performed on segments of a pier cap and pier shaft from Montreal's Champlain Bridge after nearly 60 years in service. Results of testing on extracted cores following the multi-level assessment protocol (i.e. microscopic using the DRI and mechanical using SDT) indicated a high level of deterioration had occurred in both reinforced concrete members corresponding to a free expansion between 0.15% and 0.31% in PC cores and 0.21% to 0.38% for PS cores. These results indicate the presence of significant expansion occurring within both members in excess of the yield strength of steel reinforcement and agreeing with the conclusions reached by the bridge owners that a replacement structure was necessary. Furthermore, data obtained from microscopic analysis, including extended DRI techniques found damage patterns consistent with ASR as the primary damage mechanism with the DRI numbers of cores in the dry region of the PS exhibiting an increased contribution of cracking in the cement paste indicating the additional presence of freeze-thaw damage in these members.

Beyond the successful diagnosis of the cause and extent of deterioration, the large number of extracted cores facilitated the evaluation of different core orientations (transverse, longitudinal and vertical) as well as other factors resulting in variability between different core specimens such as localized service environments (especially dry and semi-submerged regions of the PS), depth (i.e. surface and interior) and stress states (i.e. variations due to member geometry and reinforcement configurations). The present work proposes a qualitative image analysis procedure to assess crack orientation within DRI specimens (i.e. identifying crack orientation as lengthwise or widthwise within cores) which allowed trends in crack orientation corresponding to core extraction orientation. A second, quantitative, image analysis subsequently allowed crack orientation and the amount of cracking to be estimated in mechanical test specimens facilitating direct linking of anisotropy (i.e. directional properties induced in the material by

ASR damage) to mechanical properties. This is a valuable contribution to improve condition assessments of in-service structures where a limited number of cores may be extracted.

The present work was organized such that four research papers presented the comprehensive condition assessment of the PC and PS members consisting of visual and non-destructive testing performed on the members at an outdoor storage site (chapter 4) followed by in-depth analysis through microscopic (chapter 5) and mechanical (chapter 6) methods. This is followed by further assessment of longitudinal cores extracted from the PC which gave further insights into the impact of stress within the member (e.g. induced by reinforcing bar density) as well as anisotropy within cores oriented parallel to the primary reinforcement in the member. Through these four papers it is demonstrated that both members exhibited high to very high damage due primarily to the ASR mechanism. The detailed conclusions from the four paper chapters are presented in section 8.3.

Finally, ongoing work related to prognosis, which has not included as a chapter in this thesis, is summarized in section 8.2. The residual expansion testing is expected to identify an ongoing potential for further expansion within the members from the ASR with testing intended to continue until no further expansion is occurring. The residual expansion work will additionally explore the potential for the re-use of specimens used for SDT in the residual expansion test, potentially stretching the data that can be obtained from the limited number of cores extracted from in-service structures during condition assessments.

8.2 Potential for Future ASR Damage – Residual Expansion

Preliminary results from the residual expansion test, to estimate the capacity for further expansion, are presented in the following section. Residual expansion was conducted using sixteen (16) PC core specimens and twelve (12) PS core specimen with specimens split between two accelerated test conditions, 100% RH at 38 °C or submerged in 1M NaOH solution at 38 °C. Preliminary results are shown in Figure 8-1 for the 100% RH test condition and Figure 8-2 for the 1 M NaOH test condition.

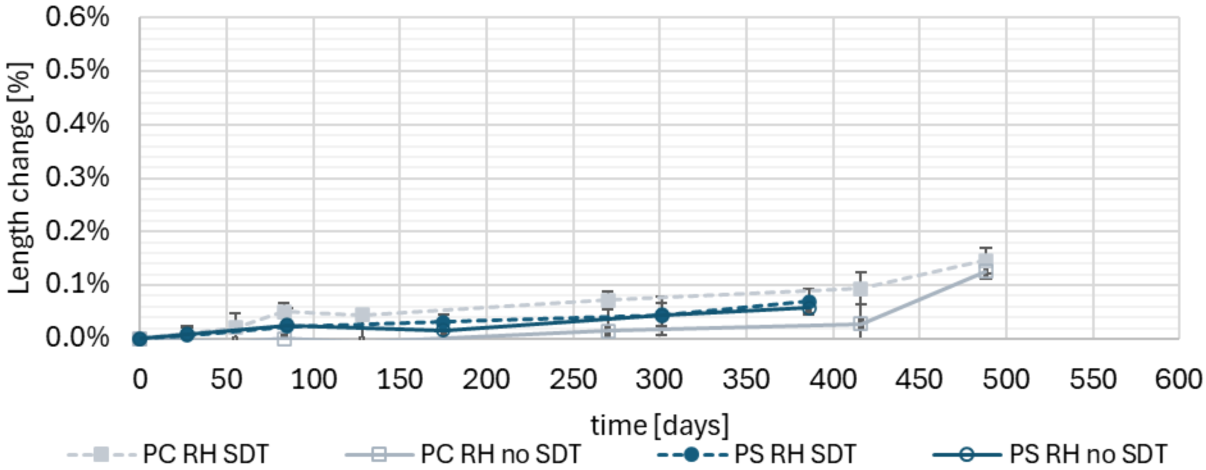

Figure 8-1 Line graph depicting length change after mass stabilization of pier cap (PC) and pier shaft (PS) specimen exposed to 100% RH at 38 °C

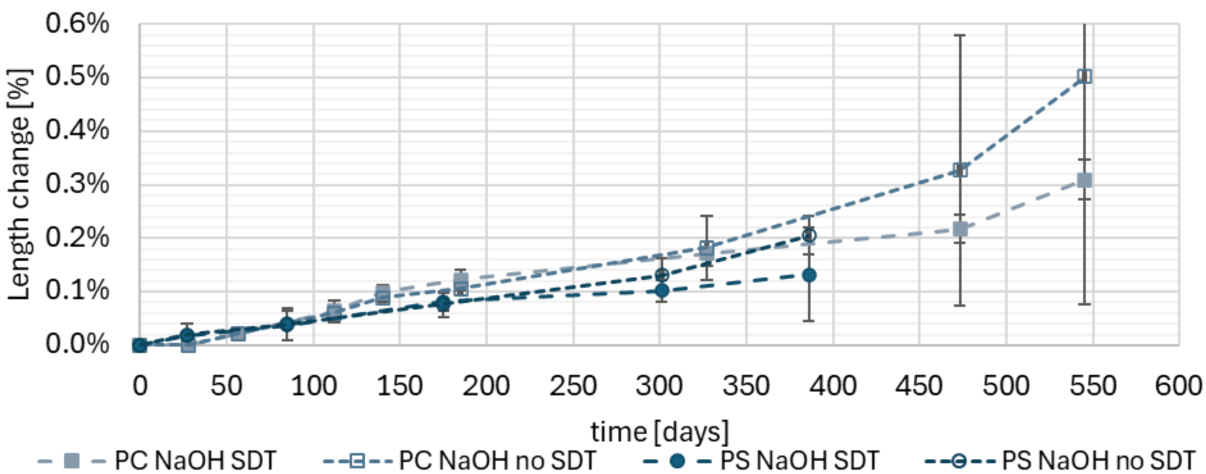

Figure 8-2 Line graph depicting length change after mass stabilization of pier cap (PC) and pier shaft (PS) specimen exposed to 1 M NaOH at 38 °C

The mass of samples was recorded at the same time as each length measurement (Figure 8-3). A larger increase in mass noted for PS samples was thought to be related to a higher ingress of moisture due to larger crack widths and voids observed in cement paste in these specimens.

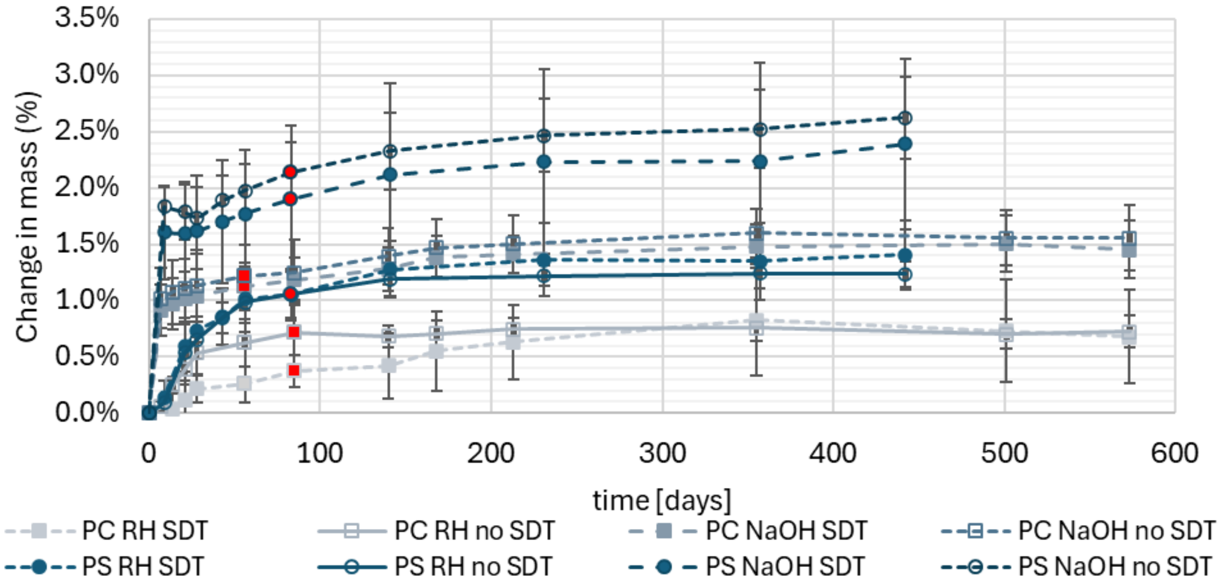

Figure 8-3 Line graph depicting change in mass for all pier cap (PC) and pier shaft (PS) residual expansion specimen where red data points indicate the zero-point chosen for length measurements

Preliminary results from the residual expansion test indicate that additional expansion was possible for both members, which is expected to have resulted in increasing levels of induced damage within the piers of the Champlain Bridge due to the ASR.

8.3 Summary of Paper Conclusions

This section summarizes the results of chapters 4 through 7.

Chapter 4 (Paper 1) presented findings from the first stage of the research. Visual assessments and non-destructive tests conducted on PC and PS segments of the former Champlain Bridge in Montréal consistently indicated high levels of damage. As such, further investigation is needed (i.e. extraction and testing of concrete cores) to assess the cause, likely ASR as per previous assessment of piers in this structure [1], and the extent of damage in these members. Nevertheless, the main findings obtained in this stage of the research were as follows:

The visual assessment identified 'Map cracking' patterns in areas with moderate reinforcement regions of both members. Reduced cracking was visible in high reinforcement regions of the PC as well as the semi-submerged region of the PS. Cracking was identified to display dominant orientations suggesting anisotropic (i.e. directional) properties within both members. In the PC and on the east face of the PS, vertical cracks (i.e., intersecting the horizontal CI lines) were both thinner and less frequent compared to horizontal cracks. In the context of an internal swelling reaction such as ASR, these differences in crack widths suggest expansion is occurring preferentially in one direction (i.e. vertically) compared to another. Quantitative visual inspection using the CI was performed indicating that the highest damage was obtained on the PS east face. The CI corresponding to this location exhibited wider and more frequent cracks intersecting the CI with cracks primarily oriented horizontally.

Ultimately, the presence of ASR in the members was not clearly indicated by inspection of exterior surfaces. This was in stark contrast to internal surfaces exposed during decommissioning of the members, which included clear indicators of ASR gel in aggregates and paste. Although the PC was encapsulated in a repair concrete 10 years before decommissioning, average crack widths were similar to average crack widths recorded on the PS. This suggests that assessment of reinforced concrete members using crack width measurements can provide insight to increasing deterioration within the member.

Non-destructive testing was subsequently performed on the exterior of the PC and PS members using rebound hammer, ultrasonic pulse velocity and surface electrical resistivity. The rebound hammer estimated an average concrete strength between 33-39 MPa in east, west and interior locations of the PS and PC. The average compressive strength on the PC bottom surfaces was estimated at 50 MPa. In the PC the rebound hammer did not identify significant differences in compressive strength on the exterior (repair concrete) surfaces compared to the interior (original) concrete. Ultrasonic pulse velocity results were less than 3.0 km/s indicating the need for further investigation (e.g. extraction of cores for laboratory analysis) which agrees with the extent of cracking observed during the visual inspection. Electrical surface resistivity measurements clearly distinguished between the PC repair concrete (low permeability to chloride ingress) and the internal concrete (higher permeability); however, there was high variation when used solely on the repair concrete. The electrical surface resistivity was comparable for the PC interior concrete and PS external and internal concrete. However, non-destructive testing was limited in areas displaying the highest deterioration such as areas with wide crack widths, like the east face of the PS.

Visual and non-destructive tests successfully identified the high level of deterioration in both the PC and PS members; however, without access to interior surfaces, the cause of the deterioration could not be clearly identified. This indicated that the extraction of concrete cores continues to be necessary to establish the cause and extent of damage in reinforced concrete members even at high levels of deterioration.

Chapter 5 (Paper 2) presented the results of microscopic investigations of extracted cores. Microscopic analysis performed using both the DRI and extended DRI versions (% microscopic features, crack density) identified that the primary deterioration mechanism affecting both the PC and PS members as ASR, corresponding to a high deterioration level of damage (i.e. free expansion 0.20% or greater). This was supported by observations of ASR products displaying distinct appearances (i.e., distinct colours and morphologies) in polished specimens from both the PC and PS. Moreover, corrosion products were also observed in surface specimens from both members. The interaction between ASR and corrosion products are mostly unknown.

Surface core specimens presented higher DRI numbers (1002 to 1133 for the PC, 773 to 1223 for the PS) compared to internal core specimens (821 to 1018 in the PC, 759 to 993 for the PS), indicating higher levels of deterioration. Surface core specimens in the PS exhibited higher DRI values in the dry regions compared to the semi-submerged exposure conditions. The amount of cracks observed in the cement paste and cracking pattern found in dry region specimens of PS indicate the presence of ASR coupled with freeze-thaw.

Extended analysis was performed wherein crack widths ≥ 0.10 mm were measured for select samples from PC and PS members. Evaluation of the location of these cracks within DRI core specimens provided additional insights into the dominant crack orientation and indicated the presence of anisotropic properties. In contrast, evaluation of all cracks observed at 16x magnification, as used for DRI, exhibited indistinct crack orientations.

Chapter 6 (Paper 3) presented the investigation of mechanical damage in cores. Mechanical deterioration was identified corresponding to marginal to very high damage in concrete cores as per [2]. Free expansion was estimated from literature results [3] for a concrete mix with a similar reactive coarse aggregate and strength. However, high damage in concrete specimens in this work required interpolation to estimate expansion. The highest damage was identified in transverse and longitudinal PS specimens with dry locations identified to have increased damage, while the lowest damage was identified in longitudinal PC specimens.

Transverse cores from the PC and PS were found to exhibit similar damage patterns and extents in surface specimens with Dynamic ME, ME and F'c values for both members resulting in values of approximately 18.5 GPa, 9.5 GPa and 27 MPa, respectively. Conversely, despite similar damage patterns (i.e. widthwise cracking in core specimen) and compressive strengths (average f'c of 22 MPa to 27 MPa), internal PC specimen presented higher Dynamic ME and ME values of 11 GPa and 12.9 GPa compared to PS specimens which presented values of 4.5 GPa and 8.3 GPa, respectively. Longitudinal and vertically oriented cores extracted from the PC and PS were not directly comparable due to the different geometries. Further consideration of aspects including crack orientation (i.e. cracks occurring parallel or perpendicular to loading) were needed to compare cores from these orientations.

Resonant frequency was used successfully to determine the Edyn of damaged concrete. Trends in Dynamic ME matching trends identified by ME were successfully identified using this method. To improve applicability of this method for field samples, multiple transverse measurements should be taken around the circumference of the core due to high variations between maximum and minimum measurements attributed to the anisotropic properties of extracted cores.

A supplemental image analysis technique was proposed to evaluate crack orientation within core specimens. The method, wherein cores are scanned with visible cracks traced and analyzed using ImageJ, provided insight into orientation of cracks in aggregate particles and cement paste. Use of crack density and orientation from supplemental image analysis for cracks in cement paste provided a good method for comparison of SDI, PDI and ME results. Core specimens presenting perpendicular (i.e. widthwise) cracks presented low ME and greater SDI and PDI values compared to cracks with parallel (i.e. lengthwise) cracks and cracks with mixed (i.e. low crack density or low density of cracks exhibiting distinct lengthwise or widthwise orientations).

Chapter 7 (Paper 4) further investigated the impact of reinforcement configuration (i.e. high vs. low reinforcement density) within the pier cap and anisotropy, specifically lengthwise cracking, on microscopic and mechanical test results for longitudinal core specimens. The main findings of this investigation can be summarized as follows:

Cores extracted from the high reinforcement top region presented higher damage when compared to cores from the middle and bottom regions which presented lower density of reinforcement. This indicates that the stress state of the concrete member caused by service loading (tensile in the top region) and reinforcement influenced the overall deterioration over time.

Specimens at the top region exhibited higher microscopic damage features with increased amounts of reaction products in cracks within the aggregate particles (i.e. increased OCA_{RP}) along with notable differences in average crack widths in aggregates (larger width cracks) compared to the cement paste (smaller width cracks). Specimens in the middle and bottom regions exhibited reduced damage features within the aggregate particles and similar average crack widths in the aggregates and cement paste.

Observed crack patterns on DRI surfaces and scans of the cores (i.e. supplemental image analysis) used for SDT indicated primarily lengthwise cracking in both aggregates and cement paste of the longitudinal core specimens investigated. This parallel cracking to the main reinforcement agrees with past research and was captured through the various multi-level tools implemented in this research.

Results indicate the need for continued research efforts to be undertaken into the effects of stress state (e.g. concrete in tension versus compression) on ASR-induced development (i.e., expansion and cracking) to better identify the impact of this damage mechanism on reinforced concrete structures with a variety of geometries, reinforcement configurations, and stress states.

8.4 Additional Contributions to Scientific and Engineering Communities

Reports submitted to Jacques Cartier and Champlain Bridges Incorporated (JCCBI)

Note that authorship is arranged with students listed alphabetically followed by supervising professors listed alphabetically and does not indicate the extent of contributions.

1) Abodrahim, A., Fowai,I., Kristufek, L., Tawil, D., Vilela Gorga, R., Martín-Pérez, B., Noël, M. and Sanchez, L.. "Factors affecting the performance of aging concrete bridges: state-of-the-art review" (256 p). (January 2023)
2) Fowai,I., Kristufek, L., Tawil,D., Martín-Pérez, B., Noël, M. and Sanchez, L.. "Visual and non-destructive testing on Champlain Bridge Members" (~250 p). (June 2023)
3) Kristufek, L., Martín-Pérez, B., Noël, M. and Sanchez, L.. "Multi-level Assessment of ASR affected members from the Champlain Bridge (Pier Cap 42W and Pier shaft 38W)" (52 p). (June 2025)

Conference papers presented to the larger research community

1) **Kristufek, L**., Tawil, D., Martin-Perez, B., Sanchez, L., and Noël, M.. Preliminary evaluation of pier cap from an ASR affected bridge in Central Canada. International Conference on Concrete Repair, Rehabilitation and Retrofitting (ICCRRR 2022). MATEC Web of Conferences. 364, 03005 (2022)
2) Tawil, D., **Kristufek, L.**, Beatriz Martin-Perez, Leandro F.M. Sanchez and Martin Noël. "Condition assessment of two prestressed concrete slabs after 60 years in service". International Conference on Concrete Repair, Rehabilitation and Retrofitting (ICCRRR 2022). MATEC Web of Conferences. 364, 03004 (2022)
3) **Kristufek, L.,** Sanchez, L., Martín-Pérez, B., Noël, M. (2024). Condition Assessment of Concrete Pier Shaft Segment from Bridge in Central Canada. In: Desjardins, S., Poitras, G.J. (eds)

Proceedings of the Canadian Society for Civil Engineering Annual Conference 2023, Volume 1. CSCE 2023. Lecture Notes in Civil Engineering, vol 495. Springer, Cham. https://doi.org/10.1007/978-3-031-60415-7_12

4) **Kristufek, L.,** Sanchez, L., Martín-Pérez, B., Noël, M. "Détermination de la condition de l'état de ponts vieillissants en béton armé: de l'évaluation visuelle à l'évaluation microscopique" 21e édition des Journées scientifiques du Regroupement francophone pour la recherche et la formation sur le béton (RF)^{2}B. July 5-6 2023. Polytechnique Montréal, Montréal, Canada.
5) **Kristufek, L.,** Sanchez, L., Martín-Pérez, B., Noël, M. (2024). Estimating Expansion in Aged Structures Using Visual, Non-destructive and Microscopic Techniques. In: Sanchez, L.F., Trottier, C. (eds) Proceedings of the 17th International Conference on Alkali-Aggregate Reaction in Concrete. ICAAR 2024. RILEM Bookseries, vol 49. Springer, Cham. https://doi.org/10.1007/978-3-031-59419-9_73

8.5 Future work

The present work presented a comprehensive condition assessment encompassing visual, non-destructive, microscopic and mechanical testing of a PC and PS member from Montreal's Champlain Bridge. The large scope of testing undertaken provides a significant contribution through the large number of cores extracted from three distinct orientations (i.e. transverse - T, longitudinal - L and vertical - V) which facilitated both microscopic (i.e. using the damage rating index) and mechanical (i.e. using SDT and compressive) testing from all orientations, representative depths (i.e. surface vs. interior) and unique micro-environments (i.e. different expected stress-states, presence of repairs and wet vs. dry service environments).

8.5.1 Future Work to Expand on Proposed Image Analysis Techniques

This work proposed two procedures to further investigate anisotropy: a qualitative (i.e. measuring crack widths and drawing crack orientation on scans of DRI specimens) and the quantitative image analysis technique.

In this thesis results of the quantitative image analysis technique has been presented as an average of all cores in a given category as defined by the member (PC or PS), core orientation (T, L or V), depth (surface vs. interior) and service condition (wet vs. dry for the PS). However, this approach reduces the effectiveness to link individual cracking to mechanical deterioration. In particular, the irregular reinforcement of the members relative to core extraction locations and localized service environments may significantly influence cracking identified (as seen by the large error bars in Figure 6-13 and Figure 6-14). This could be expanded in several ways:

1. Further evaluation of current experimental results on an individual basis with further consideration to the location where the core was extracted (i.e. reinforcement configuration, other segments of the same core, micro-environments) as well as correlation to both destructive and non-destructive mechanical techniques (i.e., resonant frequency, stiffness-damage test and compressive test results).
2. Evaluation of cores from other structures or standardized lab tests (e.g. perform the scanning method on cores from larger scale exposure site specimens where geometry is more uniform).
3. Perform this technique on cores exhibiting a larger variety of damage extents (i.e. different free expansion percentages).

8.5.2 Future Work for Microscopic Analysis

SEM and petrographic analysis of the research specimens have not been completed for this work although preliminary SEM-EDS results performed on specimens from the PC have been found to correspond with the morphology and compositions from literature (Appendix C). The use of SEM-EDS will be implemented to further confirm the diagnosis of ASR for both members using specimens from a variety of locations within the members. The following future work could be conducted:

1. Perform SEM and SEM-EDS on specimens from both the PC and PS including surface and interior locations as well as areas representing different stress states, especially in the PC,

and wet and dry locations in the PS. In some areas the large thickness of observed ASR gel may yield variable compositions due to the development of ASR over time (e.g. changing SiO_2 availability in the reaction product).

2. Comparison of SEM-EDS results to gel identified in accelerated tests such as the mortar bar test and concrete prism test. Gel viscosity impacts the amount of expansion and thus impacts the damage classification in multi-level analysis (i.e. based on microscopic – DRI and mechanical properties) so data from a field structure is of interest to the ASR research community to better correlate lab and field results.
3. SEM on regions exhibiting mixed damage mechanisms such as the example in Figure 5-7 where ASR and corrosion were observed.

8.5.3 Future Work Evaluating Potential for Further Deterioration (Prognosis)

Residual expansion testing in two accelerated conditions (i.e. 100% RH and submerged in 1M NaOH, both at 38 °C) is ongoing for specimens representing distinct core orientations and depths from the PC and PS (as described in section 8.3). These are expected to provide the following contributions:

1. Insight into the ultimate expansion extent for both the PC and PS.
2. Insight into residual expansion capacity in different regions of the PC and PS members. The capacity for residual expansion may differ due to existing service environments prior to extraction of the cores (e.g. higher or lower moisture).
3. Insight into the use of specimen previously tested using the SDT. Although the SDT is nominally considered to be non-destructive, some damage may be induced in the specimens potentially impacting RE performance. Currently the re-use of specimens tested using SDT is not recommended however the re-use of specimens may reduce the number of core specimens needed.

8.5.4 Future Work to Link Materials and Structural Analysis

This work has provided significant insights into material scale damage in the PC and PS members. Further analysis at the structural scale is needed such as finite element analysis to better understand how the level of material damage, including anisotropic properties, identified in cores from specific locations will translate to reduced capacity in the members. Structural analysis will be important for structure owners for decisions related to repair, rehabilitation or replacement. Specific aspects which may be investigated include:

1. Impact of reinforcements on damage identified in core specimens
2. Impact of live loads throughout the service life of the structure. The Champlain Bridge was operated as a toll bridge prior to the 1990's which may have reduced the traffic using the bridge. Additionally, aspects such as the size and weight of cars and trucks is expected to have changed over the service life impacting damage (e.g. areas of fatigue) to the material.
3. Impact of repair measures, including the encapsulation repair in 2004 and the addition of external strengthening measures on the PC on stress states throughout the member.

8.6 References

1. Bérubé MA, Frenette J. Évaluation de la Réactivité Alcaline dans le Béton des Piles 12, 18 et 20 W du Pont Champlain: Complément au rapport soumis en février 1994. Sainte-Foy, Quebec; 1995.

2. Sanchez LFM, Drimalas T, Fournier B, Mitchell D, Bastien J. Comprehensive damage assessment in concrete affected by different internal swelling reaction (ISR) mechanisms. Cem Concr Res. 2018;107(February):284–303.

3. Sanchez LFM, Fournier B, Jolin M, Mitchell D, Bastien J. Overall assessment of Alkali-Aggregate Reaction (AAR) in concretes presenting different strengths and incorporating a wide range of reactive aggregate types and natures. Cem Concr Res [Internet]. 2017;93:17–31. Available from: http://dx.doi.org/10.1016/j.cemconres.2016.12.001

Appendix A: Visual and NDT Data

Pier Cap visual and NDT individual data

The following section presents visual and non-destructive test data for individual surfaces of segments of the PC and PS members. Naming of data is performed with the location of each segment as identified in Figure A 1 followed by the direction faced by of each surface within that segment while in service (e.g. south-east abbreviated to SE, bottom surface facing the ground abbreviated to B).

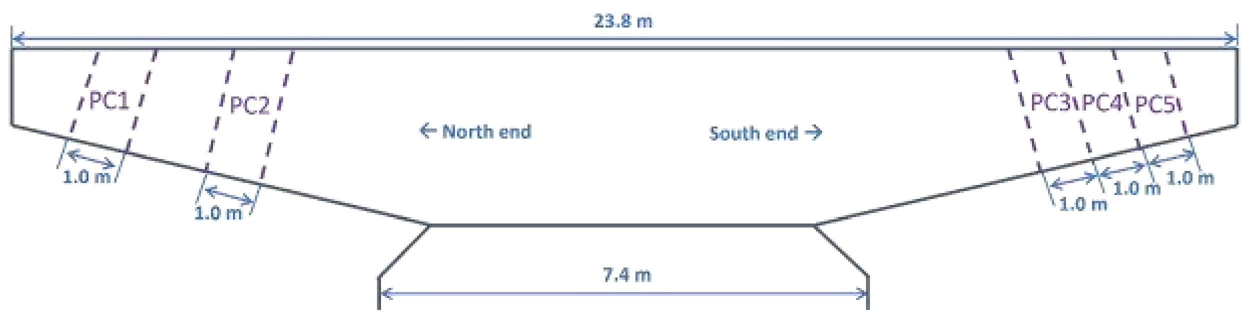

Figure A 1 PC naming convention for individual measurement locations

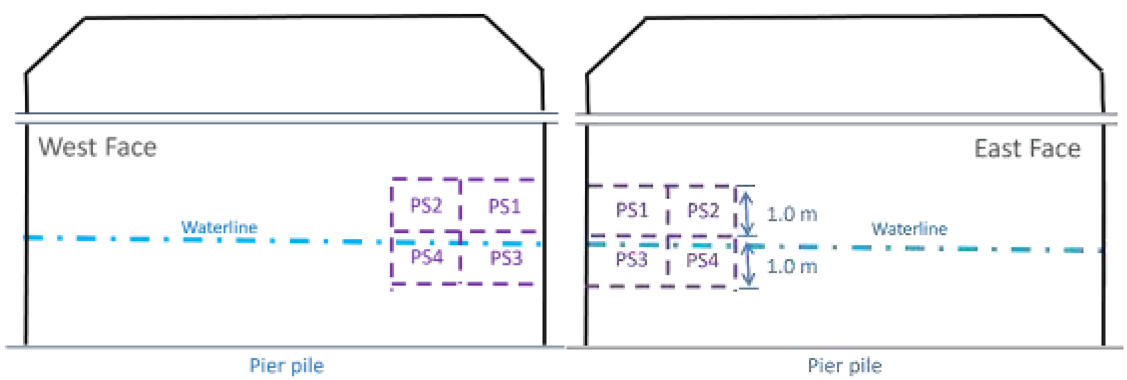

Figure A 2 PS naming convention for individual measurement locations

Results from the quantitative (i.e. CI) and semi-quantitative (i.e. crack widths from CI) visual assessments are presented in Figure A 3 and Figure A 5 for the PC and Figure A 4 and Figure A 6 for the PS, respectively. Ultrasonic pulse velocity measurements in km/s determined using the indirect method are presented in Figure A 7 for both the PC and PS members. Rebound hammer number prior to calculation of the rebound number in MPa are presented in Figure A 8.

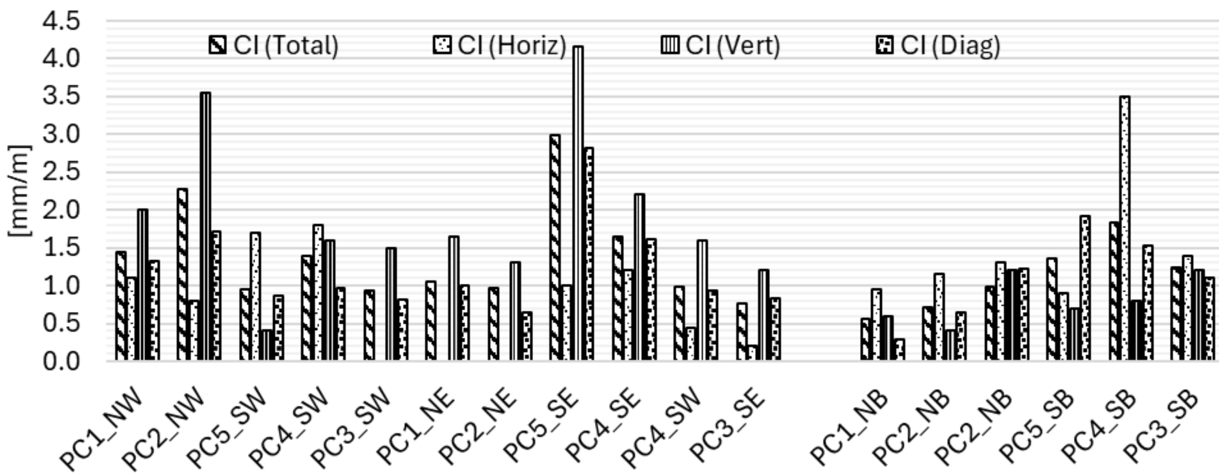

Figure A 3 CI values for PC individual locations

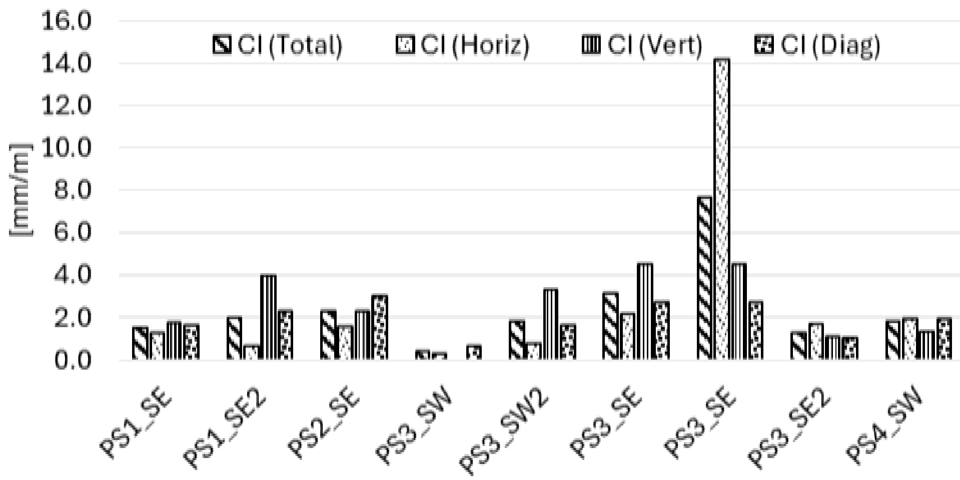

Figure A 4 CI values for PS individual locations

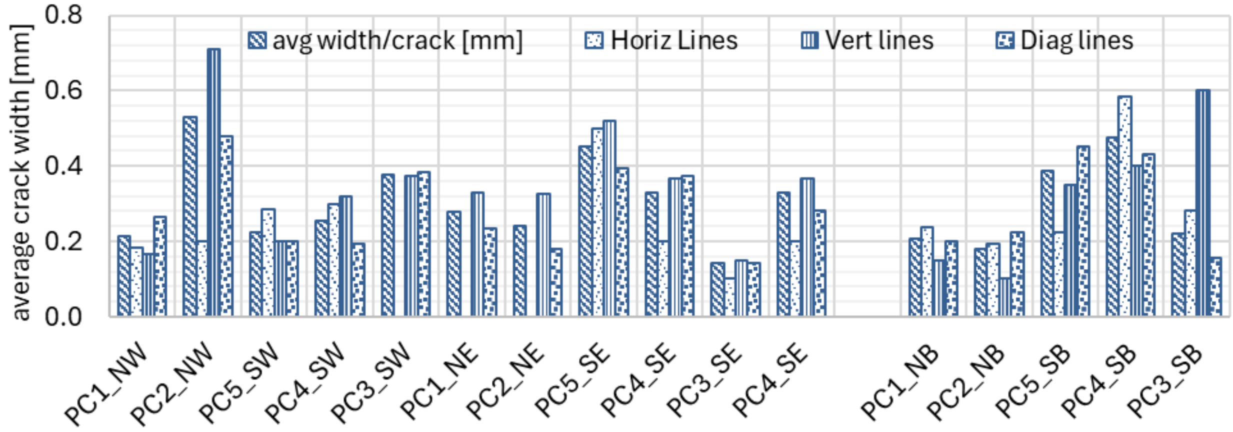

Figure A 5 Average crack width (mm) from CI for PC individual locations

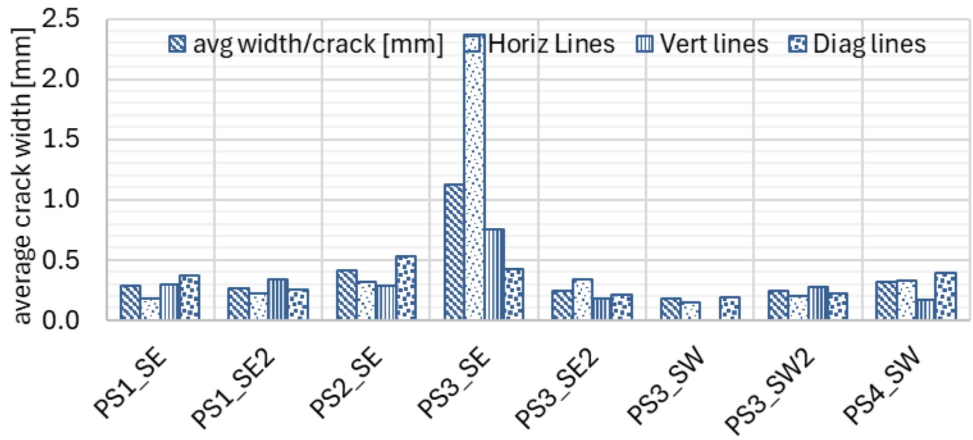

Figure A 6 Average crack width (mm) from CI for PS individual locations

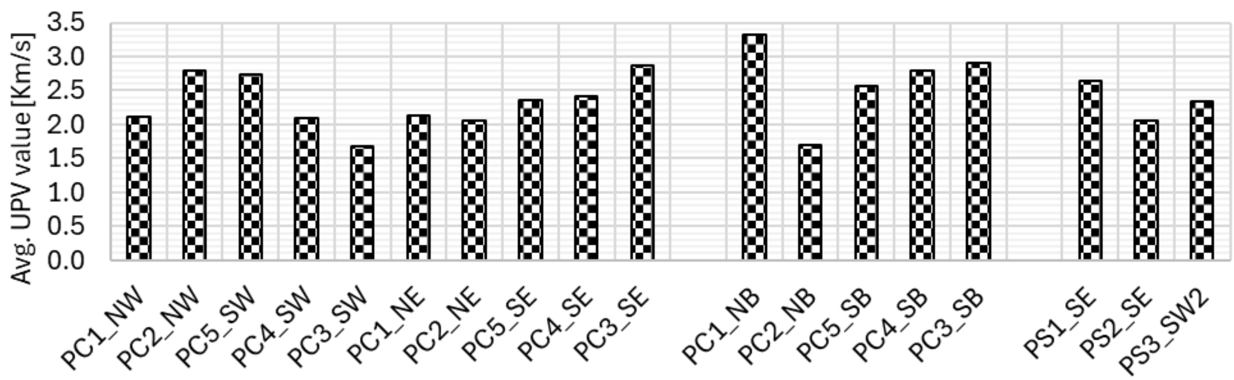

Figure A 7 Average UPV values for PC and PS individual segment surfaces investigated

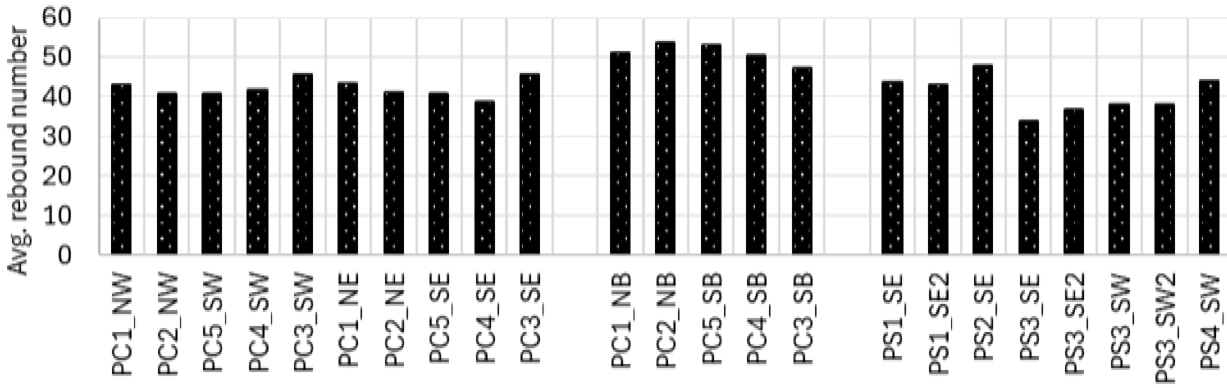

Figure A 8 Average rebound number for PC and PS individual segment surfaces investigated

Appendix B: Additional Considerations – Coring

The locations for the extraction of cores were chosen to capture both the least and most damaged regions of both members, with additional cores extracted from areas exhibiting lower damage in visual and non-destructive assessments for compressive tests prior to performing SDT. The length of individual cores extracted from the PC and PS members varied. In several core locations in the PC further the maximum depth of coring was prevented by metal plates within the member. In the PS internal damage reduced the length of extracted core segments, with breaks common in extracted cores at a depth of 10 cm from the surface. General poor cohesion was additionally noted for the initial 90 cm of core L_SE6 (left side in Figure A 9) with this section unusable for microscopic and mechanical testing.

Figure A 9 Core specimens from the PS displaying damage

Segments smaller than 20 cm in length were not suitable for mechanical testing but were used in microscopic testing. Initial specimen naming was assigned with each segment receiving a number indicating the section and surface of origin followed by a number such that increasing numbers indicated increasing depths. Subsequent cutting of core segments resulted in additional labeling using letters (i.e. a, b, c etc.) as shown in Figure A 10 and Figure A 11. This indirectly captured the extent of discontinuities present in extracted cores.

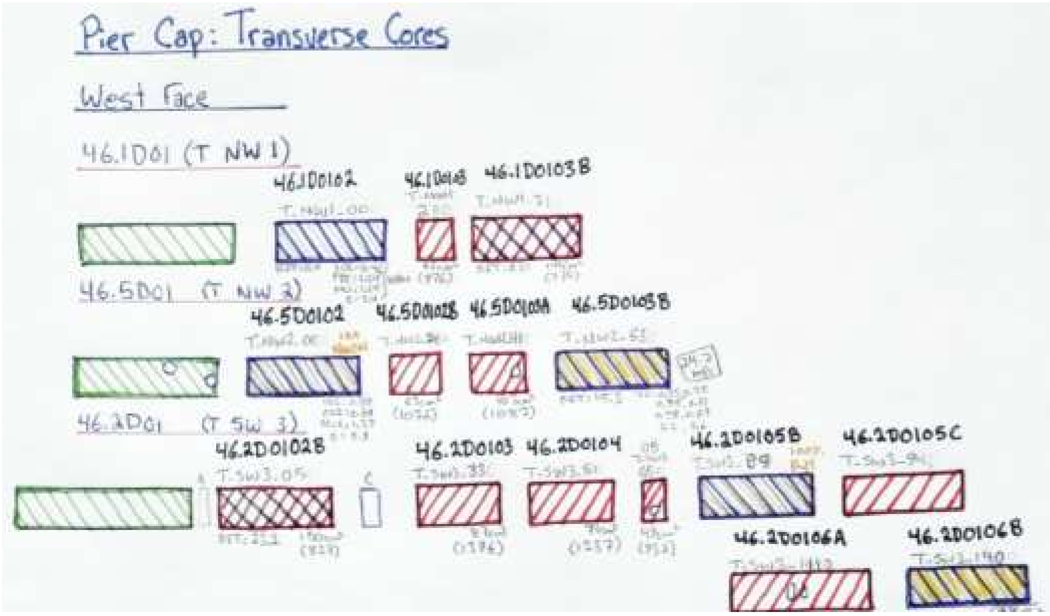

Figure A 10 Example of core segments and uses from the PC. Colours indicate the following: green = repair concrete layer, purple = RF performed, light blue = SDT performed, red = DRI performed (destructive), orange = specimen used for residual expansion (100% RH or submerged in 1M NaOH), yellow = tested in compression (destructive)

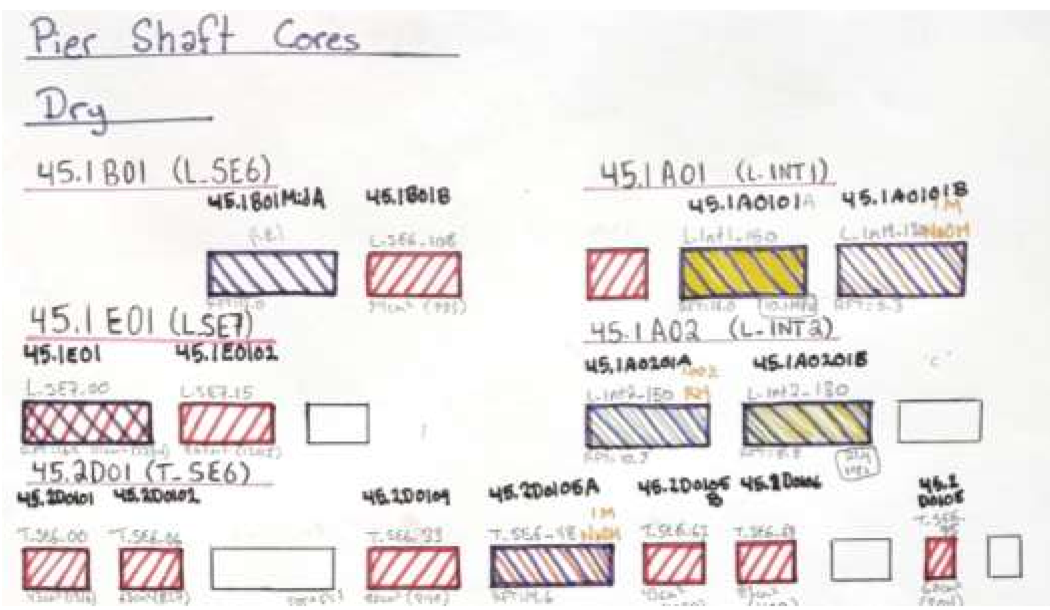

Figure A 11 Example of core segments and uses from the PS. Colours indicate the following: purple = RF performed, light blue = SDT performed, red = DRI performed (destructive), orange = specimen used for residual expansion (100% RH or submerged in 1M NaOH), yellow = tested in compression (destructive)

Appendix C: Microscopic Analysis Data

Individual DRI values

DRI results for individual specimens from the PC and PS are shown in Figure A 12 and Figure A 13. The number indicates the depth of the end nearest to the external surface.

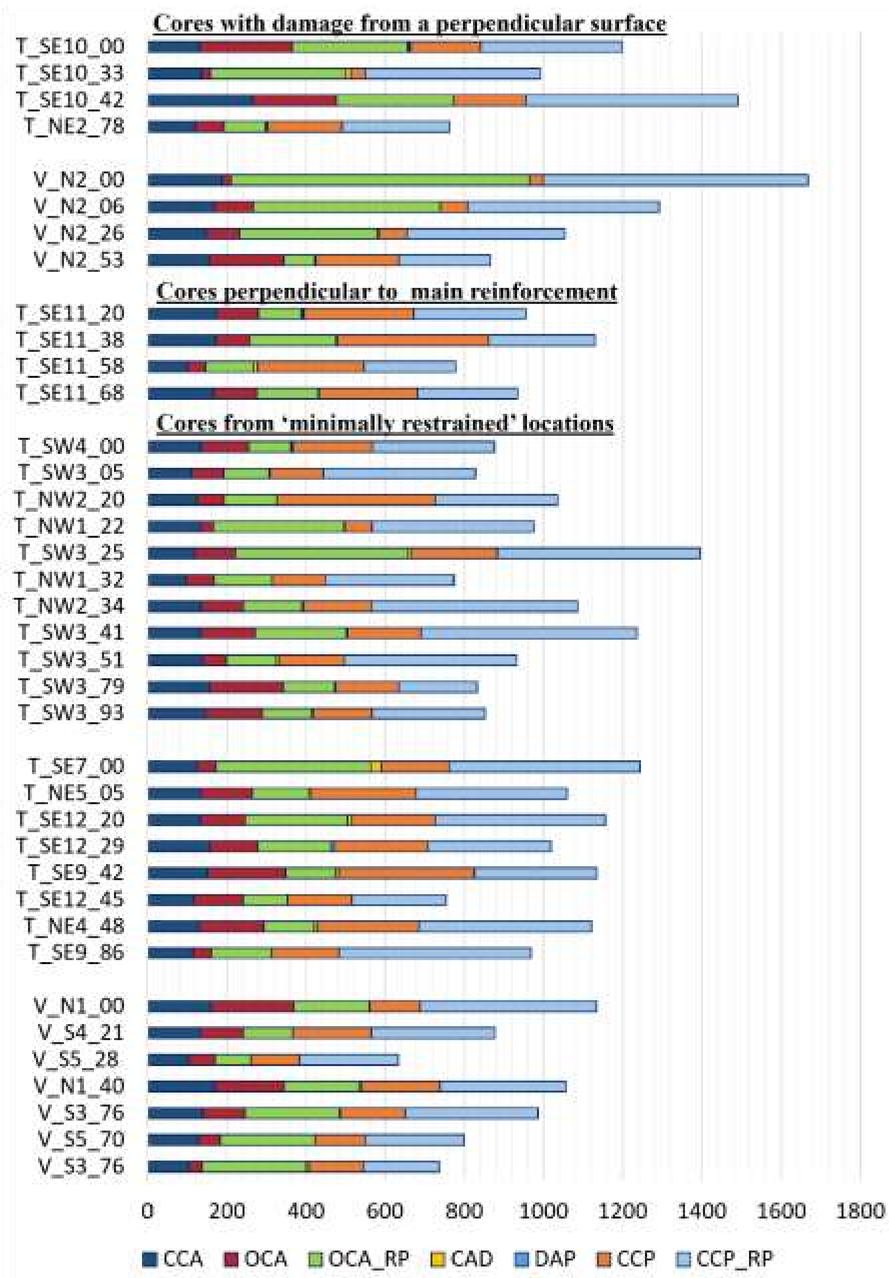

Figure A 12 Individual DRI results for PC transverse (T) and vertical (V) cores

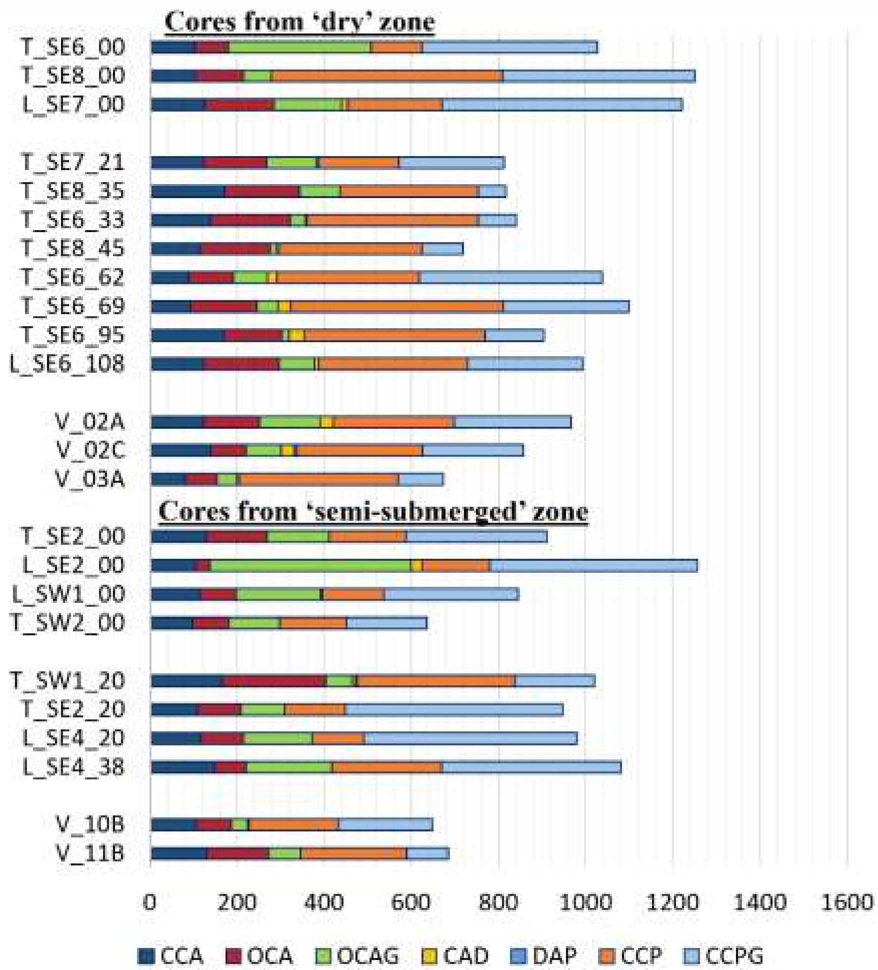

Figure A 13 Individual DRI results for PS transverse (T), longitudinal (L) and vertical (V) cores from dry and semi-submerged locations

Crack widths

Crack width measurement results, including the number of locations where cracks 0.10 mm or greater were measured are shown in Table A 1 for PC specimens and Table A 2 for PS specimens. Note that crack widths in the cement paste of PS specimens from the dry region were found to be larger compared to crack widths in other regions.

Table A 1 Crack widths in select PC DRI specimens (n = number of locations measured)

Sample	Depth [cm]	Avg. crack width aggregate [mm]	Stdev [mm]	Avg. crack width in cement paste [mm]	Stdev [mm]	# cracks in aggregate ≥0.1mm/ 100 cm^2	# cracks in cement paste ≥0.1mm/ 100 cm^2
PC_T_SE7	0	0.18 (n=14)	*0.12*	0.13 (n=12)	*0.06*	8	7
PC_T_NE5	5	0.10 (n=7)	*0.00*	0.17 (n=10)	*0.12*	4	6
PC_T_SW3	41	0.16 (n=11)	*0.06*	0.13 (n=15)	*0.04*	8	11
PC_T_SE9	42	0.13 (n=11)	*0.03*	0.14 (n=13)	*0.05*	11	13
PC_T_NE4	48	0.12 (n=14)	*0.04*	0.15 (n=17)	*0.08*	10	12
PC_T_SW3	93	0.16 (n=8)	*0.07*	0.19 (n=12)	*0.13*	10	14
PC_L_N1		0.16 (n=34)	*0.10*	0.13 (n=20)	*0.05*	39	23
PC_L_N6		0.15 (n=48)	*0.05*	0.14 (n=17)	*0.06*	45	16
PC_L_N7		0.16 (n=53)	*0.10*	0.15 (n=27)	*0.07*	42	21
PC_L_S9		0.18 (n=41)	*0.18*	0.15 (n=28)	*0.08*		
PC_L_S11		0.16 (n=39)	*0.08*	0.19 (n=11)	*0.19*	41	12
PC_L_S12		0.15 (n=10)	*0.06*	0.13 (n=11)	*0.06*	21	23
PC_L_S15		0.18 (n=47)	*0.11*	0.12 (n=14)	*0.05*	37	11
PC_L_S16		0.15 (n=7)	*0.03*	0.10 (n=3)	*0.00*	12	5
PC_V_N2	0	0.19 (n=28)	*0.07*	0.14 (n=17)	*0.05*	10	6
PC_V_S4	21	0.14 (n=15)	*0.05*	0.18 (n=7)	*0.11*	12	6
PC_V_S5	70	0.14 (n=8)	*0.04*	0.12 (n=12)	*0.03*	5	7
PC_V_S3	76	0.13 (n=12)	*0.04*	0.10 (n=1)	*NA*	13	1

Table A 2 Crack widths in select PS DRI specimens (n = number of locations measured)

Sample	Depth [cm]	Avg. crack width aggregate [mm]	Stdev [mm]	Avg. crack width in cement paste [mm]	Stdev [mm]	# cracks in aggregate ≥0.1mm/ 100 cm^2	# cracks in cement paste ≥0.1mm/ 100 cm^2
<u>DRY</u>							
PS_T_SE6	0	0.11 (n=7)	*0.04*	**0.26** (n=27)	*0.25*	7	28
PS_T_SE8	0	0.16 (n=6)	*0.07*	**0.47** (n=54)	*0.87*	6	53
PS_L_SE7	15	0.12 (n=16)	*0.04*	**0.18** (n=19)	*0.09*	11	13
PS_T_SE7	21	0.11 (n=6)	*0.02*	**0.20** (n=5)	*0.22*	4	4
PS_T_SE6	33	0.13 (n=3)	*0.05*	**0.24** (n=15)	*0.19*	1	3
PS_T_SE8	35	0.13 (n=2)	*0.04*	**0.38** (n=5)	*0.37*	2	12
PS_T_SE6	62	0.15 (n=4)	*0.05*	**0.19** (n=6)	*0.06*	6	9
PS_T_SE6	95	0.10 (n=1)	*0.00*	**0.23** (n=4)	*0.13*	1	2
PS_L_SE6	108	0.18 (n=10)	*0.10*	**0.31** (n=25)	*0.29*		
<u>WET</u>							
PS_L_SE2	0	0.22 (n=82)	*0.24*	0.22 (n=67)	*0.11*	46	38
PS_T_SW2	0	0.15 (n=11)	*0.06*	0.11 (n=4)	*0.03*	10	4
PS_L_SW1	0	0.14 (n=15)	*0.14*	0.14 (n=9)	*0.04*	19	11
PS_T_SW1	20	0.14 (n=13)	*0.11*	0.17 (n=14)	*0.13*	7	8
PS_T_SE2	20	0.12 (n=11)	*0.03*	0.13 (n=9)	*0.07*	8	6
PS_L_SE4	38	0.18 (n=20)	*0.12*	0.18 (n=17)	*0.09*		

Preliminary SEM Results

Scanning electron microscopy (SEM) and electron dispersed spectroscopy (EDS) were performed using a LaB9 filament. SEM-EDS was used to further investigate damage features observed during DRI. Samples from two locations in the Pier Cap were investigated. Preliminary results are shown from a PC core.

Reaction Products Investigated

Figure A 14 shows a reaction product which was observed to pass through an aggregate and portlandite filled pore. EDS results are presented in Table A 3.. Spectrum 9 from sample 3 was found to match results for a secondary ASR reaction product identified in a conference paper by Boehm-Courjault and Leemann 2017. Further investigation of these and other SEM specimens from the Champlain Bridge are needed to conclusively determine the nature of reaction products.

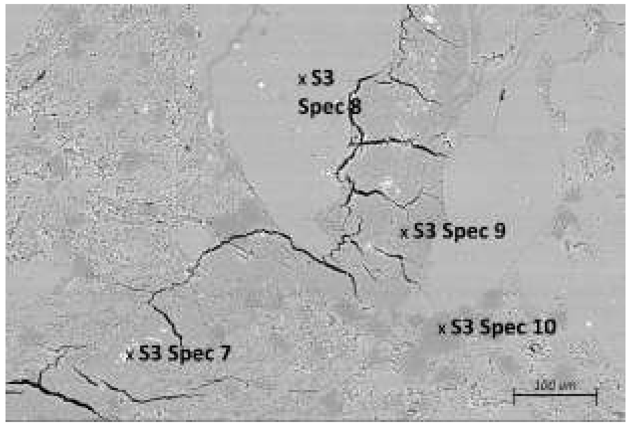

Figure A 14 SEM image (using BSD) of suspected gels

Table A 3 Atomic % of Ca, Si and (Na+K) in areas of interest

	Atomic % (O, Au and C excluded)			*Atomic ratio*		
	Ca	**Si**	**Na+K**	**Ca/Si**	**(Na+K)/Si**	**Si/Ca**
S3 Spec 8	100%	0%	0%	NA	NA	NA
S3 Spec 7	11%	26%	11%	0.42	0.42	2.41
S3 Spec 9	16%	63%	19%	0.26	0.31	3.89

Reference

Boehm-Courjault E, Leemann A. Characterization of ASR products by SEM and TEM. In: 16th Euroseminar on Microscopy Applied to Building Materials EMABM [Internet]. Les Diablerets, Switzerland; 2017. p. 27–30. Available from: https://www.researchgate.net/publication/323068964

Appendix D: Crack Orientation on Core Exteriors

Directionality to evaluate crack orientation

Crack orientation was determined using the directionality function in Image J (*https://imagej.net/plugins/directionality#fnref:1*). A variety of crack orientations can be observed in traced cracks on scans, as well as a variety of crack densities.

Range of angles for parallel and perpendicular cracks

Two ranges of angles (20° and 40°) were considered for determining the representation of cracking in samples as parallel or perpendicular to loading. Two traced samples are shown in Figure A 15 representing primarily perpendicular (PC T NW2 530) and primarily parallel (PC L S16) cracking in aggregates. Arrows indicate directions of cracking in different areas in the sample while the half circles indicate the difference in areas considered for the two ranges of angles.

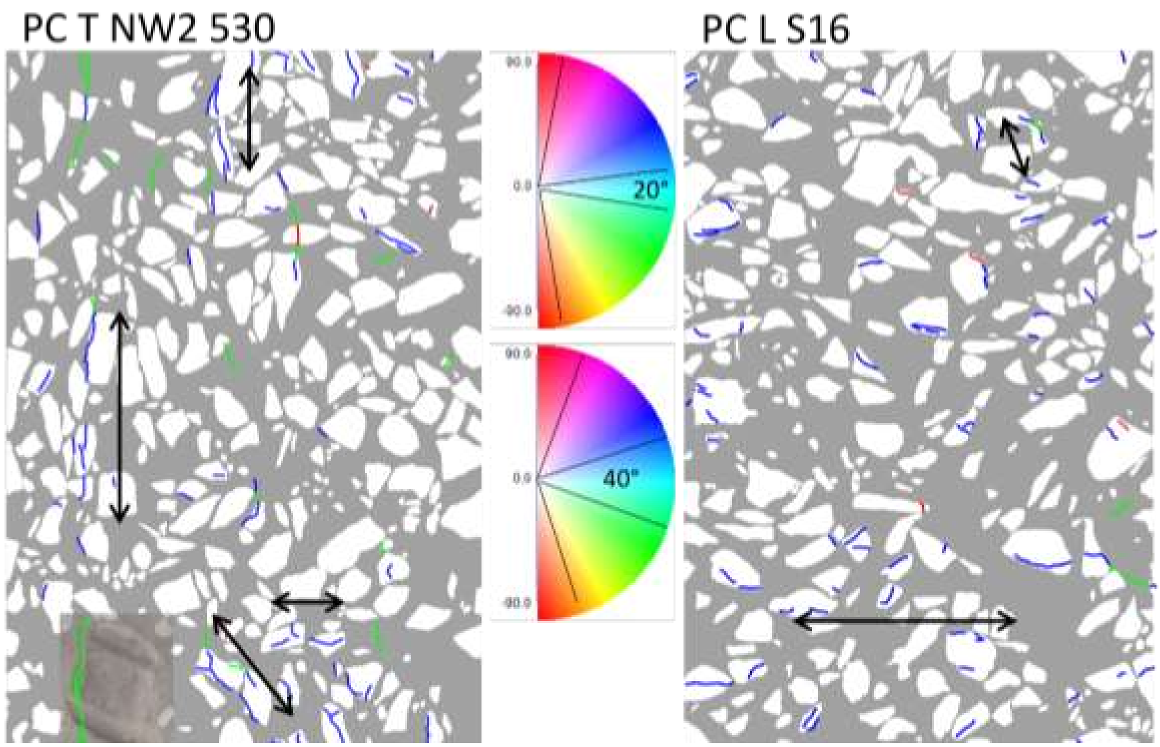

Figure A 15 Traced cracks and aggregates compared to range of angles considered for parallel and perpendicular cracks

Increasing the range of angles within which cracks are considered as perpendicular or parallel increases the percentage of cracks that fall into these categories Increases in the percentage of cracks that fall into these categories through consideration of higher ranges of angles results in similar slopes for parallel oriented lines and perpendicular cracks in aggregates of 0.4 – 0.49 % per degree while perpendicular cracks in paste increase more steeply (0.65 % per degree).

Table A 4 Average percent of cracks oriented parallel, perpendicular or other within different ranges

	Perpendicular to loading	Parallel to loading	Other (i.e. not parallel or perpendicular)
Agg 20 deg range	Avg 17.8% stdev 9.1%	Avg 15.5% stdev 7.4%	Avg 66.7% stdev 4.6%
Agg 40 deg range	Avg 27.7% stdev 12.3%	Avg 25.1% stdev 11.0%	Avg 47.2% stdev 5.3%
Paste 20 deg range	Avg 26.6% stdev 15.5%	Avg 13.8% stdev 15.9%	Avg 59.7% stdev 9.2%
Paste 40 deg range	Avg 39.5% stdev 21.5%	Avg 21.7% stdev 22.0%	Avg 38.8% stdev 8.7%

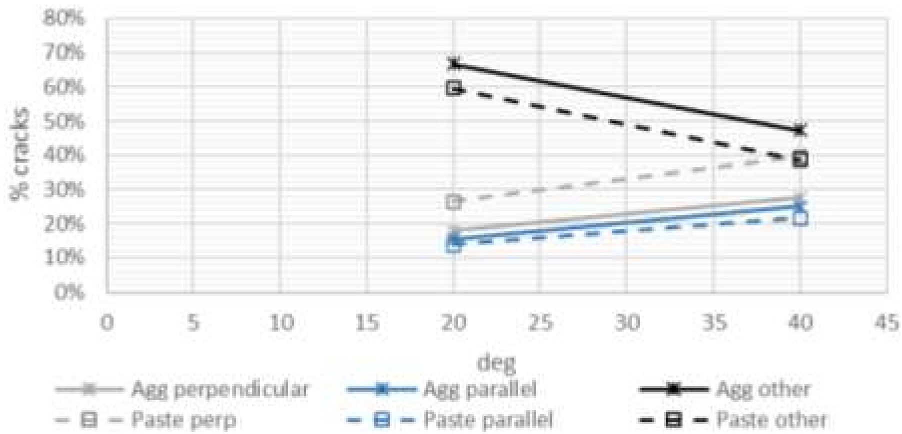

Figure A 16 Average percentage of crack types at ranges of 20 ° or 40 ° for cracks in aggregate particles and cement pastes

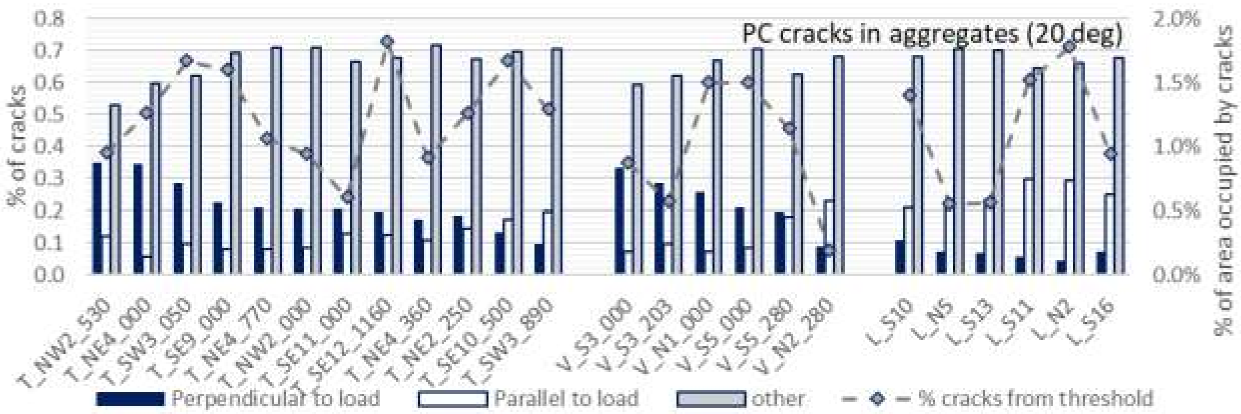

Figure A 17 Directionality for PC samples using 20 ° range for parallel and perpendicular cracks

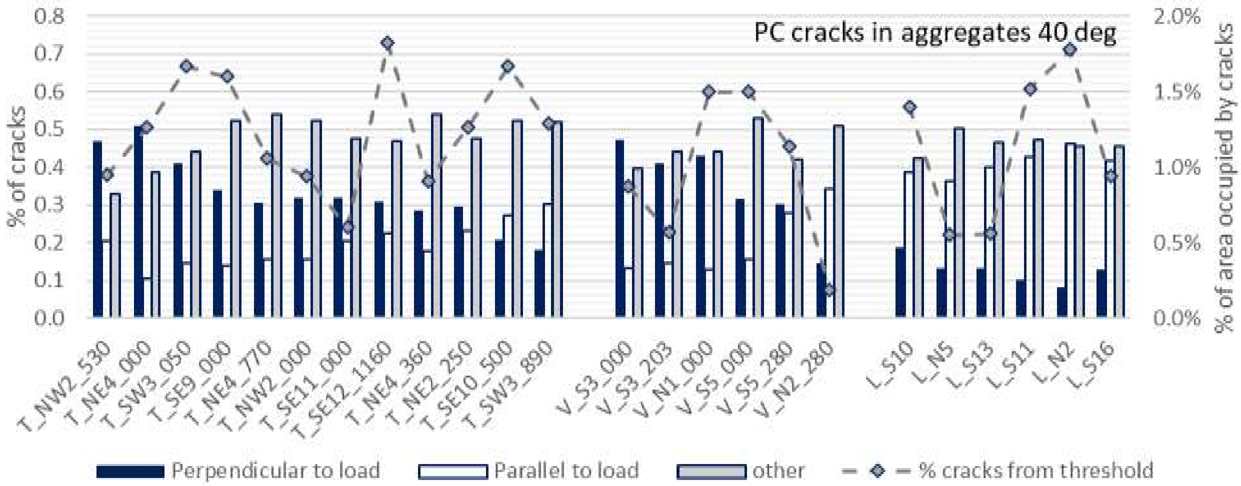

Figure A 18 Directionality for PC samples using 40 ° range for parallel and perpendicular cracks in aggregates

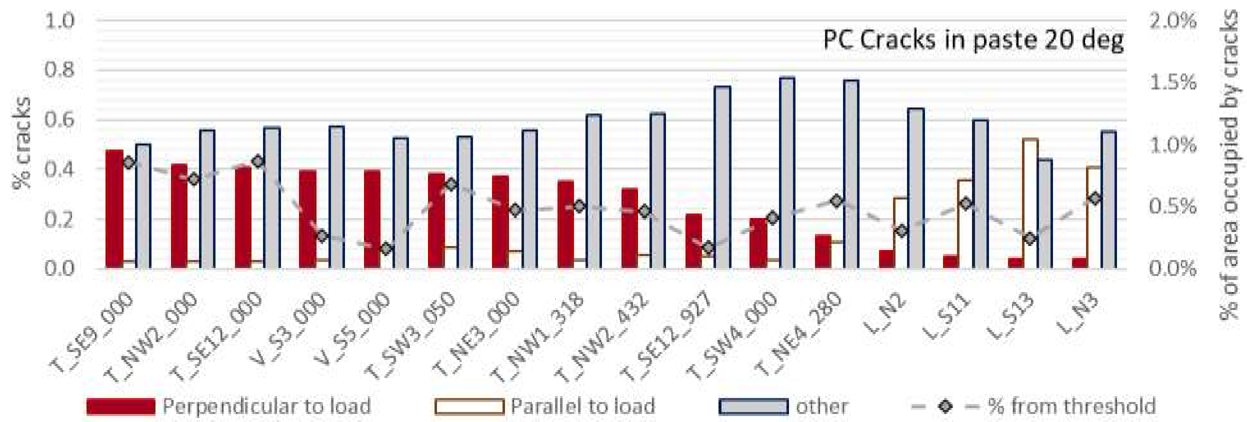

Figure A 19 Directionality for PC samples using 20 ° range for parallel and perpendicular cracks in paste

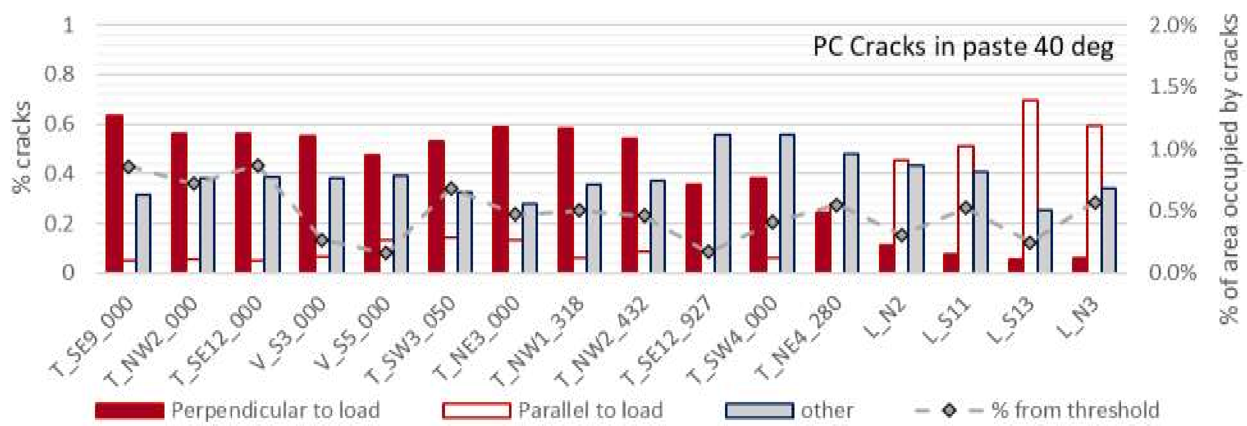

Figure A 20 Directionality for PC samples using 40 ° range for parallel and perpendicular cracks in paste

Number of Cracks

The number of observed cracks in aggregate particles and cement paste were evaluated. The number of cracks per specimen represents the number of distinct lines identified in each image of traced cracks. The next sections will discuss in detail the results obtained specifically for the PC and PS.

Pier Caps (PC)

The number of cracks for PC specimens were evaluated in aggregate particles and cement paste. Results for the average number of cracks in aggregates were found to be similar for all locations except the interior vertical specimens, with approximately 80 cracks in each specimen. By contrast, interior vertical specimens were found to have approximately 50 cracks in each specimen. Results for the average number of cracks in cement paste were found to be significantly lower with an average number of cracks ranging from 8 to 35 cracks per specimen. While no trend was observed for surface specimens compared to those in the interior, core orientation was found to impact the number of cracks with vertical cracks presenting lower values with an average of 10 cracks per specimen, compared to approximately 25 cracks in transverse and longitudinal core specimens.

Pier Shaft (PS)

The number of cracks for PS specimens were evaluated in aggregate particles and cement paste. A different number of cracks in aggregate particles were observed for transverse and longitudinal surface core specimens with transverse cores presenting an average value of 50 cracks per specimen, while longitudinal cores presented an average value of 85 cracks per specimen. Similarly, internal core specimens from transverse, longitudinal and vertical locations exhibited different average numbers of cracks with values of 60, 36 and 88 cracks per specimen, respectively. Although some variation between core specimens from dry and wet locations can be observed, error bars, indicating one standard deviation, in these regions overlap significantly and thus differences due to micro-environment are inconclusive. Results for the average number of cracks in cement paste were found to present lower numbers of cracks, similar to crack numbers in the PC. Surface transverse and longitudinal core specimens presented average values of approximately 35 cracks per specimen; however, cracks in the transverse specimen from the dry region were observed to be double the number of cracks compared in specimens from the wet region. Internal core specimens presented average values of 25, 14 and 44 cracks per specimen in the transverse, vertical and longitudinal cores, respectively. Differences between dry and wet regions for transverse and longitudinal core specimens do not indicate distinct differences, while internal vertical core specimens present distinct differences with an average of 23 cracks per specimen in the dry region, while in the wet region only 5 cracks per specimen were identified.

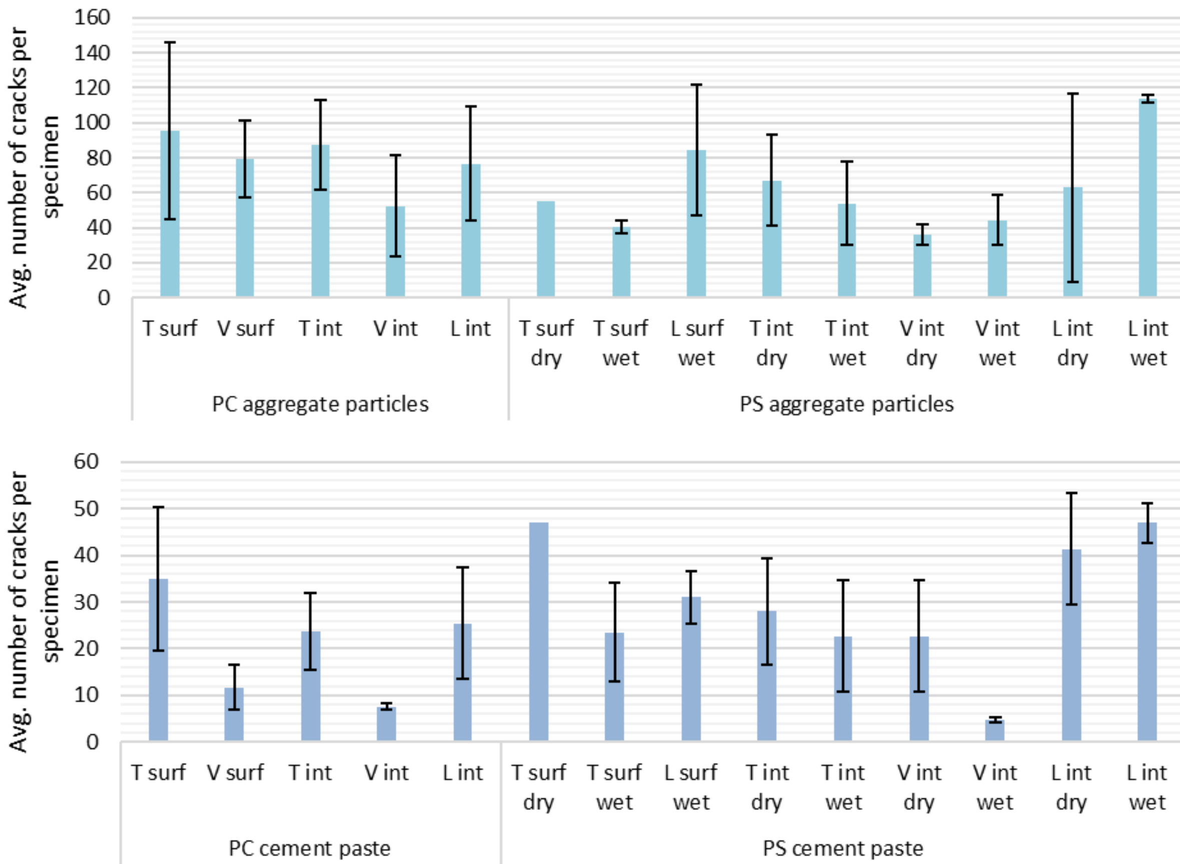

Figure A 21 Number of observed cracks in aggregate particles (top) and cement paste (bottom). Error bars indicate one standard deviation.

Crack Lengths

The length of cracks is important for understanding the extent of damage in concrete specimens. Average crack lengths in aggregate particles and cement paste are presented in Figure A 22 for specimens from the PC and PS. Average crack lengths in aggregate particles of the PC and PS were determined to be 0.86 cm and 0.94 cm and thus present similar crack lengths. Crack widths in cement paste presented average values of 1.09 cm and 1.27 cm in the PC and PS, respectively.

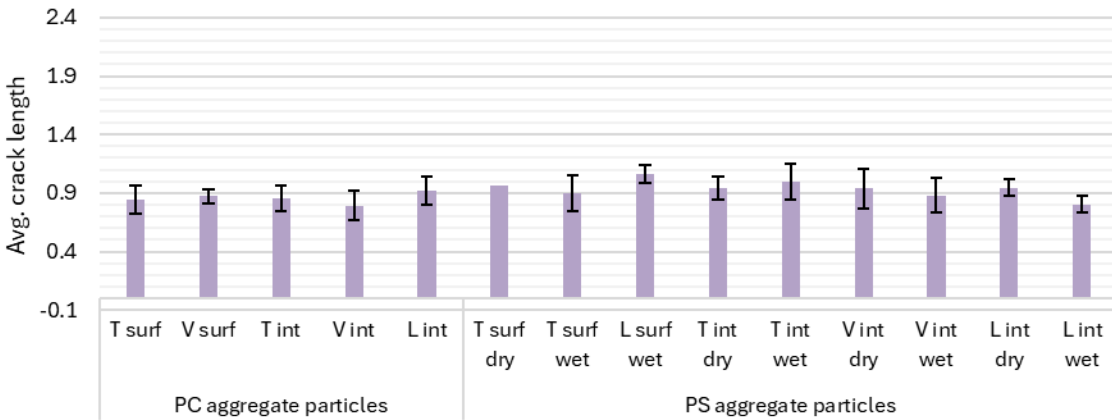

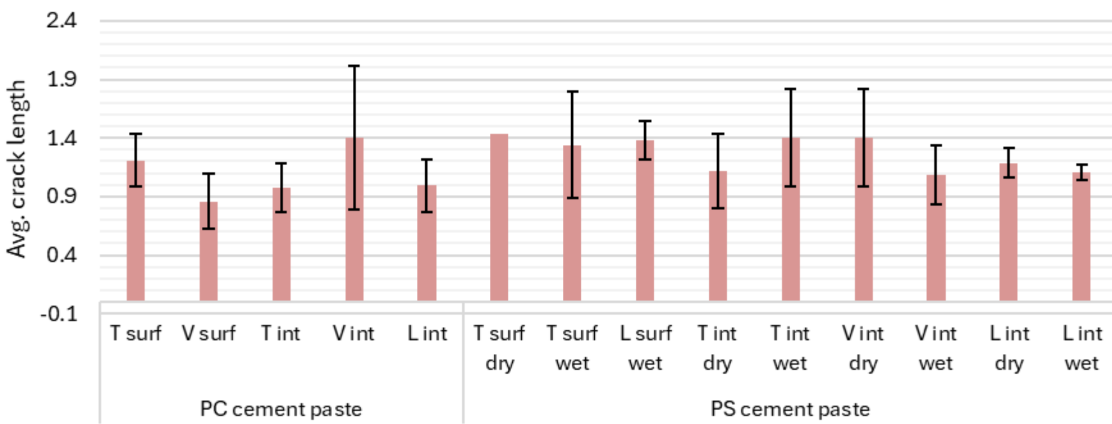

Figure A 22 Average length of observed cracks in aggregate particles (top) and cement paste (bottom). Error bars indicate one standard deviation